Behavior of Boron in 9Cr-3W-3Co Ferritic Heat Resistant Steels

E. El-Kashif, K. Asakura and K. Shibata

Department of Metallurgy, The University of Tokyo, Japan

1. Introduction

Many researchers [1-5] have reported a marked effect of small boron (B) addition on the creep rupture behavior of ferritic heat resistant steels. However the mechanisms for such an effect caused by B are still to be established. In the present study, the behavior of B in 9Cr-3W-3Co steels was examined using Alpha-particle Track Etching (ATE), Scanning Electron Microscopy (SEM), Transmission Electron Microscopy (TEM) and creep test.

2. Experimental Work

The chemical composition of the steels used are given in Table 1.These steels were vacuum melted and processed by hot forging and hot rolling to plates of 15 mm thickness. Then normalizing was carried out at 1050°C for 1 hr for all steels followed by tempering at 780°C for 2 hrs (B1, B2) and at 580°C for 10 hrs followed by 710°C for 20 hrs (B3, B4 and B4-2). B1 and B2 are boiler steels while B3, B4 and B4-2 are rotor steels. Blanks (10x10x5 mm) were thermal aged at 600°C, 650°C, 700 °C for 1,10 and 100 hrs; Creep test was also conducted at 650°C under the nominal stress (140, 160 and 200Mpa); and at 700°C under the nominal stress (100,140MPa). SEM and TEM were carried out for as received and crept samples. The precipitates were characterized by EDX analysis. ATE was carried out for as received, thermal aged and crept samples. To eliminate the effect of tempering condition on the boron distribution, a simulated heat treatment was carried out for all steels (normalizing at 1050°C for 1hr followed by tempering at 710°C for 2hrs using step heating and cooling). ATE was carried out for both normalized and tempered conditions and the creep test was conducted again using the simulated samples.

Table 1 The chemical composition (mass %) of the steels used.

Steels	C	Si	Mn	P	S	Cr	V	Nb	W	Co	B	N
B1	0.1	0.03	0.01	0.004	0.0017	9.05	0.21	0.06	2.94	3.10	0.001	0.053
B2	0.1	0.02	0.01	0.004	0.0024	9.15	0.21	0.05	2.94	3.12	0.006	0.052
B3	0.1	0.03	0.01	0.004	0.0018	8.98	0.21	0.05	2.94	3.08	0.001	0.021
B4	0.1	0.03	0.01	0.004	0.0021	8.95	0.21	0.06	2.94	3.06	0.010	0.021
B4-2	0.1	0.03	0.01	0.004	0.0021	9.12	0.21	0.06	2.89	3.05	0.011	0.019

3. Results

The creep rupture strength of steels (B1~B4) and W3 at 650°C is shown in Fig.1. Steel W3 (free B, 0.05N) is the co-used steel in the past committee of ISIJ. It can be observed that creep rupture strength of B1 (10ppm B, 0.053N) is higher than that of B2 (60ppm B, 0.052N). Also, the creep rupture strength of B4 (100ppm B, 0.021N) is higher than that of B3 (10ppm, 0.021N). Prediction of creep life using Larson-Miller parameter resulted in 10,000 hr at 650°C under 100 MPa for steel B2 and this value is similar to the value of steel W3. However steels B1, B3 and B4 shows 21,000, 27,000 and 45,000 hr respectively under the same conditions. Due to the difference in tempering condition between boiler (B1, B2) and Rotor (B3, B4, B4-2) steels, comparison can only be done for the same tempered condition. For boiler steels, increasing the B content from 10 ppm B to 60 ppm at 0.05% N content shows shorter creep rupture time. This implies that the simultaneous addition of B and N is inconvenient in boiler steels. For rotor steels, fixing the N content at 0.02% the creep rupture time increases by increasing the B content. Fujita [6] recommended that nitrogen content must not exceed 0.02% in B added heat resistant steels. Comparing SEM results of the crept steels to that of the as

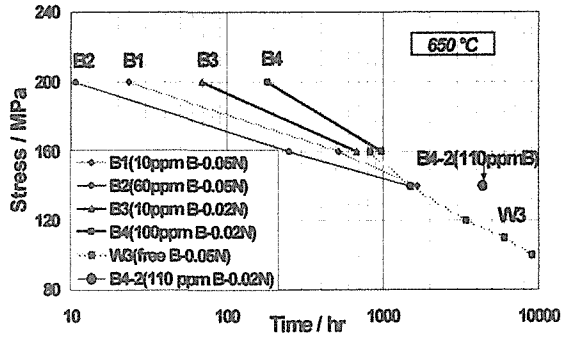

Fig. 1 Creep rupture strength of Steels at 650 °C

received steels it can be seen that the rate of precipitate coarsening is slower in high B steels (B2, B4) than in low B steels (B1, B3), which indicate that boron increases the precipitates stability against coarsening. No other precipitates rather than $M_{23}C_6$ and Fe_2W were detected by the EDX analysis and these precipitates occur along prior austenite grain boundary and inside the grain. TEM of the as received steels showed that B2 shows the largest lath width which is about 0.5 μm, this may be considered as one of the reasons for the short creep rupture time of this steel. In the crept steels at 650 °C under 160 MPa the lath-martensitic structure disappears and changes to subgrain structure. The rate of recovery is very fast in steel B2 and it shows also very low dislocation density. However, steels B3 and B4 shows very slow rate of recovery and high dislocation density. ATE of the as received steels showed very weak segregation along prior austenite grain boundaries, although there is a homogeneous distribution of B in the matrix in steel B4. Noticeable segregation was not observed for steels (B1~B4) after thermal aging at 600°C, 650°C, 700°C for 1,10 and 100 hrs. For specimens crept at 650°C, under 160Mpa and at 700°C under 100MPa, the segregation is occurred along packet boundaries only in steel B4 and the degree of segregation is higher in the specimen tested at 700°C than that tested at 650°C. The density of precipitates containing B showed maximum in steel B2 which has the shortest creep life. This high density of precipitates remains constant up to rupture. This implies that B in precipitates is not the sole mechanism of strengthening in ferritic heat resistant steels. ATE of simulated heat-treated samples shows that the segregation occurs along prior austenite grain boundary in steels (B1~B4) after normalizing but this segregation tends to varnish after tempering and replaced by homogeneous distribution of boron in the matrix. In these simulated heat-treated samples, the borides were observed along prior austenite grain boundaries and inside the grains and the maximum density of borides is obtained also in steel B2 (60ppm B, 0.052N) and the almost same borides distribution is obtained for both normalized and tempered steels. This high density of borides occurred in steel B2 under all heat treatment conditions is may be attributed to the high B-N content.

4. Conclusion

1) Increasing the B content up to 60ppm in 0.05% N steels shows remarkably lower creep rupture strength. However increasing the B content in 0.02% N steels shows an inverse effect.

2) SEM showed that boron in steels increases the stability of precipitates against coarsening. TEM revealed that the stability of the matrix against recovery reaches maximum in low N steels B3 and B4, while this stability is very weak in high N -high B steel B2.

3) ATE showed that segregated B along packet boundaries and free B in solid solution are more effective on strengthening than boron contained in precipitates. Further research is required concerning BN and fine precipitates such as VN and Nb(C, N) in these steels.

References

[1] Takahashi N. and Fujita T., Tetsu-to-Hagane, 61 (1975), pp. 2597-2604.
[2] Azuma T. and Tanaka Y., Iron and Steel Institute of Japan, (1999), pp.102-108.
[3] Harada Y. et al., CAMP- Iron and Steel Institute of Japan, 11 (1995), p.1469.
[4] Uchida H. and Shintani T., Tetsu-to-Hagane, 82 (1996), pp. 244-252.
[5] Activity report of the research committee, Iron and Steel Institute of Japan (1999), pp87-107.
[6] Fujita T., Materials for future power plants, Adv. Materials and Processes, 157(2000), pp. 52-61.

Creep Characteristics of Pd Added 9Cr Heat Resistant Steels at High Temperature over 650℃

H. Okada[1], K. Yamada[1], S. Muneki[1], H. Okubo[1], M. Igarashi[2] and F. Abe[1]
1) National Institute for Materials Science, Japan
2) Sumitomo Metal Industries, Japan

1. Introduction

Recently FePd-based $L1_0$ type ordered phase α" was found to form coherently inside grain in the steel with Pd and to be useful to increase the creep resistance of high-Cr ferritic steel like MX carbonitride [1]. Re addition to this steel was also found to increase the amount of α" and prevent the growth of Laves phase, as a result remarkably reduced the minimum creep rate in the lower stress condition [2]. In this study, creep tests and microstructural observation were carried out on Pd and Re added 9Cr ferritic steel in order to evaluate the effect of Pd and Re addition on creep properties at elevated temperatures.

2. Experimental Procedure

Chemical compositions of the steels used for this test are shown in Table 1. Two 180kg-ingots of Pd & Re-added steel MC1 and reference steel MB1 were prepared by vacuum induction melting. The ingots were hot forged and hot rolled into 25mm-thick plates. The plates were normalized at 1373K for 4h. MB1 was tempered at 1043K for 4h, and MC1 was tempered at 823K for 4h followed by tempering at 1043K for 4h. This double tempering is reported to give optimum microstructre consisting of fine dispersion of α" and MX in side lath decorated with $M_{23}C_6$ along lath, block, packet and prior austenite boundaries [3]. Creep test, tensile test and aging test were carried out at the temperature range of 873 to 1023K. Microstructural observations were conducted with optical and scanning electron microscopy on both steels before and after aging.

Table 1 Chemical compositions of the steels. [mass%]

Mark	C	Si	Mn	Cr	W	V	Nb	N	B	Pd	Re
MB1	0.08	0.30	0.51	9.0	2.9	0.20	0.05	0.05	0.005	-	-
MC1	0.10	0.04	0.36	9.0	2.9	0.19	0.05	0.03	0.005	0.70	0.49

3. Results and Discussion

Below 973K, MC1 showed superior creep resistance to MB1, as shown in Fig. 1 and 2. Both MB1 and MC1 showed the bending of stress vs. minimum creep rate curve at around 0%-offset stress of each temperature. Stress exponents of MB1 under low stress condition were about 5.5 and independent of test temperature. While, those of MC1 were varied from 4 to 9 and depended on temperature. Amount of MX was not affected by aging temperature as shown in Fig. 3. Although the amount of MX for MC1 was about 30% less than that for MB1, fine α" precipitated uniformly at low temperature in MC1, as shown in Fig. 4. From these results it was suggested that the stress exponent at lower stress condition depended on the fine dispersions such as MX and α". Further more MC1 showed homogeneous creep deformation at lower stress condition comparing with MB1, as shown in Fig.5. Prevention of growth of precipitates such as Laves phase and $M_{23}C_6$ with Re was considered one of the causes of this excellent creep characteristic.

References

[1] M. Igarashi, et al., Repot of 123rd Committee on Heat-Resisting Metals and Alloys, Jpn. Soc. for the Promotion of Sci., 39(1998), 355-362 *(in Japanese)*
[2] H. Okada, et al., CAMP ISIJ, 14(2001), 1290 *(in Japanese)*
[3] M. Igarashi, et al., ISIJ International, 41 (2001), Supplement, S105-S105

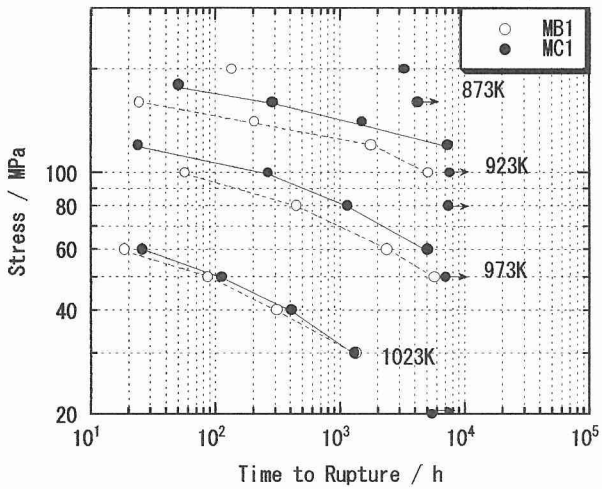

Fig. 1 Comparison of creep rupture test results between MB1 and MC1 showing the superior creep property of MC1 up to 973K.

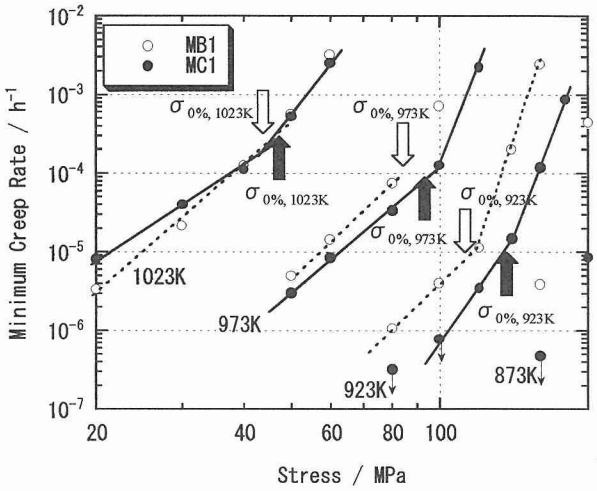

Fig. 2 Stress dependence of minimum creep rate of the steels showing the bending at the 0% off-set stress: $\sigma_{0\%}$ of each temperature.

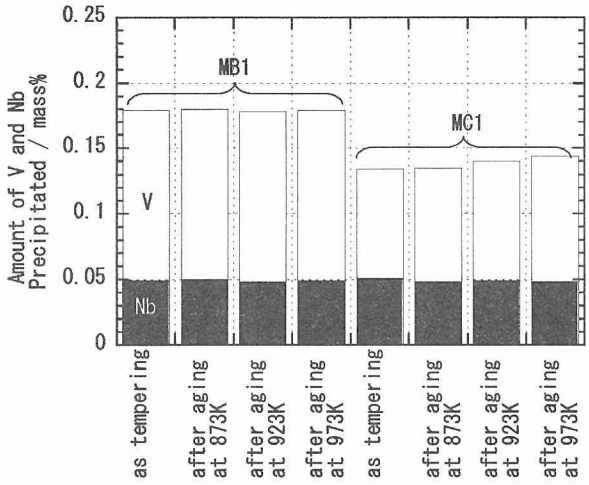

Fig. 3 Amount of precipitated V and Nb before and after aging for 1000h showing little effect of aging and the difference of the amount between the steels.

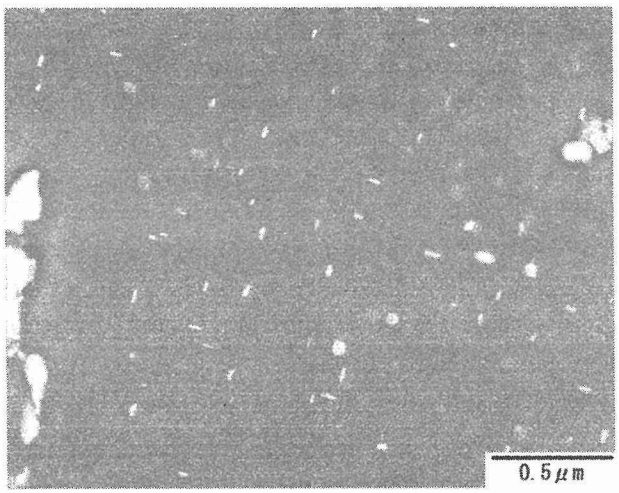

Fig. 4 Secondary electron images of MC1 aged at 873K for 100h showing 100nm-length disk-like α" precipitating coherently to the bcc matrix.

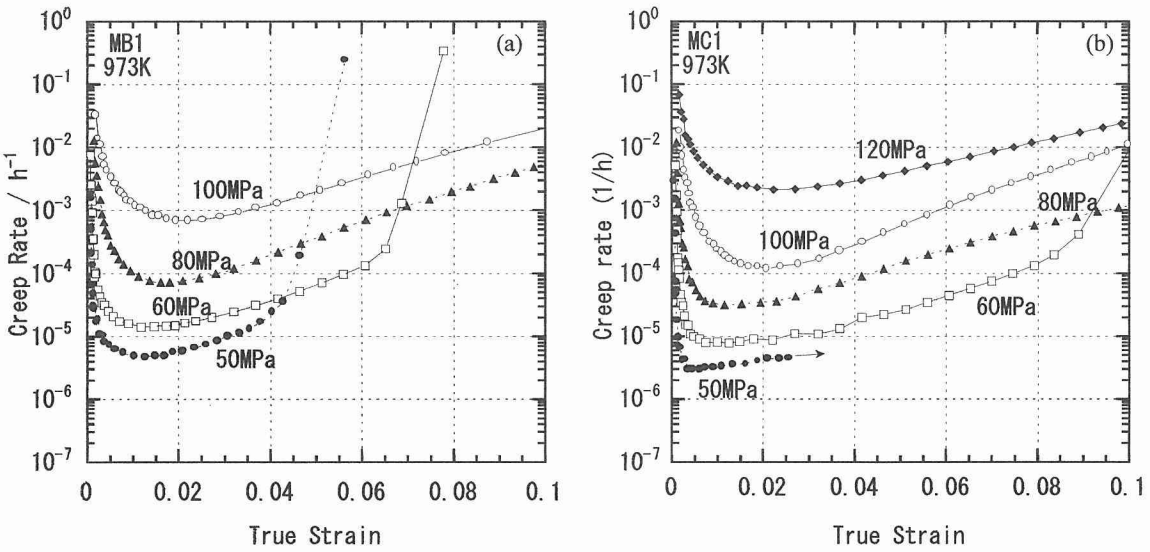

Fig. 5 True strain vs. creep rate curves of MB1: (a) and MC1: (b) crept at 973K showing loss of creep ductility of MB1 and homogeneous creep deformation of MC1 under low stress condition.

Relation between Rupture Strength and Substructure

M. Tamura[a], H. Sakasegawa[b], Y. Kato[b], A Kohyama[b],

H. Esaka[a] and K. Shinozuka[a]

a National Defense Academy of Japan, Japan
b Institute of Advanced Energy, Kyoto Univ., Japan

1. Introduction

Many creep equations have been developed, where steady state creep rate is described as a function of temperature, stress and microstructural parameters such as grain size, dislocation density and so on. Creep phenomena have been well understood qualitatively based on these equations. However, the microstructural parameters generally have not yet been calculated using creep data. Some of the authors have developed a new creep equation [1,2] which can predict the equivalent obstacle spacing for a mobile dislocation using only rupture time. Sub-grain size and particle size are measured using a transmission electron microscope and the results are compared with the predicted values.

2. Experiment

Creep rupture tests have been made at around 650℃ on ultra low carbon steels containing about 0.1% of TaN and a small amount of W, separately. High chromium martensitic steel containing 0.04% of TaC was also tested as a comparison. A hot rolled plate of each steel was heat treated as shown in Table 1.

Table 1 Chemical composition (%) and heat treatment

Steel	C	Cr	W	V	Ta	N	Normalizing	2nd heat treatment
FETA1	0.0031	-	-	-	-	0.0019	1200℃	650℃ for 500h
FETA2	0.0028	-	-	-	0.093	0.0130	1200℃	650℃ for 500h
FETA4	0.0026	-	0.031	-	-	0.0018	1200℃	650℃ for 500h
F15CA	0.100	7.71	2.1	0.18	0.04	0.0043	1200℃	800℃ for 2h

3. Results and discussion

Microstructures of FETA1, 2, 4 are full ferrite and F15CA has tempered martensitic structure. Thin films were observed under TEM for some ruptured specimens and sub-grain sizes were measured. Two kinds of TaN particles of 13 and 56 nm in average diameter were precipitated in FETA2. In F15CA both fine TaC particles of 13 nm and massive $M_{23}C_6$ precipitates were observed. Metallurgical characteristics of the experimental steels are listed in Table 2. Maximum inter-MX particle distance of FETA2 is calculated from the average particle size assuming that all Ta forms TaN. Maximum inter-MX particle distance of F15CA was calculated as follows: average diameter of TaC is measured as 13.3 nm using the extracted replica and total amount of Ta as tempered state are analyzed

chemically and all of it is assumed to form TaC.

Fig.1 shows the results of creep rupture tests at around 650℃ in air. The data are plotted in a semi-logarithmic diagram according to the new creep theory [1,2]. Linear relationship is confirmed within the test conditions, though the test duration is limited due to oxidation or nitrization. FETA4 contains a small amount of W which corresponds the maximum solubility in ferrite avoiding precipitation of Laves phase. Rupture strength of FETA4 is only a little higher than that of FETA1, pure iron, at 650℃. Rupture strength of martensitic steel, F15CA, is much higher than those of FETA1 and FETA4. Rupture strength of FETA2, a TaN-containing steel, is lightly lower than that of F15CA. However, since the slope of a stress-time to rupture curve of FETA2, $-\partial\sigma/\partial\log(t)$, is much smaller than that of F15CA, it is possible that rupture strength of FETA2 is superior to the martensitic steel, F15CA, at a low stress level.

Table 2 Amount of precipitates and metallurgical parameters (μm)

Steel	Hardness HV10	Precipitates (%)	Sub-grain Size	Maximum inter-particle Distance	Equivalent obstacle spacing, d/p
FETA1	66	-	9.45	-	3.88
FETA2	99	0.1% TaN *	1.41	0.131	0.35
FETA4	73	-	ND	-	0.79
F15CA	168	0.025%TaC+1.56%M23C6	3.48	0.204	0.18

*: calculated ND: not determined

Equivalent obstacle spacing against mobile dislocations, d/p, can be estimated using only time to rupture [1,2]. 3.88, 0.35, 0.79 and 0.18 μm were calculated as the obstacle spacing for the reference steel, TaN and W-containing steels and martensitic steel, respectively. Table 2 shows that d/p for pure iron is comparable to the sub-grain size and d/p's for the MX hardened steels are much smaller than each sub-grain size and comparable to the maximum inter-MX particle distances for each. The value of d/p for FETA4 is smaller than that of pure iron, though the sub-grain size is not yet determined, and the result implies that the creep resistance of FETA4 is controlled by dislocation motion dragging of solute W atoms.

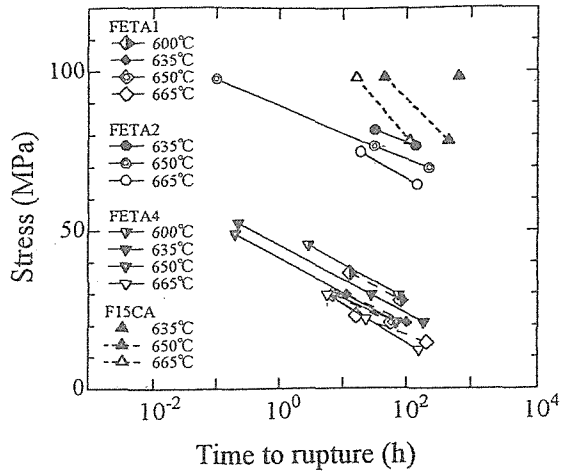

Fig.1 Semi-logarithmic plot of time to rupture and stress for the experimental steels.

The above suggests that the proposed method for the estimation of the equivalent obstacle spacing is reasonable.

[1] Tamura, M. Esaka, H and Shinozuka K., ISIJ Int., 39(1999), pp.380-387.

[2] Tamura, M. Esaka, H and Shinozuka K., Mat. Trans. JIM, 41(2000), pp.272-278.

A Study on the Variation of the Hardness and the Creep Rupture Strength with Thermal Histories in a Mod. 9Cr-1Mo Steel

S. H. Ryu *, Y. S. Lee *, B. O. Kong *, J. T. Kim *
* Material Development Research Team, Doosan Heavy Ind., Korea

1. Introduction

The Modified 9Cr-1Mo steel identified as T91, P91 and F91 in the ASME specification has been widely used for the construction of modern power plants. The available data on the influence of process parameters during manufacturing and fabrication on its properties are not sufficient. According to Allen [1] and Brett [2], abnormal heat treatments causing the low hardness below 190 Hv resulted in premature failures of individual components. There are practically the thermal cycles deviating from normal temperatures in the transition zones or the whole component during and after hot forming, welding, straightening and local heat treatment. In this study, the influence of various thermal cycles on the hardness and the creep rupture strength was analyzed in the base metal and the weldments made in tube and pipe of a Mod.9Cr-1Mo steel.

2. Experimental procedure

The chemical compositions of the alloy studied are given in Table 1. The dimensions of the tube and the pipe were OD 50.8mm x WT 8.7mm and OD 425mm x WT 62mm, respectively. The as-received hardness values of the tube and the pipe were 200 to 227 Hv.

Table 1. Chemical composition of Mod.9Cr-1Mo steel used for this study (wt%).

Alloy	C	Si	Mn	Ni	Cr	Mo	V	Nb	N	Ti	Al
Mod.9Cr-1Mo	0.09	0.28	0.37	0.05	8.43	0.92	0.19	0.08	0.049	0.007	0.014

The thermal cycles consisted of the first heating (normalizing) at 850°C to 1070°C for 1 hour and the second heating (tempering) at 550°C to 830°C for 1 to 100 hours followed by air cooling. Here, the first and the second heating simulate the high temperature exposures caused by hot forming, normalizing after hot forming and straightening and the low temperature exposures such as PWHT and PFHT respectively. The creep test specimens with 6.5mm diameter were cut off from the tube and the pipe with different thermal cycles. Creep tests were performed at 600°C and initial stresses of 140 MPa and 108 MPa in air.

3. Results and discussions

3.1 The variation of the hardness with thermal cycles

Transformation temperatures (Ac1 and Ac3) of the grade 91 steel are generally found between 820°C and 850°C for the Ac1 and between 880°C and 940°C for the Ac3 respectively, although they are dependent on chemical compositions and heating rates. Fig.1 shows the effect of normalizing temperature on the as-tempered hardness. The hardness value after tempering at 730°C increased with increasing normalizing temperature. However, as tempering temperature increased above 780°C, normalizing at temperatures beyond the Ac3 had nearly no effect on the as-tempered hardness. Fig.2 indicates the variation of hardness with tempering at temperature range of 550 to 830°C for the normalized specimens at two temperatures of 850°C just above the Ac3 and 1050°C corresponding with normal normalizing temperature. The lowest hardness was occurred at tempering just below the Ac1, subsequent to normalizing at temperatures just above the Ac1. Among the thermal cycles in twice identified as normalizing and tempering, the low hardness was remarkably influenced by the normalizing at temperatures just above the Ac1 of the inter-critical region between the Ac1 and the Ac3 rather than tempering. The hardness in the softened zone of weld HAZ lowered continuously during a number of repair welding and repeated PWHT and achieved to be about 168 Hv, which was about 18% lower than that of the as-received base metal.

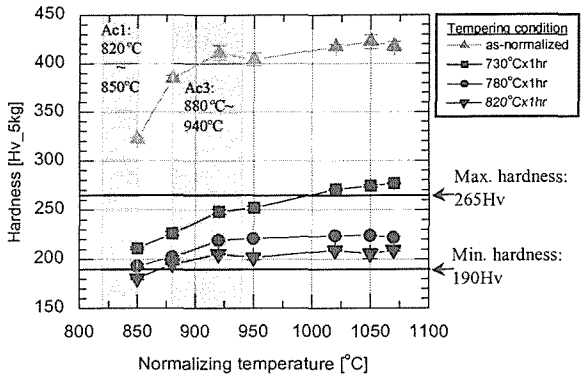

Fig.1 Variation of the hardness with normalizing for 1 hour at various temperatures.

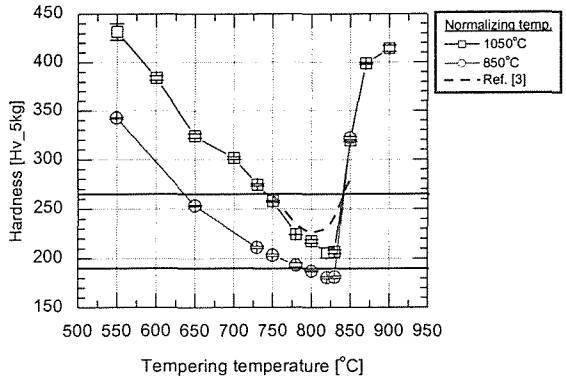

Fig.2 Variation of the hardness with tempering for 1 hour at various temperatures.

3.2 The variation of the creep rupture strength with hardness

Fig.3 shows the creep rupture strength (CRS) at 600°C of a Mod.9Cr-1Mo steel with normal hardness and abnormal low or high hardness. T91 with normal hardness, 210Hv, indicated the longest rupture life. CRS of T91 with hardness value lower or higher than normal value was relatively deteriorated. Especially, the CRS of the specimen with the lowest hardness, 155Hv, was found to be below the allowable stresses of T91 base metal determined in ASME specification. The low value was attributed to the fully recovered dislocation structure and the weakening of precipitation hardening associated with the abnormal thermal cycles. The lowest CRS of the T91 steel was still superior to that of the plain 9Cr-1Mo steel, T9, without V and Nb elements. T91 with 170Hv lies at lower bound of ORNL data band but above the allowable stresses of ASME specification. The specimen with the highest hardness, 420Hv, contained fully untempered martensite and indicated higher CRS compared to the specimens with low hardness. However, it is expected that higher hardness values have no beneficial effect on long-term CRS due to the microstructural unstability.

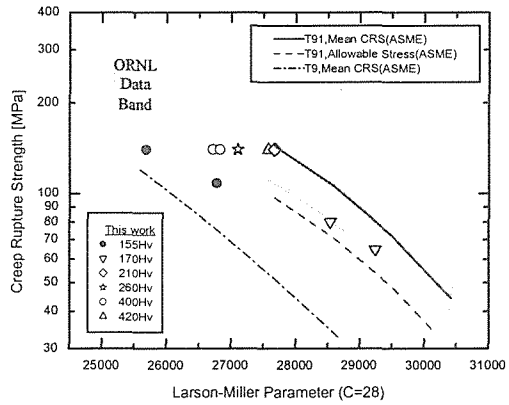

Fig.3 Comparison of the creep rupture strength (CRS) at 600°C measured at this work with reference data.

4. Conclusions

1) The low hardness was occurred at the heating (tempering) just below Ac1 subsequent to heating (normalizing) at temperature especially just above Ac1 of inter-critical region between the Ac1 and the Ac3. The low hardness was remarkably influenced by abnormal normalizing rather than tempering.

2) The low hardness, 155Hv, showed low creep rupture strength below the allowable stresses of T91 base metal in the ASME specification. This low value was attributed to the fully recovered dislocation structure and the weakening of precipitation hardening associated with the abnormal thermal cycles.

References

[1] Allen, D. J. and Brett, S. J., Proc. of Int. Conf. on Case Histories on Integrity and failures in Industry (CHIFI), Milan, Italy, 28 Sep. - 1 Oct. 1999, pp.133-143.

[2] Brett, S. J., Proc. of the 3rd Conf. on Advances in Materials Technology for Fossil Power Plants, Univ. of Wales Swansea, UK, 5th April – 6th April 2001, pp.343-351.

[3] Ertuchtigung eines modifizierten 9Cr1Mo Stahles für des praktischen Einsatz bis 600 ° , ECSC Report, EUR 14575 DE, 1993, pp.54-57.

Embrittlement in Copper Bearing Heat Resistant Martensitic steels

Y. Futamura, T. Tsuchiyama and S. Takaki
Dept. of Materials Science and Engineering, Kyushu University, Japan

1. Introduction

From the viewpoint of improving the power generating efficiency, higher creep strength is required for high chromium martensitic steels which are widely used as structural materials in power generating plants. The strength of these martensitic steels is mainly derived from high density of dislocation, thus it is important to retard the recovery of martensite during creep deformation for prolonging the creep-rupture time. We have already reported that the addition of copper (Cu) is effective for retarding the recovery because of the dislocation pinning effect by finely dispersed Cu particles[1]. However, the addition of Cu more than 2% reduces the ductility of these steels. If the ductility is kept high enough even at high temperature, the creep properties of the Cu bearing martensitic steels could be improved more. In this study, creep deformation behavior and microstructural changes were investigated in Cu bearing 9%Cr martensitic steels, and then the mechanism of embrittleness was discussed in terms of the segregation and precipitation behaviors of Cu at grain boundary.

2. Experimental procedure

9%Cr-1%Cu and -4%Cu steels with ultra low carbon were mainly used in this study. Specimens were solution-treated in an Ar gas atmosphere and then quenched into water. In order to remove the effect of grain size on creep deformation behavior, austenite grain size of these steels were controlled to be around 80μm by varying the solution treatment conditions; 1273K-3.6ks for the 9%Cr-1%Cu steel and 1423K-7.2ks for the 9%Cr-4%Cu steel. Creep tests were carried out under a condition of 873K-140MPa. Microstructures were observed with Scanning Electron Microscope (SEM). Cu content segregated at grain boundary was measured by Auger Electron Spectrometry (AES).

3. Results and discussion

Fig. 1 shows creep curves of the 9%Cr-Cu steels crept under the condition of 873K-140MPa. With increasing Cu content, creep strength is markedly improved but the ductility is gradually decreased. For instance, 9%Cr-4%Cu steel exhibits a slight plastic deformation, and the rupture elongation is only 10%. **Fig. 2** represents scanning electron micrographs obtained from the area just nearby the fracture surface in the crept 9%Cr-1%Cu and -4%Cu steels. In the 9%Cr-1%Cu steel, prior austenite grains are elongated to the tensile direction with

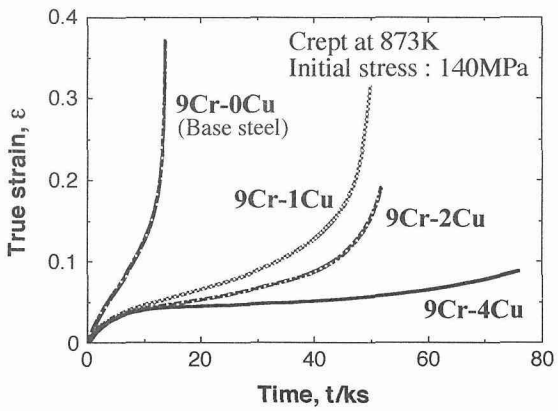

Fig. 1 Creep curves in 9%Cr steels with various Cu contents.

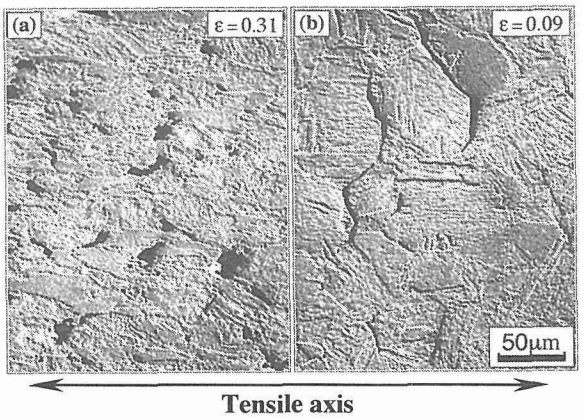

Fig. 2 Scanning electron micrographs obtained from the area nearby the fracture surface in 9%Cr-1%Cu (a) and -4%Cu (b) steels. Specimens were crept at 873K-140MPa.

sufficient ductility. However, in the 9%Cr-4%Cu, equiaxed prior austenite grain structure is retained, and intergranular cracks are generated along the grain boundaries which are located in the perpendicular direction to the tensile axis. SEM observations of the 9%Cr-4%Cu steel crept for 50.4ks (ε=0.05) revealed that the grain boundary has been densely decorated with many precipitated Cu particles as shown in **Fig. 3**. The particle size (>0.2μm) is much larger than that within the matrix (<0.05μm). It is also found that several voids are formed adjacent to the large Cu particles precipitated on the grain boundary. The voids were seemed to be linked each other and formed large ones on the grain boundary. The formation of large voids should lead to the intergranular cracks, and this causes a sudden brittle fracture at the early stage of creep deformation in high Cu steels.

Fig. 4 represents Auger electron spectrums obtained from the transgranular and intergranular fracture surfaces in the 9%Cr-4%Cu steel which was annealed at 1273K for 50.4ks after the preannealing at 1523K for 7.2ks[†1]. This result demonstrates that Cu atoms have segregated at austenite grain boundaries and the content of segregated Cu reaches 50at% or more on the solution treatment. The marked segregation should result in the preferential precipitation and coarsening of Cu particles on the prior austenite grain boundaries during the creep deformation. Therefore, suppression of Cu segregation is one of important keys to improve the ductility in high Cu steels.

[†1]Austenite grains were intentionally enlarged by this treatment to make the grain boundary fracture easy. Since this heat treatment is different from the solution treatment for creep test pieces, the content of segregated Cu is not quite same between the specimens. But the tendencies should be similar in the segregation behavior.

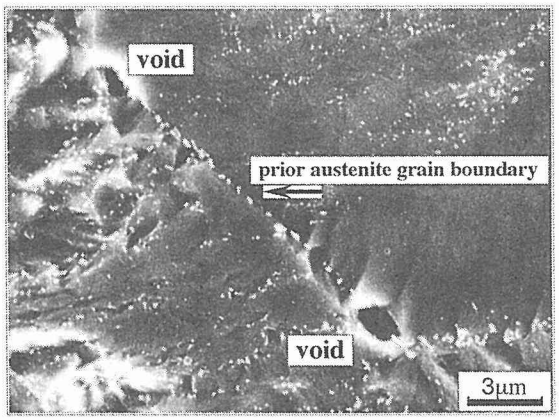

Fig. 3 Scanning electron micrograph taken around a prior austenite grain boundary in 9%Cr-4%Cu steel. Creep deformed to 0.05 at 873K.

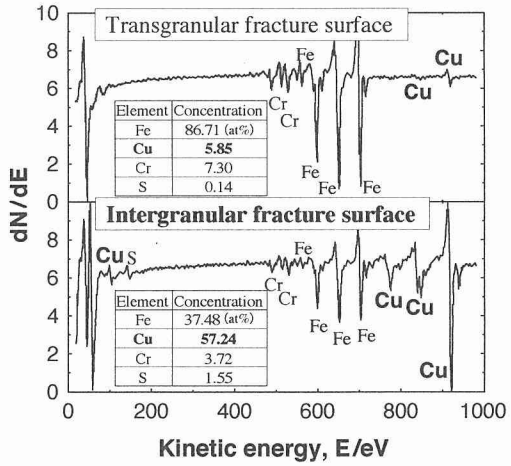

Fig. 4 Auger electron spectrums obtained from the transgranular and intergranular fracture surfaces in 9%Cr-4%Cu steel which was annealed at 1273K for 50.4ks after the preannealing at 1523K for 7.2ks, and then water-quenched to room temperature. The specimen was fractured at 173K to obtain brittle fracture surface.

4. Conclusions

(1)Cu addition to martensitic 9%Cr-Cu steels improves their creep strength at 873K but markedly reduces the creep-rupture elongation. The 9%Cr-4%Cu steel exhibits brittle intergranular fracture along prior austenite grain boundaries.

(2)The intergranular fracture is caused through the linkage of voids initiated at large Cu particles on the grain boundaries.

(3)The precipitation of large Cu particles is promoted by the marked grain boundary segregation of Cu atoms which has occurred during the solution treatment prior to the creep testing.

Reference

[1] Y. Futamura, T. Tsuchiyama and S. Takaki ISIJ International **41**(2001), pp.S106-110.

Steam Oxidation Characteristics and Preventive Maintenance Technology of Materials for Boilers

M. Ishikawa, Y. Fukuda
Babcock-Hitachi K.K., Japan

1. Introduction

In power generation boiler, steam oxidation of heat exchanger tubes and pipes could be a matter of concern. Thick oxide scale formed inside the tubes of high temperature zone can increase the tube temperatures and unexpectedly shorten the tube lives. Resultant exfoliation of scales can cause tube failures in particular portions such as U-bends and erosion of turbine blades in the downstream side. These problems could become more serious in USC boiler. Therefore, we established an estimation method of scale growth rate of tubing materials and creep damage evaluation considering scale growth and also studied scale exfoliation mechanism.

2. Growth rate and control method of steam oxidation scales

It is generally assumed that the steam oxidation can be approximated to a parabolic rate law as follows;

$$\Delta W^2 = kpt \qquad (1)$$

Where ΔW is the scale thickness or weight gain, kp the rate constant and the oxidation time. Fig.1 is steam oxidation test results for several austenitic steels. Exfoliation of the scale is generated at interface between inner and outer scale when the inner scale becomes over 50 μ m. The shot blasting is very effective in order to suppress steam oxidation of 18-8type stainless steels under 700℃.

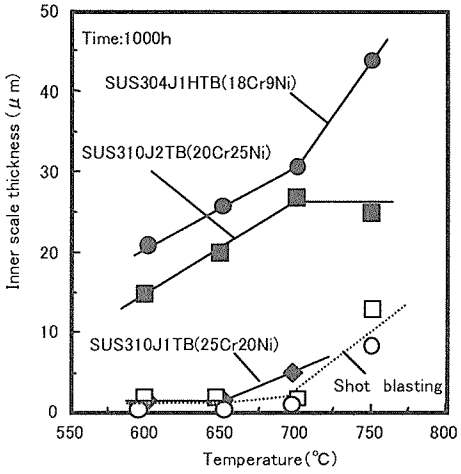

Fig.1 Steam oxidation behavior of austenitic Steels [1]

On the other hand, Cr and Si contents in the alloy influence Kp of 2～12Cr ferritic steels as follows[1].

$$kp = A \cdot \exp\{-E/(2.3RT)\} \qquad (2)$$

$$E = 332.2 - 17.43[Cr] - 68.95[Si] \qquad (3)$$

$$\log A = 15.9 - 1.11[Cr] - 4.49[Si] \qquad (4)$$

Where, E is the apparent activation energy, A the frequency factor, R the gas constant, T the absolute temperature, [Cr] and [Si] are the concentrations of the corresponding elements in mass.%. Fig. 2 is the plots of log Kp calculated for Eq. (3),(4) and (5) versus observed log Kp in the laboratory tests. The calculated and observed corrosion rate constants reveal an approximate 1:1 relationship.

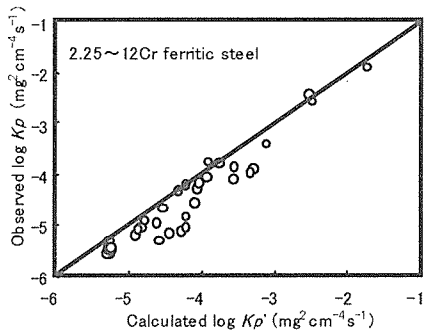

Fig.2 Comparison of the calculated Kp' and observed Kp

3. Exfoliation mechanism of steam oxidation scale

The scale exfoliation is generated by the excessive strain over the adhesion of the scale. For example, Fig. 3 shows the exfoliation strain of 2.25Cr1Mo tube sampled from actual plant. The exfoliation strain decreases with increase of scale thickness and the minimum value is about 0.2%. Fig.4 is relationship between calculated strain in the plant outage and scale growth temperature. The main reason of scale exfoliation in austenitic steels should be excessive compressive strain in inner scale. On the other hand, the tension strain is generated in the ferritic steel and the value is smaller than the austenitic

steels. Therefore, it can be said that the ferritic steel is better in the scale peelability than austenitic steel. However, the scale exfoliation may be enhanced over 550℃, since 0.1～0.2% tensile strain which is similar to finite strain for scale exfoliation is generated.

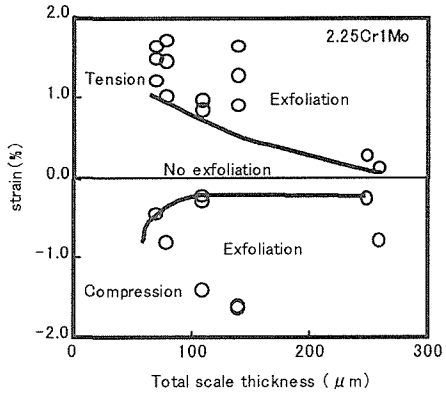

Fig.3 relationship between exfoliation strain and scale thickness.

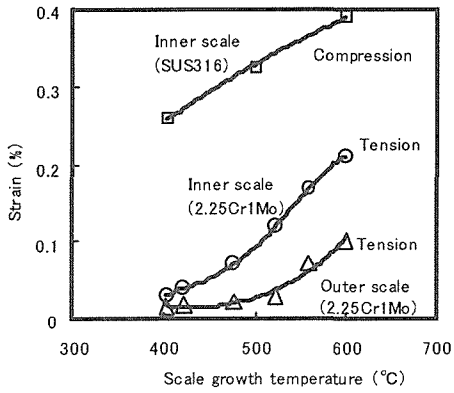

Fig.4 Scale growth temperature and strain in the plant outage

4. Creep damage evaluation considering scale growth

Creep damage evaluation considering the metal temperature increasing caused by the heat transfer inhibition of scale and decrease in wall thickness is required because the thick scale is formed in the inside and outside of the tubes in high steam temperature zone. Fig.5 shows flow diagram of creep damage evaluation and Fig.6 shows the example of creep damage evaluation results based on the method shown in Fig.5. With Fig.6, it is proven that creep damage increases rapidly by the stress increment by rise of the metal temperature and decrease in wall thickness.

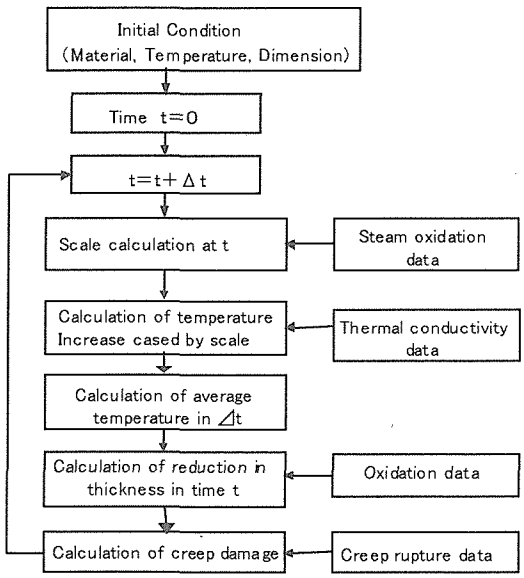

Fig.5 Creep damage evaluation flow of boiler tube

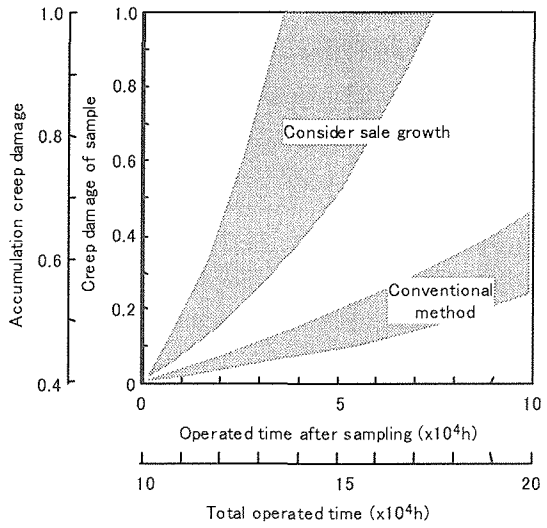

Fig.6 Example of creep damage evaluation

References

[1] T. Sato, K. Tamura. K. Mitsuhata, K. Sakai, Proc.of 7th Mechanical Material and Processing (1999)

[2] Y. Fukuda, K. Tamura and K. Suzaki, Proc. of Int. Symp. on Plant Aging and Life Predictions of Corrodible Structures, Sapporo, Japan., May 15-18 (1995) pp.835-840

Automated Image Processing and Analysis of Fracture Surface Patterns Formed during Creep Crack Growth in Austenitic Heat-Resisting Steels with Different Microstructures

M. Tanaka*, R. Kato*, Y. Kimura** and A. Kayama***
* Department of Mechanical Engineering, Akita University, Japan
** Nippon Systemware Company Ltd., *** Furukawa Company Ltd.

1. Introduction

Grain-boundary fracture is the dominant fracture mechanism in commercial heat-resistant alloys at high temperatures. There are generally no characteristic patterns on grain-boundary fracture surfaces of high-temperature components, such as striation in fatigue and river pattern in brittle fracture, which give information about fracture origin or growth direction of the main crack. Grain-boundary fracture surfaces have a self-similarity, and the morphological feature was estimated by the fractal dimension on the ruptured specimens of heat-resistant alloys [1]. The fractal dimension of the fracture surface patterns (the fractal dimension of the grain-boundary fracture surface profiles, D_f) can be correlated with the grain-boundary microstructures (the fractal dimension of the grain-boundary surface profiles, D_{gb}) and the creep-rupture properties [1]. Grain-boundary fracture pattern may also change during crack growth in materials during creep at high temperatures. It is desirable for quantitative estimation of microstructures and fracture surfaces by a computer to process images automatically, since difference in manual image processing may affect the result of fractal analysis [2]. In this study, a computer program was developed for automated image processing. The fractal dimension of the grain-boundary fracture surface profiles was then estimated using a software on the processed images of the fracture patterns in the austenitic heat-resisting steels with different grain-boundary microstructures. Micorstructural features affecting the two-dimensional fracture patterns during crack growth process were also experimentally discussed.

2. Experimental procedure and image processing

Creep crack growth experiments were carried out using the surface-notched specimens of the 21Cr-4Ni-9Mn steels with serrated grain boundaries (D_{gb}=1.233) and those with straight grain boundaries (D_{gb}=1.094) (grain diameter=9.9×10^{-5} m) at 973 K [3]. Details of the heat treatments were described in the reference [3]. The crack depth, which includes the notch, was estimated from the measurement of surface crack length [4].

The fractal dimension of the grain-boundary fracture surface profiles (D_f) was estimated at the central part of the fracture surface profile (about 1.7 mm) at the distance (x) of 0.3, 0.7 and 1.4 mm from the notch root on the ruptured specimens. A computer program (Visual Basic) was developed for automated image processing. In the program, a red line with one pixel width is drawn on images (bitmap file) for fractal analysis in the following process:

(1) The threshold value is automatically obtained by the mode method from the brightness histogram of original images (Fig. 1a), and the binarization of the images is then

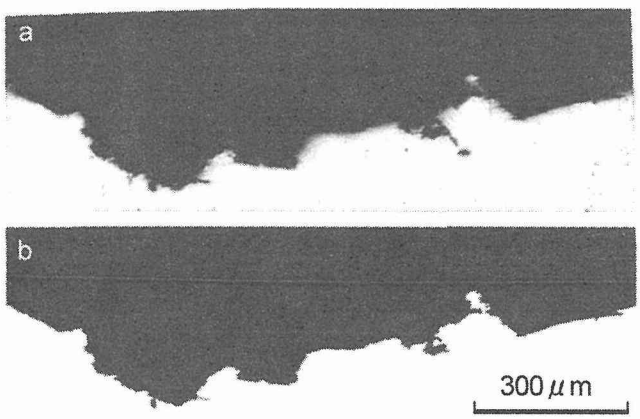

Fig. 1 Example of automated image processing (straight grain boundaries, σ_g=167 MPa, x=0.3 mm).
a. original image b. processed image
(σ_g: gross section stress)

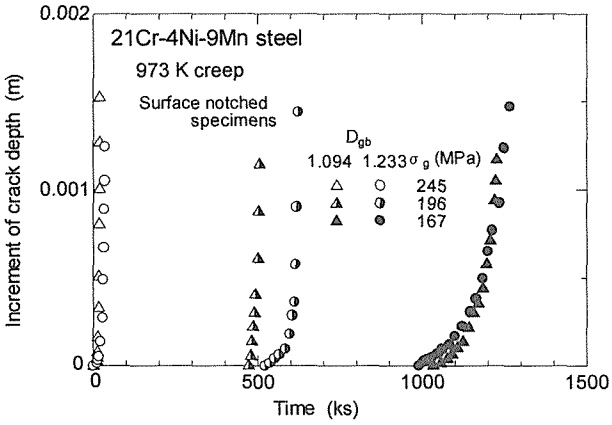

Fig. 2 Increment of crack depth during creep at 973 K.

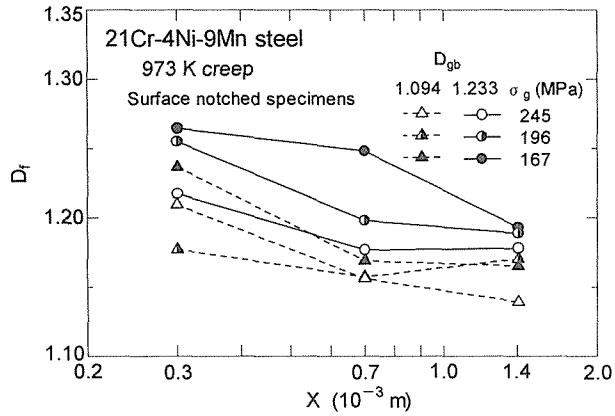

Fig. 3 Change in the fractal dimension (D_f) with the distance from the notch root (x).

made according to the threshold value.

(2) A binary image processing is employed to eliminate "isolated points" in both white and black regions. A red line with one pixel width is then drawn between these two regions to connect one pixel with one of eight neighbouring pixels.

(3) Final binary image processing is carried out to eliminate "islands", and the red line is then converted in order to connect one pixel with one of four nearest neighbouring pixels (a red line is actually drawn in Fig. 1b).

3. Results and discussion

Figure 2 shows the increment of crack depth during creep at 973 K. The crack growth period is longer in the specimens with serrated grain boundaries (D_{gb}=1.233) than in those with straight grain boundaries (D_{gb}=1.094), and is longer under the lower gross section stresses. Grain-boundary cracks initiated at the notch root of the specimens. The fractal dimension of the grain-boundary fracture surface profiles (D_f) was estimated in the scale length range larger than one grain-boundary length (about 6×10^{-5} m). The value of D_f decreases with increasing the distance form the notch root, namely, with crack growth. The value of D_f is larger in the specimens with serrated grain boundaries (D_{gb}=1.233) than in those with straight grain boundaries (D_{gb}=1.094), and is larger in the specimens crept under the lower gross section stresses (σ_g). These results were correlated with the number of grain-boundary microcracks linked to the fracture surface. The microcracks also decreased with increasing the distance from the notch root and with increasing gross section stress, since the increase of net section stress resulted in the decrease in the time required for initiation and growth of the microcracks in the intensely creeping region ahead of the main crack. The number of the microcracks was larger in the specimens with serrated grain boundaries (D_{gb}=1.233) in which the crack growth period was longer and the creep ductility was larger compared with the specimens with straight grain boundaries (D_{gb}=1.094) [5]. Thus, automated processing and analysis of the fracture surface patterns may give an important information about the fracture initiation site and the crack growth direction by tracing the fracture surface from simpler morphology to more complicated one. Two-dimensional fracture surface analysis can reveal the underlying microstructures in fractured components, which are difficult to be detected by three-dimensional fracture surface analysis.

References

[1] Tanaka, M, J. Mater. Sci., **27** (1992) 17, 4717-4725.
[2] Tanaka, M., Kayama, A., Kato, R. and Ito, Y., Fractals, **7** (1999) 3, 335-340.
[3] Tanaka, M., Z. Metallkd., **88** (1997) 3, 217-224..
[4] Tanaka, M., Iizuka, H. and Ashihara, F., J. Mater. Sci., **23** (1988) 11, 3827-3832.
[5] Tanaka, M. Miyagawa, O., Sakaki, T., Iizuka, H., Ashihara, F. and Fujishiro, D., J. Mater. Sci., **23** (1988) 2, 621-628.

The Occurrence of Grain Boundary Serration and Its Subsequent Effect on the Improvement of Creep-Fatigue Resistance in Austenitic Stainless Steels

S. W. Nam*, H. U. Hong and K. J. Kim
Department of Materials Science and Engineering, Korea Advanced Institute of Science and Technology, 373-1 Kusong-dong, Yusong-gu, Taejon 305-701, Korea
Tel: +82-42-869-3318, Fax: +82-42-869-3310, E-mail: namsw@cais.kaist.ac.kr
*Jointly Appointed at the Center for the Advanced Aerospace Materials
Pohang Univ. of Sci. and Tech., San 31 Hyoja-dong Nam-gu, Pohang, 790-784, Korea

Extended Abstract

It has been well understood that grain boundary cavitation is the most serious damage mechanism of austenitic stainless steels under creep-fatigue interaction conditions[1]. The carbides at the grain boundaries provide preferential sites for cavity nucleation owing to stress concentration during the fatigue cycle[1]. Hence, these carbide characteristics, such as distribution, density and morphology, etc., should be considered as the important factors to characterize creep-fatigue property.

Recently, the present authors [2] found that grain boundary serration in AISI 316 stainless steel occurs in an early stage of the aging treatment prior to the $M_{23}C_6$ carbides precipitation. Moreover, it is investigated that the grain boundary serration strongly affects to reduce the density of carbide and the interfacial energy between carbide and matrix. This may means that the modified grain boundary carbides give beneficial effect for the cavitation resistance of austenitic stainless steel during creep-fatigue conditions.

It has been reported that, during aging treatment, no grain boundary serration occurs in 304 stainless steel so that acute triangular type carbides formed on the straight grain boundaries are predominant [3].

In this study, the modified heat treatment is applied to an AISI 304 stainless steel to obtain the serrated grain boundary. From this investigation, the modification of carbide characteristics through the grain boundary serration has also been proven to improve the creep-fatigue resistance of 304 stainless steel.

In order to serrate the grain boundary in austenitic stainless steel, the modified heat treatment process is designed. Table 1 shows the heat treatment conditions at each case. Figure 1 shows the change in the grain boundary configuration and carbide morphology with the hate treatment. As shown in Figure 1, the conventionally heat treated steel has triangular carbides on the straight grain boundary. On the other hand, the modified heat treated steel has

planar carbides on the serrated grain boundary.

Table 1 Change in carbide morphology with heat treatment procedures.

Conventional heat treatment	:	1323K/1h/WQ + 1033/50h/WQ
Modified heat treatment	:	1323K/1h → FC → 1033/50h/WQ

(a) Conventionally heat-treated steel b) Modified heat-treated steel

Figure 1: $M_{23}C_6$ carbides on the grain boundary after full aging heat treatment at each case.

Using these two kinds of specimens, creep-fatigue tests were conducted at 873K. Figure 2 shows a comparison of low cycle fatigue resistance of both steels at 873K. Under creep-fatigue conditions, the life of the modified heat treated steel is almost twice as long as that of the conventionally heat treated steel.

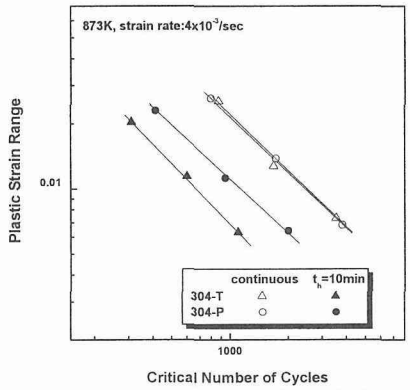

Fig. 2 : Comparison of low cycle fatigue life of the two steels at 873K

Hence, using life prediction model[4], the values of the cavity nucleation factor, P', are evaluated to be 4.7×10^{12} m^{-2}in the conventionally heat treated steel and 2.9×10^{12} m^{-2} in the modified heat treated steel. These results are closely related with the difference in creep-fatigue lives. This result also implies that the carbide modification through the grain boundary serration, which can be quantified as P' values, leads improvement of the cavitation resistance for the enhancement of creep-fatigue life.

Reference

[1] J.W. Hong, S.W. Nam and K.-T. Rie, Literature example for extended abstract in ICASS. J. Mater. Sci., 20 (1985), 3763-3779.

[2] H.U. Hong and S.W. Nam, Literature example for extended abstract in ICASS. accepted by Mater. Sci. Engng. A, 2001.

[3] H. U. Hong, B. S. Rho and S. W. Nam, Literature example for extended abstract in ICASS. accepted to Mater. Sci. Engng. A, 2001

[4] B.G. Choi, S.W. Nam, Y.C. Yoon and J.J. Kim, Literature example for extended abstract in ICASS. J. Mater. Sci., 31 (1996), 4957-4966.

Influence of Dynamic Strain Ageing on Tensile Deformation and Fracture Behaviour of Type 316 LN Austenitic Stainless Steel

B. K. Choudhary, K. Bhanu Sankara Rao and S. L. Mannan
Materials Development Group,
Indira Gandhi Centre for Atomic Research, Kalpakkam, India

1. Introduction

Dynamic strain ageing (DSA) results from the interaction between solute atoms and mobile dislocations during plastic deformation at intermediate strain rates and is of great practical importance in austenitic stainless steels [1]. The range of temperatures in which DSA has been reported to occur in austenitic stainless steels coincides with the operating conditions for stainless steel components in fast breeder reactors. The upper region of this temperature range overlaps the range of temperatures in which creep dominates and is of technological interest. The present work on the influence of strain rate and temperature on DSA and its effects on elevated temperature tensile properties is a part of the detailed investigation on flow and fracture behaviour of nitrogen alloyed low carbon type 316LN stainless steel. Type 316LN SS has been chosen for the high temperature structural components of the proposed prototype fast breeder reactor at Kalpakkam. Serrated flow, an important manifestation of DSA, observed in this investigation is presented and the cause for the occurrence of DSA has been identified. Other than serrated flow, the present paper deals with various aspects of DSA such as peaks/plateaus in flow stress and work hardening rate, negative strain rate sensitivity on strength values, ductility minima and fracture behaviour.

2. Experimental Details

Type 316LN austenitic stainless steel of chemical composition (wt. %) Fe–0.021C–1.74Mn–0.0023P–0.002S–17Cr–12Ni–2.4Mo–0.078N, used in this investigation was solution annealed at 1373 K for 30 min. followed by quenching in water. The average grain size measured by linear intercept method was 85 μm. Tensile tests were conducted on solution annealed specimens in an Instron model 1195 at temperatures ranging from 300 to 1123 K employing nominal strain rates in the range 3×10^{-5}–3×10^{-3} s^{-1}. Use of suitable chart speed gave a stain resolution of 7.5×10^{-4} and zero load suppression provided a stress resolution of 0.80 MPa.

3. Results and conclusions

The alloy exhibited serrated/jerky flow during tensile deformation at intermediate temperatures, whereas at room and high temperatures load-elongation curves were smooth. Detailed analysis on the type and nature of serrations, the critical strain for the onset of serrations and the evaluation of apparent activation energy suggested that type 316LN stainless steel exhibits two temperature regimes of serrated flow i.e., a low temperature regime (523-598 K) and a high temperature regime (673-1023 K), separated by a retardation bay. In the retardation bay, serrations were either absent or only mild irregularities could be noted. In the low temperature regime type A serrations were observed, while in the high temperature regime type A in the beginning, mixed type A+B/B at intermediate temperatures and mixed A+C/C at high temperatures were observed. Both lower and upper end

temperatures for the occurrence of different types of serrations decreased with decrease in applied strain rate. Evaluation of apparent activation energy of 115 kJ mol^{-1} in the low temperature regime is ascribed to the vacancy-carbon pair. Based on the value of 210 kJ mol^{-1} obtained in high temperature regime, chromium diffusion has been suggested as the cause of serrations in this regime. Systematic increase in the magnitude of stress drop with increasing strain and temperature and with decreasing strain rate observed for type A serrations is ascribed to the increased strength of locking due to increase in solute concentration in the atmosphere. The occurrence of type A+C/C serrations was always associated with decreased magnitude of stress drop as well as decrease in strain to disappearance of serrations with increasing temperature. The cessation of type C serrations at high temperatures has been attributed to precipitation reaction.

The variation of normalised flow stress with temperature at various strain levels exhibited a gradual decrease up to 523 K. The flow stress exhibited a plateau in range 573-1023 K followed by a marginal decrease at 1123 K at true plastic strain levels of 0.2 and 2 %,. Flow stress peaks were discernible with increasing strain levels of 5, 10 and 20 % at intermediate temperatures followed by a rapid decrease in the flow stress value at high temperatures. The upper end temperatures for the occurrence of plateaus/peaks in flow stress decreased with increasing true plastic strain levels. At all strain rates, the variation in ultimate tensile strength (UTS) with temperature exhibited a three stage behaviour i.e., a gradual decrease from 300 to 523K followed by peak at intermediate temperatures and a rapid decrease at high temperatures. Negative strain rate sensitivity on strength values has been observed at intermediate temperatures. The variation in average work hardening rate has also shown peak at intermediate temperatures. Both the strength values and work hardening rates decreased rapidly with decreasing strain rate and increasing temperatures indicating dynamic recovery at high temperatures. The ductility values also exhibited a rapid decrease from 300 to 523 K followed by minima at intermediate temperatures and a rapid increase at high temperatures. In the ductility minima temperature range, the alloy exhibited typical shear fracture, while at all other temperatures failure was characterised by dimples. The peaks/plateaus in stress values and work hardening rate, negative strain rate sensitivity, ductility minima and shear fracture at intermediate temperatures observed in the present investigation represent anomalous behaviour and are considered to be the other important manifestations of DSA. This anomalous behaviour is attributed to the increased rate of dislocation multiplication, higher dislocation density and reduced recovery arising due to DSA.

Reference

[1] Rodriguez, P, Serrated plastic flow. Bull. Mater. Sci. 6(1984), No. 4, pp. 655-663.

CREEP STRENGTHENING OF TYPE 316 STAINLESS STEEL WELD METAL BY NITROGEN

M.D. Mathew, K. Bhanu Sankara Rao and S.L. Mannan
Indira Gandhi Centre for Atomic Research, India

1. Introduction

High temperature structural components of India's Prototype Fast Breeder Reactor (PFBR). will be made of type 316 stainless steel (SS) containing 0.024 - 0.03 wt% carbon and 0.06 - 0.08 wt% nitrogen. Low carbon grade 316 SS has been chosen to avoid sensitisation of the heat-affected zone during welding. Nitrogen is specified as an alloying element to compensate for the decrease in strength due to lowering the carbon content. For the welding electrode, carbon and nitrogen have ben specified in the range 0.045 - 0.055 wt% and 0.06 - 0.10 wt% respectively. These specifications were made with the intention to impart adequate creep strength and to retard transformation of delta-ferrite into brittle intermetallic phases at elevated temperatures in the weld metal. Although the influence of nitrogen on the mechanical properties of wrought austenitic stainless steels has been studied fairly extensively [1], very little information is available on the creep behaviour of nitrogen-bearing austenitic stainless steel welds. This study has been carried out to understand the long-term creep behaviour of nitrogen-alloyed 316 SS weld metal (designated as 316(N) SS), and the results are compared with the creep properties of 316 SS weld metal having similar carbon content but devoid of nitrogen.

2. Experimental

Weld pads were prepared by welding 20 mm thick plates using 4 mm diameter basic coated electrodes. All-weld creep specimens were taken parallel to the welding direction. Table 1 gives the chemical composition of 316 SS and 316(N) SS weld metals. The amount of delta-ferrite in 316 SS and 316(N) SS weld metals were 4.5 and 4.2 ferrite numbers (FN) respectively.

Table 1
Chemical compositions (in wt.%) of 316 SS and 316(N) SS weld metals.

Element	C	Ni	Cr	Mo	Mn	Si	S	P	Cu	B	N
316 SS	.06	11.9	18.8	2.06	1.42	.58	.01	.01	.05	.0005	-
316(N) SS	.052	11.5	18.6	2.2	1.74	.64	.007	.022	.04	.0009	.067

3. Results and Discussion

Constant load creep rupture tests were carried out at 823, 873 and 923 K at various stress levels in the range 100 - 300 MPa. The maximum rupture life in this investigation was 20,000 hours. Alloying with nitrogen decreased the steady state creep rate by one to two orders of magnitude depending upon the temperature and stress level. Figure 1a shows a comparison of steady state creep rates of nitrogen-free and nitrogen-bearing weld metals at 823 K. At all the three temperatures, a power law relationship was obeyed between steady state creep rate and stress by both the weld metals. The stress exponent (n) in the power-law relationship varied in the range of 10 to 20. These values of n suggest that dislocation creep is the rate controlling

mechanism of creep deformation in 316 and 316(N) weld metals. The influence of nitrogen on creep rupture strength at 873 K is shown in Fig. 1b. Rupture strength of 316(N) was substantially higher than that of 316 SS at all the test conditions. Typically, rupture strength at 1000 hours increased by about 30% in the temperature range 823 to 923 K. In the case of the base metal, it was observed that rupture strength increased by about 28% under the same test conditions [2].

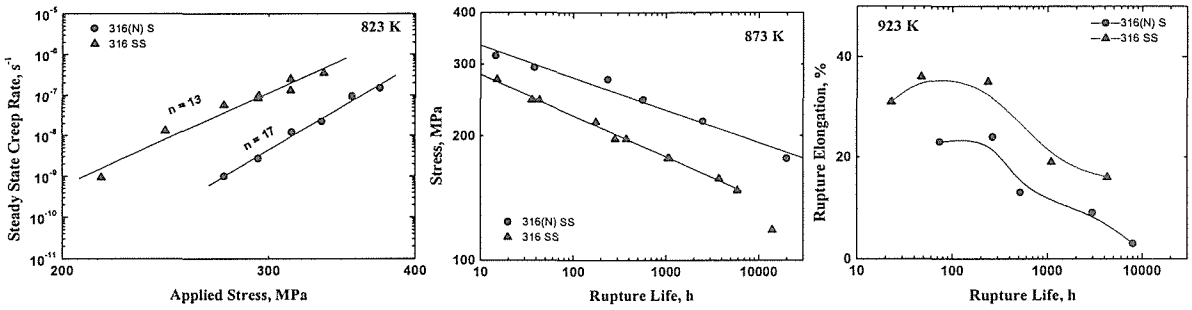

(a) (b) (c)

Figure 1. Comparison of creep properties of 316 and 316(N) SS weld metals.
(a) steady state creep rate, (b) rupture life and (c) rupture ductility.

Rupture ductility generally decreased with increase in rupture life. 316(N) SS showed lower rupture ductility as compared to 316 SS at all the test conditions as shown typically in Fig. 1c. Nitrogen lowered rupture ductility in the base metal also [2].

Nitrogen is known to be an effective solid solution strengthening element in wrought austenitic stainless steels from cryogenic to high temperatures without concomitant loss of toughness. Creep and low cycle fatigue properties are improved by alloying with nitrogen generally upto 0.5 wt%. Several mechanisms have been suggested for the increase in strength due to nitrogen, like solid solution hardening, decrease in stacking fault energy, formation of interstitial-substitutional solute complexes, order strengthening and precipitation strengthening [1]. Nitrogen delays the onset of carbide precipitation to longer ageing times. Presence of nitrogen is also known to delay the rate of coarsening and coalescence of carbides. The presence of nitrogen in the carbides decreases the mismatch between the precipitate and the austenite matrix thereby reducing the interfacial energy and inhibiting precipitate coarsening. Besides, nitrogen reduces the diffusivity of carbon and chromium atoms. The comparative decrease in steady state creep rate and increase in rupture life of 316(N) SS weld metal is attributed to the combined influence of the above mentioned factors.

4. Conclusion

Alloying 316 SS welding electrode with nitrogen yielded significant improvements in the creep properties of the weld metal. Steady state creep rate decreased upto two orders of magnitude. Rupture strength increased by about 30 %. However, rupture ductility decreased on alloying with nitrogen.

References

[1]. High Nitrogen Steels, Valentine G Gavriljuk and Hans Berns (eds.), 1999, Springer-Verlag, New York.
[2]. M.D.Mathew, G.Sasikala, K.Bhanu Sankara Rao and S.L.Mannan, *Materials Science and Engineering*, A148(1991)253.

- Application of Continuous Casting and Hot-Direct Rolling Process for Scrap Steels
- Structures Resistant to Hydrogen Embrittlement
- The State of Hydrogen and Its Effect on Fractures
- Structures Resistant to Fatigue

(Room 303)

Integrated Microstructure Control for Ultra Fine Grained Steel by Advanced Processing of Melting, Solidification, Solid Phase Transformation and Deformation

Toshihiko Emi
School of Materials Science & Engineering, Seoul National University
Seoul 151-744, Korea Fax: +82-2-884-1413 emi35@gong.snu.ac.kr

Controlling microstructure of structural steel for ultra-fine grain size requires fine control of chemistry and advanced versions of thermo-mechanical controlled processing (with the application of large strain). Precautions are, however, necessary for the melt preparation and solidification without which the grain size control may not display its full capability to improve the mechanical properties of the steel materials.

The precautions include the minimization and/or optimization of non-metallic inclusions and impurity elements in the melt and during solidification, and the minimization of the segregation of impurity elements during solidification. Precise control is also required of the concentration of elements that form precipitates during solidification, cooling, reheating and solid phase transformations.

State-of-the-art measures taken to achieve the above precautions are discussed with reference to secondary refining to reducing the impurity elements and inclusions to extra-low concentrations and fine-tuning the melt with micro-alloying elements.

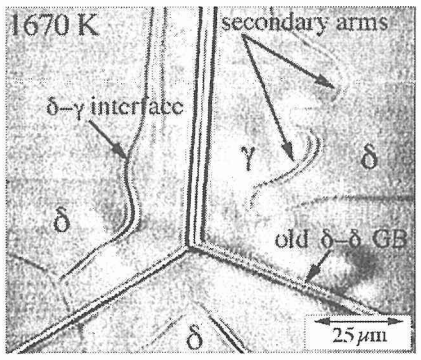

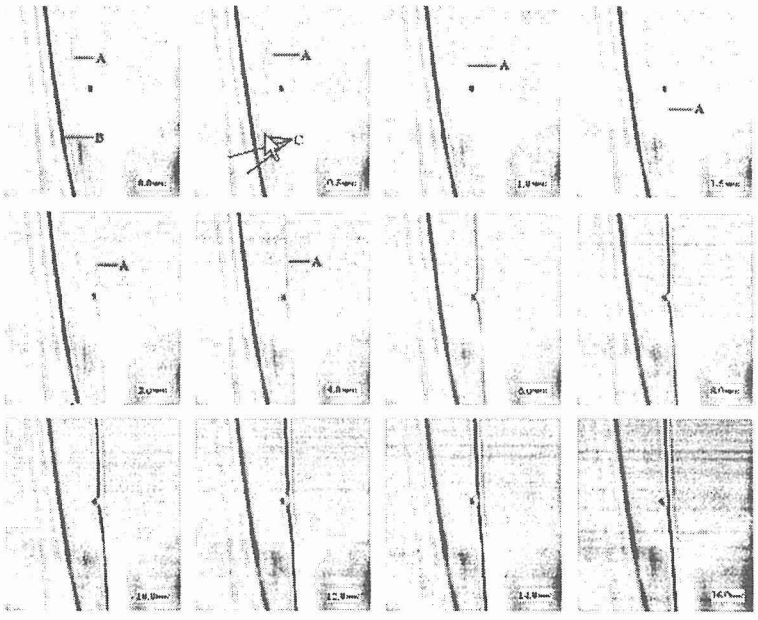

Fig. 1 Photograph and schematic diagram of the nucleation and growth of γ-phase in δ-matrix during δ→γ transformation of low carbon steel (C: 0.045, Si 0.01, Mn 0.22, S 0.007, P 0.017, sol.Al 0.040 mass%, super cooling ≤ 7K) (left)

Fig. 2 Pinning and depinning of grain boundary by alumina inclusion (size ≅ 1μm) during near-isothermal growth of γ-grain of 0.045%C steel (see Fig. 1 for chemistry) (right)

Also, effective measures are summarized to avoid the entrainment of exogenous inclusions and the segregation of.impurity elements during solidification in continuous casting. Influence of inclusion engineering to control the chemistry, size distribution, morphology and coherency with the precipitates is addressed with respect to grain size control in a variety of applications

With regard to the grain size refinement and texture control, γ-grain refinement prior to γ/α transformation is a necessity in continuous production system in industry. Possibility to achieve this during solidification and cooling seems to be limited in view of own in-situ observation on the nucleation and growth of γ-grains in δ-matrix (Fig. 1) and the incapability of pinning the grain boundary movement during the growth of γ-grain by inclusions that are stable at such elevated temperatures (Fig. 2).

Inverse transformation on reheating obviously gives much better capability for the γ-grain refinement for the size of materials usually encountered in industrial production where solidification structure is subject to slow cooling. Subsequent roughing helps refining the solidification structure, but during the roughing, substantial coarsening of γ-grains is unavoidable. Thin slab casting combined with in-line rolling might offer an interesting possibility, i.e., in-line rolling could be so designed as to give better refining of γ-grains and α-grains during γ/α transformation and/or rolling in α-range with large strain, provided that large strain forming and rapid cooling is made possible during the in-line rolling and controlled cooling in the run out table. However, inherent disadvantage in thin slab casting, i.e., limited total reduction, leaves coarse solidification structure before the in-line rolling that is unfavorable for the grain refinement. This should be resolved probably by the combination of cast structure improvement and the precipitates-strain interaction. Concerted interaction between the formation of relevant precipitates and strain-induced recrystallization is one of the central issues not only in solid-state forming but also in cast-rolling.

Recent elaboration has revealed that the following three avenues (and their variants) make it possible to form ultra fine grained steel materials in laboratory- to bench-scale production:

(1) forming with large strain in meta-stable austenite range followed by transformation to ferrite,
(2) forming with large strain in ferrite range followed by dynamic recrystallization, and
(3) forming with large strain in ferrite range followed by inverse transformation to austenite due to heat generated by the forming, and subsequent transformation to ferrite.

These avenues require increased reduction, decreased reheating-/rolling-temperature, and hence high mill constant and roll rigidity/ endurance. Continuous hot rolling in (ferrite + austenite) range or ferrite range with lubrication and large reduction hot rolling with intensive water cooling between the mill stands, both commercialized in recent years, appear to offer promising ways to industrialize them.

Key issues and problems inherent to these advanced thermo-mechanical processing are critically reviewed, some emphasis being placed on eco-technological aspect.

Present State and Expected Progress in Simulation of Solidification Structure

T. Matsumiya
Nippon Steel Corporation, Japan

1. Introduction

Since solidification structure must be optimized for desired materials properties thorough solidification processing, simulation for its estimation is very valuable. Solidification macrostructure affects mechanical properties of matrix, such as strength and toughness of steel products and macrosegregation in continuously cast brooms. Solidification microstructure relates to microsegregation and secondary precipitation, which often determine the macrostructure. Solidification nanostructure is supposed to be a new word, but it relates to the materials function that stems from nano scale structure, e.g., extraordinary magnetic and mechanical properties of amorphous matrix metals with dispersed nano crystalline. In this paper simulation of solidification structure at various levels are reviewed and future direction is also discussed in the presentation.

2. Solidification Nanostructure

Nucleation of crystalline in the under cooled melt of Lenard-Johnes (L-J) particle system was studied with molecular dynamics (MD) simulation [1]. It was found that crystalline with icosahedral structure predominates at the beginning of nucleation and crystalline with body centered and face centered cubic and hexagonal closed pack structure increases later. This phenomena reminds us the scattered quasi-crystalline nucleated in the amorphous metals. Landman, et al. showed with MD by the use of a three body potential that solid-liquid interface is very sharp in directional solidification of silicon with the growth direction of (111) while it is defuse with the growth direction of (100) and that the defuse (100) interface is saw-like interface consisting of (111) facets [2,3]. The results coincide the observations. They also showed that solidified structure becomes amorphous when the cooling rate exceeds $2x10^{12}$K/sec, which can be achieved by laser-annealing experiment [3]. Growth rate [4] and solute trapping [5] were also studied by MD with L-J particles and it was found that solid-liquid partition coefficient varies as a function of interface velocity as theoretically derived by Aziz [6].

3. Solidification Microstructure

Phase field method (PFM) is considered to be a powerful tool for microstructure study. According to the recent review by Ode, et al. [7], multi-phase-field and multi-component model has been developed and various phenomena which relate to solidification microstructure are studied, such as columnar and equiaxed dendrite growth, Ostward ripening, pushing/engulfment of alumina particles in steel solidification, peritectic transformation, solute trapping at solidification front, etc. Not only the simulated morphology of dendrite is very similar to the observations, but also the quantitative agreement of simulated secondary arm spacing as a function of local solidification time agrees very well with experiments. The effect of fluid flow on the evolution of dendrite morphology can be simulated by PFM. Front tracking method is also applicable to it [8]. Once the morphology and size of dendrite is given, a combined simulation of solute diffusion and local thermodynamic equilibrium can also predict microsegregation and secondary precipitations [9].

4. Solidification Macrostructure

Brown and Spittle simulated columnar and equiaxed macrostructure evolution by Monte

Carlo (MC) below the melting temperature with consideration of nucleation and growth driven by solid-liquid energy difference and grain boundary energy [10]. Rappaz and Gandin simulated them by Cellar Automaton (CA) with consideration of probabilistic heterogeneous nucleation at the mold-liquid interface and in the bulk liquid and growth of grains with probabilistically assigned crystal orientations and successfully estimated the solidification structure of aluminum ingots with various efficiencies of heterogeneous nucleation sites [11]. They later combined temperature and solute field simulation with finite element method with CA [12]. Nogami, et al. also simulated the micro- and macrostructure of continuously cast steel slabs and welding by MC simultaneously solving solutes and thermal field by finite difference method [13]. Phenomenological model simulation can also be used for macrostructure. For example, Harada, et al. simulated columnar to equiaxed transition and equiaxed grain size of continuously cast blooms modeling dendrite arm remelting by electromagnetic stirring, which is the source of nuclei, remelting and sustaining of the nuclei in the super heated liquid pool simultaneously solving the thermal transport in the liquid pool [14].

References

[1] Swope, W.C. and Andersen, H.C., 10^6-partcle molecular-dynamics study of homogeneous nucleation of crystals in a super cooled atomic liquid. Phys. Rev. B 41(1990), No.10, pp.7042-7054.

[2] Landman, U., et al., Molecular-dynamics simulation of epitaxial crystal growth from the melts. I. Si(100). Phys. Rev. B 37(1988-II), No.9, pp.4637-4646.

[3] Landman, U., et al., Molecular-dynamics simulation of epitaxial crystal growth from the melts. II. Si(111). Phys. Rev. B 37(1988-II), No.9, pp.4647-4655.

[4] Gilmer, G. H. and Grabow, M. H., Molecular Dynamics Studies of Crystal Growth and Thin Films. Supercomputer Research, 1987, Am. Chem. Soc., pp.218-236.

[5] Celestini, F. and Debierre, J. -M., Nonequilibrium molecular dynamics simulation of rapid directional solidification. Phys. Rev. B 62(2000I), No.21, pp.14006-14011.

[6] Aziz, M. J., Model for solute redistribution during rapid solidification. J. Appl. Phys., 53(1981), No.2, pp.1158-1168.

[7] Ode, et al., Recent Advances in the Phase-field Model for Solidification. ISIJ Int., 41(2001), No.19, pp.1076-1082.

[8] Juric, D., Direct Numerical Simulation of Solidification Microstructure Affected by Fluid Flow. Model. Cast. Adv. Solidi. Process. 8, 1998, TMS-AIME, pp.605-612.

[9] Matsumiya, T., Analyses of Segregations and Chemical Compositional Change of Nonmetallic Inclusions during Solidification of Steels. Mat. Trans. JIM, 33(1992), No.9, pp.783-789.

[10] Brown, S. G. R. and Spittle J. A., Computer simulation of grain growth and macrostructure development during solidification. Mater. Sci. Tech., 5(1989), April, pp.362-368.

[11] Rappaz, M. and Gandin, Ch. –A., Probabilistic Modeling of Microstructure Formation in Solidification Processes. Acta. Metall. Mater., 41(1993), No.2, pp.345-360.

[12] Gandin, Ch. –A. and Rappaz, M., A Coupled Finite Element-Cellar Automaton Model for the Prediction of Dendritic Grain Structure in solidification Process. . Acta. Metall. Mater., 42(1994), No.7, pp.2233-2246.

[13] Nogami, A. et al., Simulation of continuously cast micro- and macro structure wih complex system modeling. Proc. JIM Fall Meeting, 2002, p.98.

[14] Harada, H., et al., Numerical Modeling of Columnar to Equiaxed Transition with Consideration of Molten Steel Flow, Int. J. of Cast metals Res. (2002), to be published.

Microstructure Evolution of Low Carbon Steel Produced by Compact Stip Production[1]

Huo Xiangdong Liu Delu Chen Nanjing Kang Yonglin Fu Jie
Zhou Deguang

Department of Material Physics and Chemistry,
University of Science and Technology Beijing, 100083 Beijing, China

Compact Strip Production (CSP) is a process for the production of hot strips from a continuous cast thin slab. Since the first CSP plant was set up at Nucor Steel in 1989, a number of mini mills have been established or under construction. There are many metallurgical differences between CSP and the traditional continuous rolling (cold charge) process. Compare with the same composition steel strips produced by traditional cold charge process, the hot strips produced by CSP has finer microstructure and much higher strength as well as good ductility. In the present work a low carbon steel containing 0.05C, 0.04Si and 0.38Mn produced by the CSP technique has been studied. Specimens, cut from the slab and plate of the same stock after each rolling pass, were examined by optical and electron microscopy at room temperature. Electron microscopic investigation on the strip has also been carried out.

Because of the low slab thickness and high slab surface area, there are many differences between the thin slabs and the conventional thick slabs. The characteristics of the thin slab are its fine equiaxed grain zone at surface layer and dentritic zone through out the whole central area of the slab (Fig.1). The mean secondary dendrite arm spacing varied from 125μm to 156μm.

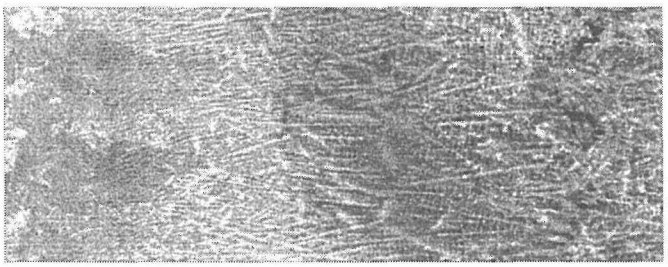

Fig.1 Microstructure of the slab produced by CSP processing

Microstructure of the hot strips consists of uniform polygonal ferrite with small amount of pearlite. Average grain size of the ferrite is about 5.7μm for a strip with thickness of 4mm. Above 380 MPa yield strength with elongation larger than 35% is obtained.

Fig.2 shows a series of microstructure of the same stock after each pass during continuous rolling. The average grain size for the central area of the samples from 1st to 6th pass is 41.6, 25.2, 21.4, 20.2, 13.1, 6.7μm respectively. It is revealed that the larger change of microstructure appeared between the first and second pass. This is also the case for the final two passes. The difference of as cast microstructure between surface and central area is gradually decreased during continuous rolling . Pearlite, distributing on the grain boundaries of ferrite, gradually become uniform and dispersive.

[1] 1. Supported by the State foundation for key project: New Generation of Steels (No: G1998061500)

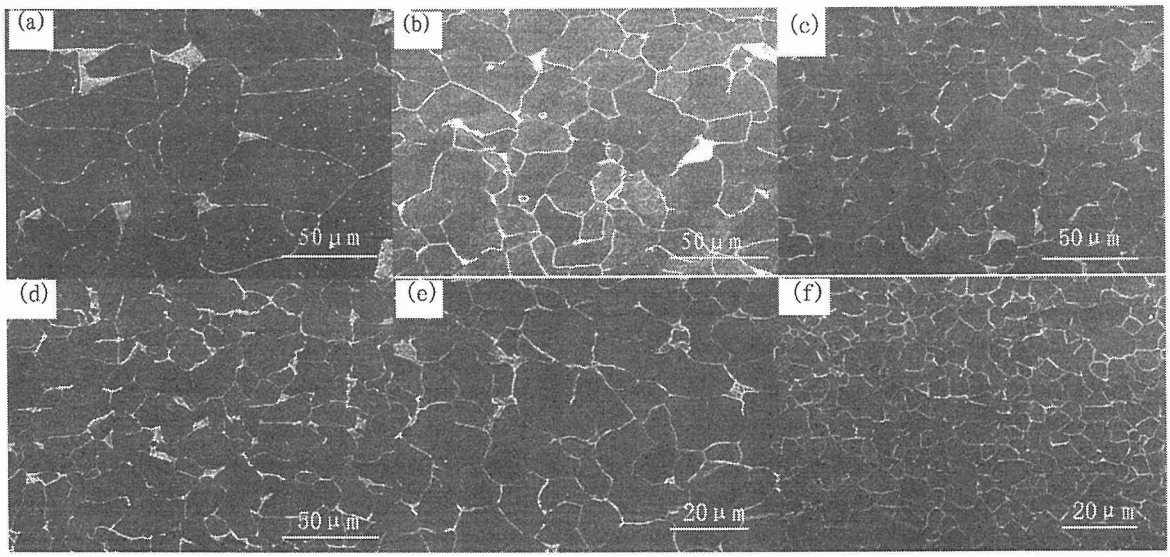

Fig.2 Microstructure for the central area of the same stock after each pass during continuous rolling.
a) first pass b) second c)third d)fourth e)fifth f)sixth

The absence of a cooling and reheating cycle and a limit total reduction are all not beneficial to grain refinement[1]. However, the ferrite grain of the steel strip produced by CSP in Zhujiang Steel is much finer than that of the steels by conventional processing. Firstly, the great rolling reduction plays an important role. It can be concluded that recrystallization of austenite at high temperature and stain accumulation at lower temperature contribute to grain refinement. Secondly, remarkable grain refinement effects can be obtained by the oxide and sulfide precipitations. Large number of nano-scaled precipitates has been observed in the ferrite matrix and grain boundaries of the steel strip. Electron diffraction study shows that these oxide precipitates are Fe_3O_4 with spinel structure. Their dimension is smaller than 20nm. Small sulfide particles with 30~300nm in size have also been observed in the steel[2,3]. Lastly, Control cooling after rolling is also beneficial to grain refinement for the steel strip. Microstructure evolution of the steel during continuous rolling and effects of the dispersive oxide precipitation are discussed.

---

[1] Cobo.S.J and Sellars.C.M., Microstructural evolution of austenite under conditions simulating thin slab casting and hot direct rolling,Ironmaking And Steelmaking,29(2001), No.3, pp.230-236.
[2] Liu Delu, Fu Jie, Kang Yonglin, et al.,Oxide and Sulfide Dispersive Precipitation and Effects on Microstructure and Properties of Low Carbon Steels, J. Mat. Sci. Tech., 18(2002),No.1,pp. 7-9.
[3] Liu Delu, Huo Xiangdong, Wang Yuanli, Fu Jie, Kang Yonglin, Chen Nanjing, Oxide and Sulfide Dispersive Precipitation In Ultra-low Carbon Steels, J. of University of Sci. & Tech. Beijing,8(2001) , No.4, pp.314-315.

Evolution of Size, Composition and Morphology of Primary and Secondary Inclusions in Si/Mn and Si/Mn/Ti Deoxidized Steels

Han S. Kim[1], Hae-Geon[1] Lee and Kyung-Shik Oh[2]

1. Department of Materials Science and Engineering, Pohang University of Science and Technology (POSTECH), Pohang, Korea
2. Technological Research Laboratory, POSCO, Pohang, Korea

1. Introduction

Inclusions formed in Si/Mn and Si/Mn/Ti deoxidized structural steels were investigated to elucidate mechanisms of evolution of size, composition and morphology of primary and secondary inclusions in laboratory specimens subjected to different thermal histories.

2. Experimental Procedure

Si/Mn and Si/Mn/Ti steels were prepared by melting about 300g of electrolytic steel with various alloying elements in a MgO crucible using an induction melting furnace. At the time of 30 seconds after deoxidation, portion of the melt (about 150g) was withdrawn into fused silica tubes by suction and quenched in water to form rod-shaped specimens. The melt remaining in the crucible (about 150g) was held at 1600℃ for 10 minutes to remove primary inclusions by flotation, followed by continuous cooling to the room temperature in the furnace by turning off the power, where the cooling rate was measured to be 32℃/min in average. The quenched specimens were sliced into pieces. Some of them were used in investigating primary inclusions formed in the liquid state, and others were subjected to isothermal holding at 1200℃ for 20 minutes and then cooled to investigate the effect of the holding on inclusions. Morphology, size and composition of inclusions have been evaluated using SEM-EDS analysis. Table 1 shows the chemical composition of the prepared steels.

Table 1 Chemical composition of specimens, (mass%).

	C	Mn	Si	S	Ti	Tot.O
MSWQ	0.11	1.56	0.110	0.0072	-	0.0099
MST1WQ	0.10	1.48	0.095	0.0072	0.0034	0.0098
MST2WQ	0.09	1.45	0.093	0.0070	0.0061	0.0080
MST3WQ	0.10	1.51	0.105	0.0054	0.0104	0.0064
MST4WQ	0.10	1.47	0.100	0.0037	0.0122	0.0048
MSFC	0.11	1.55	0.111	0.0071	-	0.0021
MST3FC	0.1	1.52	0.104	0.0055	0.0056	0.0012

3. Results

Table 2 shows average chemical compositions of inclusions found in water-quenched and furnace-cooled steels. Primary inclusions found in steels quenched from 1600℃ contained very low sulfur, and hence MnS precipitation on them was hardly found. Typical morphology of complex inclusions found in furnace-cooled steels is presented in Figure 1. MnS precipitated on manganese silicate inclusions in MSFC steel mostly grew inward the inclusions, while MnS precipitated on Ti-oxide in MST3FC grew outward the inclusions wrapping them. As the inclusion size increased, the number of MnS precipitates on an inclusion also increased. In the case of MSFC steel, multiple precipitations of MnS on an oxide was observed when the oxide was greater than about 3μm. Both MnO and MnS

contents were found higher in smaller secondary inclusions.

Table 2 Average chemical compositions of inclusions, (at%).

	Mn	S	Si	Ti	Al	Mg
MSWQ	56.67	7.39	35.94	-	-	-
MST3WQ	34.03	1.89	5.06	57.46	1.56	-
MSFC	54.58	21.42	24.00	-	-	-
MST3FC	29.55	21.84	1.31	43.57	0.97	2.76

In order to interpret and predict the behavior of inclusion precipitation and growth during solidification, a model [1] has been developed, which incorporates both thermodynamic and kinetic considerations. With this model, size and compositional evolution of inclusions was analyzed during solidification and the result was found to be in good agreement with the experimental results. Titanium in steel had a tendency to reduce SiO_2 content in inclusions (See Figure 2) and to associate with MnO in the inclusions to form a stoichiometric Mn/Ti relationship in the inclusions. If Ti content in Si/Mn/Ti deoxidized steels was low, the secondary inclusions were found to form with multiple phases; namely, manganese silicate phase, Mn-Ti oxide phase and MnS phase. The MnS phase always precipitated in the manganese silicate phase. The proportion of manganese silicate phase in an inclusion decreased with increase in the Ti content in the steel, and eventually completely disappeared with the Ti content above a certain level (70ppm in the present steel compositions). In this case MnS was found to precipitate outside Mn-Ti oxide inclusions and grew into the steel matrix. It has been revealed that the difference in growth behavior of MnS on oxide is closely related to the solidus temperature of oxide seed.

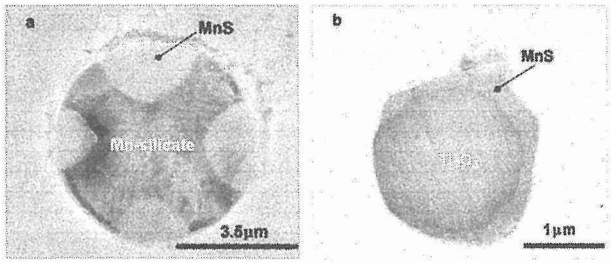

Figure 1 Morphological image of typical inclusions in furnace-cooled steels (a: MSFC, b: MST3FC).

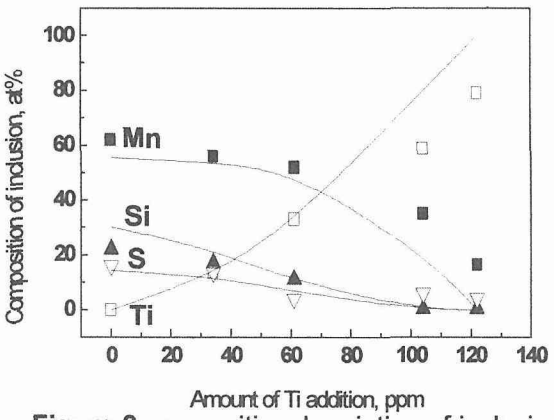

Figure 2 compositional variation of inclusions with Ti content for each steel held at 1200℃ for 20 minutes after water quenching from 1600℃.

4. Conclusions

Result of thermodynamic analysis and growth simulation showed good agreement with observation. Nature of inclusions in Si/Mn/Ti steels with varying Ti content could be appreciated during deoxidation, solidification and reheating processes.

References

[1] Han S. Kim and Hae-Geon Lee, CAMP-ISIJ, Vol.15 (2002), Accepted

Research on the Cleanliness of D Grade Q345 Steel Used in Architectural Structure

Zhang Caijun, Cai Kaike, Ai Liqun
University of Science and Technology Beijing , Beijing 100083, P.R.China
Yuan Weixia, Yu zhixiang
Wuhan Iron and Steel (Group) Corporation, Wuhan 430080, P.R.China

1. Introduction

In order to acquire good welding, ductility, toughness and Z direction performance for Q345D steel, two features have been required. Firstly, the carbon equivalent(Ceq) and crack-sensitivity(Pcm) should be limited to meet the demand of welding. Secondly, the steel cleanliness should be improved to satisfy the need of ductility and toughness, which includes lowering non-metallic inclusions and controlling their morphology, composition and size distribution.

Q345D steel is widely used in structure in China. In this paper, the variation of the total oxygen content and the behavior of non-metallic inclusions have been studied systematically for Q345D steel by trace experiments, sampling and analyzing.

2. Experiment Study

The production process of Q345D steel is BOF→ Ar-stirring in the ladle → slab CC in NO. 3 steel making plant of Wuhan Iron and Steel (Group) Corporation (WISCO). The chemical compositions of this steel are C:0.14~0.19%, Si:0.15~0.4%, Mn:1.4~1.6%, P<0.0025%, S<0.0025% and Als:0.02~0.07%.

Steel samples have been carried out in the ladle before and after Ar stirring, in the tundish and slab at the start, end, transitions and steady state of casting. The trace elements such as Ba, Sr, La are added into the ladle slag, tundish flux and tundish lining refractory respectively. Slag samples have been carried out in the ladle and tundish. After those samples have been prepared, the total oxygen has been measured, the micro and macro inclusions have been observed and analyzed by microscope observation, SEM and Slime. Meanwhile, the slag and inclusions compositions have also been measured related to inclusion absorption and slag entrainment tracing.

3. Experiment Results and Discussion

3.1 The evolution of total oxygen during each process

The total oxygen(T[O]) in each process has been shown in Figure 1. During Ar-stirring treatment, the total oxygen has been decreased from 160ppm to 18ppm, and the removal ratio of the T[O] is up to 88.75%. At the same time, the total oxygen content of slab is 9~12ppm, which is high level in cleanliness compared with other steel making plant in the world.

3.2 The evolution of micro inclusions during each process

Before ladle stirring, the main micro inclusions in the steel are spherical Si-Mn-Al compounds, which are caused by the deoxidation reaction. After Ar-stirring, these inclusions are mostly removed, and the residue inclusions are single or cluster Al_2O_3 and small amount of sulfide. As shown in Figure 2, through Ar-stirring treatment, the number of the micro inclusions has been reduced from 11.81/mm^2 to 3.48/mm^2, and the removal ratio is up to 70.5%.

3.3 The evolution of macro inclusions during each process

The evolution of macro inclusions during each process has been shown in Figure 3. During Ar-stirring treatment, the weight of the macro inclusions is decreased from 175.65mg/10kg steel to 38.5mg/10kg steel, and the removal ratio is up to 78.08%. Macro inclusions weight of transition and end slab is 3.5 and 6.6 times as much as that of steady slab respectively. Furthermore, the slag composition analyzing proved that the mold powder has been entrained into the molten steel and remained in the slab, which is the main source of macro inclusions in

the slab.
The cleanliness in each process is listed in Table 1.

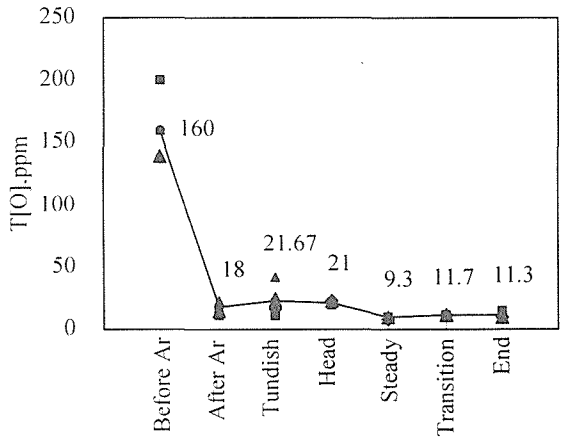

Fig. 1 The total oxygen content in each process

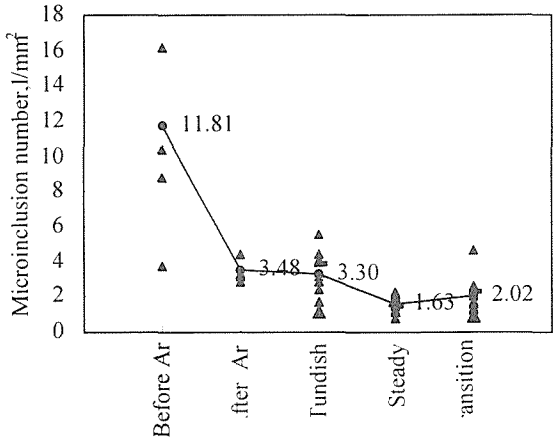

Fig. 2 The micro-inclusions amount in each process

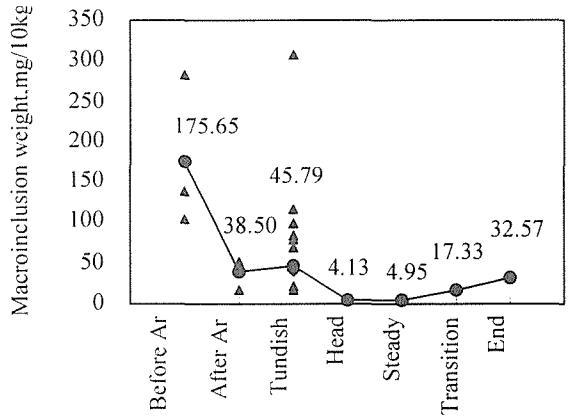

Fig. 4 The macro inclusions weight in each process

Table 1 The cleanliness in each process

		T[O] ppm	Micro inclusions (l/mm^2)	Macro inclusions (mg/10kg)
Before Ar		160	11.81	175.65
After Ar		18	3.48	38.50
Tundish		21.67	3.30	45.79
Slab	Head	21	/	4.13
	Steady	9.3	1.63	4.95
	Transition	11.7	2.02	17.33
	End	11.3	/	32.57

4. Conclusions

1) The total oxygen content of slab is 9~12ppm with the number of the micro inclusions 1.63~2.02/mm^2, and the macro inclusions in slab 4.95mg/10kg steel. It is high level in cleanliness by such a process compared with other steel making plant in the world.

2) The refining of molten steel during Ar-stirring treatment has a significant effect on the removal of non-metallic inclusions, the removal ratio of the total oxygen, micro inclusions and macro inclusions are up to 88.75%, 70.5% and 78.08% respectively.

3) Most of the micro-inclusions in the slab are single or cluster Al_2O_3 and the rest are Si-Mn-Al compounds and sulfide.

4) It has been proved by trace experiment that the mold powder has been entrained into molten steel and remained in the slab, which has become the main source of macro-inclusions in the slab.

5) It has been shown that the cleanliness of the unsteady slabs is deteriorated, so more measurement should be taken during unsteady casting period based on the research.

References

[1] Z.Liu and K.Cai, Purity Steel Production Technology. Iron & Steel, 35(2000), No.2, pp.25-32

[2] L.Zhang and K.Cai, Experimental and Theoretical Study on the Cleanliness of Steel, 84 Steelmaking Conference Proceedings. 84(2001), ISS Warrandale PA, pp.275-291

Surface Hot Shortness due to Cu after Simulated Cooling of Continuous Casting and Hot Direct Rolling

Chihiro Nagasaki and Koji Shibata

Department of Metallurgy, School of Engineering, The University of Tokyo

7-3-1 Hongo, Bunkyo-ku, Tokyo 113-8656, Japan

1. Introduction

Suppression of surface hot shortness due to copper is one of the most important requirements for the promotion of recycling of steels. The surface hot shortness is caused by liquid embrittlement during hot working of steels containing copper. Liquid Cu-enriched phase is formed through selective oxidation of iron at the steel/scale interface during heating beyond the melting point of Cu, and the liquid phase penetrates into austenite grain boundaries during hot rolling, which causes surface cracking. Shibata et al. have clarified the effects of alloying elements, impurities, grain size of austenitic phase, heating condition (atmosphere and temperature) and deformation rate on the surface hot shortness [1-3]. In addition, they showed several methods and the mechanism of suppressing the shortness. For instance, increasing the contents of Si, P, Mn, S, C and B to suitable levels can reduce the susceptibility to the surface hot shortness through restraining the penetration (Si, P, and B) and changing the morphology or the amount of the liquid Cu-enriched phase (Si, Mn, S and B).

However the specimens in their experiments were heated at certain temperatures and cooled at fairly high rate. Namely the heating pattern is somewhat different from CC-HDR processes, and the effects of cooling pattern, austenite grain size and atmosphere have to be clarified. Therefore, in this research, the effects of heating and cooling conditions simulating the CC-HDR processes on the surface hot shortness due to copper was examined.

2. Experiments

Chemical composition of the steels used in this research is shown in Table 1. Ingots were hot-rolled to plates with thickness of 15 mm. Cubic specimens of 10x10x10 mm^3 were machined from the hot-rolled plates. The specimens were oxidized in air following heat patterns of a slab in CC-HDR process [4], which is shown in Fig. 1. Some specimens were heated at 1373 K for 1.8 ks as the reheating pattern for comparison, because experimental data have been so far accumulated for this heating pattern. The morphology of Cu-enriched phase at the steel/scale interface was observed by optical microscopy. The reduction in the size of the specimen by oxidation was also measured.

The tensile test was performed after heating for 1.8 ks at 1373 K. The surface hot shortness

Table 1. Chemical composition of steels (mass%)

	C	Si	Mn	P	S	Cu	Ni	Cr	Al	Ti	N	O
A	0.106	0.010	0.52	0.023	0.003	0.50	0.01	0.01	0.003	0.001	0.0026	0.0030
B	0.120	0.008	0.50	0.019	0.002	0.48	0.01	0.004	0.016	0.001	0.0028	0.0039

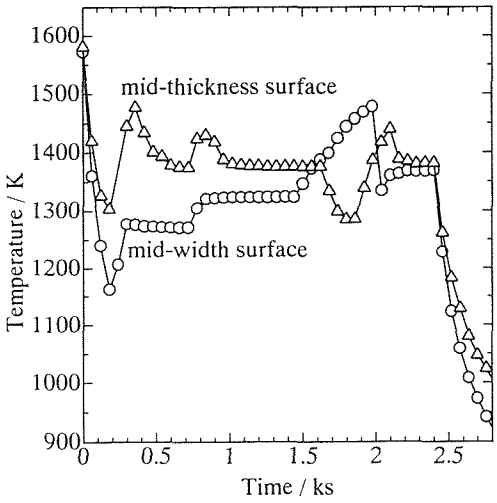

Fig. 1. Simulated heat patterns at each position of slab in CC-HDR process.

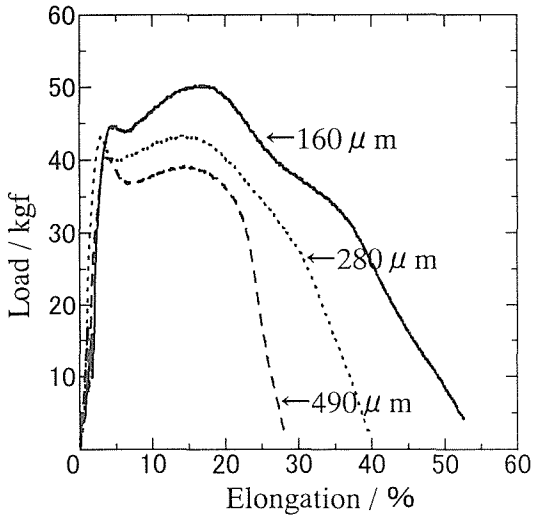

Fig. 2. Effect of grain size on hot shortness in the specimen of the steel A at 1373 K.

is evaluated by comparing the maximum load of the load-elongation curve obtained by hot tensile tests in Ar gas and in air.

3. Results and Discussion

Austenite grain size is coarsened by heating at higher temperatures. The effect of austenite grain size on the surface hot shortness is shown in Fig. 2. Before heating at 1373K in air and performing tensile tests, the grain size of the specimen was varied by heating in Ar gas at temperatures higher than 1373K. Increasing the grain size enhances the hot shortness.

The size of the specimen is reduced by oxidation, as shown in Table 2. The oxidation in the heat patterns of CC-HDR progresses more rapidly compared to that in the reheated pattern because the specimens are heated for longer time at higher temperatures.

In the specimen heated following CC-HDR, the steel/scale interface was ragged and film-like Cu-enriched phase was reduced, which seems to decrease the susceptibility to the surface hot shortness.

Table 2. Reduction in length of specimen edge by oxidation for each heat pattern (mm).

Heat pattern	steel A	steel B
Reheating (1373 K, 1.8 ks)	0.10	0.04
Simulated CC-HDR (Mid-width surface of slab)	0.17	0.15
Simulated CC-HDR (Mid-thickness surface of slab)	0.22	0.19

References

[1] S. Seo, K. Asakura, and K. Shibata: ISIJ Int., 37(1997), No.3, pp. 240-249.

[2] K. Shibata, S. Seo, K. Asakura, and Y. Akiyama: Trans. Mater. Research Soc. Jpn., 24(1999), No.3, pp. 333-336.

[3] C. Nagasaki, M. Kaga, K. Shibata, K. Asakura and M. Hatano, ISIJ Int. 42(2002), Supplement, pp. S57-S61.

[4] N. Moritama, M. Okimori, E. Ikezaki and K. Isogami, Tetsu-to-Hagane, 74(1988), pp.1227-1234.

Microstructure and mechanical properties of Cu-containing TRIP-aided Low carbon cold-rolled steels

Chang Gil Lee, Sung-Joon Kim, Tae-Ho Lee, and Chang-Seok Oh
Korea Institute of Machinery and Materials, Changwon 641-010 Korea

1. Introduction

With ever increasing environmental requirements, the challenges ahead steelmakers are immense. As one example, the usage of scraps increases in steelmaking process, and the accumulation of tramp or trace elements becomes a big problem due to their harmful effect on the mechanical properties and formability. The challenges facing the industry are therefore to reduce the cost for refining the tramp elements and maximize the recyclabililty of steel scraps.

Recently, numerous studies have been carried out on the TRIP-(transformation induced plasticity) aided multiphase steels based on Fe-C-Mn-Si, since the TRIP steels are good candidates for ECO (environmentally conscious)-materials owing to their simple composition and excellent combinations of high strength-high ductility [1-5].

Although typical TRIP steels consisting of 0.2-0.4% C, 1.0-2.5% Mn, and 1.2-2.0% Si have been widely studied in order to get higher strength and ductility [3, 6-7], the effect of tramp elements, especially Cu, on the microstructure and mechanical properties have scarecely been reported.

In the present study, therefore, Fe-0.15C-1.5Mn-1.5Si TRIP-aided cold rolled steels with or without Cu were prepared, and the effect of Cu on the microstructure, volume fraction of retained austenite, mechanical properties and formability were discussed.

2. Experimental Procedure

Two kinds of steel ingots having nominal compositions Fe-0.15C-1.5Mn-1.5Si-(0.5Cu), were fabricated by vacuum induction melting. Steel ingots were hot-rolled into sheets of 3 mm in thickness, and were cold-rolled into sheets of 1 mm in thickness. The intercritical annealing was conducted at the temperature of the fraction ratio of ferrite and austenite being 50:50 using a salt bath. The isothermal treatment was carried out in the temperature range of Ms~(Ms+20°C) for 1~20 minutes, and then air-cooled.

Tensile specimens with a gage length of 25.4 mm and a width of 6.3 mm were deformed at room temperature at a crosshead speed of 2 mm/min. using a tensile tester, and yield strength, tensile strength, and elongation were measured. A sodium metabisulfite solution ($Na_2S_2O_3 \cdot H_2O$ 10g + H_2O 100 ml) was used in conjunction with the nital etching to identify the phases. Volume fraction of the retained austenite was measured using an X-ray diffractometer (XRD). Mo-K_α characteristic ray was used, and the volume fraction of retained austenite, V_γ, was calculated from the integrated intensity of ferrite and austenite peaks.

Formability of specimens were measured using limiting dome height (LDH) with the blank holding force between 35 and 40 tons, and the forming limit curve (FLC) was drawn after measuring major and minor strain using optical grid analyzer (OGA).

3. Results and Discussion

Optical micrographs show that the Cu-containing steel has finer grain size and higher volume fraction of retained austenite than the Cu-free one, predicting that the mechanical properties of Cu-containing steel is better than that of Cu-free steel. As a matter of fact, the yield strength and tensile strength of Cu-containing steel were higher by 35 MPa and 90 MPa, respectively, than those of Cu-free steel. The total elongations were measured as 36.4% and 29.2% in Cu-containing and Cu-free steel. Thus, the strength and ductility balance of

Cu-containing steel is much more excellent that the Cu-free steel probably due to the higher volume fraction of retained austenite and the steadier transformation of retained austenite to martensite during tensile deformation.

The LDH values of Cu-containing and Cu-free steels were 28 mm and 25 mm, respectively. The better formability of Cu-containing steel can be explained by the higher work hardening exponent in spite of the similar stability of retained austenite in both steels. The forming limit curves of both steels were similar to those of Keeler-Goodwin diagram and are located in between the Keeler-Goodwin band, meaning that both steels have reasonable stamping formability.

Finally, the strengthening mechanism of Cu-containing TRIP steel was examined using high resolution TEM after long aging treatment at 500°C. The ε-Cu precipitates were not observed until after aging 20 hours. However, mottled microstructure was observed after aging 20 minutes, and 9R precipitates of 2-5 nm size were identified after aging 10 hours. These 9R precipitates are transforming to 3R and subsequently to ε-Cu after longer aging. Thus, the hardening of matrix ferrite after isothermal heat treatment may be from the solid solution hardening effect of Cu.

4. Conclusions

The addition of 0.5% Cu in 0.15% TRIP-aided cold rolled steel sheet greatly enhances the tensile properties and formability due to the higher volume fraction of retained austenite. Thus, Cu can be used as a beneficial tramp element in considering recyclability of steels.

References

1) K. I. Sugimoto, N. Ushi, M. Kobayashi, and S. I. Hashimoto : *ISIJ Inter.*, **32**, 1311 (1992).
2) K. I. Sugimoto, N. Ushi, M. Kobayashi, and S. I. Hashimoto : *Metall. Trans. A*, **23A**, 3085 (1992).
3) H. C. Chen, H. Era, and M. Shimizu : *Metall. Trans. A*, **20A**, 437 (1989).
4) S. K. Kim, H. C. Shin, J. H. Chung, and Y. W. Chang : *J. Korean Inst. of Met. & Mater.*, **36**, 151 (1998).
5) O. Matsumura, Y. Sakuma, and H. Takechi ; *Scripta Metall.*, 1987, **21**, 1301 (1987).
6) H. C. Chen, H. Era, and H. Shimizu : *Metall. Trans. A*, **20A**, 437 (1989).
7) Y. Sakuma, O. Matsumura, and H. Takechi : *Metall. Trans. A*, **22A**, 489 (1991).

Structure Formation of Continuously Cast 0.1 mass% C Steel with High Phosphorus

N.Yoshida and K.Nagai
Materials Creation Research Group, National Institute for Materials Science, Japan
O.Umezawa
Department of Mechanical Engineering and Materials Science,
Yokohama National University, Japan

1. Introduction

Phosphorus, P, is one of the major impurities restricted in steel making, since high P causes low toughness and poor weldability. Grain refining by thermo-mechanical treatment improves both strength and toughness [1] and it may suppress the harmful effects of P. In the present study, macro- and micro-structures of continuously cast (CC) 100 mm thick slab of 0.1 mass% C steels with various P contents have been characterized and discussed in terms of the γ grain growth and the α structure formation on cooling for the as-cast materials from the viewpoint of the fabrication of finer microstructures.

2. Experimental

Carbon content of the steels tested in the present study was 0.10 mass% and the P content ranged between 0.01 and 0.20 mass%, i.e. 0.01P, 0.10P and 0.20P (Table 1). Slabs with a thickness of 100mm were produced with a laboratory-scale continuous caster at Sumitomo Metal Industries Ltd./Corporate R&D Labs, Hasaki (Table 2). Both macroscopic and microscopic structures of the slabs were observed. Microscopic segregation maps of solutes for the slabs at a quarter thickness were examined by EPMA. Based on the segregation map, a local equilibrium calculation was made to evaluate the stability of the δ and γ phases. Thermo-chemical calculation with a multi-component system database [2] was also applied to the equilibrium condition of the Fe-P-Mn pseudo-ternary systems.

3. Results and discussion

(1) Structure of cast slabs

The columnar structure prevails through the thickness in all the steels. In the 0.10P, the

Table 1. The chemical compositions of test steels (mass%).

C	Si	Mn	P	S
0.10	0.17	0.60	0.01~0.20	0.003

Table 2. Casting conditions.

Melt	2.5 ton
Size of slab	100 mm^T × 800 mm^W × 3 m^L
Casting velocity	0.8~1.0 m/min

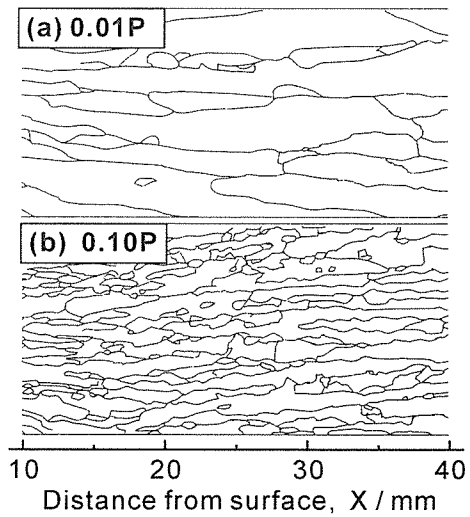

Fig.1 Prior γ grain structure at 1/4 thickness of CC slab: (a)0.01P and (b)0.10P .

prior γ grain size is smaller than that in the 0.01P as shown in Fig.1. The prior γ grain size D_γ in the square conversion and the primary dendrite arm spacing S_1 at the quarter thickness are shown in Fig.2. D_γ for 0.10P and 0.20P is smaller than 0.8 mm, although that for the 0.01P is about 1.6 mm. On the contrary, S_1 is about 0.3mm for all the steels. The coarseness number D_γ^2/S_1^2, the ratio of powered γ grain size to powered primary dendrite arm spacing, for 0.10P and 0.20P is a fifth of that for 0.01P. Thus the P addition prevents γ-grain from coarsening.

The P addition also dramatically changes the α-grain structure. The globular α grains in the prior γ grain are detected in the slabs for 0.10P and 0.20P.

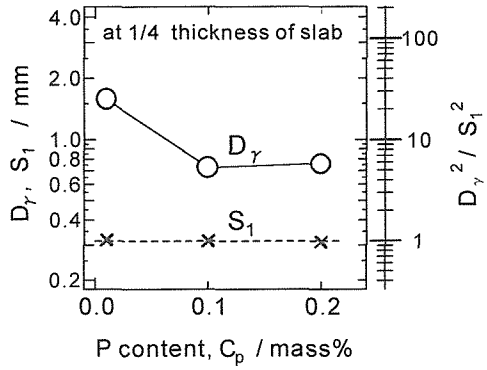

Fig.2 Effect of P content on γ grain size.

(2) Stabilization of δ-ferrite

Figure 3 shows the distribution of major segregating solutes, P and Mn, at the quarter thickness and the contour lines of transformation temperatures, A_{e4}(δ / γ) and A_{e3}(γ / α), in the Fe-0.10C-0.15Si-P-Mn system. The maximum P concentration is over 0.2 mass% for 0.10P and over 0.4 mass% for 0.20P. The high P concentration stabilizes the δ-phase and decreases the finish temperature of the δ / γ transformation. Hence, the remaining δ-phase may pin the γ-grain boundary migration in the temperature range of rapid growth of γ-grain.

The P segregation also affects the γ / α transformation. The P concentration also increases the A_3 temperature or retains δ phase (dashed circles for 0.20P in Fig. 3). Retained δ in the γ-grain may be a predominant site for γ / α transformation. Thus the globular α-grain may originate from the retained δ-phase.

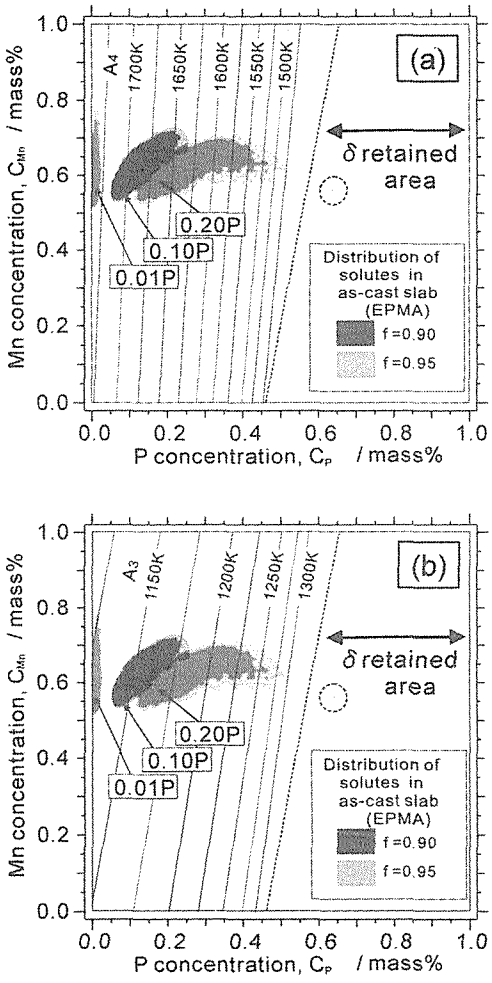

Fig.3 Distribution of solutes at 1/4 thickness of as-cast slabs and contour lines of phase transformation in Fe(0.10C-0.15Si)-P-Mn system. (a) A_{e4} (δ / γ) and (b) A_{e3} (γ / α) temperatures.

4. Conclusions

The addition of P decreases the γ grain size and changes the α-grain structure. Hence, P brings about a fine solidification structure in 0.1 mass% C steels.

References

[1] T.Hanamura, T.Yamashita, O.Umezawa, S.Torizuka and K.Nagai: Proc. Inter. Sympo. on Ultrafine Grained Steels, Fukuoka, ISIJ(2001), pp.228-231.

[2] B.Jansson, M.Schalin, M.Sellby and B.Sundman: Proc. 2nd Inter. Sympo. Computer Software in Chemical and Extractive Metallurgy, ed. by C.W.Bale and G.A.Irons, The Mat. Soc. of CIM(1993), pp57-71.

Microstructural change by heavy deformation after reheating for cast slabs of 0.1mass% carbon steel

T.Yamashita, S.Torizuka, and K.Nagai
Materials Creation Research Group, NIMS, Japan

1. Introduction

Austenite structure prior to thermo-mechanical processing can be classified into three categories. Type 1 is the as-cast structure observed in slabs (Fig.1(a)). This structure has coarse and elongated austenite grains with macro- and micro-segregations. Type 2 is the reheated cast structure observed in reheated slabs (Fig.1(b)). The austenite grains are refined and equiaxed with micro-segregation. Type 3 is the hot-rolled and reheated structure observed in hot-rolled plates (Fig.1(c)). The austenite grains are small and equiaxed with little segregation. Torizuka et al. previously reported that fine ferrite grain structures could be obtained by a heavy deformation even from the coarse austenite grains for the Type 3 structure[1]. It is worthwhile to investigate whether a similar method is applicable for the Type 2 structure to establish an ideal rolling process for the cast slabs.

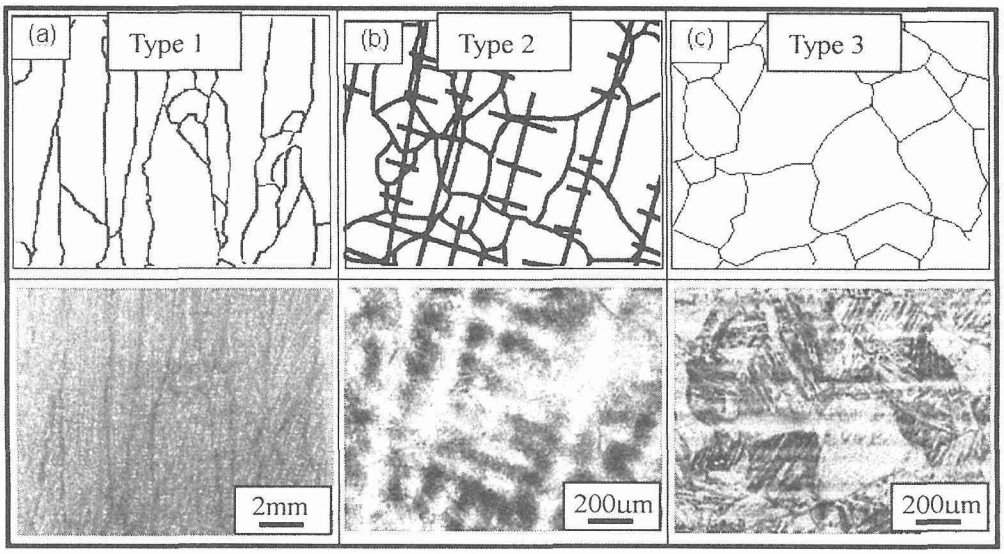

Fig.1 Three kinds of austenite grain structures : (a) as-cast slab, (b) cast and reheated slab (c) hot rolled and reheated plate. Top : Schematics, Bottom : light micrographs.

2. Experimental

The chemical composition of the as-cast steel with a Type 2 structure, HPH1, is listed in Table 1. Specimens with a thickness of 12mm, a width of 15mm and a length of 16mm were soaked for 60s at 1223K or 1473K. The austenite grain size was 20μm and 200μm, respectively. Then, they were compressed by a pair of anvils at 1093K in the γ region. The specimens were compressed from 12 to 3mm in thickness (75% in nominal reduction) at a nominal strain rate of 10/s and then cooled at 10 K/s. The compression direction was parallel to the growth direction of the primary dendrite arms.

Table 1. Chemical compositions of the steels used (mass%).

	C	Si	Mn	P	S
HPH1	0.11	0.16	0.58	0.01	0.003

3. Results

Figure 2 indicates the change of the ferrite grain size by the strain. When the austenite grain size is small, 20μm, the fine ferrite grain size that is smaller than 5μm can be obtained within the strain range investigated for the Type 2 structure as well as for the Type 3 one. When the austenite grain size is large, 300μm, the ferrite grain size becomes smaller with an increase in the strain and reaches 5μm at the heaviest strain.

Figure 3 represents a variation of the ferrite grain structure of the HPH1 steel. When the austenite grain size is large, the Widmanstatten ferrites form clearly but disappear at the heaviest strain. On the other hand, no Widmanstatten ferrite forms when the austenite grain size is small. Eventually the fine-grained polygonal ferrite structure forms regardless of the austenite grain size at the heaviest strain.

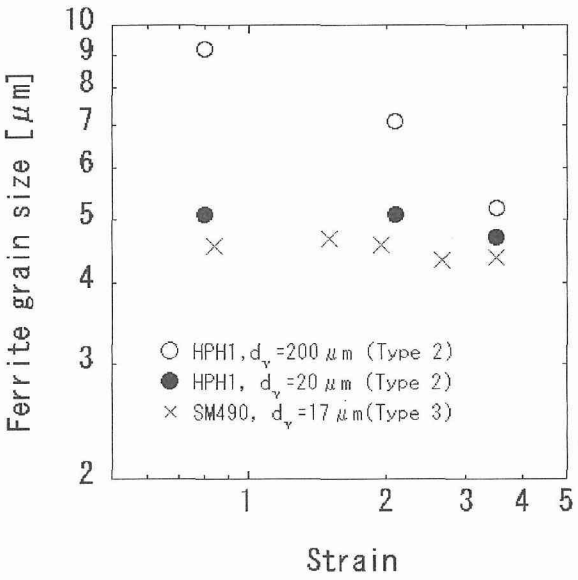

Fig.2 Relationship between compression strain and ferrite grain size (deformed temperature : 1093K) .

We can conclude that the fine ferrite grain structure can be obtained by a heavy deformation for the Type 2 structure as well as for the Type 3 one.

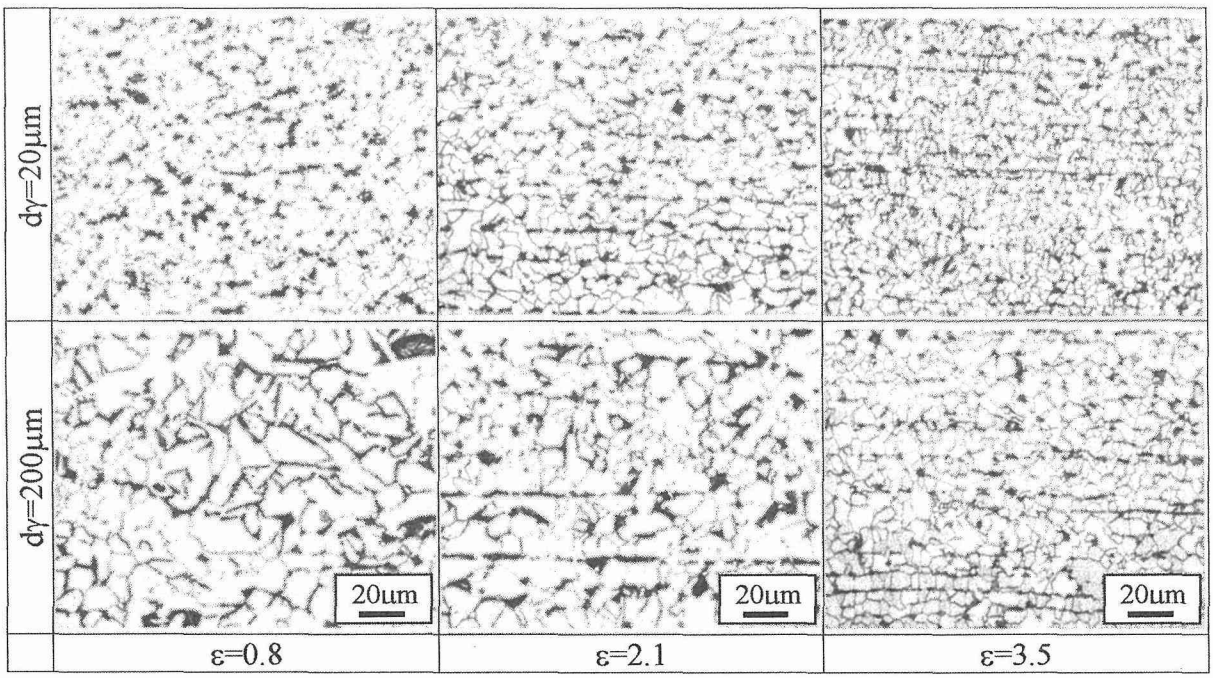

Fig.3 Variation of ferrite structure by strain (ε) for two austenite grain sizes (d_γ) in HPH1 steel. Specimens were compressed by the given strain at 1093K at a strain rate of 10/s and then cooled at 10K/s.

References

[1] S.Torizuka and K.Nagai : CAMP-ISIJ, 14(2001), pp.402-405.

Research and Development of New Hot-Direct Rolling Process

K.Yamamoto(1), R.Hashimoto(1), H.Furumoto(1),H.Nakajima(1), H.Takatani(1) and H.Tsukamoto(2)

(1) Mitsubishi Heavy Industries, Ltd. Hiroshima R&D center, Japan
(2) Ryomei Engineering Co. Ltd., Japan

Synopsis

In the steel making industry, the reduction of the energy consumption and CO_2 emission are required. The amount of recycled steel scrap is increasing as shown in Fig.1[1]. The thin slab CC(continuous casting) process as well as the electric furnace process is also increasing because of low energy consumption as shown in Fig.2[2]. Furthermore, the strip CC process, which can produce thin strips of several mm thickness directly from molten steel, has started commercial operations for stainless steels[3].

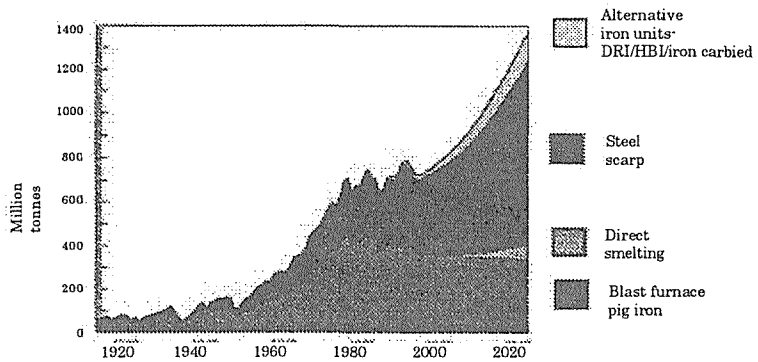

Fig.1 World steel production by type and source of iron units. (1910-2020)[1]

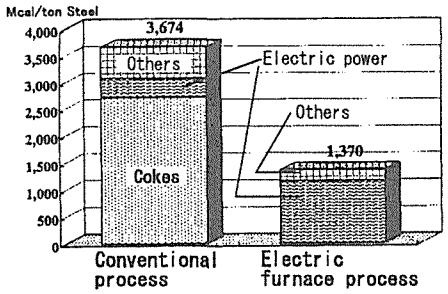

Fig.2 The comparison of energy consumption between the conventional process and the electric furnace process[2]

The thin slab CC[4] process which consists of a thin slab CC, a tunnel furnace, rolling mills, cooling equipments and a coiler is compact process and low-energy consumption process. Cast thin slabs are hot-charged in a tunnel furnace and directly rolled. The profiles of rolled sheets are accurately controlled by pair cross mills[5].

The strip CC process as shown in Fig. 3 is more compact, and its energy consumption and CO_2 emission are lower than those of conventional processes. The strip casting has a characteristic of rapid solidification, which can disperse impurities such as Cu as an influence

of hot brittleness in steel scrap. The strip CC process is expected to be a process for thin strips produced from steel scrap with a high content of Cu without hot brittleness, owing to the rapid solidification and the hot-direct rolling process which does not need long time for heating. The trail strip casting for the 0.1%C carbon steel including 0.3%Cu which simulates steel scrap was conducted by using the test machine of 600mm wide drums. The stable casting has been achieved in that steel without surface cracks. The strip has sufficient mechanical properties for the standard of JIS - SS400 (hot rolled sheet), and its strength can be controlled by rolling conditions.

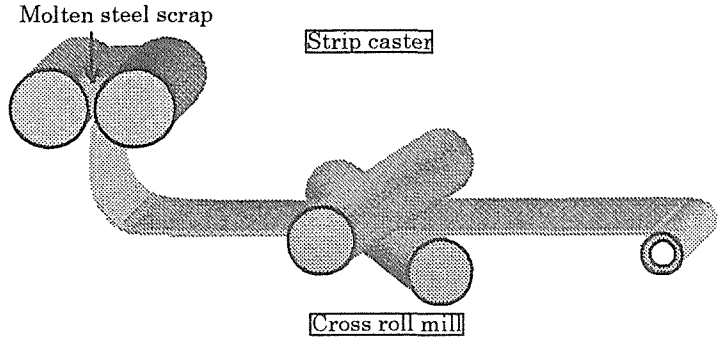

Fig.3 The strip CC process.

The large-angled cross rolling is an effective technique for controlling microstructure and properties of rolled products by applying shear deformation along the width direction as shown in Fig. 4[6]. It is expected to be effective for fine grained steel by shear strain and for control the decrease of the absorbed energy and the anisotropy of formability by changing the texture.

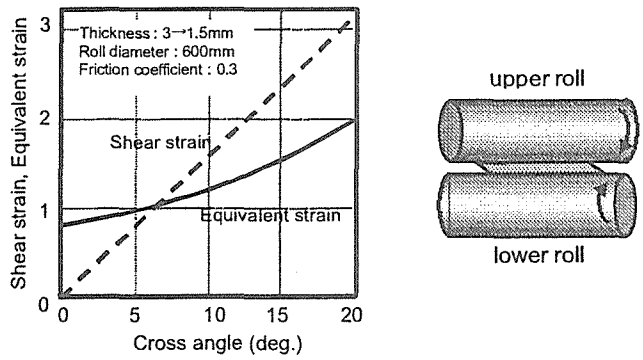

Fig. 4 Relationship between cross angle and strain[6]

Reference

[1] Seminar on Steel Industry and Recycling, Düsseldorf, 24-27 April (1995), source: IISI

[2] M. Ohji and M. Nishio, Bulletin of ISIJ, 7 (2002) No.3, pp.178-184

[3] H.Nakajima, H.Takeuchi, H.Hosoda, K.Yamada, T.Tanaka, S.Shoda, K.Isogami, S.Kuratani, K. Yamamoto and K. Kunimasa, CAMP-ISIJ, 15 (2002), pp. 208

[4] Y.Shimizu, Y. Yamasaki, J.Iwatani, T.Takeguchi and A.Kametani, Mitsubishi Heavy Industires, Ltd. Technical Review 37 (2000), No.2, pp.45-47

[5] H.Tsukamoto, K.Morimoto and R.Ohzono, Memorial Symposium of the 100th Rolling Theory Committee, Development and Prospect of Theory and Technology of Steel Rolling, ISIJ (1996), pp.89-96

[6] H.Tsukamoto, Workshop of "Feasibility study on materials design with a low environmental load for a resources circulating society", March 27th, Tokyo (2000)

Microstructure Control in Near-Net Fabrication Process

K. Nagai
Materials Creation Research Group, NIMS, Japan

1. Background

In the present Japan the electric steel occupies 30% and more in the total steel production. Estimation on the future amount of the scrap says a gradual increase in this century. On the other hand, the population turns to decrease after around 2015 and then the domestic steel needs will decrease with a decrease in the population. Eventually the scrap will amount to the domestic needs before the middle of this century. In this sense a resource circulating society of steel is the inevitable one in the near future Japan. Global environmental issue or significant reduction in green house gas emission is another key point for our sustainability. Steel industry is responsible for about 30% in the total CO_2 emission in Japan. As one the vital limitations Japan has very scare space for landfills in her territory. Hence, the marked reduction in industrial wastes is also vitally required. For our survival the steel fabrication must adjust itself properly to these coming circumstances. One of the major concerns is material design for recyclability and another is steel processing based scrap.

2. Near-net fabrication processes in steel

Compared with the current oxygen steel processing, so-called neat-net processes have some advantages from the viewpoints of environmental issues. Among the near-net processes, thin-slab casting and strip casting are promising ones, since their estimated CO_2 emission per unit steel weight is about a fifth that in the oxygen steel process. And further the layout size and the investment cost is very much smaller. This is also favorable for small-scale and scattered works from an ideal design of efficient, ecological, and economical recycle system network in Japan. So far scrap steels, or steels from scrap, are inferior to the oxygen steels in terms of their properties. In the near-net processes, to control their properties at the high level is the hottest challenge in the development. In other words, microstructure control for high performance is the main vector in R&D.

3. Microstructure control

Microstructure control has belonged to solid-state scientists or downstream engineers for long time. Transformation, recrystallization, and precipitation are major fields in the microstructure control for desired strength and ductility. Inclusions are also important to control some fracture problems. People used to believe the repetition of γ/α and α/γ transformations is the necessity for better properties of steels. Although whether this is not true has not yet been clarified thoroughly, continuous cast (CC) products have shown good performance and then the CC process replaced the precedent process. Combined with thermo-mechanical controlled processing (TMCP), so-called continuous processing built up and ruled its kingdom. After decades, new demands have arisen for better performance even for the CC products. The engineers have begun to look into the solidification control for this purpose in one side and now pay attention on much more sophisticated TMCP technology in the other side. The keyword is again microstructure control. Tiny compound control, finer solidified structure control, and ultra refined grain structure fabrication are new key technologies.

4. Ultrafine refinement of ferrite grain

Ultrafine refinement of ferrite grains has been aimed at worldwide in recent years. As one of such the national projects, NIMS has performed the ULTRA STEEL project. In the first five-year-project, NIMS produced in a laboratory scale a 18 mm thick and 20 m long bar and

a 12 mm thick, 60 mm wide and 2 m plate with a full of ferrite grains of 0.5 μm in diameter. With the lean and recyclable chemical compositions, the strength is doubled and the toughness markedly improved. A week point of the ultrafine-grained steel, a poor ductility, is basically overcome with a fine dispersion of cementites. Thus, this is very promising for basis of the resource circulating society. In the next step, the idea should be built in the new TMCP processing.

5. Rapid solidification

An advantage in the near-net shape casting is rapid solidification to bring about finer solidified structures. In addition, there must be unveiled possibilities in low temperature liquid steel in terms of the existence and the utilization of some unknown compounds. However, basic understanding about the effect of cooling rate on solidified structure and further phenomena like δ/γ transformation is quite insufficient. And further steel scrap includes many kinds of impurities. We should know how those impurities behave and affect in the process. In our project, we have studied the microstructural control and improvement of mechanical properties for low-grade steels containing P, Cu, etc. The impurities are not only elements which are highly effective in solid solution or precipitation strengthening, but are also elements that affect the transformation structure due to their segregation. For example, concentrated P in the final solidification regime stabilizes the δ-ferrite and decreases the temperature for completing the transformation into a γ single phase. Hence, the pinning effect of the δ-ferrite on the γ-grain boundary migration must be kept in the temperature range of rapid γ grain growth.

6. Attempts for advanced thermo-mechanical processing

Adjustment and control of the chemical potential of liquid steel with high impurities, refinement of rapidly solidified structure by the aid of impurity segregation and δ-ferrite, and further attempts are due to investigate in our project. In the final stage of the processing, TMCP is again the issue to utilize. However, normally the cast thickness is too small to be insufficient to high reduction necessary for fine microstructure control. Therefore, novel ideas to make use of the TMCP most efficiently are needed. As one of the new ideas we are pursuing the multidirectional deformation for controlling the texture of the rolled products. Or we can introduce more plastic strain at a given reduction in the plate thickness. After a series of fundamental studies, we intend to build up a combined new process of rapid solidification and plastic deformation as a tool for efficient and powerful microstructure control.

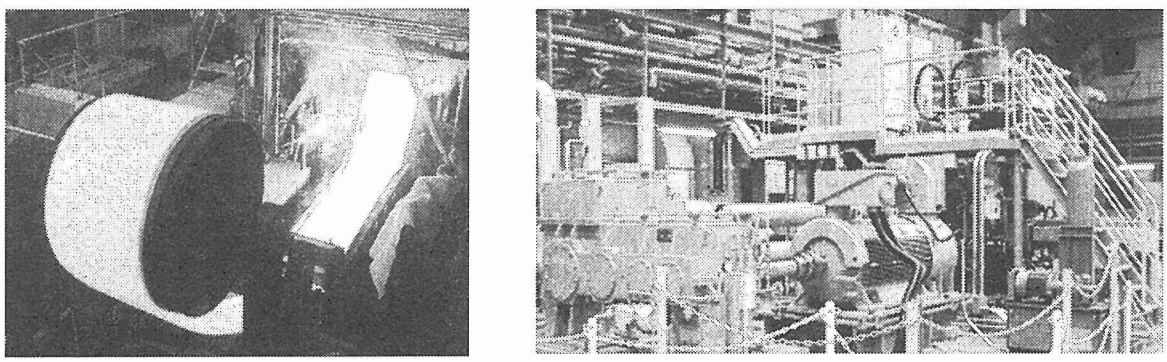

Fig. Strip Caster (left) and Cross Roller (right).

Effect of Diffusion of {100} Parallel to the ND Plane by Cross Roll Rolling on the Charpy Impact Properties in Low Carbon Steels

T.Hanamura, S.Torizuka and K.Nagai
National Institute for Materials Science

1. Introduction In the α and γ two phase region rolling for low carbon steels, {100} textures have been known to form, leading to a higher frequency of separation fracture and a decrease of the upper shelf energy in the Charpy impact tests [1]. If the {100} texture is diffused, the Charpy impact properties are expected to change drastically. There is a possibility that cross roll rolling can create shear deformation horizontally perpendicular to the rolling direction. It has also been examined that the shear introduced in a cross roll rolling can develop textures different from those produced by conventional rolling [2]. Therefore, in this study, cross roll rolling is applied to low carbon steels with the aim of diffusing the {100} texture, and the effect of {100} texture diffusion on their mechanical properties is examined.

2. Experimental Low carbon steel samples (0.15wt.%C-1.5wt.%Mn-0.3wt.%Si) with a width of 55 mm, a thickness of 50 mm, and a length of 300 mm were annealed for 30min at 1173K and then multi-pass rolled in a reverse manner at 1023K to 10mm thickness at different cross angles, including 0, 5 and 10 degrees. The conventional X-ray diffraction technique with a Cu-Kα radiation was used to measure {100} and {110} pole figures. Charpy impact tests in the temperature range between 78K and 373K were also conducted.

3. Results The whole view of the cross roll rolling mill with its cross angle set at 10 degrees is shown in Fig.1. Both inner housings of upper and lower rolls rotate oppositely to make two rolls crossed. The preferred orientation in the {100} pole figure is determined to be predominantly {100} parallel to the ND plane, and its intensity decreases with an increase in the cross angle, as shown in Fig.2. This means that the {100} texture is diffused by increasing the cross angle. The Charpy impact test was conducted on each sample, and the DBTT in the impact absorption energy was found to shift to lower temperatures by more than 50 K when rolled at the cross angle of 5 degrees as shown in Fig.3. The lowest temperature at which the sample shows an upper shelf energy of higher than 250J is decreased from 248K to 198K by cross roll rolling. The frequency of separation is remarkably suppressed by cross roll rolling.

References

1) S.Matsuda, Y.Kawashima, S.Sekiguchi, and M.Okamoto: *Tetsu to Hagane* Vol.68, (1982),435.
2) T.Hanamura, T.Higuchi, T.Yamashita, O.Umezawa, T.Inoue, S.Torizuka and K,Nagai : CAMP-ISIJ Vol.13(2000)1254.

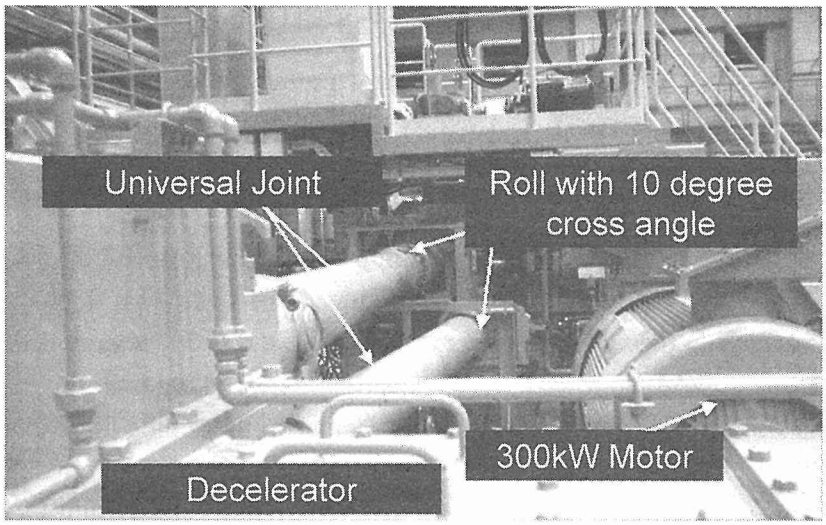

Fig.1: Cross roll rolling mill with the cross angle set at 10 degrees.

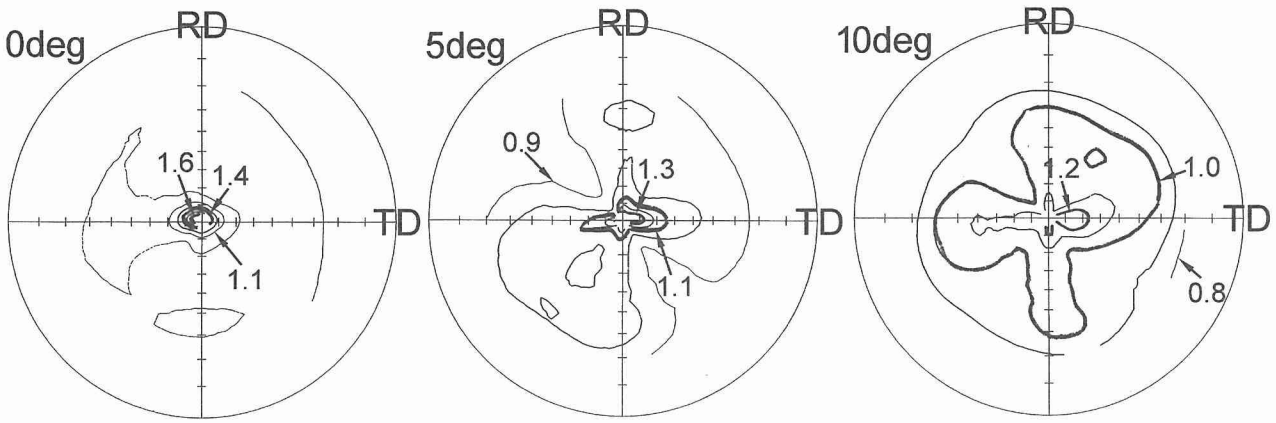

Fig.2: {100} pole figures for low carbon steels cross-roll rolled at cross angles of 0, 5 and 10 degrees.

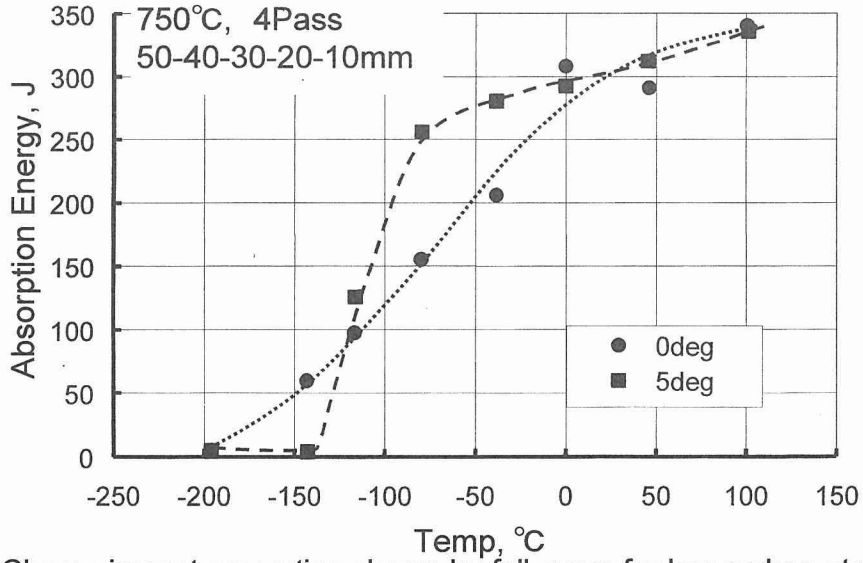

Fig.3: Charpy impact properties shown by full curve for low carbon steels multi-pass rolled with the cross angle of 0 and 5 degrees.

Effect of Microstructure on the Yield Ratio and Low Temperature Toughness of API Steels

S. G. Kim*, Y. M. Kim, S. Lee, Y. J. Lim** and N. J. Kim
Department of Materials Science and Engineering and Center for Advanced Aerospace Materials, Pohang University of Science and Technology, Pohang 790-784, Korea
*POSLab, Gwangyang, Korea
**Quality Technology Dept. POSCO, Pohang, 790-360 Korea

1. Introduction

In recent years, there have been increasing demands for high-performance linepipe steels which have not only high strength but also good low temperature toughness. It is also required for the steels to have low yield ratio. Moreover, the improvement in strength should not impair the weldability and resistance to environment degradation, especially HIC. The basic difficulty in optimizing these properties comes from the fact they are often inversely correlated, i.e. an increase in the strength is achieved at the expense of the yield ratio and toughness, and vice versa. Therefore to develop the high performance API steels, the individual effect of microstructural features on these properties should be clearly elucidated. The objective of the present study is to elucidate the effects of microstructural features on the yield ratio and toughness of high strength API steels.

2. Results & Discussion

Several alloy systems with different microstructures, i.e. ferritic-pearlitic steels, ferritic steels with acicular ferrite as 2nd phase, acicular ferritic/bainitic steels with ferrite as 2nd phase, and fully acicular ferritic/bainitic steels, have been manufactured by modifying the alloy compositions as shown in Fig. 1.

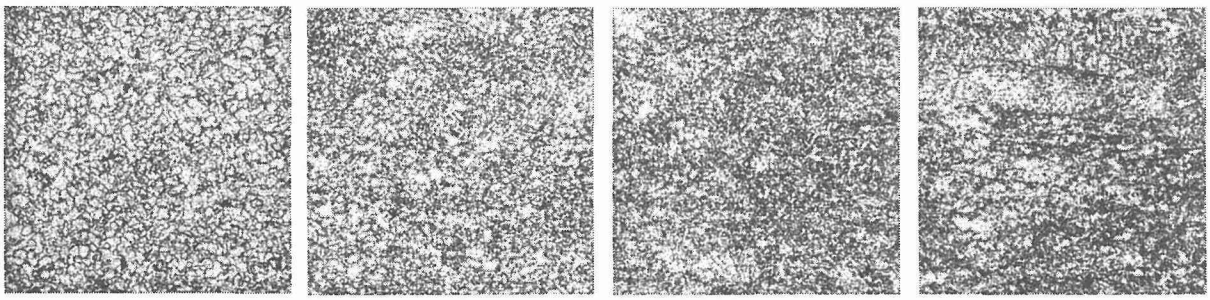

Fig. 1. Optical microstructures; a) ferrite-pearlite, b) ferrite-acicular ferrite, c) acicular ferrite-ferrite, and d) acicular ferrite.

It shows that, in general, the ferrite base steels should have ferrite grain size smaller than 10 μm to have acceptable yield strength and low temperature toughness. However, reducing the ferrite grain size increase the yield ratio in the ferrite base steels. The yield strength of the ferrite base steels can be increased (above X-80 grade) by the introduction of acicular ferrite as a second phase. But these steels have yield ratio higher than 85%, which is not acceptable.

However, modification of matrix from ferrite to acicular ferrite results in improvements in both yield strength and yield ratio. This is mainly due to the abundance of mobile dislocations in acicular ferritic structure. However, fully acicular ferritic steels have worse low temperature toughness (i.e., higher DBTT) than the other types of steels. It has been shown that the low temperature toughness of acicular ferrite steels can be improved by the

introduction of polygonal ferrite as a second phase. This is mainly due to the refinement of effective grain size by the introduction of second phases.

It has also been shown that the yield ratio is largely dependent on the work hardening rate, which is also dependent on the microstructure. Stress-strain behavior of steels has been analyzed by using the Holloman equation and the modified Swift equation. It has been shown that the Holloman equation cannot describe the stress-strain behavior of steels since it underestimates the strength at low strain levels. However, the Swift equation can adequately describe the stress-strain behavior of steels and the relationship between the yield ratio and work hardening exponent has been derived using as follows;

$$YR = \frac{S_y}{S_u} = \frac{(b + \ln(1 + e_y))^N}{(1 + e_y)} \frac{\exp(N - b)}{N^N}$$

where b is the additive strain constant, e_y is the engineering strain at yield strength (usually 0.002), and N is the work hardening exponent.

The linear relationship has been established between $\ln(\sigma)$ and $\ln(\varepsilon_p+b)$ by setting the appropriate values of b for each type of microstructure. The values of b range from 0.002 to 0.03, depending on the microstructure with the lowest value of b associated with heavily dislocated structure. Fig. 2 shows the relationship between the yield ratio and work hardening exponent of various steels. The experimental results agree well with the results calculated using the above equation. It shows that the ferrite base steels have larger work hardening exponents than the acicular ferrite or bainite base steels. Increasing the ferrite grain size increases the work hardening exponent of the ferrite base steels, thereby decreasing the yield ratio. In the case of acicular ferrite or bainite base steels, increasing the volume fraction of soft second phase of polygonal ferrite increases the work hardening exponents, resulting in a decrease in yield ratio.

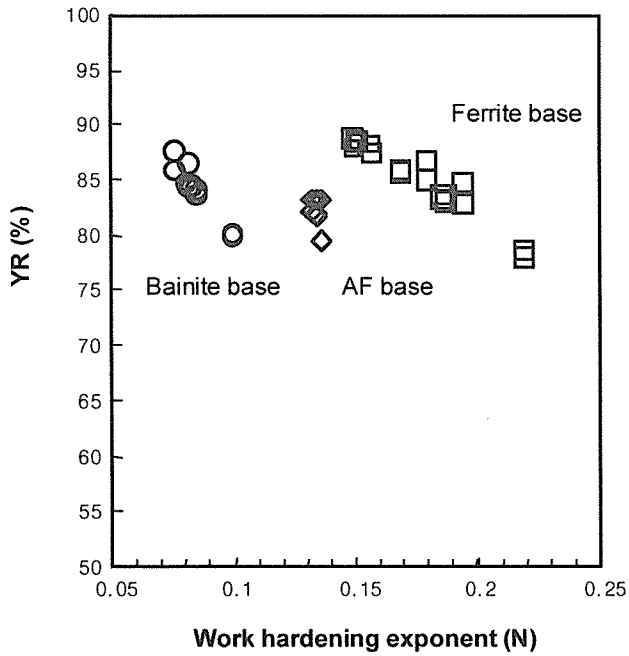

Fig. 2. Relationship between yield ratio and work hardening exponent of various steels.

Based on the correlation of microstructure and mechanical properties, optimum microstructure for the development of high performance API steels can be suggested. Acicular ferrite or bainite base steels have the advantage of higher yield strength and lower yield ratio over ferrite base steels. The problem of poor low temperature toughness of these acicular ferrite or bainite base steels can be overcome by the introduction of polygonal ferrite as second phase, which reduces the effective grain size.

The Nature and Consequences of Coherent Transformations in Steel

J.W. Morris, Jr., C.S. Lee[1] and Z. Guo[2]
Department of Materials Science and Engineering, University of California, Berkeley, and Center for Advanced Materials, Lawrence Berkeley Laboratory, Berkeley, CA 94720, USA
[1]Present Address: POSCO, Pohang, Korea
[2]Present Address: Intel Corporation, Santa Clara, CA

1. Introduction

Recent research on the next generation of structural steels has emphasized the improvement of properties through the control of grain size. Grain refinement is used to increase strength via the Hall-Petch relation, lower the ductile-brittle transition by increasing resistance to transgranular cleavage, and reduce susceptibility to hydrogen embrittlement by minimizing interfacial fracture along grain or lath boundaries [1].

To utilize grain refinement effectively it is important to understand the meaning of the "grain size" and its connection to the measurable features of the microstructure. Mechanistic analysis suggests that, in fact, the effective grain size has a different meaning for strength, cleavage fracture and hydrogen resistance. Moreover, the connection between the effective grain size and the appearance of the microstructure depends on whether the microstructure is obtained by coherent or incoherent transformation from the parent austenite. The present paper concentrates on the nature and consequences of coherent transformations.

2. Discussion and conclusions

It is well known that the martensitic transformation in steel is crystallographically coherent: the martensite product has either a Kurdjumov-Sachs (KS) or a Nishiyama-Wasserman (NW) relation to the parent austenite. However, recent research has shown that diffusional transformations are often coherent as well. Both the ferrite produced on cooling deformed austenite [2-4] and the acicular ferrite nucleated on inclusion particles can be coherent [4].

A coherent transformation from austenite to ferrite (or martensite) can be regarded as the sum of two sequential crystallographic changes. First, the fcc austenite is deformed by the tetragonal "Bain strain" to transform it into bcc ferrite. The tetragonal axis of the Bain strain is one of the three <100> cube directions in austenite. Hence there are three distinct "Bain" variants of the product ferrite. The second step in the transformation is a supplementary shear and rotation that brings a {110} close-packed plane of the ferrite parallel to a {111} close-packed planes of the austenite, and aligns a <111> (KS) or <100> (NW) direction of the ferrite with a <110> close-packed direction of the austenite. There are eight distinguishable ways to establish a KS correspondence, and four ways to achieve a NW correspondence for each Bain variant. This degeneracy means that there are a total of 24 KS variants and 12 NW variants for the coherent transformation. However, the transformation strain is almost entirely determined by the Bain variant; the different KS and NW variants associated with a given Bain variant have transformation strains that differ through relatively small shears.

Since the ferrite variants that form from a given prior austenite grain are crystallographically related to the same parent, they are crystallographically related to one another. This fact qualifies the possibility of refining the effective grain size through coherent transformations. We first consider fracture. Iron cleaves on {100} planes. As can be made clear by drawing appropriate pole figures, a {100} plane is tilted by a large angle on crossing a boundary between different Bain variants, but is tilted by a relatively small angle on crossing a boundary between KS or NW variants associated with the same Bain variant. It follows that the effective grain size with respect to transgranular cleavage is largely determined by the distribution of Bain variants, and is not significantly affected by boundaries between variants with the same Bain axis. To refine the grain size, we need to maximize the density of boundaries between different Bain variants. We shall discuss thermal, thermomechanical and mechanical processes that accomplish this [5,6].

Like most bcc metals, iron deforms plastically by slip on multiple slip systems. The most common is <111>{110}. However, an appropriate pole figure shows that there is only a slight tilt in a {110} plane on crossing a variant boundary, even if the two variants have different Bain axes. While further research needs to be done, this result suggests that coherent transformations are not particularly effective in refining the effective grain size for strength (that is, the effective grain size that appears in the Hall-Petch relation). Research toward processes that achieve high strength may be more profitably focused on ways of achieving fine prior austenite grain size and incoherent transformation to ferrite [7].

Acknowledgement

This work was supported by the Director, Office of Science, Office of Basic Energy Sciences, Division of Materials Sciences and Engineering, of the U.S. Department of Energy under Contract No. DE-AC03-76SF00098.

References

[1] J.W. Morris, Jr., in Ultrafine Grained Steels, ed. S. Takaki and T. Maki, Iron and Steel Institute of Japan, Tokyo, 2001, p. 34-41
[2] B. Duflos and B. Cantor: in Proc. 3rd Int. Conf. on Rapidly Quenched Metals, B. Cantor, ed., Inst. Metals, London, 1978, vol. 1, p. 110
[3] P.J. Hurley, B.C. Muddle and P.D. Hodgson, Mater. Sci. and Tech., 16(2000), 1376-1379
[4] C.S. Lee, J.W. Morris, Jr., Z. Guo and D.H. Seo, in The Development of High Performance Structural Steels for the 21st Century, POSCO, Pohang, Korea, 2002, p. 139-142
[5] Z. Guo, PhD Thesis, Dept. Materials Science and Eng., Univ. California, Berkeley, 2001
[6] J.W. Morris, Jr., Z. Guo, C.R. Krenn and Y.H. Kim, ISIJ International, 4 (2001), 599-611
[7] J.W. Morris, Jr., Z. Guo and C.S. Lee, in The Development of High Performance Structural Steels for the 21st Century, POSCO, Pohang, Korea, 2002, p. 43-54

Improvement of Delayed Fracture Resistance in High Strength Steels by Control of Grain Boundary Structure

K.Tsuzaki, Y.Kimura and T.Hara
Materials Engineering Laboratory, National Institute for Materials Science
1-2-1 Sengen, Tsukuba, Ibaraki 305-0047, Japan

1. Introduction

Hydrogen-induced delayed fracture is one of the most serious problems in high strength steels for actual application. Since its crack initiation usually occurs along prior-austenite grain boundary, control of boundary structure is one of promising ways to obtain better fracture resistance without addition of special alloying elements. In this paper, our two attempts [1,2] on this issue are briefly described. In both cases, refinement of boundary facet size and boundary carbide was intended in a commercial SCM440 steel (0.40%C, 0.24%Si, 0.81%Mn, 0.02%P, 0.01%S, 1.03%Cr, 0.16%Mo, and the balance Fe).

2. Serrated Grain Boundary Plane introduced by Modified Ausforming

Modified ausforming process consists of plastic deformation at around 1100K and following quenching. The deformation temperature is higher than that for typical ausforming (around 700K), so that diffusion occurs more dominantly and grain boundary migration readily takes place. It is thus expected that grain boundary plane is not flat but serrated, resulting in decrease of grain boundary facet size. Moreover, dislocations introduced by deformation are inherited into martensite and may act as preferential nucleation sites of carbides during tempering. This results in uniform distribution of carbides without coarse film-like grain boundary carbide.

A 5m bar with 7.75mm in diameter was austenitized at 1323K for 720s in nitrogen gas and then air-cooled to 1048K, followed by rolling with a bar rolling simulator consisting of 4 rolling stands. When the finish rolling temperature was raised to 1063-1093K, there was a total reduction in area of 50%. After water spray quenching, it was subsequently tempered at 813K for 10s with an induction heating line (heating rate=150K), followed by water quenching. Through this processing we obtained the specimen with a tensile strength level of 1579MPa. A conventional QT specimen was also prepared for comparison. The specimen was austenitized at 1153K for 0.9ks and then oil-quenched. It was tempered at 673K for 1.8ks in a salt bath furnace, and a tensile strength of 1586MPa was obtained.

In the ausformed specimen, prior-austenite grains are elongated along the rolling direction (Fig.1(a)) and grain boundary planes are serrated in size of 1μm (Fig.1(b)). SEM and TEM observations confirmed that fine carbide particles are uniformly distributed in the ausformed specimen, while coarse film-like carbides are seen in the QT specimen.

Hydrogen embrittlement susceptibility was examined with hydrogen pre-charged round-notched specimens, where the stress concentration factor (Kt) was 3.6 and the applied stress on the minimum cross section area was 0.9 times tensile strength. The critical hydrogen content (Hc), below which the specimen does not fracture, was 0.53 mass ppm for the ausformed specimen, while it was 0.13 ppm for the conventional QT specimen. Moreover, the fracture mode was changed from intergranular fracture to quasi-cleavage fracture.

3. Ultra Fine-Grained Martensite with Retained Carbide

Second particles retards grain growth by pinning effect, resulting in fine austenite grains. Moreover, if retained carbide particles exist on a boundary plane, growth of the carbide takes place during tempering rather than new carbide particles form on the boundary. We can thus expect that coarse film-like carbide never form.

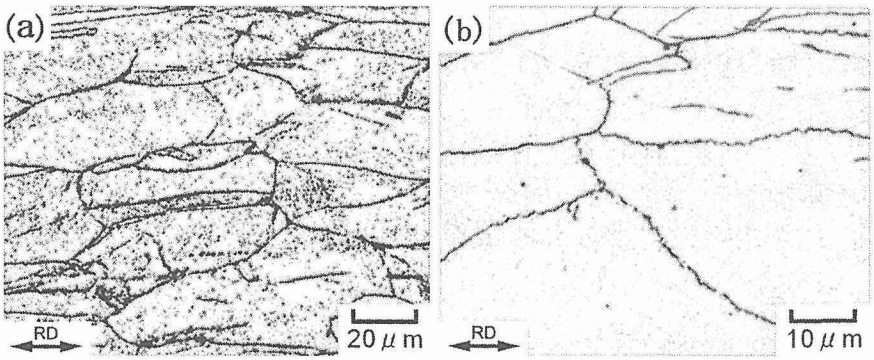

Fig. 1 Light micrographs showing prior-austenite grain boundaries in the ausformed SCM440 steel.

In order to obtain relatively large carbide particles that are not dissolved but act as pinning sites during austenitization, warm bar rolling at 873K was performed as a spheroidizing treatment. Afterwards, quick quenching treatment at 1093K for 1s at a heating rate of 150K/s was carried out with an induction heating device. For conventional QT specimens, the normalized bar was austenitized at 1153K for 2.7ks and then oil-quenched. The same tempering process at 723K for 5.4ks was applied to both the specimens. Tensile strength was 1424MPa for the former and 1403MPa for the conventional QT specimen.

Very fine austenite grains were obtained by the present process in comparison with that of the conventional QT specimen (Fig.2). The average grain size of prior-austenite was 3μm in the present process and 17μm for the QT specimen. It was confirmed by SEM and TEM observations that carbide particles with 100nm in diameter at largest were uniformly distributed in the as-quenched condition and no coarse film-like carbide was seen after tempering in the present process.

Constant loading tests with hydrogen pre-charged samples with Kt=4.9 were performed at applied stress of 0.9 times tensile strength, and improvement of fracture resistance by grain refinement was observed. Kc was 0.24ppm for the fine grained specimen and 0.11ppm for the QT specimen. However, this improvement of Hc was smaller than that by applying modified ausforming. SEM fractography revealed that intergranular fracture areas are still observed in the fine-grained specimen, although their size is significantly reduced in comparison with the QT specimen. This indicates that the austenite grain size of 3μm is not small enough to suppress intergranular fracture completely.

References

[1] S.Terasaki, S.Sakashita, S.Takagi, Y.Kimura and K.Tsuzaki, *Proc. of the Workshop on New Generation Steel(NG Steel 2001)*, The Chinese Society for Metals, Beijing, 2001, pp.239-244.

[2] Y.Kimura, S.Takagi, S.Terasaki, T.Hara and K.Tsuzaki, *Proc. of the 4th Workshop on the Development of High Performance Structural Steels for 21st Century*, POSCO, 2002, pp.89-98.

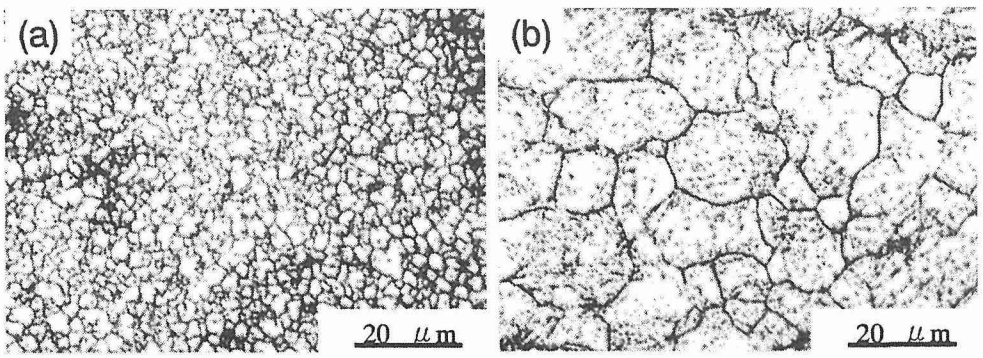

Fig.2 Austenite grain structures of the fine-grained specimen (Dγ=3μm) (a) and the conventional QT specimen (Dγ=17μm) (b). SCM440. Light micrographs.

Effect of Molybdenum on Mechanical Property and Delayed Fracture Resistance of High Strength Steel

W. J. Hui[1], H. Dong[1], Y.Q. Weng[2]
1 Central Iron and Steel Research Institute, Beijing, P.R.China;
2 The Chinese Society for Metals, Beijing, P.R.China

1. Introduction

There are few studies on the effect of Mo on delayed fracture resistance of high strength steels. Based on 40Cr steel, four steels with different Mo contents were prepared to study the effect of Mo on mechanical properties and delayed fracture resistance of high strength steel.

2. Experimental procedures

The compositions of the steels used were listed in Table 1. The experimental ingots were obtained in a 50kg vacuum induction furnace and hot forged to 15mm bars in diameter.

Table 1 Chemical composition of steels investigated (wt-%)

Steel	C	Mn	Si	P	S	Cr	Mo	V	Nb	Als
5M	0.40	0.44	0.24	0.002	0.003	1.11	0	0.28	0.038	0.004
6M	0.42	0.48	0.30	0.003	0.003	1.12	0.52	0.30	0.038	0.005
7M	0.42	0.46	0.27	0.002	0.003	1.12	1.15	0.30	0.042	0.006
8M	0.40	0.44	0.25	0.003	0.002	1.12	1.54	0.30	0.042	0.005

The tensile specimen (25mm gauge length and 5mm diameter), V-notch Charpy impact specimens (10×10×55mm), notched tensile specimen (5mm diameter having a groove R0.15, 60° with a depth of 1mm) were machined longitudinally from bars. These specimens were all normalized in a salt bath for 30 minutes at 1123～1193K,air cooled, then austenitized at 1133～1203K for 30 minutes, oil quenched. Then most specimens were tempered at temperatures from 673K to 923K at 50K intervals for 2 hours and cooled in air.

The ratio of σ_C to σ_N (delayed fracture strength ratio) is defined here to evaluate the delayed fracture resistance of the steels used. σ_N is notch maximum tensile stress in air compared with σ_C in solution. Walpole solution with a pH value of 3.5 was used.

3. Results and Discussion

The variations of mechanical properties of the steels with temperatures were showed in Fig.1(a) and Fig.1(b). With the rise of tempering temperatures, the strength of the steels used decreases and the toughness increases. There is a significant secondary hardening of steels 5M,6M,7M and 8M when the tempering temperature is higher than about 773K and this hardening reaches a peak at about 873K. The addition of strong carbide former V and Mo not only retards softening but also forms fine alloy carbides which produce a hardness and strength increase at higher tempering temperatures. As steel 5M does not contain Mo, therefore it is proposed this secondary hardening be mainly caused by the precipitation of V_4C_3.

Tensile strength increases and impact energy decreases with increasing Mo content. The increase of strength with Mo content is greater at lower Mo contents than at higher ones. Fig.1(b) also shows that the addition of Mo helps to reduce or even eliminate the impact energy valley at tempering temperature between 550℃ to 630℃ at which secondary hardening occurs.

Fig.2 (a) summarized the relationship between delayed fracture strength ratio σ_C / σ_N with tensile strength. σ_C / σ_N decreases with increasing tensile strength. Fig.2 (b) shows the

effect of Mo content on σ_C / σ_N at two strength levels 1400MPa and 1500MPa. It could see that σ_C / σ_N increases with increasing Mo content up to about 1.1 wt-%. Further increases in Mo content cause a tendency of decrease of σ_C / σ_N. By the time the Mo content increases to 1.5 wt-%, σ_C / σ_N is still higher than that of 0 wt-% Mo and 0.5 wt-%Mo.

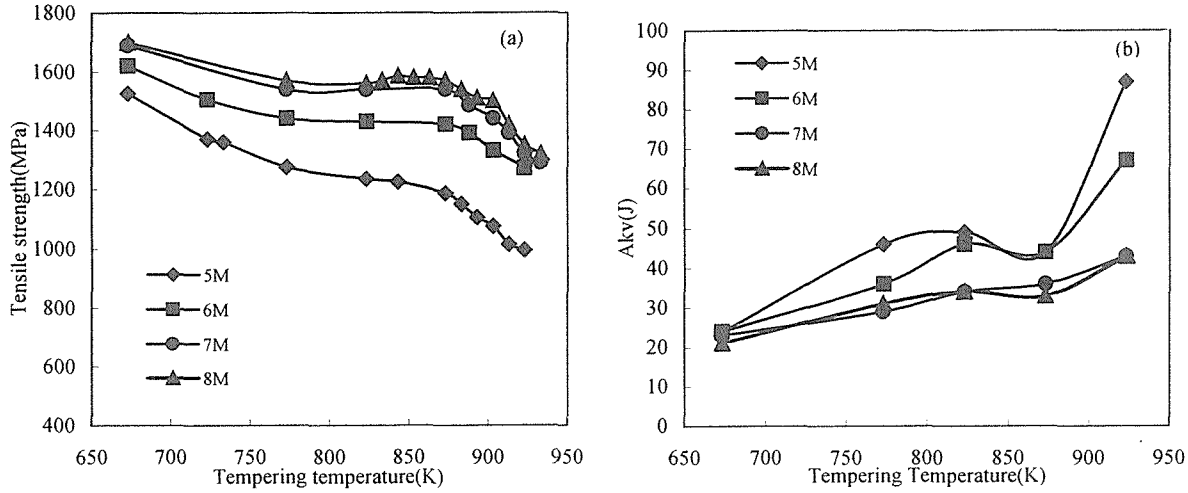

Fig.1 Variation of tensile strength (a) and impact energy (b) with tempering temperature

This beneficial effect of Mo on delayed fracture resistance was suggested to be the results of the following factors: (1) Mo raising the tempering temperature for a given strength, thus (a) reducing the dislocation density, (b) affecting the distribution of carbide particles, especially carbide coverage on prior austenite grain boundaries as described by Li and Lei[1] and (c) the precipitation of very finely dispersed MC particles. (2)solid solution strengthening of Mo which may provide improved strength for a given level of resistance to delayed fracture.

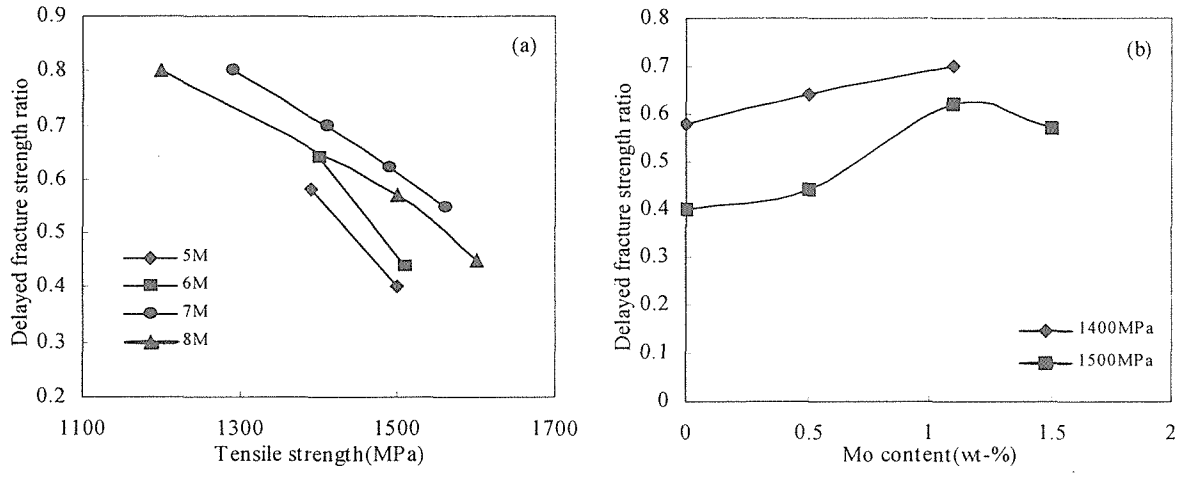

Fig.2 Effect of tensile strength (a) and Mo content (b) on delayed fracture strength ratio

4. Conclusion

(1) Strength increases and toughness decreases with increasing Mo content. This tendency slows down when the Mo content is over about 1.1 wt-%.

(2) Delayed fracture resistance at tensile strength of 1400MPa and 1500MPa increases with increasing Mo content until it reaches a maximum at about 1.1 wt-% Mo.

References

[1] Li,G.F, Wu,R.G and Lei,T.C, Carbide-matrix interface mechanism of stress corrosion cracking behavior of high-strength CrMo steels. Metall. Trans. 23A(1992), No.10, pp.2879-2885.

The Properties of a Low Carbon Steel with Carbide-free Bainite/Martensite Duplex Microstructure

D.-Y. Liu, B.-Z. Bai, H.-S. Fang, Z.-G. Yang
Department of Materials Science and Engineering, Tsinghua University, Beijing 100084, P.R. China

1. Introduction

Martensite microstructure is popularly employed in steels with high strength and good toughness after tempering except for the well-known embrittlement (TME) in the vicinity of 350℃. Bainite may present together with martensite in various cases. The effect of bainite on the mechanical behavior of bainite/martensite duplex steel during tempering is little studied, which is important from both theoretical and practical viewpoints.

2. Experimental Method

The vacuum induction melted experimental low carbon steel contains 1.8%wtSi and 0.5%wtCr, 2.2%wtMn, which is designed to obtain carbide free bainite (CFB) during air cooling with an increased tempering resistance. Standard short tensile specimens and Charpy U-notch impact specimens was used for mechanical testing. The specimens were austenitized at 890℃ for 15 min, followed by quenching into water or air cooling to room temperature and subsequent tempering for 2 hours. The amount of CFB of the air-cooled specimen was determined by dilatometry using Formaster-F phase transformation measure equipment. The residual austenite amount was measured on a LDJ9600 vibration sample magnetometer.

3. Results and Discussion

Strength and toughness properties of the steel with full martensite (M) and CFB/M mixed microstructures are shown in Figs.1 and 2 as a function of the tempering temperature. The ultimate tensile strength decreases as the tempering temperature increases. The yield strength reaches a maximum after tempering in the vicinity of 360℃. At temperature higher than that, the ultimate tensile strength and yield strength of the steel with full martensite drop off more rapidly than that with CFB/M mixed microstructures, which indicates that the CFB retards the softening during tempering, especially, when temperature is over 360℃. This renders the high yield/tensile strength ratio of the steel with CFB/M mixed microstructures at high tempering temperature, as shown in Fig.1b. In Figs. 2a, the reduction in area of the steel with mixed microstructures is lower than that of the steel with full martensite, but the total elongation is almost the same. This means that the steel with CFB/M mixed microstructure has a higher uniform elongation. In Fig.2b, it is seen that the impact energy of the steel with CFB/M mixed microstructure are larger than those of full martensite after tempering above 280℃ remarkably. The maximum plateau in the impact toughness of the steel with CFB/M occurs at a higher temperature. It is interesting to note that the combination of strength and toughness of the steel with CFB/M mixed microstructure is superior to that with full martensite after tempering within the range 360 to 400℃.

From dilatometry measurement, the air-cooled tensile and impact specimen possesses 18~25% (volume) CFB which is composed of bainitic ferrite and carbon enriched retained austenite. The total retained austenite amount in air-cooled tensile specimen is about 9%, while that in the water quenched specimen is less than 1%. No blocky retained austenite was observed by transmission electron microscopy in both air-cooled and water quenched specimens, which suggests that almost all retained austenite remains in CFB. It is believed that stable retained austenite improves the toughness of the steel. Tables 1 and 2 show the influence of tempering and mechanical deformation on austenite stability. After tempering above 340℃ the thermal stability of the retained austenite decreases rapidly, while the mechanical stability of the retained austenite decrease after tempering above 360℃. This may

explain the peak in the impact toughness curve around 360℃ tempering.

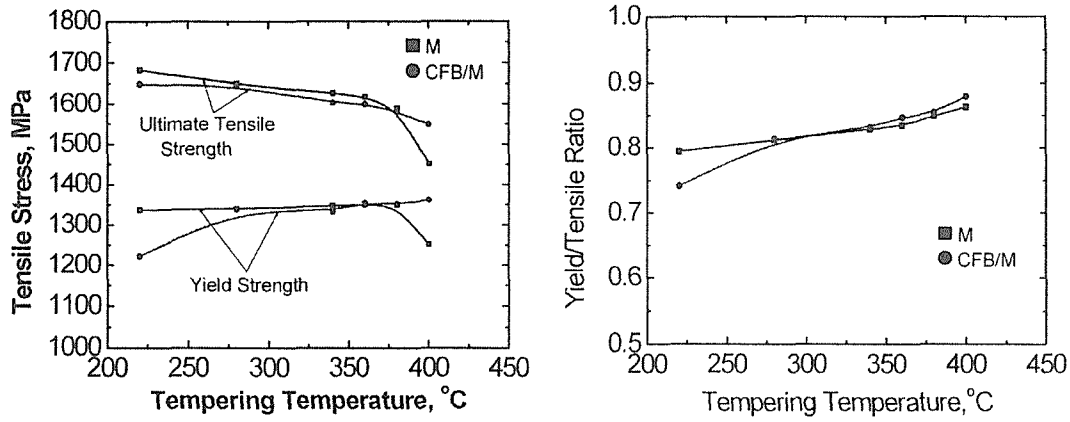

(a) (b)

Fig.1 (a) The variation of tensile stress and (b) yield/ultimate tensile strength ratio with tempering temperature of the experimental steel with M and CFB/M microstructure

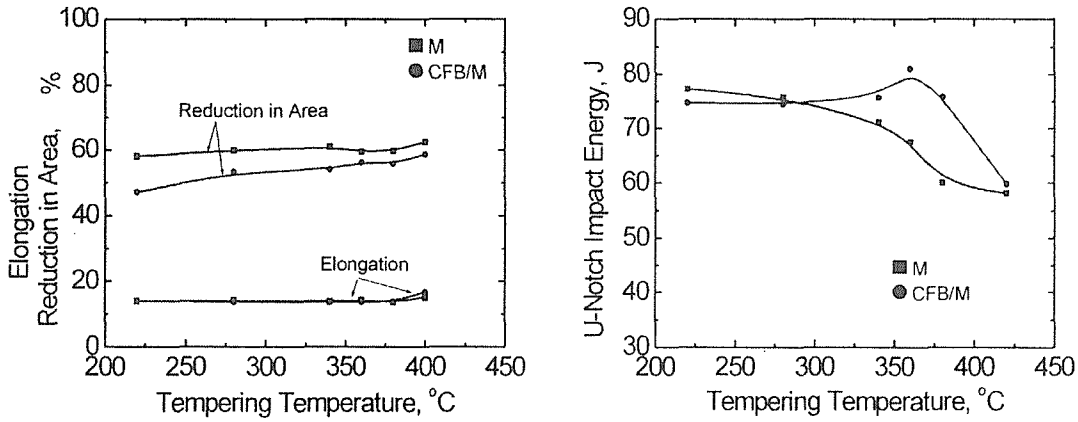

(a) (b)

Fig.2 The variation of (a) elongation and (b) the impact energy with tempering temperature of the experimental steel with M and CFB/M microstructure

Table 1 The amount of total retained austenite in carbide free bainite/martensite mixed microstructure (%vol) varies with the tempering temperature

	As-quenched	220℃	280℃	340℃	360℃	380℃	420℃
Tensile Specimens	8.7	8.2	7.2	7.3	5.9	5.8	
Impact Specimens		7.2	7.3	7.3	6.0	5.9	4.4

Table 2 The effect of 3% plastic deformation and tempering temperature on the amount of total retained austenite (%vol) in carbide free bainite/martensite mixed microstructure

	As-quenched	220℃	280℃	340℃	360℃	380℃
Before Deformation	8.7	8.2	7.2	7.3	5.9	5.8
After Deformation	–	5.2	6.9	7.2	5.9	3.8

4. Conclusion

The experimental steel with CFB/M microstructure achieves better combination of toughness and strength than that with fully martensite after tempering within 360 to 400℃. The presence of CFB retards the TME temperature of the steel. The beneficial properties of CFB/M microstructure is due to the existence of residual austenite, which is stable up to tempering at 340℃.

Delayed Fracture Properties of 1500MPa Bainite/martensite Dual-Phase High Strength Steel and its Hydrogen Traps

J. L. Gu, K.D. Chang, H.S. Fang, B.Z. Bai

Department of Materials Science and Engineering, Laboratory of Advanced Materials, Materials Research Center, Tsinghua University, Beijing, 100084, China

1.Introduction

The delayed fracture properties of high strength steels with tensile strength exceeding 1200MPa are usually lower, which is unfavourable for their wide applications, and the delayed fracture properties of high strength steels are related to their susceptibility to hydrogen embrittlement. Therefore, controlling the hydrogen traps in high strength steels could improve the delayed fracture properties of high strength steels. In the paper, the delayed fracture properties of 1500MPa bainite-martensite dual-phase high strength steels and its hydrogen traps have been investigated.

2. Experimental Procedure

The materials investigated were U20Si, XBU25A, U25A, U20DSi, 30CrMnSiA. Except 30CrMnSiA high strength steel was supplied by fu Sun steel corporation, the other steels were of vacuum-induction melting bainitic steel,their compositions were given in Table 1. The details of the heat treatment were shown in Table 2.

The experiments of stress corrosion cracking(SCC) were carried out in 3.5% NaCl solution at 298K, using modified wedge-opening-loading(WOL) specimens with thickness B=15mm to determine the critical stress intensity factor K_{ISCC} and da/dt.The microstructure of materials and the fractographies of SCC specimens were observed by SEM.

Hydrogen permeation tests were conducted in home-made electrochemical permeation apparatus with double cell. All tests were done at 298K. Based on the data recorded by the computer, the permeation curve of current(J)—time(t) can be drawn. The apparent diffusion coefficient(D_A) was evaluated from the relationship:

$$D_A=l^2/6t_l \qquad (1)$$

Where l: specimen thickness, t_l: time lag, which was the time taken for the permeation to reach 0.63 of its steady-state value. The mean trap parameter(α),the difference of trap parameter($\Delta\alpha$) and the trap binding energy (E_B) were caculated according to McNabb and Foster[1] model.

3. Results and Discussion

U20Si, XBU25A, U25A and U20DSi are bainite-martensite dual-phase high strength steels. Their microstructures are shown in Figure 1. From Figure 1 it can be seen that the microstructure of bainite-martensite dual-phase high strength steels for thermomechanical heat-treatment is markedly fined. Table 3 indicates that K_{ISCC} increases, da/dt and D_A decreases as the microstructure is fined and retained austenite increases. Since da/dt is related to segregation of hydrogen, the lowered D_A reduces segregation of hydrogen and leads to lowered da/dt. The fractographic analysis suggests that the fracture mode of SCC for bainite-martensite dual-phase high strength steels is quasicleavage; By contrast, the fracture mode of SCC for 30CrMnSiA is intergranular.The trap binding energy (E_B) of retained austenite and bainite-martensite plate boundaries was calculated, which is 40.44kJ/mol and 28.13kJ/mol, respectively. The results showed that K_{ISCC} of bainite-martensite dual-phase high strength steels which is superior to that of 30CrMnSiA is due to distributed homogeneously hydrogen traps.

4.Conclusions:

The delayed fracture properties of bainite-martensite dual-phase high strength steels is superior to quenched tempering high strength steels, which is related to retained austenite and fined bainite-martensite plate boundaries acting as hydrogen traps.

References:

1) A. McNabb. and P. K. Foster: Trans. AIME, **227** (1963), 618.

Table 1 Chemical compositions of the specimen

Specimen	Elements(wt.%)										
	C	Si	Mn	Cr	Mo	Ni	W	V	Ti	S	P
U20Si	0.27	1.8	1.8	0.3	-	-	-	-		0.009	0.007
XBU25A	0.27	1.3	1.8	0.3	-	-	-	-		0.009	0.007
U25A	0.27	1.3	1.8	0.3	-	-	-	-		0.009	0.007
U20DSi	0.27	0.3	1.8	0.3	-	-	-	-		0.009	0.007
30CrMnSiA	0.33	0.97	0.88	0.90	0.02	0.08	0.02	0.01	0.01	0.003	0.012

Table 2 Processing parameters

Specimen	Austenitizing Temperature (K)	Holding Time (min)	Cooling Mode	Tempering Temperature (K)	Volume of Retained Austenite(wt%)
U20Si	1173	18	Air cooling	553	9
XBU25A	1173	18	Air cooling	553	6
U25A	1173	18	Air cooling	553	6
U20DSi	1173	18	Air cooling	553	3
30CrMnSiA	1153	18	Oil quenching	713	

Table 3 Mechanical properties and diffusion coefficients(D_A) of steels

Steel	K_{ISCC} ($MPam^{1/2}$)	da/dt($x10^{-5}$) mm/s	D_A ($\times 10^{-6} cm^2 s^{-1}$)
U20Si	51.5	1.2	0.348
XBU25A	53.8	1	0.335
U25A	44.6	1.8	0.423
U20DSi	40.5	2.7	0.613
30CrMnSiA	36.2	3.2	0.710

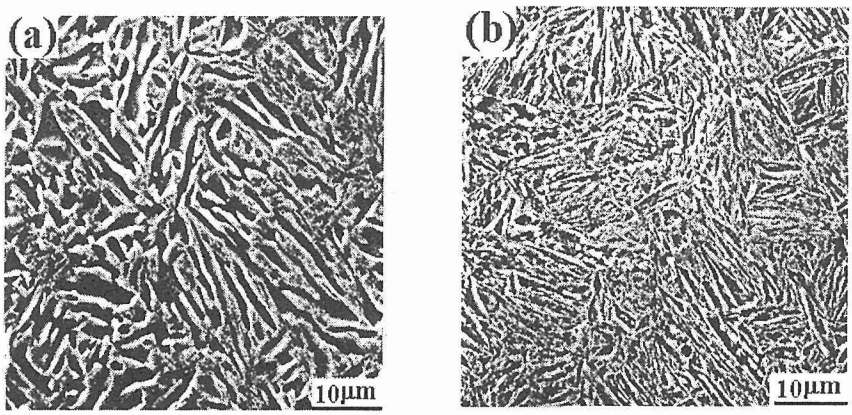

Fig.1 SEM micrographs for two materials: (a) U25A; (b) XBU25A.

High Strength Stainless Steel: 3000 MPa and More

Markus O. Speidel, Ming Ling Cui-Zheng,
Paolo Cobelli and Hannes Speidel

Institute of Metallurgy
Swiss Federal Institute of Technology, ETH
CH 8092 Zurich, Switzerland

The mechanical properties of high nitrogen austenitic stainless steels are presented.

The effects of
- grain boundary hardening
- solid solution hardening
- dislocation hardening (cold work)
- dislocation hardening (hot work)
- precipitation hardening (strain ageing)

on yield strength, ultimate tensile strength and elongation to fracture are reviewed in a systematic way, using steels which crystallize in the face centered cubic crystal lattice and contain up to 1.2 weight-percent nitrogen, together with appropriate amounts of chromium, manganese, nickel and other alloying elements, the basis being iron.
The above mentioned hardening mechanisms are analyzed singly and combined. With certain hardening mechanisms combined, strength levels higher than 3000 MPa can be achieved.

The ductility, as measured by the elongation to fracture, and the impact toughness of these austenitic stainless steels depends on the hardening mechanisms, the hardness level and the basic alloy composition. In austenitic steels with nitrogen contents of about one weight percent in solid solution there is a ductile-to-brittle transition temperature which can approach service temperatures. Major influences on the ductile-to-brittle transition temperature are identified, particularly the nitrogen concentration in the alloys.

Nitrogen in solid solution has a profound influence on the temperature of dynamic recrystallization and hence on thermomechanical processing and the resulting mechanical properties.

Recrystallization is also influenced by the presence of small volume fractions of very stable nitride formers, such as titanium, niobium and vanadium. Therefore, it is possible to heat treat steels of appropriate composition to predictable mechanical properties through joint control of the composition and the grain size.

The production of such high nitrogen austenitic stainless steels using conventional equipment has now become possible as a result of recent alloy development. It is shown that these steels can achieve strength to density ratios (at equal ductility) which are not only excellent compared to other classes of steel, but which surpass the light metals based on titanium, aluminium and magnesium alloys.

High strength, high nitrogen austenitic stainless steels surpass all other steels and indeed, all other materials in their combination of strength and fracture toughness, as expressed by the product of yield strength and fracture toughness.

Thus, the new high strength high nitrogen austenitic stainless steels are seen as the favourite structural material in the transportation industry, ocean engineering and building industry of the 21^{st} century.

Local Approach to Transferability Analysis of Brittle Fracture

Fumiyoshi Minami
Department of Manufacturing Science, Graduate School of Engineering, Osaka University
2-1, Yamada-Oka, Suita, Osaka 565-0871, JAPAN

Introduction

A marked progress in the recent fracture mechanics methodology is found in the quantification of the constraint effect on the brittle fracture. In a large scale yielding condition, the resistance to brittle fracture evaluated with conventional fracture mechanics parameters (K, CTOD and J) depends to a large extent on the crack size and geometry of specimens: Deep notch bend and compact specimens give apparently smaller cleavage resistance than the shallow notch bend specimen and notched tension plates. Namely, the standard fracture toughness specimen presents a very conservative evaluation of the cleavage resistance. This is due to a constraint loss effect, which depresses the near crack-tip stress fields of the shallow notch bend and tension specimens in a large scale yielding state. In order to overcome such problem, Beremin, French fracture mechanics group, proposed a new fracture driving force called the Weibull stress. The Weibull stress is derived from a statistical characterization of a local instability of microcracks which are responsible for cleavage fracture. The Weibull stress is enlarged with increasing the intensity and extent of the near crack-tip stress fields. The derivation of the Weibull stress does not need the assumption of the crack size and geometry of specimens, so that the critical Weibull stress at fracture is expected to be independent of these factors.

The main advantage of the Weibull stress criterion is the transferability analysis of fracture mechanics test results obtained with different geometries and loading conditions. In this paper, the key idea of the transferability analysis is mentioned and some encouraging results are presented. The goal of the study is to establish a standard procedure for the fracture assessment considering the constraint loss effect, which links the structural design and materials evaluation with a reasonable specification.

Procedure for Fracture Transferability Analysis

The fracture transferability analysis riles on the Weibull stress criterion: The critical Weibull stress at cleavage fracture initiation is independent of the specimen geometry and loading conditions. The Weibull stress σ_W is defined by the integration of a near-tip effective stress σ_{eff} over the fracture process zone V_f in the form:

$$\sigma_W = \left[\frac{1}{V_0} \int_{V_f} [\sigma_{eff}]^m \, dV_f \right]^{1/m} \tag{1}$$

where V_0 and m are a reference volume and a material parameter, respectively. The m-value reflects the distribution of microcracks for the material, and generally is in the range 10 to 40. The critical Weibull stress $\sigma_{W,cr}$ at brittle fracture initiation obeys the Weibull distribution with two parameters m and σ_u

$$F(\sigma_{W,cr}) = 1 - exp\left[-\left(\frac{\sigma_{W,cr}}{\sigma_u} \right)^m \right] \tag{2}$$

which is considered as a material property independent of the size and geometry of specimens.

Figure 1 shows the procedure for the fracture transferability analysis. It consists of the following steps:

(1) The determination of the Weibull parameters m and σ_u of the material. Usually the standard fracture toughness specimen with a deep notch is employed. In principle, any specimen geometry can be used as far as it brings about brittle fracture. The iteration procedure is used conventionally to determine m and σ_u, which connects the statistical fracture test results with the corresponding near-tip stress fields addressed by the 3D FE-analysis.

(2) The calculation of the Weibull stress for the target specimen. Using the m-value determined, the evolution of the Weibull stress for the target specimen is calculated If the target specimen is subjected to dynamic loading or prestrain, the stress-strain curve for the Weibull stress analysis should reflect such effect.

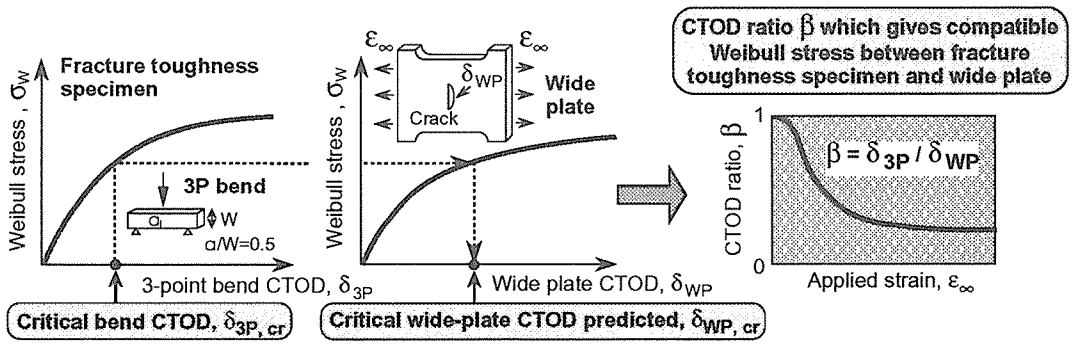

Fig. 1 Procedure for fracture transferability analysis based on the Weibull stress criterion and definition of CTOD ratio β.

(3) The evaluation of the fracture performance of the target specimen. Finding the load level at which the target specimen produces the compatible Weibull stress with the fracture toughness specimen, the fracture performance of the target specimen is predicted. The prediction is conducted in the range of the fracture toughness results.

A fine FE-mesh generation is required to obtain a reliable value of the Weibull stress. The selection of the reference volume V_0 does not affect the fracture transferability analysis, because the use of a different volume V_0^* scales the Weibull stress of each specimen by the same magnitude of $[V_0/V_0^*]^{1/m}$. Hence, a unit volume for V_0 is convenient for calculating the Weibull stress. It was demonstrated by the previous studies that the critical Weibull stress is independent of the specimen thickness and geometry, crack size, loading rate, prestraining and the strength mismatch as far as brittle fracture is dominant in the material.

Application of Weibull Stress Criterion to Fracture Prediction

Examples of the fracture transferability analysis based on the Weibull stress criterion are presented. Figure 2 shows the prediction of the fracture performance of a large hollow-section beam. The material used was a high strength structural steel of 490 MPa strength class. The fracture toughness was designed to be in a low level to cause brittle fracture at the service temperature of steel-framed structures. The follow-section beam included shallow V-notches of 1 mm depth at the edge of the beam flange, and tested in a three-point bend manner at 0°C. The critical CTOD value at 0°C of the standard fracture toughness specimen was about 0.15 mm. Conventional fracture mechanics approaches are not applicable, because they have developed for the cracked body. The fracture load of the hollow-section beam predicted by the Weibull stress criterion agrees well with the experimental results.

Figure 3 shows the combined effect of dynamic loading and prestrain on the critical CTOD of the fracture toughness specimen. A low toughness structural steel of 490 MPa strength class was tested at the room temperature. The loading rate and prestrain level were selected in the light of the post-investigation of the Kobe Great Earthquake happened on January 17, 1995. The dynamic loading and prestrain decreased the fracture toughness to a large extent. This is attributed to the elevation of the flow stress of the material. The Weibull stress criterion predicts well the toughness deterioration in the dynamic and prestrained conditions.

The strength mismatch effect on the fracture resistance of welded joints in the ductile-to-brittle transition range, and the residual stress effect caused by a warm preloading were also successfully predicted in the recent papers.

Fracture Toughness Scaling for Fracture Control Design

In order to apply the Weibull stress criterion to the fracture control design of structural components, the constraint correction of CTOD is made as a function of the deformation level of the components. The CTOD ratio β is defined as

$$\beta = \delta_{3P} / \delta_{WP} \tag{3}$$

where δ_{WP} is the CTOD of a wide plate subjected to tension, and δ_{3P} is an equivalent CTOD at which the standard fracture toughness specimen gives a compatible Weibull stress with the wide plate (see Fig 1). The CTOD ratio β is controlled mainly by the work hardening property of the material and the crack depth in the wide plate. The CTOD ratio β was implemented in the fracture assessment guideline, Method of Assessment of Brittle Fracture in Steel Weldments Subjected to Cyclic and Dynamic Large Straining (WES-TR 2808 : 2000) published by the Japan Welding Engineering Society. In WES-TR 2808, a practical application of β is given for the fracture performance assessment of large-scale column-to-beam connections.

Currently, the following researches are executing to establish the fracture control design with the Weibull stress:

(a) Quantification of the CTOD ratio β for the mismatched welds, such as the EB and Laser welded joints.
(b) Physical correlation between the Charpy impact properties and the material fracture toughness.
(c) Fracture assessment of structural components with geometrical discontinuity.
(d) Application of the Weibull stress criterion to the evaluation of interface fracture and hydrogen induced cracking.

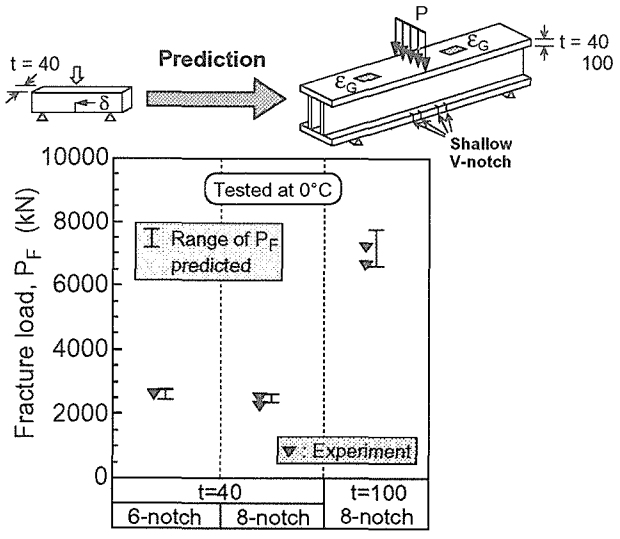

Fig. 2 Prediction of specimen geometry effect.

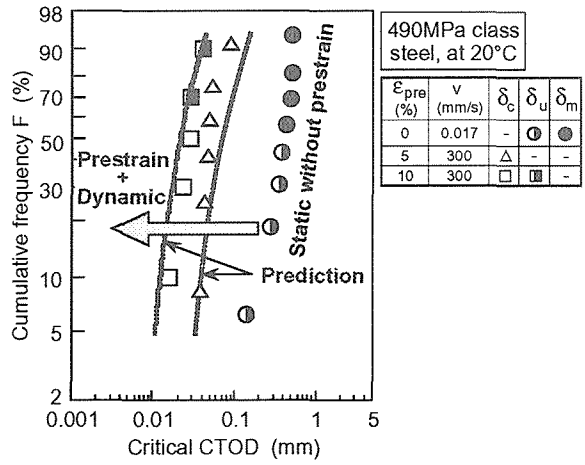

Fig. 3 Prediction of dynamic loading and prestraining effects.

Evaluation of Hydrogen Embrittlement Fracture of High Strength Steel with Local Approach

S. Takagi [1] *, T. Inoue [1], S. Terasaki [1], K. Tsuzaki [1] and F.Minami [2]
[1] Materials Creation Research Group, NIMS, Japan
* present address: Kawasaki Steel Corp. , Japan
[2] Depertment of Manufacturing Science, Osaka Univ., Japan

1. Introduction

Delayed fracture is one of the main factors which prohibits the utilization of ultra high strength steels with tensile strength over 1000MPa for construction components and automobile parts. However, no adequate method is available to evaluate the susceptibility of ultra high strength steels to delayed fracture.

Delayed fracture is generated by hydrogen in steels and affected by the degree of stress concentration. Hydrogen intrudes into steels when steels are corroded. Thus, in the delayed fracture evaluation, it is important to consider two factors; hydrogen intrusion from the environment into a steel part and hydrogen embrittlement (HE) susceptibility of the steel used. This paper focuses on the quantification of the latter factor.

In the HE test of notched specimens, hydrogen atoms accumulate in a region of the maximum hydrostatic stress by stress assisted diffusion, and the hydrogen induced cracking occurs from the weakest point in that region. Yamasaki and Takahashi [1] reported that the HE in high strength martensitic steels where the cracking mode is of intergranular fracture type is controlled by the first crack generation, i.e., the propagation of the first crack results in the final failure. This suggests that in high strength steels the HE behavior is determined by a local stress and hydrogen concentration around the maximum hydrostatic stress point near the notch root. In the present study, the stress and hydrogen parameters that control the HE are developed.

2. Experiment

A quenched and tempered JIS SCM440 steel (0.40C-0.24Si-0.81Mn-1.03Cr-0.16Mo (mass%)) and a tensile strength of 1403MPa was used. Round bars were austenitized at 1153K for 45 min and quenched in oil. Then they were tempered at 723K for 90 min, subsequently quenched in water. The diameter of the HE tests specimens was 10mm. The stress concentration factor Kt was changed from 2.1 to 6.9 by altering the curvature of the circumferential notch. The applied stress was in the range 0.33 to 0.72 times the tensile strength σ_{nB} (= 2148MPa) of the notched specimen. The average hydrogen content in the specimens was measured by a thermal desorption analysis using Q-mass at a heating rate of 100K/h. The total hydrogen content desorbed up to 573K was defined as a diffusible hydrogen content. These samples, HE tests method and conditions were the same reported in ref. [2] - [4].

Stress distributions in the specimens were analyzed using FE-code, ABAQUS / Standard ver.5.8. The minimum element size was about 1μm.

The Weibull stress defined by Eq.(1) was calculated as a driving force of HE fracture [3], [5].

$$\sigma_W = \left[\frac{1}{V_0} \int_{V_f} (\sigma_{eff})^m \, dV_f \right]^{\frac{1}{m}} \quad (1)$$

V_0 : reference volume of fracture unit (1mm^3 in this paper)
V_f: fracture process zone taken as a region where maximum principal stress exceeded 0.8 times its peak value
m : Weibull shape parameter (changed from 10 to 30 in this paper)
σ_{eff} : effective stress for fracture in fracture process zone (maximum principal stress in this paper)

The hydrogen content accumulated at a point Hc* was calculated by equ.(2) [3], [4] and diffusible hydrogen content in the fracture process zone Hc*(ave.) was calculated by summention of Hc*(element).

$$Hc^*(element) = Hc \times \exp\left\{\frac{-\Delta\sigma_h(element)\Delta V}{RT}\right\} \quad (2)$$

$\Delta\sigma_h$ (element): difference between hydrostatic stress in each element used FE-analysis and region apart from the notch section

V : partial molar volume of hydrogen in bcc-Fe ($2\times10^{-6}m^3/mol$)

Hc : maximum value among diffusible hydrogen contents of unfailured specimens under same shape of specimen and applied stress

R : gas constant, T : test temperature (=300K)

3. Results and Discussion. .

Nozue [6] considered that the peak values of the maximum principal stress (σ_p(peak)) and the peak value of diffusible hydrogen contents (Hc*) locally accumulated near the notch root for the specimens with Hc control the HE fracture. Fig.1 shows the result of the HE susceptibility evaluation with our experiment by σ_p(peak) and Hc* [2]. The relationship between these parameters depends on Kt. That is because the stress distributions of the same σ_p(peak) condition (for example, A and B in Fig.1) depend on Kt[2], [3].

The HE fracture is triggered by the first cracking at the prior-austenite grain boundary, the weakest link model may be applied to the HE phenomena. Thus the stress distribution must be considered in the HE susceptibility evaluation. From these two point of view, we tried to evaluate the HE susceptibility with the Weibull stress σ_w. The diffusible hydrogen content in the fracture process zone (Hc*(ave.)) was adopted as the hydrogen parameter. The results of the HE susceptibility evaluation by σ_w and Hc*(ave.) are shown in Fig.2. The Weibull shape parameter of m=15 was used for the present steel. The E fractures in various conditions of Kt and applied stress are uniquely controlled by σ_w and Hc*(ave.).

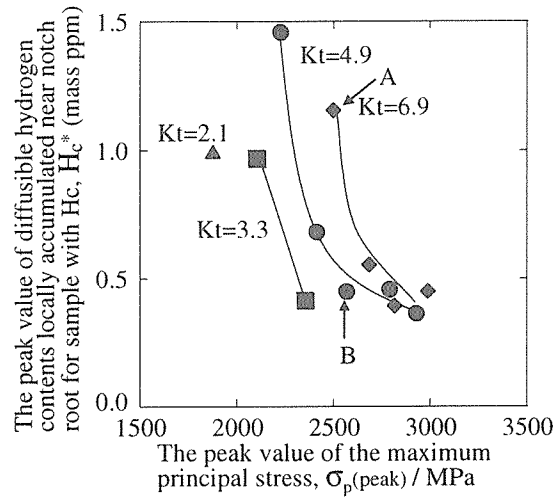

Fig.1 Relationship between $\sigma_{p(peak)}$ and Hc^*

4. Summary

This paper aimed at clarifying the stress and hydrogen parameters that control the HE. A commercial 0.4%C-1%Cr-0.16%Mo steel (JIS SCM440 steel) with a tensile strength of 1403MPa was used.

It was demonstrated that the local approach analysis employed in this paper is effective for the evaluation of HE susceptibility of high strength steel. Further study is going on to establish the HE fracture evaluation procedure based on the Weibull stress approach.

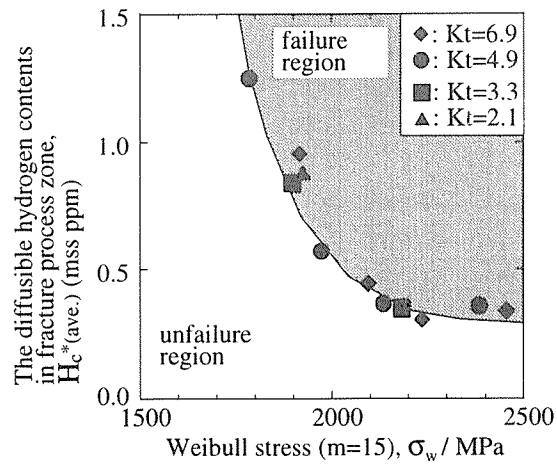

Fig.2 Relationship between σ_w and Hc^*(ave.)

References

1) S.Yamasaki and T.Takahashi : Tetsu-to-Hagane **83**(1997) pp.454-459.
2) S.Takagi, T.Inoue, K.Tsuzaki and F.Minami : Tetsu-to-Hagane **86**(2000) pp.689-696..
3) S.Takagi, T.Inoue, K.Tsuzaki and F.Minami : Proc. of the 7th. Int. Symp. JWS, 2001, KOBE, pp.1159-1164.
4) S.Takagi, T.Inoue, K.Tsuzaki and F.Minami : J. Japan. Inst. Metals **65**(2001) pp.1073-1081.
5) F.Minami, C.Ruggiieri, M.Ohata and M.Toyoda : J.Soc. Mat.Sci.Jpn. **45**(1996) p.544-551.
6) A.Nozue : Advances in Delayed Fracture Solution, (The Iron and Steel Institute of Japan, Tokyo, 1997) p.197-206.

Interactions Between Fatigue Damage and Hydrogen

M. Nagumo, H. Shimura, T. Chaya
Department of Materials Science and Engineering, Waseda University
H. Hayashi and I. Ochiai
R&D Section, Suzuki Metal Co.

Interaction between fatigue damage and hydrogen appears typically as the corrosion fatigue, early crack growth and reduction in fatigue life in corrosive environments. One mechanism so far proposed for corrosion fatigue is the enhanced uptake of hydrogen due to breakage of protective surface film. Another example of fatigue-hydrogen interaction is the so-called giga-cycle fatigue of high strength steels in which the fatigue limit decreases associated with the appearance of optically dark area around non-metallic inclusions [1]. Involvement of hydrogen in the fatigue failure is now fairly evident, but the mechanism is a matter to be examined.

The aspect we are to take is the interaction of hydrogen with defects created during fatigue, rather than hydrogen itself. It has been revealed that enhanced susceptibility to delayed fracture caused by alterations of environment, such as the applied stress [2] or external hydrogen potential [3], was not associated with the enhanced entry of hydrogen. A proposed model of hydrogen-related failure [4] assumes strain-induced formation and agglomeration of vacancies with the aid of hydrogen, facilitating easy formation and linking of microvoids. On the other hand, in research on fatigue, there have been substantial observations that suggest vacancy production in persistent slip band as documented in a review article [5]. Then, the fatigue-hydrogen interaction could be examined with respect to vacancies produced during fatigue and involvement of hydrogen in that process. In the present paper, increase in the susceptibility to delayed fracture associated with fatigue damage of high-strength martensitic steels is shown. Accumulation of fatigue damage, involving creation of point defects, has been revealed by means of hydrogen thermal desorption analysis (TDA), utilizing hydrogen introduced into specimen as a probe of defects [6,7].

A delayed fracture test in a 20% NH_4SCN aqueous solution at 50℃ was conducted with a 5-mm-diameter round bar of a JIS SUP12 steel, 0.57C-1.45Si-0.68Mn-0.69Cr (wt%), oil-quenched after being austenitized at 910℃ for 15 min and tempered at 460℃ for 9 min to a tensile strength of 1815 MPa. Prior to the delayed fracture test, the specimens were subjected to a rotational bending fatigue test under constant stress amplitude at a rotational speed of 500 rpm. Two levels of fatigue cycles were chosen, one close to and the other a half of the fatigue life.

The delayed fracture test results are shown in Fig.1 for the as-heat-treated specimens (N) and for specimens pre-fatigued for 4×10^4 cycles (A) or for 8×10^4 cycles (B), respectively. Some B specimens were subjected to annealing at 200℃ for 1 h after pre-fatigue, and their delayed fracture data are also included in Fig.1. Hydrogen was pre-charged for 24 h prior to the delayed fracture test. Figure 1 indicates that the time to fracture was reduced for the specimens subjected to pre-fatiguing, with the reduction becoming more pronounced as the number of fatigue cycles increased. Low-temperature annealing of the B specimens after fatigue recovered the time to fracture to nearly that of the N specimens. These results indicate that specimens subjected to fatigue have high susceptibility to delayed fracture and point defects created during fatigue play a role in the increased susceptibility.

Then, the accumulation of fatigue damage was examined with the same steel utilizing hydrogen as a probe of defects. A martensitic steel of the tensile strength of 1493MPa for pre-stressed concrete (PC) bar, which has an inferior fatigue property to that of the Si-Cr steel,

was also used for comparison. Specimens subjected to various fatigue cycles and subsequently annealed at 200℃ for 1h were prepared. In order to detect defects, hydrogen was introduced to fatigued specimens and was subjected to TDA. Hydrogen charging was conducted by cathodic electrolysis using 3%NaCl + 3g/lNH_4SCN aqueous solution at a current density of 0.75 mA/cm^2 for a period to attain the saturated hydrogen concentration.

In Fig.2, the hydrogen contents, i.e. the integrated desorption peak intensity up to 400℃ of absorbed hydrogen, in fatigued or subsequently annealed specimens are shown as a function of fatigue cycles. The total hydrogen conctent decreased initially, but turned to increase with the progress of fatigue. The decrease in hydrogen content by annealing implies that a part of hydrogen traps in the fatigued specimens is point defects, presumably vacancies. The amount of the decrease, which corresponds to vacancy density, is separately plotted in Fig.2. It is noted that the decrement increased continuously after the turning point of the total hydrogen conctent, which showed again a substantial decrease at just before the failure. The increase in vacancy density in the course of fatigue is consistent with the delayed fracture results shown in Fig.1.

According to our model on hydrogen-related failure [4], vacancy creation is the primary factor that controls the susceptibility. Various mechanisms can be considered for strain-induced formation of vacancies, but it may take place preferentially associated with interactions of dislocations in the area of high dislocation density. Most probable sites are in slip bands as revealed on fracture surfaces characterized by striations and quasi-cleavage in which crack extends along lath boundaries coincident with the orientation of dislocation cell walls. Persistent slip band developed in fatigue may act in a similar way and lead to the formation of microvoids and their linking. The effect of hydrogen on fatigue properties will be also discussed from the viewpoint of vacancy density increased by coupling with hydrogen.

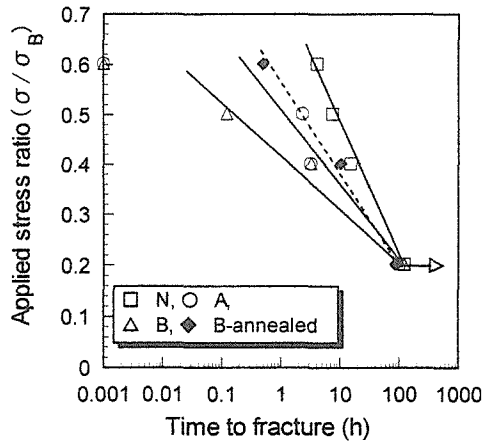

Fig.1 Delayed fracture test results of pre-charged Si-Cr steel specimens.

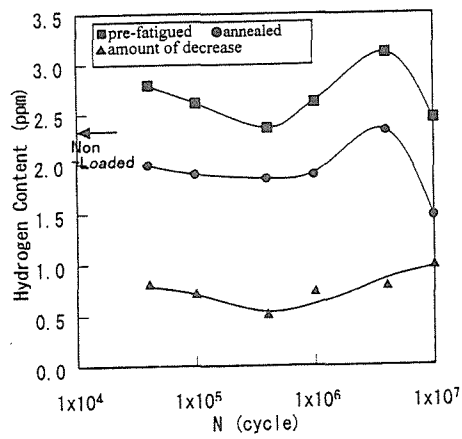

Fig.2 Hydrogen content in pre-fatigued or subsequently annealed PC bar specimens. The lowest curve is the difference of the upper two curves.

References:

[1] Y. Murakami, H Konishi, K. Takai and Y. Murakami: Tetsu-to-Hagane, 86(2000), 777-783.
[2] K. Izutsu, K. Takai and M. Nagumo: Tétsu-to-Hagané, 83 (1997), 371-376.
[3] M. Nagumo, H. Uyama and M. Yoshizawa: Scripta Mater., 44(2001), 947-952.
[4] M. Nagumo, M. Nakamura and K. Takai: Metallur. Mater. Trans. A, 32A (2001), 339-347.
[5] C. Laird: in *Physical Metallurgy* 4th Ed., ed. R. W. Cahn and P. H. Haasen, p. 2293, Elsevier Science, Amsterdam, (1996).
[6] M. Nagumo, K. Ohta and H. Saitoh: Scripta Mater., 40 (1999), 313-319.
[7] M. Nagumo, T. Yagi and H. Saitoh: Acta Mater., 48 (2000), 943-951.

Atomistic behavior of hydrogen in iron from *ab-initio* calculations

Y. Tateyama and T. Ohno
Computational Materials Science Center, NIMS, Japan

1. Introduction

Hydrogen embrittlement (HE) in Fe-based structural materials (*e.g.* steels) has been a long-standing problem. A major cause is that atomistic behavior of H even in pure Fe has not been fully understood yet because the observation of H is very difficult due to the low H solubility (~10^{-5} at. %) [1]. To overcome this situation, atomistic simulation with high accuracy can be a most powerful tool. In this paper, we investigate interstitial (diffusible) H states and H effects on defects in pure Fe on atomic scale by means of accurate *ab-initio* calculations. Based on these results, we discuss the microscopic processes of HE phenomena in Fe-based materials.

2. Calculation

We use *ab-initio* method with plane wave basis and pseudopotential, which is known as most accurate in relaxed structures as well as electronic states. Spin polarization essential for the Fe stability is incorporated in the electronic states calculations. Zero-point motion energy of H is calculated by Schrodinger equation with H adiabatic potential that is evaluated by *ab-initio* calculations. Heat of solution for H as well as various defect energies in bcc Fe are formulated by the supercell scheme, and obtained from the results of calculations with a 54-atoms supercell. The calculated fundamental properties of bcc Fe are in excellent agreement with experiments, which are shown in Fig. a.

3. Results

Our calculations including zero-point motion of H clarify that a localized state at a T site, not delocalized one, is the most stable for interstitial H in bcc Fe. The resulting heat of solution for interstitial H is 0.32eV, which is in good agreement with experiments (0.30 eV) [1]. Concerning the stability of monovacancy-hydrogen complexes (VH_n), the calculated H trapping energies for VH_n (n=1-3) well explain the experimental results quantitatively (Fig. b). The results clearly show that VH_2, not VH_6 as previously believed [2], is the most stable (Fig. c). This VH_2 leads to 0.5 eV decrease of the monovacancy formation energy, which corresponds to 10^7 times increase of the monovacancy concentration at 300 K. It is also found that clusterization of VH_2 is energetically favorable. This is contrary to the previous scenario related to VH_6, where the clusterization is unfavorable due to the decrease of H trap sites in the vacancy. This VH_2 clusterization leads to formation of tabular vacancy clusters along {100} or {110} plane so as not to lose the stable H sites in the cluster (Fig. d). Such anisotropic clusters can be probable candidates for crack nucleation (void formation), since both are major fracture planes in bcc Fe.

4. Discussion

The results of H-enhanced vacancy formation and anisotropic clusterization in bcc Fe are likely to give more feasible explanations for the microscopic processes in the HE-related phenomena. These could explain H-enhanced lattice decohesion [3] without postulating improbable accumulation of interstitial H. Also, they would be directly connected to material thinning in the HELP theory [4], which has been ambiguous so far. The increase of vacancy can contribute to the experimentally observed enhancement of dislocation mobility as the elastic shielding mechanism, by facilitating dislocation intersection and jog motions. Thus our results suggest that vacancy processes, which have never been extensively discussed as yet, are expected to be more relevant than interstitial H to the microscopic processes of HE in Fe-based materials. As demonstrated here, determination of atomistic behavior of H in bcc Fe will be indispensable for further understanding of macroscopic HE phenomena in Fe-based

structural materials.

a

	This work	Expt.	Other calc.
a_0 (Å)	2.85	2.866	2.76,2.86
B_0 (GPa)	152	168	235,155
M_0 (μ_B)	2.24	2.22	2.05,2.32
H^F_{1V} (eV)	2.00	1.6-2.0	2.25,2.76
Ω^F_{1V} ($/\Omega_0$)	0.86	0.95	0.55

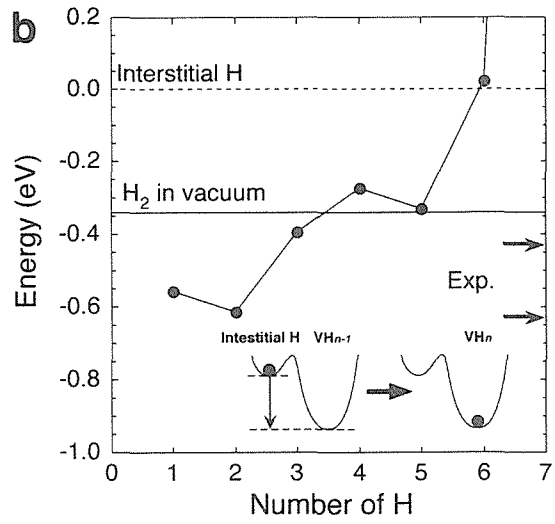

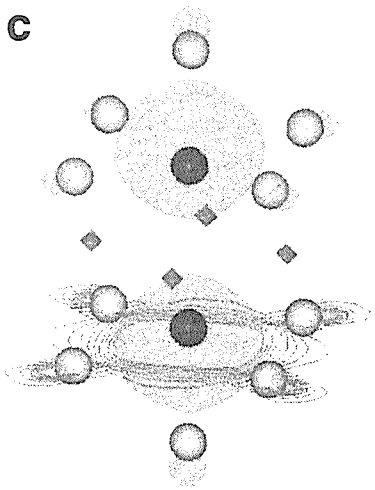

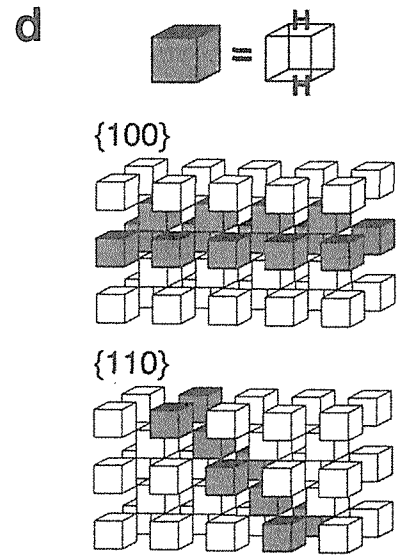

Figure (a) Fundamental properties of bcc Fe in our calculations with the results of experiments and the other calculations. (b) H trapping energies for VH_n. (c) Configuration of VH_2 in bcc Fe. Dark and light spheres show H and Fe atoms, respectively. Electron density related to Fe-H bonding is also shown as gray clouds. (d) Tabular vacancy clusters on the {100} and {110} planes, which are probable in the presence of H.

References

[1] Fukai, Y. *The Metal Hydrogen system* (Springer-Verlag, Berlin,1993).

[2] Myers, S. M. *et al.* Hydrogen interactions with defects in crystalline solids. *Rev. Mod. Phys.* 64(1992), pp.559-617.

[3] Oriani, R. A. and Josephic, R. H. Equilibrium aspects of hydrogen-induced cracking of steels. *Acta Met.* 22(1974), pp.1065-1074.

[4] Tabata, T. and Birnbaum, H. K. Direct observations of hydrogen enhanced crack propagation in iron. *Scripta Met.* 18(1984), pp.231-236.

QUANTITATIVE VISUALIZATION OF HYDROGEN EVOLVED FROM STEEL BY HYDROGEN MICROPRINT TECHNIQUE

K. Ichitani, S. Kuramoto, A. Nagao and M. Kanno,
Department of Material Science, School of Engineering,
The University of Tokyo, Japan

1. Introduction

In delayed fracture process, hydrogen has been reported to affect both crack nucleation and propagation, and, according to generally accepted idea, accumulation of diffusible hydrogen atoms at a stress concentration region precedes crack initiation. However, few experiments have been conducted to determine the distribution of hydrogen in the stress concentrated region around a notch or a crack tip. One reason for this is that hydrogen cannot be detected by common analyzing apparatuses. Moreover, since hydrogen diffuses much faster in ferritic and martensitic steels than do other impurity elements, direct analysis of hydrogen concentration at a fracture surface would be difficult even if a highly sensitive analyzer is available. In order to make a breakthrough in this situation the present authors have been trying to apply a hydrogen microprint technique (HMT) [1], which is a kind of visualization of hydrogen, to a examination of behavior of hydrogen in relation to the delayed fracture of steels. If quantitative information on hydrogen in a sample could be extracted from the results of this visualizing method, new knowledge may be obtained about mechanism of the delayed fracture. Thus, in the present study released hydrogen of various amounts was quantitatively visualized by a high sensitive HMT modified by the present authors [2], and its detection efficiency was compared with that of the conventional HMT.

2. Experimental Procedure

Plate specimens of 1 x 27 x 27 mm^3 were cut from a steel sheet which had a composition of 0.84% C, 0.74% Mn, 0.19% Si, 0.013% P, 0.0013% S in mass percent and balance Fe and had a pearlitic microstructure. One side of the specimen was polished with 0.1 μm alumina paste to a mirror-like finish, and the other side with 1200 grid paper. The mirror-like surface was successively electroplated with a nickel layer of 50 nm thickness from a watt bath in a similar way performed in an electrochemical hydrogen permeation method [3] to improve the sensitivity of the HMT [2]. The nickel plated surface was then covered with a gelatin based nuclear emulsion (Ilford L-4, diluted 2 times), and subsequently the specimen was mounted on a charging cell in such a way that the surface without the gelatin film faced a cathodic solution as illustrated in Fig. 1, and charged with hydrogen cathodically under several charging conditions. Hydrogen atoms dissolved in the specimen diffused through it and then they emerged from the specimen surface covered with the gelatin film. In this occation, they reduced silver ions in the silver bromide crystals to metallic silver as written by the following reaction: $Ag^+ + H = Ag + H^+$. After elapse of a prescribed exposure time, the remaining silver bromide crystals were washed away by immersing the specimen in a fixing solution (and thus the silver particles present on the surface indicate sites from which hydrogen has been released). After the specimen was rinsed with distilled water and dried, the silver particles present on it were observed with a scanning electron microscope (SEM) and analyzed with a an energy dispersive X-ray spectrometer (EDXS). The amount of hydrogen

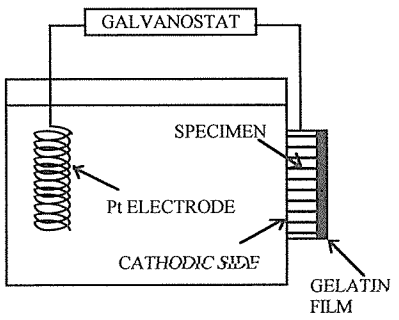

Fig. 1. The charging cell used.

released under each charging condition was determined by an electrochemical hydrogen permeation method.

3. Results and Discussion

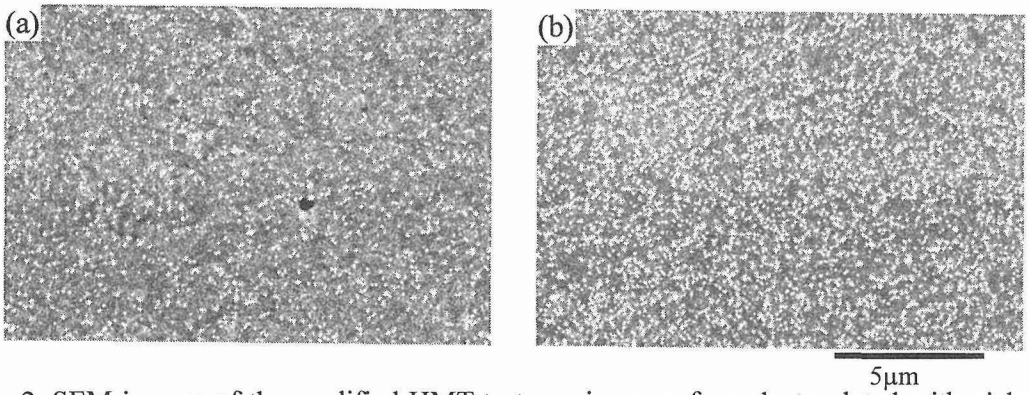

Fig. 2. SEM images of the modified HMT test specimen surface electroplated with nickel and charged with hydrogen for 5 min (a) and 40 min (b).

Fig. 2 shows typical SEM images for charging times of 5 and 40 min. The number of white silver particles observed increases clearly with charging time, i.e., with the amount of hydrogen released.

In Fig. 3, the X-ray intensity of silver from which a background has been subtracted is plotted as a function of the amount of hydrogen determined by the electrochemical permeation test. The intensity is compared with that obtained by the conventional HMT, i.e., the one obtained using the specimen without nickel plating. It should be noted that the modified HMT with nickel plating yields the reproducible X-ray intensities increasing with the amount of hydrogen ranging from 0.4 – 4.2x10^{-3} mol/m^2, though the conventional HMT cannot detect theses amounts of hydrogen because of its low detection efficiency. In order to determine the detection efficiency of the modified HMT, the X-ray intensity was converted to the amount of silver in units of mol/m^2 by using a calibration curve. This curve was obtained by analyzing silver films with EDXS under the same condition as for the previous analysis. Fig. 4 gives the result of the conversion and indicates that the detection efficiency is about 40 %. Rough estimation of the efficiency of the conventional HMT yielded 1 %, and thus it was revealed that the modified HMT had 40 times as large efficiency as the conventional one.

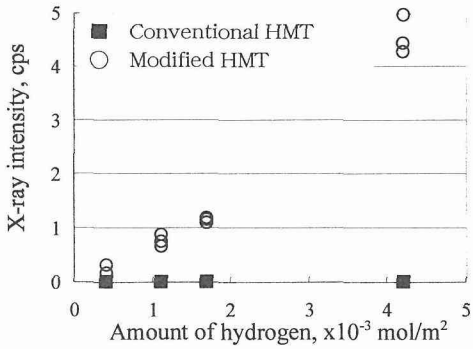

Fig. 3. X-ray intensity of silver particles on the HMT specimen surface is plotted as a function of the amount of hydrogen released.

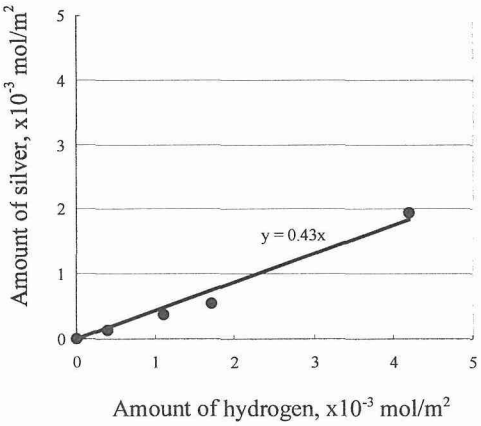

Fig. 4. The relationship between the amount of hydrogen emitted from the specimen surface and that of silver remaining on the surface.

References

[1] Ovejero-Garcia, J, Journal of Materials Science, 20 (1985), 2623-2629.
[2] Ichitani, K. Kuramoto, S. and Kanno, M, Proceedings of International Conference for Hydrogen Effects on Material Behavior and Corrosion Deformation Interactions, TMS(2002) (inprint).
[3] Tsubakino, H. Mizuno, T. and Yamakawa, K, Transactions ISIJ, 26 (1986), 732-736.

Microstructural study of 1500MPa CrMo steel by use of TEM, EDS mapping and EELS

Xiaozhong Zhang, Yue Ma and Jun Yuan

Department of Materials Science and Engineering, Tsinghua University

Beijing 100084, P.R. China

Three samples were used in this work. Sample 1 was commercial steel 42 CrMo and sample 2 and sample 3 were high strength CrMo steel with higher tensile strength. The compositions of the samples are listed in the table 1. The sample 1 was oil-quenched at 880°C for 15min and then aged at 350°C for 120 min. The sample 2 and sample 3 were oil-quenched

Table1 compositions of samples

	C (%)	Si (%)	Mn (%)	Cr (%)	Mo (%)	P (%)	S (%)	Nb (%)	V (%)
1	0.39	0.29	0.8	1.08	0.22	0.025	0.019	-	-
2	0.42	0.27	0.46	1.12	1.15	<0.005	<0.005	0.042	0.30
3	0.42	0.27	0.46	1.12	1.15	<0.005	<0.005	0.042	0.30

at 930°C for 30min and then aged at 550°C and 600°C respectively for 120 min. The tensile strength of sample 2 and sample 3 were 1580MPa and 1600MPa respectively.

EELS and EDS elemental mapping were performed using a field emission gun transmission electron microscope (TEM, JEM-2010F, JEOL) equipped with energy dispersive spectrometer (EDS, Link ISIS, Oxford) and electron energy-loss spectrometry (EELS, GIF, Gatan). When necessary, samples were ion milled to remove any surface oxide. Spectra were deconvoluted by the Fourier-log method [1] to remove multiple scattering components and were background subtracted by fitting the preedge background with a power law function.

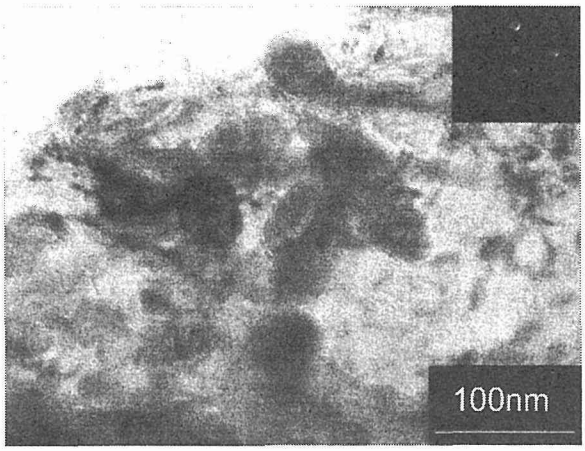

Fig.1 VC particle

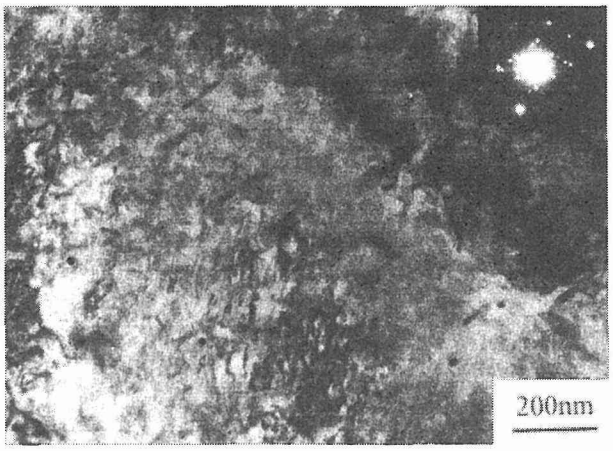

Fig.2 Mo_2C particles

In sample 3, VC and Mo_2C particles were found (Fig.1 and Fig.2). They were less than 50nm in diameter. While in sample 2, no such particles were found. They acted as hardened

particles, so the tensile strength of sample 3 was not lower than that of sample 2.

We developed a new method to study the grain boundaries in steel by use of EELS. In this work, the EELS and EDS mapping techniques were used to study the grain boundary in CrMo steel. The density of state of iron was measured by the normalized intensity of white line. Fig.3 shows the Fe edge of EELS recorded at bulk and grain boundary (GB) of the sample 1 and sample 3. As far as we know, the mechanical property of the grain boundary compared with the bulk can not just be determined by the shape of the spectra. We measured the occupancy of the 3d state of iron with the white line in EELS spectra, using a method similar to D.A. Muller's[2-3]. Our calculation shows that, in sample 1, the occupancy of 3d state of iron at grain boundary is 0.19 electron/atom higher than that in bulk, while in sample 3 there is no obvious difference between the occupancy of 3d state of iron in bulk and at grain boundary. As intergranular fracture occurred in sample 1 while transgranular fracture occurred in sample 3, we conclude that if the grain boundary has a high occupancy of 3d state than the bulk the sample tends to have intergranular fracture, while if the grain boundary has almost the same occupancy of 3d state as the bulk, the sample tends to have transgranular fracture.

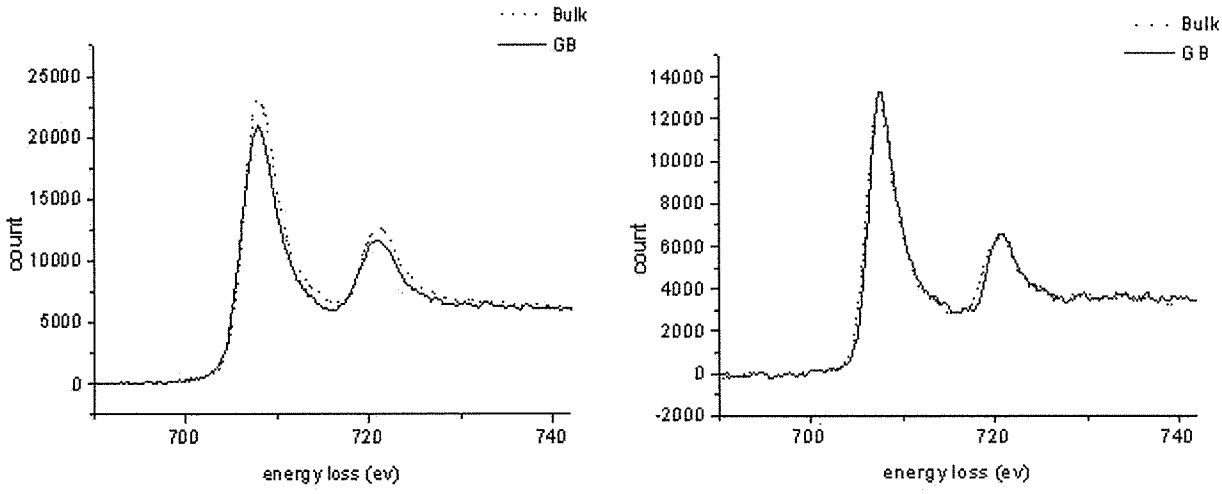

(a) (b)

Fig.3 EELS spectra of Fe edge at the grain boundary and in the bulk for (a) sample 1 and (b) sample 3

The main deference in composition between sample 1 and sample 3 is that there are more Mo (1.22%), some V and little Nb in sample 3. EDS elemental mapping were performed on a typical grain boundary area in sample 3. There are some Mo and Cr segregation in the grain boundary. Some V rich areas were found near the grain boundary. The enhancement of the bonding in grain boundary in this sample can be ascribed to the Mo segregation to grain boundary and V enrichment near the grain boundary.

References

[1] D. W. Johnson and J. C. H. Spence, J. Phys., D7(1994), pp.771.

[2] Muller D A, Batson P E, Subramanian S, Sass S L, and Silcox J, Phys. Rev. Lett., 75(1995), pp.4744.

[3] Muller D A, Batson P E, Subramanian S, Sass S L, and Silcox J, Acta Metall. Mater., 44(1996), pp.1637

EF-TEM and HREM Observations of V-bearing Steels

T.Hara, T.Tsuchida and K.Tsuzaki
Materials Engineering Laboratory, National Institute for Materials Science
1-2-1 Sengen, Tsukuba, Ibaraki 305-0047, Japan

1. Introduction

Hydrogen-induced delayed fracture is one of the most serious problems in high strength steels for actual application. The utilization of adequate hydrogen-trapping sites has recently been investigated[1] to improve the delayed fracture resistance. Vanadium-bearing tempered martensitic steel is considered as one of the typical steels that contains hydrogen trapping sites. It is considered that the VC precipitated during tempering acts as the hydrogen trapping site. The VC precipitate was widely investigated in 1950's-70's from the aspect of secondary hardening[2]. However, the relationship between the hydrogen absorption property and the size and distribution of the VC precipitate still has not been understood. In the present study, hydrogen absorption property of the V-bearing steel was controlled by changing tempering temperature. Furthermore, Energy-Filtering TEM (EF-TEM) and High-resolution TEM (HREM) observations were performed to understand the relationship between the hydrogen absorption property and the microstructure.

2. Experimental

The chemical composition of the V-bearing steel used in the present study is Fe-0.40C-0.31Si-0.33Mn-1.00Cr-0.70Mo-0.35V(mass%). The samples were austenitized at 1193K for 45min, followed by oil quenching. Based on the calculation with Thermo-Calc, the VC with a volume fraction of 1% is expected to be retained at 1193K. These quenched samples were tempered at temperatures from 573K to 973K for 90min and followed by water quenching. Hydrogen was introduced into the specimen by an electrolytic cathode charge at constant charging condition. The hydrogen contents of the charged specimens were measured by the thermal desorption analysis method using a quadrupole mass spectroscopy. The FE-TEM (JEOL 2010F, 200kV) was used for microstructure observation. An attached post-column type energy-filter system (Gatan GIF2000) was utilized to obtain elemental maps.

3. Results and Discussion

3-1. Hydrogen absorption property

Figure 1 shows the effect of tempering temperature on the hydrogen absorption contents for the V-bearing steel. The results for Fe-0.4C samples are drawn simultaneously, for reference. In the V-bearing steel, hydrogen content increased gradually up to 773K, increased sharply at around 873K, and decreased considerably at 973K. This hydrogen absorption behavior is quite different from that of Fe-0.4C alloy. Retained and precipitated VC must be closely associated with the characteristic effect of the tempering temperature of the hydrogen absorption for the V-bearing steel.

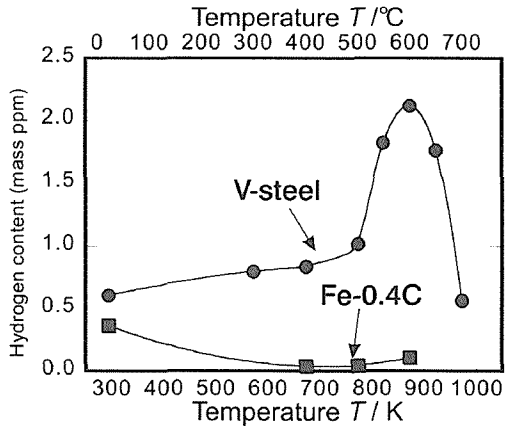

Fig. 1 Effect of tempering temperature on the hydrogen content introduced into the specimens by the cathode charging for the V-bearing steel and the Fe-0.4C alloy.

3-2. EF-TEM observation

Elemental mapping by the EF-TEM method was performed to observe the distribution of additional elements, directly. Fig. 2 is a V-mapping image of the as-quenched specimens. Many retained V-containing particles are clearly observed. Most of the particles are spherical and about 20nm in diameter. Further observations confirmed that the size and the distribution of the retained VC observed by the EF-TEM elemental-mapping are almost the same for all of the specimens even after the tempering at 973K. The existence of these retained VC particles is considered as one of the reasons that the hydrogen content does not change markedly and remains high when the specimens are tempered up to 673K.

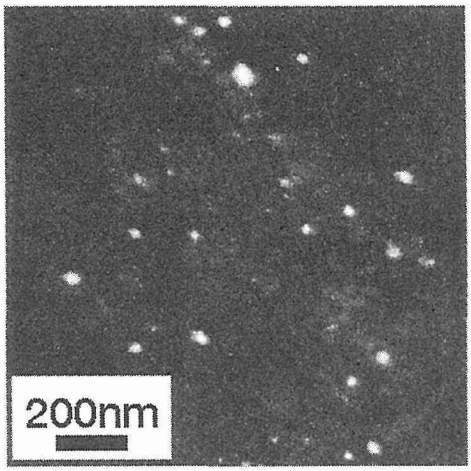

Fig. 2 V map image by EF-TEM for the as-quenched V-bearing steel. Bright points indicate V containing particles.

3-3. HREM observation

The HREM observations were carried out for the specimens tempered at 667K, 773K, 873K, and 973K to understand the VC precipitation in more detail. Fine plate-shaped precipitates were found to exist only in the specimens tempered at 873K, A typical example is shown in Fig. 3. This photograph was taken along the [100]α direction. The precipitates are thin plates and their broad interface is {011} α with a good coherency. This observation result indicates that this precipitate is consistent with the VC that had been previously reported: i.e., the crystal structure is NaCl type cubic and has a 'Baker-Nutting' orientation relationship to the ferrite matrix ({100}VC // {100} α, <100>VC // <110> α). The typical size of the precipitates is 5-10nm long with a thickness of 1nm. The existence of this plate-shaped fine VC in a sample tempered at 873K must be contribute to high hydrogen absorption.

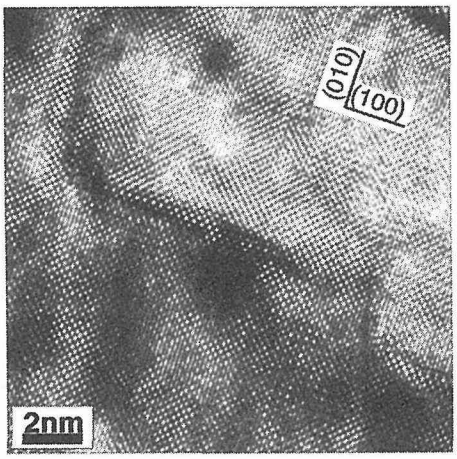

Fig. 3 HREM observation of the plate-shaped VC precipitates in the specimen tempered at 873K.

Conclusions

The relationship between the microstructure and the hydrogen absorption property of a V-bearing steel was investigated by the EF-TEM and HREM observations. The main results are as follows:

(i) Retained VC with the dimension of around 20nm were observed by the V-mapping for all tempering temperatures. One of the reasons for the high hydrogen content is the retained VC.

(ii) The hydrogen content becomes extremely high when the tempering temperature is around 873K. The precipitation of the plate-shaped fine VC observed by the HREM causes this hydrogen absorption property.

References

[1] S.Yamazaki and T.Takahashi, Tetsu-to-Hagane 83(1997),454-459.

[2] R.G.Baker and J.Nutting, in 'Precipitation Process in Steels' ISI spec. rep., 64(1959),1-22.

In Situ SEM Study on Hydrogen-induced Cracking of Ni_3Al+NiAl

J.X. Li, Y.B. Wang, L.J. Qiao, W.Y. Chu and H.Q. Li

Department of Materials Physics and Chemistry, University of Science and Technology Beijing, Beijing 100083, China

In order to develop nickel aluminides such as NiAl and Ni_3Al for applications at elevated temperature, extensive works have been focused on improvement of their mechanical properties. Many of studies indicated that the room temperature brittleness of both Ni_3Al and NiAl alloys was related to hydrogen. Therefore, it can be deduced that there exists hydrogen embrittlement in two-phase alloy of Ni_3Al+NiAl. In this article, HIC of the two-phase alloy of Ni_3Al+NiAl during dynamic charging would be recognized using a WOL constant deflection specimen. On the other hand, initiation and propagation of HIC were *in situ* studied using a notched tensile specimen in scanning electron microscopy(SEM).

The two-phase alloy used in this study had a composition in weight pct of 16.99Al, 0.05Si, 0.009C, 0.0011O, 0.0002N, and balance Ni. The alloy was homogenized in argon at 1280°C for 6h, followed by air-cooling. Calculation showed that the volume ratio Ni_3Al / NiAl in the two-phase alloy was 63/37. The yield strength and the ultimate tensile strength of the alloy were 305 and 369MPa, respectively, and the elongation was 2.3%.

The specimens included a single-edge notched tensile and a modified wedge opening-loading (WOL) specimen. The stress intensity factor of the modified WOL specimen is

$$K_I = \frac{EV}{\sqrt{W}} \frac{F(a/W)}{C(a/W)}$$

Hydrogen was introduced through dynamic charging in a 0.5mol/L H_2SO_4+0.25g/L As_2O_3 solution with a current density of 10mA/cm^2, which correspond to a hydrogen concentration of 12.6×10^{-4}%. For the WOL constant deflection specimen, hydrogen-induced crack initiated at the notch tip after dynamic charging for 10h. Thereby, initiation of hydrogn-induced crack was evidently related to diffusion and enrichment of atomic hydrogen.

The length of the propagated crack vs time curve was measured, and further *da/dt* was replotted in terms of K_I. Results showed that the crack growth rate in the second stage was $(da/dt)_{II}$=0.019mm/h and the threshold stress intensity factor of hydrogen-induced cracking, K_{IH}, was 15.7 MPa·m$^{1/2}$.

During *in situ* extending in SEM, when the localized plastic deformation is large enough, the slip band could be observed. There was contrast change between Ni_3Al and NiAl phases due to large plastic deformation. For the specimen without hydrogen charging, results showed that slip bands mainly appeared in the Ni_3Al phase but the crack grew mainly in NiAl phase. During loading, microcrack initiated and propagated preferentially within the NiAl phase ahead of the crack tip. The microcrack didn't initiate and propagate along slip bands although there also existed slip bands in the NiAl phase. The Ni_3Al phase was barrier to the crack propagation. Only when the stress concentration ahead of a crack tip was large enough, the main crack could propagate throughout the Ni_3Al phase. but no microcrack initiation occurred in the Ni_3Al phase. The fracture surface of the uncharged specimen was a typical cleavage. The fracture unit was much larger than the size of the Ni_3Al phase.

For the specimen precharged for 136h with i=50mA/cm^2, which corresponded to hydrogen concentration of 24.7×10^{-4}%, the hydrogen-induced crack initiated and propagated preferentially along the Ni_3Al/NiAl interfaces, when the applied stress was much smaller than that for the uncharged specimen. The Ni_3Al phase was still barrier to the crack propagation. The fracture surface of the precharged specimen was an interphase fracture. The fracture unit was about 20μm, corresponding to the size of the Ni_3Al phase. On the other hand, there were some secondary microcracks along the Ni_3Al/NiAl interface in the fracture.

Key Words: Ni_3Al+NiAl, HIC, in situ extending in SEM

Environment Assisted Cracking of TiAl - Thermodynamics and Electrochemical Considerations

T.Sundararajan, T.Haruna*, S.Fujimoto* and T.Shibata*
National Institute for Material Science, 1-2-1 Sengen, Tsukuba 305-0047, JAPAN
* Department of Materials Science and Processing, Osaka University, Suita 565, Osaka, JAPAN

1. Introduction

Intermetallic titanium aluminides have attractive specific properties including strength at elevated temperatures and creep resistance. Their structural applications demand a certain reliability and damage tolerance over years. Attention towards environment-assisted cracking (EAC) has become the matter of interest since the TiAl was identified to undergo the EAC in the atmospheric condition. It was reported that the EAC susceptibility increases when the specimens are tested in hydrogen gas and moist air conditions even at room temperature, in comparison with dry oxygen and vacuum conditions [1]. This clearly indicates that hydrogen entry to the material results in severe EAC. In the present paper, the focus on the environmental assisted cracking nature of TiAl in aqueous solution at wide pH range will be discussed. The mechanism in which the TiAl undergoes to EAC was discussed using several analytical techniques and the model was proposed for the severe EAC in a particular domain.

2. Materials and methods

Hot forged and annealed TiAl specimens were mechanically polished by emery paper up to #1500 and subsequently electropolished. The electrolyte used for electropolishing was 59vol% methanol, 35vol% n-butanol and 6vol% perchloric acid. The temperature and potential were maintained at –25°C and 11V, respectively. Duration for the electropolishing was fixed to 15 minutes to obtain a mirror finished surface. Slow strain rate test (SSRT) was carried out with a strain rate of 3.3×10^{-5} s^{-1}. Test solution used for the SSRT test was 0.05 M Na_2SO_4. The pH was maintained by using H_2SO_4 and NaOH. The solution was purged with nitrogen gas for 72 ks prior and during the test. Platinum and Ag/AgCl were used as counter and reference electrode, respectively. All the potentials reported here are converted into standard hydrogen electrode (SHE). X-ray diffraction (XRD), Scanning electron microscope (SEM) Thermal desorption spectroscopy (TDS) and micro hardness studies have been undertaken on the fractured specimens.

3. Results and Discussion

The maximum stress values obtained during the slow strain rate tensile test (SSRT) were distributed in the potential-pH diagram of Ti/water and Al/water systems. On the EAC map, susceptibility was divided into four regions depending on their maximum stress values. Especially, in the cathodic potential of acidic pH shown the severe EAC, where the material exhibits the very low maximum stress. From the potential-pH diagram of Al/water system, it does not give any clue whereas Ti/water system shown in Fig.1. inferred the distinct indications as follows: In the oxide stable region, the specimens showed almost no EAC susceptibility. In the hydride stable region, the specimen showed relatively high EAC susceptibility compared to that in the oxide stable regions (TiO_2 and Ti_2O_3). The highest susceptibility was observed in the Ti^{2+} stable region. The results indicate that different surface reactions occurring at different potential and pH play an important role in the EAC behaviour of this material.

To confirm the role of this thermodynamic dependence (surface condition at different pH and potential) to the EAC behaviour, the specimens fractured at five different potentials

(+200, OCP, -600, -1250 and –2000 mV; pH-3) were investigated with surface analytical techniques. The reasons for choosing these potentials are to represent the different region in the potential-pH diagram of Ti/water system. Fig. 2. shows the XRD spectra of the fractured specimens at different applied potentials with reference to that of the as-annealed specimen. No drastic change occurred on the surface when the specimen tested at open circuit potential and an applied potential of +200 mV (oxide stable region). However, the specimen fractured at –1250 mV (ion stable) showed an additional peak along with the substrate TiAl (111) peak. The additional peak was identical to hydride. On the other hand, specimen fractured at –2000 mV does not show any hydride peak though it falls in the hydride stable region. SEM micrographs of the side surface of specimen fractured at –1250 mV showed a distinct difference from other tested conditions. The surface of the specimen became more roughen with lots of small crack. These cracks were absent in the other tested specimens.

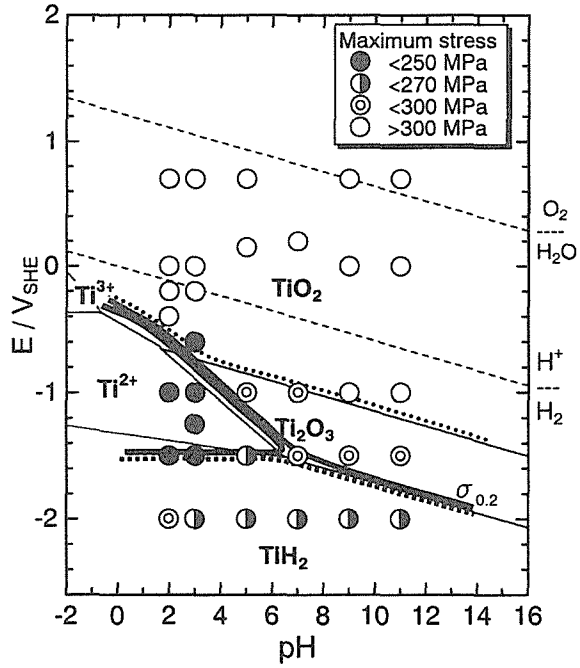

Fig. 1. Distribution in maximum stress values in the potential-pH diagram of Ti-H_2O system[2)]

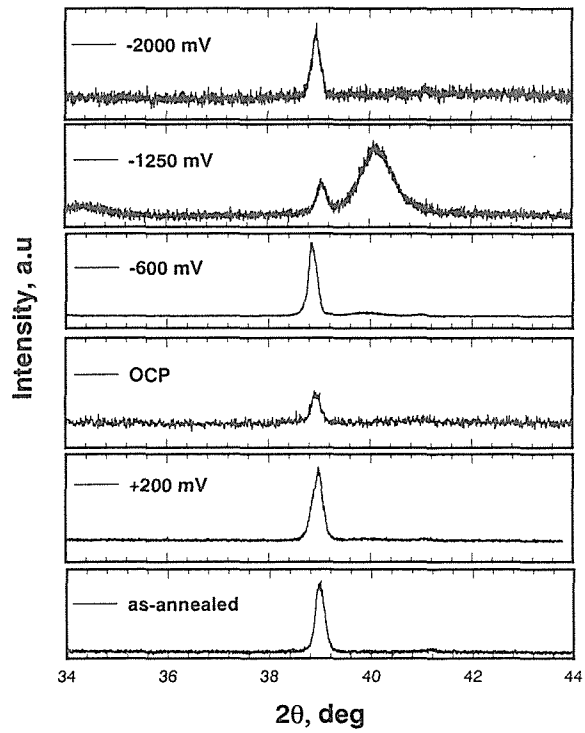

Fig. 2. XRD spectra of as-annealed and fractured specimens

The micro hardness values were obtained from the surfaces of the all the five specimens and the results showed that the hardness values of the fractured specimen had the inverse trend with the maximum stress obtained from the respective ones. Hydrogen present in the TiAl charged at different potentials were assed using TDS. From the results, the specimen charged at –1250 mV showed an order of magnitude higher value than the other tested condition.

4. Conclusion

An attempt was made to understand the EAC behaviour of TiAl in the thermodynamics and electrochemical viewpoint. From the results, it showed that the hydride formation in the acidic pH is the severe cause for the EAC of this material.

5. Reference:

1) Takasugi, T, Hanada, S and Yoshida, M, J.Mater.Res., 7(1992), No 10, pp 2739-2746
2) Haruna, T, Shibata, T, Iwata, T and Sundararajan, T, Intermetallics, 8(2000), pp 929-935.

High Strength Steels for Automobile Application

T. Kitayama
Engineering Research Department 3, Tochigi R&D Center, Honda R&D, Japan

1. Introduction

NIMS, the organizer of this conference, has carried out the project for Ultra-Steel (STX-21) for 5 years, and has gotten a lot of fundamental data and excellent results. It has set the target of putting them to practical use within the next 5 years. Therefore, I would like to offer this conference some advice, based on my experience as a material engineer in the automotive industry.

At first, I will give an example of the relation between the failures of an actual automotive part, a connecting rod, and the forces applied to it. Then I will give my opinion about the importance of the communication and the integration between material researchers and designers. The shortened term conrod will be used in place of the "connecting rod".

2. Mechanics of a Connecting Rod and its Failures

2.1. Mechanics

In the internal combustion engine, the air-fuel mixture is burned in the cylinders of the engine, and the temperature and the pressure of the burned gas reach, for example, about 2,000 – 3,000 K and 8MPa each, though varying widely with the engine specification. This pressure turns the crankshaft by means of the pistons and the conrods. This results in the accelerating movement of the conrod. The movement consists of the translation along its axis and oscillation around the small end of conrod.

The forces applied to the conrod are an explosion load, a piston side force, a vertical inertia force, an oscillating inertia force, and a reaction force from the crankshaft. The first two forces are the static ones, the next two are the dynamic ones (inertia forces), and the last reaction force is balanced with the sum of the above four forces. There is another force applying to the side of the big end of the conrod. This force is caused by thrust positioning.

The inertia force is experienced, for example, when a bus starts from the dead stop. Observing from the outside of the bus, the passengers have an accelerated movement, and there is not an inertia force. But observing from a person on the bus, the passengers do not move, and the inertia force is present. When we think of the forces applied to the conrod and its failures, it is necessary to stop the movement of conrod. Therefore, the coordinates for observing the movement are set on the conrod. In this case the inertia force is present. The acceleration of the translation causes the vertical inertia force, and the acceleration of the oscillating movement causes the oscillating inertia force. The oscillating inertia force is also called whip moment, because it is similar to what is felt in whip.

2.2. Failures

Table 1. The Failures of Conrod at Each Position by Each Force

	Vertical Force (Static Force + Inertia Force)	Whip Moment	Thrust Force
Shank	Buckling Tension-Compression Fatigue		
Small End	Fretting Fatigue		
Big End	Scuffing Due to the Worsening of Circularity	Fretting Fatigue Due to the Worsening of Circularity	Scuffing Wear
Mating Face	Fretting Fatigue	Fretting Fatigue	

Table 1 shows the relation between the failures of the conrod at each position and the forces applied. These failures are roughly divided into the static plastic deformation (buckling), dynamic fracture (fatigue), and the sliding failure (scuffing and wear). The fatigue is further divided into the tension-compression fatigue and the fretting fatigue. The fretting fatigue can be also classified into the sliding failure, because the cause of the fretting is small relative motion between two contact surfaces.

The conrods in passenger cars are usually made of micoralloyed steels, whose bending fatigue strength is around 400MPa. In many cases improvement of the bending fatigue strength does not raise the fretting fatigue strength.

3. Communication and Integration

In putting a new or advanced material into practical use, it is important to induce the communication and the integration between material researchers and designers. The term integration does not mean compromise or domination, but creative solution that profits both [1].

3.1. Creation of the New Techniques for the Evaluation of Machine Parts

Most of the topics of material are too difficult for designers to understand. Therefore, the communication interface had better been positioned with fundamental mechanics in mind.

About 10 years ago my colleagues struggled with the fretting fatigue fracture of conrod at its big end. The cause of the fracture was the worsening of circularity of the big end because of the whip moment. It took much longer time to understand the cause than had been expected. The reason was our thinking of that time. We were evaluating the circularity stiffness of the big end by applying the vertical force. The whip moment had been ignored and forgotten for a long time. Finally this problem was solved by the close collaboration among the material engineers, engine evaluation engineers, and engine designers.

These experiences greatly improved the communication ability of each engineer who had taken part in this solution program. The success of application program about new material will owe mainly to the communication ability of both material researchers and designers.

3.2 Fracture Splitting

Fracture splitting is the term used to describe the new technology for producing mating faces. In this technology the big end of the conrod is brittle-fractured along the mating line, and then the two separate parts are mated and fastened by conrod-bolts [2]. This can prevent the mating faces from fracturing by fretting fatigue, can save the dowel pin for positioning, and so on. This idea appeared probably in EU about ten years ago and mass production has already started in EU, US, and Japan.

I think that the fracture splitting technology is one of the excellent examples of integration between material researchers and designers.

4. Summary

The communication and the integration between material researchers and designers are necessary in order to put new material into practical use as a machine product. It makes the communication much better for material researcher and designers to collaborate for creating the parts evaluating techniques. An elementary knowledge of mechanics is necessary for even material researchers to take part in this collaboration.

References

[1] Graham, P. Ed., "Mary Parker Follett: Prophet of Management", Boston, Harvard Business School Press, 1995.

[2] Olaniran, M. A. and Stickals, C. A., SAE Technical Paper Series, No.930033.

Corrosion Fatigue Life Improvement in High Strength Suspension Spring Steel

T.Nakayama, A.Inada, M. Shimotsusa, and N.Ibaraki
Kobe Steel, Ltd., Japan

High stress suspension spring steel design is required to reduce the weight reduction of automobiles. The corrosion fatigue of spring must be taken into consideration to meet this requirement, because suspension springs are exposed to corrosive environments such as de-icing salts and suddenly loses corrosion fatigue life, when the tensile strength is increased, as shown in Fig.1. The analysis of corrosion fatigued samples revealed that crack initiation occurred from corrosion pits and crack propagation was accelerated by hydrogen, as illustrated in Fig.2. So, the authors have researched and developed new high strength suspension spring steel, UHS1900, designed with a maximum shear stress of 1200MPa and having excellent corrosion fatigue life from the standpoints of the improvement of corrosion resistance and hydrogen embrittlement (HE).

Corrosion resistance was improved through rust composition control with the addition of Cu, Ni, and Ti, as shown in Fig.3. Fig.4 compares weight loss of SAE9260 and UHS1900 obtained from cyclic corrosion test, confirming better corrosion resistance of UHS1900. Fig.5 presents rust composition and Cl distribution in rust layer of both steels. It indicates that protective amorphous rust to prevent the invasion of corrosive species such as chloride could be more easily formed in UHS1900, resulting in the increase of its corrosion resistance.

On the other hand, HE resistance was improved through the introduction of a hydrogen trapping site with the addition of Ti and V. Superior HE resistance of UHS1900 was experimentally confirmed in Fig.6. Lots of fine precipitates of TiC with sub-micron size were found to exist in matrix in UHS1900 by TEM observation. In addition, it was found from thermal desorption spectrometry analysis of SAE9260, UHS1900, and Ti-free UHS1900 after cathodic hydrogen charging that the quantity of diffusible hydrogen in the UHS1900 was remarkably small at the same current density. These facts suggest that fine precipitate of Ti system (TiC), which could act as diffusible hydrogen trapping site, plays an important role in the HE resistance in UHS1900.

Finally, UHS1900 with 1200MPa in maximum shear stress was confirmed to be approximately the same life as the conventional SAE9260 with 1100MPa in maximum shear stress by the spring corrosion fatigue test shown in Fig.7. As a result, 15 to 20% weight reduction has been successfully achieved by replacement of the spring steel from SAE9260 to UHS 1900.

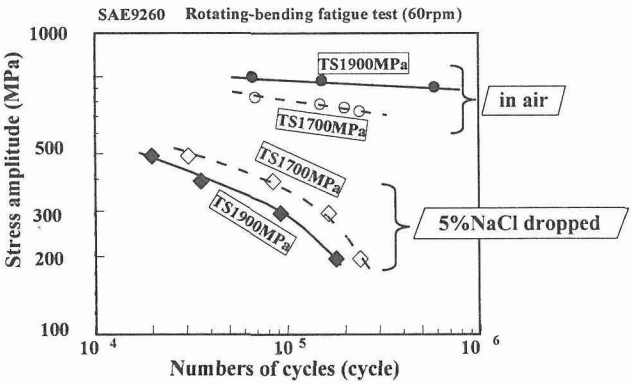

Fig.1 Effect of tensile strength (TS) on air and corrosion fatigue life of SAE9260.

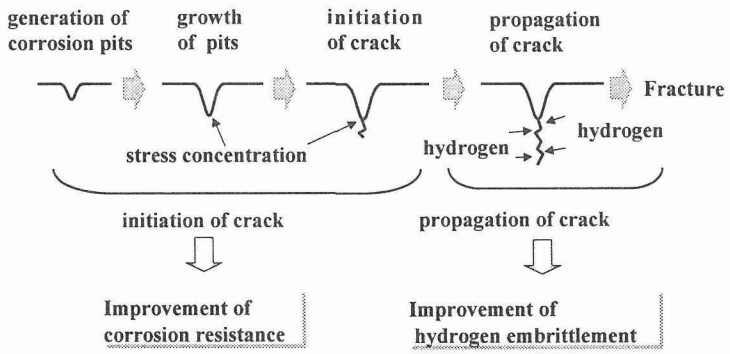

Fig.2 Corrosion fatigue (CF) mechanism of spring and concept for improving CF life.

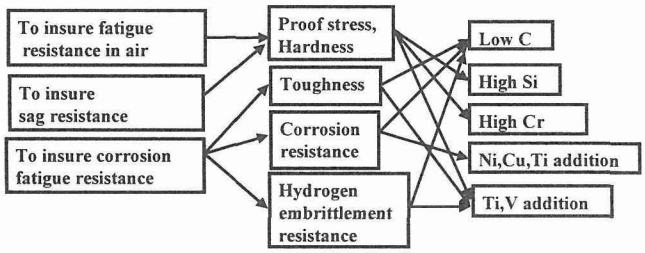

Table Chemical composition of the UHS1900 [mass%]

Steel	C	Si	Mn	Cu	Ni	Cr	V	Ti
UHS1900	0.40	1.80	0.20	0.25	0.52	1.05	0.17	0.070
SAE9260	0.60	2.00	0.90	tr.	tr.	0.15	tr.	tr.

Fig.3 Chemical composition designing of a new higher strength steel resistant to CF.

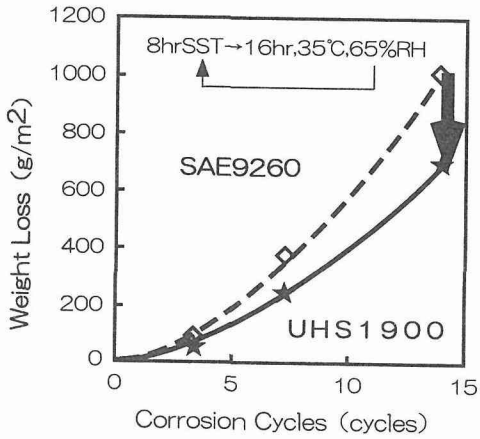

Fig.4 Weight loss of SAE9260 and UHS1900 as function of corrosion cycle.

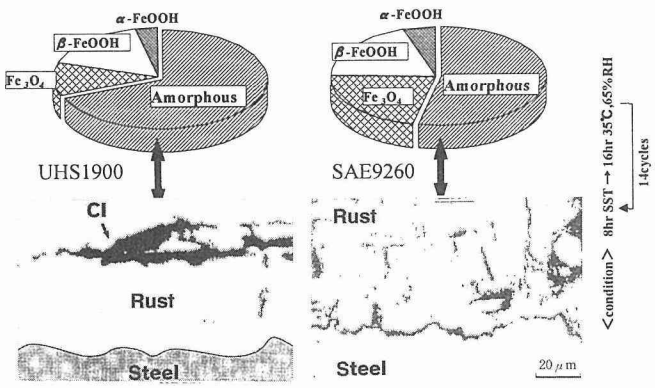

Fig.5 Rust composition and Cl distribution in rust layer of SAE9260 and UHS1900.

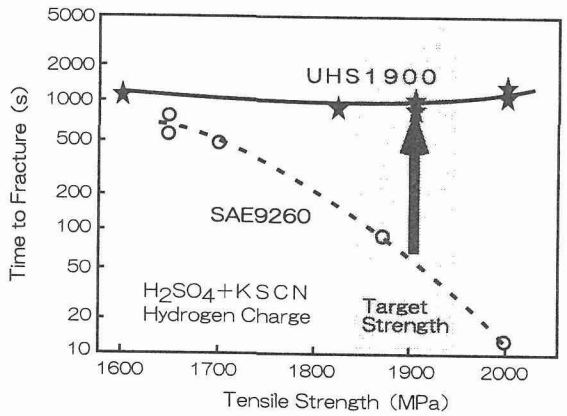

Fig.6 Hydrogen embrittlement resistance of SAE9260 and UHS1900 as a function of TS.

Suspension Spring Steel	Applied Stress [MPa]	Corrosion Fatigue Life (×10⁴ cycles) 3 4 5 6
UHS1900 (TS1900MPa)	750±450	
SAE9260 (TS1700MPa)	700±400	

Fig.7 Spring corrosion fatigue test result of SAE9260 and UHS1900.

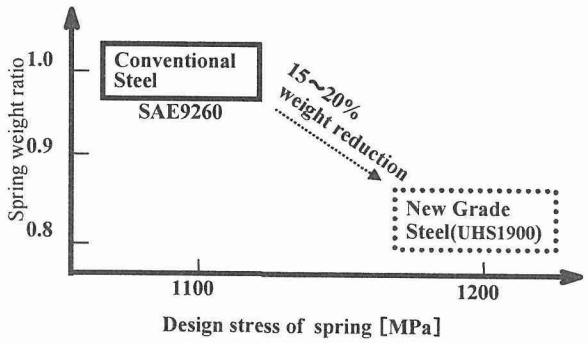

Fig.8 Achievement of weight reduction by replacement from SAE9260 to UHS1900.

The Study of Fatigue Properties on a 1500*MPa* Bainite/Martensite Dual-phase High Strength Steel

Dong-Yuan Wei Jia-Lin Gu Hong-Sheng Fang Bai-Zhe Bai
Department of Materials Science and Engineering, Laboratory of the Advanced Materials,
Materials Research Center, Tsinghua Univerisity, Beijing, P.R. China,100084

1、Introduction

The high strength steels of which strength exceeds 1200 *MPa*, its fatigue strength will be directly depend on their strength and toughness. The microstructure of a novel bainite/martensite dual-phase steel is carbide free bainite/martensite dual-phase structure, at the same time there are retained austenite films in the bainite lath and between the bainite laths and the martensite laths, its tensile strength is above 1500*MPa* and it has better combination of strength and toughness. Up to now, there has been few publication of the fatigue properties of bainite/martensite dual-phase high strength steel.

2、Experimental Materials and methods

The used low alloy C-Si-Mn-Cr steel prepared by high purity materials was vacuum induction melted, getting a 25kg ingot and it was forged at 1200℃, then was kept at 700℃ for 2h and furnace cooled to room temperature. The specimens were austenitized at 900℃ for 20*min*, afterward air cooling and tempered for 2 hours at 280℃ and 370℃, respectively. The fatigue specimens used were the smooth Hourglass-Shaped specimens of high frequency axial fatigue, the gauge part was polished. The fatigue crack propagation test used compact-tension specimens. The tensile-compress fatigue test was preformed on the Servo-electro-hydraulic Instron-1603 testing machine , the test frequency was 165 Hz. The fatigue limit was measured with the fatigue cycle coefficient R= -1 and the cycle number of $N_f = 1 \times 10^7$. The fatigue fracture morphology and microstructure were observed by *S*-450 scanning electron microscope.

3、Experimental Results

The fatigue data of used bainite/martensite dual-phase steel are shown in the table 1. From the table 1 it is observed that the fatigue limit of the bainite/martensite dual-phase high strength steel at different temper temperatures is all larger than 635 *MPa*. In addition, through the cycling fatigue failure number, it is suggested that the real value of the fatigue limit of the bainite/martensite dual-phase high strength steel tempered at 370℃ might be superior to that of tempered at 280℃.

The da/dN-$\triangle K$ curves of the bainite/martensite dual-phase high strength steel are shown in the Fig.1. Fatigue threshold($\triangle K_{th}$) is a parameter charactering beginning fatigue crack propagation. The $\triangle K_{th}$ values under different conditions are about 12.5 ~ 12.8$MPam^{1/2}$. The fatigue crack propagation rate is decreasing significantly with increasing load ratio in the same temper temperature (280℃ or 370℃) and observably with increasing temper temperature in the same load ratio(R =0.1 or R =0.3). The fatigue crack propagation curve of the bainite/martensite dual-phase high strength steel of tempered at 280℃ and R =0.3 forms obvious plateau, its $(da/dN)_{II}$ value is about 10^{-5}*mm/Cycle*. The fatigue crack propagation rate is the largest under the conditions of tempering at 280℃ and R =0.1, but the $(da/dN)_{II}$ of tempering at 370 ℃ is about 5.0×10^{-6}*mm/Cycle* in R =0.3.

The structure morphology of the bainite/martensite dual-phase high strength steel tempered at 280℃ is shown in the Fig.2. There are certain thick retained austenite films in the original austenite grain boundaries and the plate boundaries of the lower bainite and martensite and the bundle boundaries. The structure characteristic of the bainite/martensite dual-phase high strength steel tempered at 370℃resembles that of tempered at 280℃.

The fatigue cracks in Fig.3a initiate from the specimen surface and then grow along radial direction,

the tearing ridges exhibit radiating distribution. The sign "□" area in Fig.3a is amplified and shown in Fig.3b, the tearing ridge is larger, there are a little secondary cracks and frictional marks, but the fatigue striation hasn't been found, the fatigue fracture mode is transgranular quasi-cleavage failure.

5、Conclusion

1) The fatigue limits of bainite/martensite dual-phase high strength steel are all larger than 635*MPa*.

2) The fatigue crack threshold values ($\triangle K_{th}$) of bainite/martensite dual-phase high strength steel are about 12.5~12.8$MPam^{1/2}$. The fatigue crack propagation rate is decreasing significantly with increasing load ratio in the same temper temperature, and decreasing observably with increasing temper temperature in the same load ratio. The $(da/dN)_{II}$ is in the range of 5.0×10^{-6}~$10^{-5}mm/Cycle$.

3) It is believed that improvement of the fatigue properties of the bainite/martensite dual-phase high strength steel depends on its microstructure.

Table 1. The Fatigue Strength Date of Bainite/Martensite Dual-Phase Steel

Experimental Materials and Process	Fatigue Limit $\sigma_{-1}(MPa)$	Cycle Number n_f	Remarks
Tempering at 280℃	750	3.739×10^6	Failure
	>635	1.000×10^7	Non-failure
Tempering at 370℃	750	6.257×10^6	Failure
	>635	1.000×10^7	Non-failure

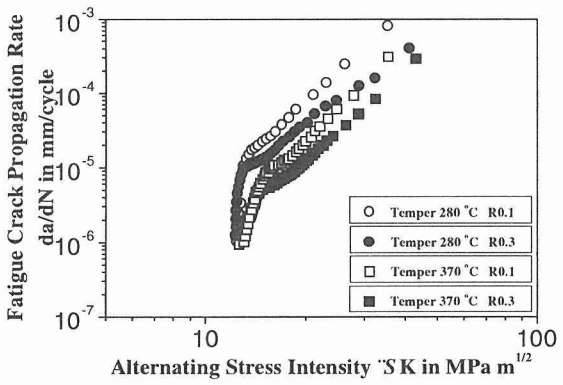

Fig.1 The da/dN -$\triangle K$ Curve of the Bainite/Martensite Dual-Phase Steel

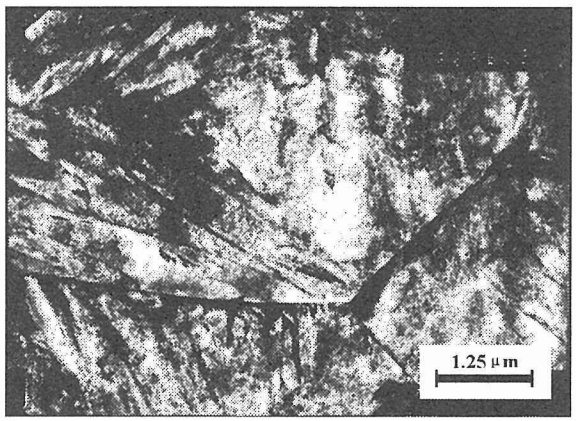

Fig 2. The Structure Morphology Tempered at 280℃ (TEM)

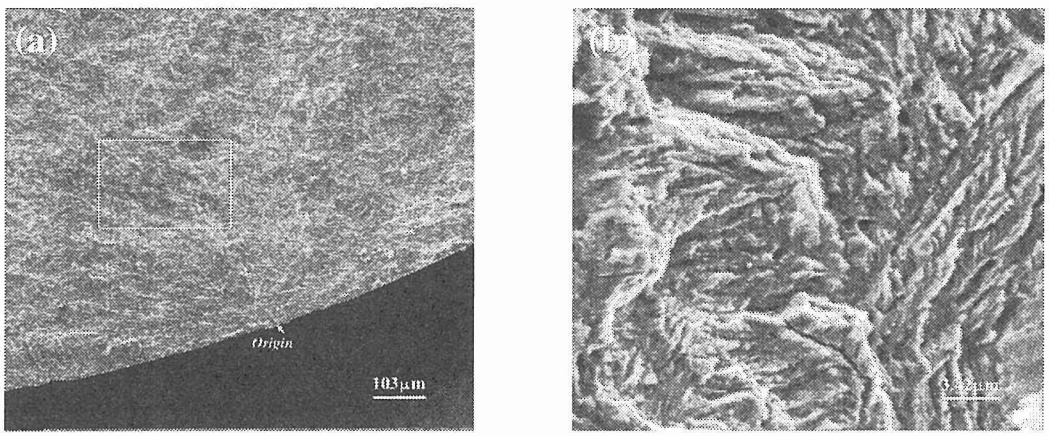

Fig 3. The SEM Micrographs of Fatigue Fracture Surface (Tempering at 280℃)
Cycle Stress Amplitude 750 *MPa* Cycle Number 3.739×10^6

Influence of Nonmetallic Inclusions on Fatigue Strength of High Strength Steels

Y. Murakami
Department of Mechanical Engineering Science, Kyushu University, Japan

Resent topics of ultralong life fatigue problems are overviewed mainly based on the data of the authors' group. The mechanism of elimination of conventional (classical) fatigue limit is discussed based on fractographic investigations[1,2] and microstructural analysis[3]. The crucial influence of hydrogen trapped by inclusions is pointed out with regards to the particular morphology(Optically Dark Area, ODA)in the vicinity of inclusions at fracture origin[2,4] (Fig.1).

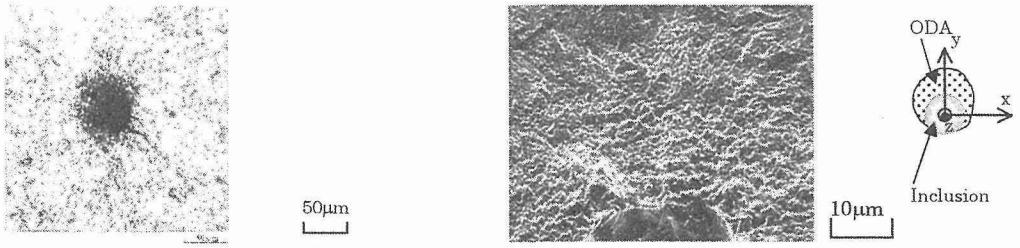

(a) Optical microscope image [2]

(b) SEM image with a high resolution obtained by tilting the specimen 30deg. from z to y axis.[4]

Fig.1 Images of ODA obtained by different type microscopes (SCM435). $\sigma = 560$ (MPa), $N_f = 1.11 \times 10^8$, $\sqrt{area}$ = 29.2 (μm), $\sqrt{area}'$ ($\sqrt{area + ODA}$) = 55.3 (μm)

Specimens having longer lives have a lager ODA[2]. Specimens with lower hydrogen content have a smaller ODA at the same number of cycles and it is presumed that lower hydrogen content retards the growth of ODA (Fig.2).

Direct evidence of hydrogen trapped by inclusions at fracture origin is shown by SIMS (Secondary Ion Mass Spectrometry) method[3]. Another evidence of influence of hydrogen is revealed by etching the vicinity of inclusions at fracture origins for the specimens with different hydrogen content. The specimens having high hydrogen content have a large darkly etched area and lower hardness beside inclusions [4](Fig.3).

Figure 4 shows an indirect evidence of hydrogen effect on crack growth. It is presumed that when the size of ODA exceeds a critical value, the fatigue crack growth without the influence

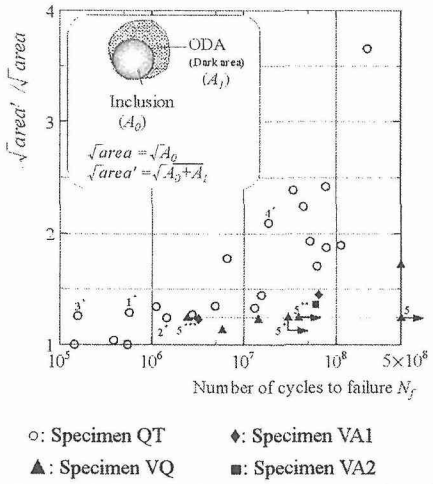

Figure 2 The relationship between the size of ODA and the cycles to failure (SCM435) [2].

Heat treatment	QT			VQ		
Hydrogen	0.7~0.9ppm			~0.01ppm		
σ (MPa)	682	681	560	600	634→886	540
N_f	5.40×10^5	1.55×10^7	2.17×10^6	1.43×10^7	1.00×10^8 →9.49×10^8	4.97×10^9
$\sqrt{area}$ (μm)	48.7	27.6	15.7	55.6	20.9	35.4
$\sqrt{area}'$ (μm)	48.7	39.6	57.4	67.8	26.4	60.6
(a) Fracture surface at fracture origin			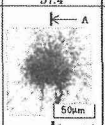	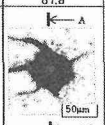	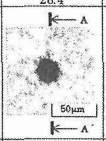	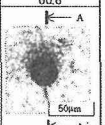
(b) Cross section A-A′ of (a) Etched with			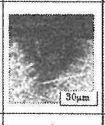	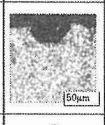		
Mark	○	□	△	●	◆	▼

σ: Stress amplitude. N_f: Number of cycles to failure. $\sqrt{area}$: Inclusion size. $\sqrt{area}'$: Inclusion size + ODA size.
QT: Heat treated in a RXgas followed by quenching and tempering. VQ: Heat treated in a vacuum followed by quenching

Figure 3 Different features revealed by etching the vicinity of inclusions at fracture origins of specimens containing different hydrogen content (SCM435) [4].

of hydrogen starts and the threshold stress intensity factor range ΔK_{ODA} at this stage coincides with ΔK_{th} for small cracks.

The fatigue design method for ultralong life fatigue is proposed based on *the* $\sqrt{area}$ *parameter model* [1], i.e.

$$\sigma_W = C(HV+120)/\left(\sqrt{area}\right)^{1/6}\cdot[(1-R)/2]^{\alpha} \quad (1)$$

, where fatigue limit σ_W in MPa, C =1.56 for subsurface inclusion, C =1.43 for surface inclusion, $\sqrt{area}$: inclusion size in μm, R: stress ratio $\sigma_{\min}/\sigma_{\max}$, $\alpha = 0.226 + HV\times 10^{-4}$

In addition to the influence of internal hydrogen, we must note the influence of statistical factor of inclusion distribution inside materials. The maximum size of inclusions contained in a specimen depends on specimen size, or so-called control volume of a specimen and number of specimens to be tested, and also on testing methods such as tension-compression or rotating bending. Figure 5 [3] clearly shows the influence of statistical factor and test methods on S -N data [3]. In this case, in terms of control volume testing one tension-compression specimen [3] of Fig.5 is equivalent to testing 300 specimens of Fig.5 in rotating bending [5].

Thus, for estimating the lower bound of scatter of fatigue strength we need to estimate the maximum size of inclusions contained in the total control volume. Inclusion rating by *the statistics of extremes* is available for the prediction of the maximum inclusion [1,6].

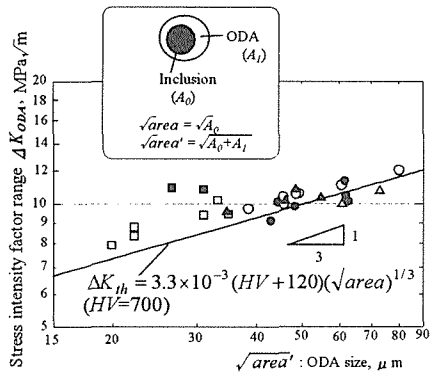

○: Specimen NN(QT) : Quenched and tempered
●: Specimen NN(VQ): Heat treated in a vacuum followed by quenching and tempering
Δ: Specimen NT: Quenched and tempered
▲: Specimen NO: Quenched and tempered
□ ($N_f > 10^6$), ■($N_f < 10^6$): Data by Sakai et al. [7]

Figure 4 Relationship between $\sqrt{area'}$ and ΔK_{ODA} (SAE52100) [8]. $\Delta K_{ODA} = 0.5\Delta\sigma\sqrt{\pi\sqrt{area}}$, where $\Delta\sigma = 2\sigma_a$ for R= -1.

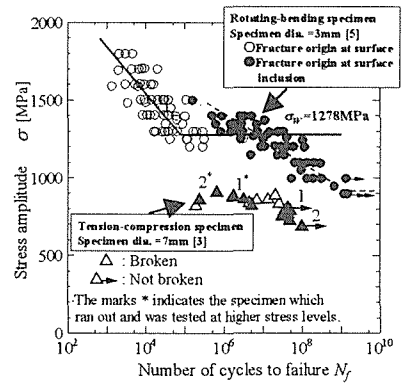

Δ: Specimen QT: Quenched and tempered
▲:Specimen VQ: Heat treated in a vacuum followed by quenching and tempering

Figure 5 Variation of S-N data by loading types and specimen sizes (SAE52100) [3]

Reference list

[1] Murakami, Y. Metal Fatigue: Effects of Small Defects and Nonmetallic Inclusions, Elsevier Ltd., Oxford (2002).

[2] Murakami, Y., Nomoto, T. and Ueda, T., Fatigue Fract. Engng. Mater. Struct. 22 (1999) pp.581-590.

[3] Murakami, Y., Yokoyama, N. N. and Takai, K., J. Soc. Mater. Sci. Japan (2001) pp.1068-1073.

[4] Ueda, T. and Murakami, Y., to be submitted.

[5] Sakai, T., Takeda, M., Shiozawa, K., Ochi, Y., Nakajima, M., Nakamura, T. and Oguma, N., J. Soc. Mater. Sci., Japan, 49-7 (2000) p. 779.

[6] Murakami, Y., J. Research of National Institute of Standards and Technology, Vol. 99, No1 (1994) pp. 345-351.

[7] Sakai, T., Satou, Y. and Oguma, N. (2001) *Trans. of the Japan Society of Mechanical Engineers*, A, **67**-664, p.1980.

[8] Nagata, J. and Murakami, Y., to be submitted.

1500-MPa-Plus-Class Martensitc Steel

-Creation of Martensitic Microstructures with High Resistance against Giga-Cycle Fatigue-

Saburo Matsuoka
Evaluation Research Group,NIMS, Japan

1. Introduction

As one subject of "Ultra steel project", 150K task force has been studying on 1500-MPa-plus-class high strength steels since April 1997. The material creation group has been creating the new martensitic microstructure with the high resistance against delayed fracture and giga-cycle fatigue. The evaluation group has been developing the new evaluation method of delayed fracture and accelerated testing technique for giga-cycle fatigue. In addition, 150K task force involves the nanotechnology group. The guideline principles of material creation were born from the microstructure analysis by an AP-FIM, AFM and TEM and from the nanoindentation by an ultra-micro hardness tester. The achievements of giga-cyle fatigue will be described in the following.

2. Double fatigue strength

Fig. 1 shows the research targets of giga-cycle fatigue. When the tensile strength, σ_B, is lower than 1200 MPa, the surface-type fracture occurs and fatigue limit, σ_w, is given by $\sigma_w=0.5\,\sigma_B$ for various martensitic steels. When $\sigma_B<1200$ MPa, the fish-eye-type fracture occurs and fatigue limit saturates. Therefore, the first target is to insure $\sigma_w=0.5\,\sigma_B$ by clearing of the fish-eye-type fracture. The second target is to realize $\sigma_w>0.5\,\sigma_B$.

There is an inclusion such as Al_2O_3 at the fish-eye-fracture site. Recently, Murakami and others [1] found that optically dark area, ODA, was formed around the inclusion and suggested that ODA could be the area where the hydrogen embrittlement crack propagates. We demonstrated from the nanoindentaion results of inclusions in high strength steels that the fish-eye-type fracture is dominated not only by the size of inclusion but also by its mechanical properties[2]. In the recent steel making process, the inclusion is controlled as to reduce both the size and mechanical properties.

Accordingly, the following principles are established to clear of the fish-eye-type fracture and to improve the fatigue strength. (1) Applying the inclusion-control technique reduces the stress concentration of the inclusion. (2) Modified-ausforming strengthens the base metal against the hydrogen embrittlement and clears of ODA around the inclusion. 150K task force has proven that modified-ausforming improved the delayed fracture properties.

Inclusion-controlled SUP12 steel was modified-ausformed at the conditions of 1118 K x 30 minutes, 30 % reduction at 1027 K and water cooling, and tempered at 703 K x 60 minutes. The tensile strength was 1742 MPa. Fig. 2 shows that Fish-eye-type fractures still occurred for the modified-ausformed steel[3]. The fatigue limit, σ_w, at 10^8 cycles was, however, higher than the expected one from $\sigma_w=0.5\,\sigma_B$ for the surface-type fracture. This means that the first target in Fig. 1 is achieved, even though the fish-eye-type fracture occurs.

The fatigue limit is, furthermore, estimated to be 1120 MPa for the modified-ausformed steel in Fig. 2, if fish-eye-type fractures are cleared. The fatigue limit is almost double, as compared with the limit of about 600 MPa for the quench-tempered steel. Since the double fatigue limit corresponds to $\sigma_w=0.62\,\sigma_B$, it is expected that the second target of $\sigma_w>0.5\,\sigma_B$ will also be achieved.

3. Accelerated fatigue testing

Giga-cycle fatigue test up to 10^9 or 10^{10} cycles is required to determine the fatigue limit for the fish-eye-type fracture. The giga-cycle fatigue test, however, take a long time: 10^9 and 10^{10}-cycle tests take 3 months and 3 years, respectively, using conventional fatigue testing machines with a frequency of 100 Hz. Recently, high-speed fatigue testing machines have been developed, including ultrasonic and high-speed servohydraulic machines. A 10^{10}-cycle fatigue test can be completed in 10 days or 3 months, respectively, using an ultrasonic (20 kHz) or high-speed servo-hydraulic (1 kHz) machine.

Giga-cycle fatigue tests at 100 Hz, 600Hz and 20 kHz were conducted for 433-K-tempered

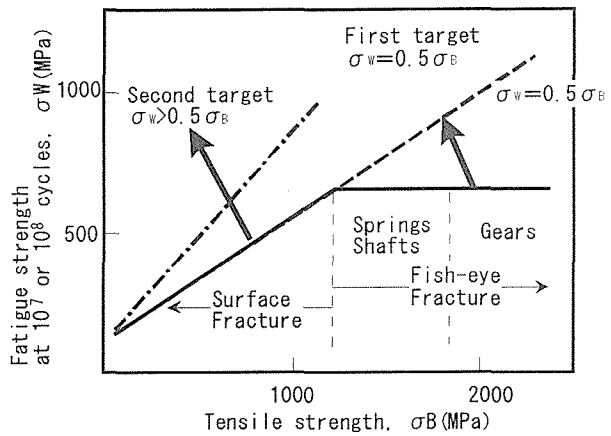

Fig. 2 Research targets of giga-cycle fatigue for1500-MPa-plus-class martensitic steel.

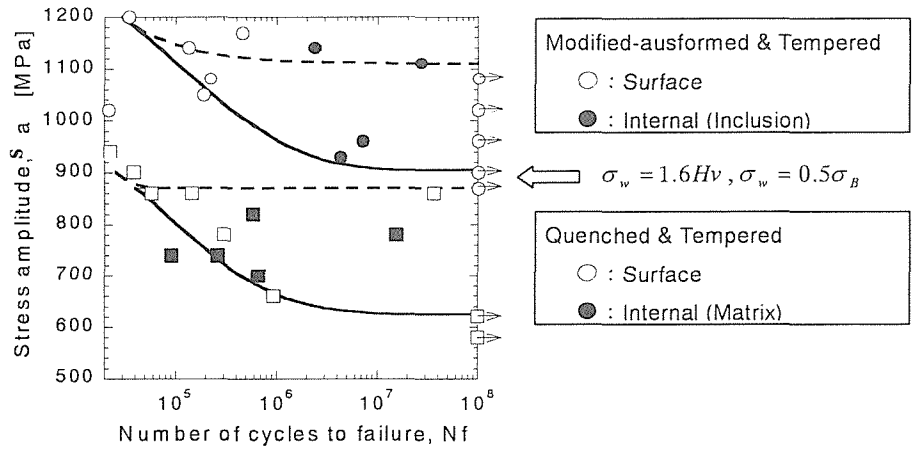

Fig. 8 S-N properties for modified-ausformed SUP12 steel.

SNCM439 steel [4]. The breaks in almost all the specimens were caused by internal Al_2O_3 inclusions leading to fish-eye-type fractures. The inclusion sizes were 9 – 82 μm in $\sqrt{}$area. Modified S-N curves were obtained In order to clarify the effect of inclusion sizes on fatigue lives. $\sigma_w' = 1.56 (HV+120)/(\sqrt{}area)^{1/6}$ is the fatigue limit in the case of fish-eye-type fracture, which was estimated by applying Murakami's equation. HV is Vickers hardness in kgf/mm^2 and $\sqrt{}$area is the inclusion size of the fracture origin in μm. The modified S-N diagram shows two instructive results. The one is that the fatigue limit clearly appears in the modified S-N diagram between 10^9 and 10^{10} cycles. The other is that fatigue lives and the fatigue limits are independent of frequency. The latter result suggests that the giga-cycle fatigue damage, especially the formation of ODAs is not a simple hydrogen embrittlement process and that the interaction between hydrogen embrittlement and fatigue damage processes could be important to understand the giga-cycle fatigue.

4. Summary

I believe that we found a new field for giga-cycle fatigue in the 1800-MPa-class martensitic steel. Our next target is the 2000-MPa-plus-class martensitic steel for springs, bearings and others.

Reference

[1] Murakami T, Nomoto T and Ueda T, Fat. Fra. Eng. Mat. Struct., 1999:22:581.
[2] Nagasima N, Matsuoka S and Miyahara K, Trans Jap. Society Mech. Eng. 1999:65A:447
[3] Sawai T, Kimura Y, Tsuzaki K, Takeuchi E and Matsuoka S, Trans Jap. Society Mech. Eng.2002:68A:49
[4] Furuya Y, Matsuoka S, Abe T and Yamaguchi K, Scripta Matetialia 2002:46:157

The fatigue behaviors of fine grained high strength alloy structural steels

S. X. Li[1], Z. G. Yang[1], W. C. Yu[1], Z. X. Yin[1], G. Yao[1], G. Y. Li[1],
Z. M. Chu[2], M. Q. Wang[3], W. J. Hui[3], H. Dong[3] and Y. Q. Weng[3]
1. Shenyang National Laboratory for Materials Science, Institute of Metal Research, Chinese Academy of Sciences, Shenyang 110016, China
2. Beijing Research Institute of Mechanical and Electric Technology, Beijing 100083, China
3. Central Iron and Steel Research Institute, Beijing 100081, China

Abstract

To develop the 1400-1500 MPa high strength steels with better anti-delayed fracture resistance and higher fatigue strength, the medium carbon alloy structure steels were prepared by modifying the commercial 42CrMo steel. The modified steel is referred as ADF1 in which the small quantities of V and Nb were added. Under conventional heat treatment, the prior austenite with fine grain size of about 8 μm was obtained; under the treatment of high electric current density pulse the fine grain sizes of 1.7-4 μm were obtained(Fig. 1). The 0.2% proof stress and ultimate tensile strength of ADF1 steel are as high as 1315-1465MPa and 1400-1540 MPa respectively. The strengths of these steels are much higher than the commercial 42CrMo steel that with proof stress of around 1080MPa and ultimate tensile strength of around 1180MPa under quenching and tempering. The elongation and reduction in area of ADF1 are about 13-15and 53-55 percent respectively which is close to the corresponding values of commercial 42CrMo steel.

The fatigue strengths σ_{-1} of smooth bar and σ_{-1N} of notched bar were tested for these steels under rotating bending at 10^7 cycles. The up-and-down method was adopted to determine the fatigue strength(Fig. 2). The results are summarized in Table 1. It is found that the steel with medium grain size(4μm) has the highest ultimate tensile σ_b (1540MPa)and fatigue strength σ_{-1} (767MPa). The fatigue strength σ_{-1} is about 1.6 times as high as the fatigue strength of conventional 42CrMo steel(485MPa). However, the notch sensitivity on fatigue strength is rather greater than the other two cases.

The shape and size of microstructures such as prior austenite, martensitic lath, carbides as well as the inclusions were studied. The effects of these microstructures on mechanical properties, particularly, the inclusions on the fatigue behavior were discussed.

At present, the bolt for automobile was made by ADF1 under ADF1-I heat treatment. It has been installed on the automobile and successfully passed the testing on sites. If the sizes of the inclusions of ADF1 steel can be reduced further, a type of exceptional high strength steel bolt with prior austenite sizes of 2-4 μm could be produced and applied on automobile

industry.

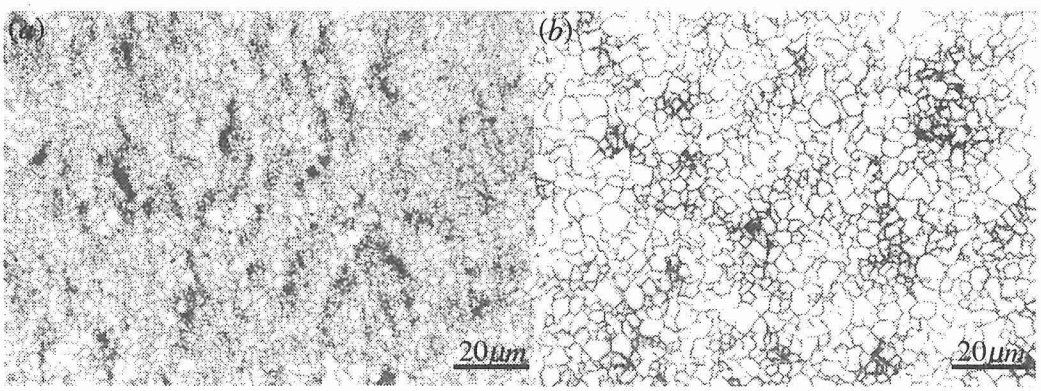

Figure1. The prior austenite grains under (a)ADF1-III and (b)ADF1-II heat treatment procedures

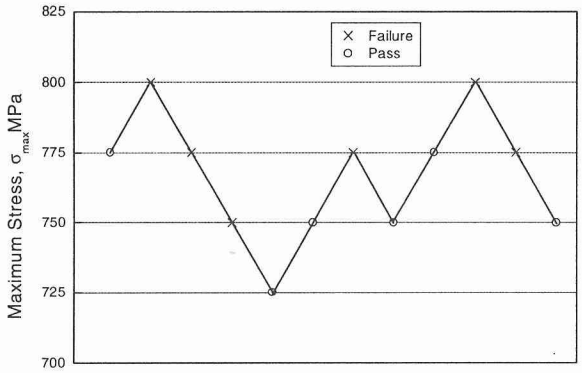

Figure 2. The up-and –down method to determine the fatigue strength (σ_{-1}=767MPa, S=18.8MPa) of ADF1 under heat treatment of ADF1-II

Table 1. The properties of ADF1

Heat treatment	Grain size μm	$\sigma_{0.2}$ MPa	σ_b MPa	σ_{-1} MPa	σ_{-1N} MPa	q	σ_{-1}/σ_b
ADF1-I	8	1315	1400	738±22.3	445±20.4	0.50	0.52
ADF1-II	4	1465	1540	767±18.8	417±10.2	0.64	0.50
ADF1-III	2	1370	1440	745±17.5	425±14.7	0.57	0.51

ADF1-I: 940 °C oil quenching +600 °C tempering
ADF1-II: Electric current pulsing to 920 °C oil quenching +600 °C tempering
ADF1-III: Electric current pulsing to 880 °C oil quenching, repeat to 3 times +600 °C tempering

- Corrosion Control of Infrastructure
- New Stainless Steels
- Surface Modification and Surface Treatment
- Novel Methods in Surface Analyses

(Room 406)

Prevention of Chloride-Induced Corrosion Damage to Bridges

S. D. Cramer, B. S. Covino, Jr., S. J. Bullard, G. R. Holcomb, J. H. Russell, Margaret Ziomek-Moroz, Albany Research Center, USDOE, Albany OR USA 97321
Y. P. Virmani, Turner-Fairbank Highway Research Center, FHWA, USDOT, McLean VA USA 22101-2296
J. T. Butler, Joseph T. Butler, Inc., Wadsworth OH USA 44282
F. J. Nelson, Oregon Department of Transportation, Salem OR USA 97310
N. G. Thompson, CC Technologies, Dublin OH USA 43016-8761

According to the National Bridge Inventory Database, there are approximately 600,000 bridges in the United States[1]. Half of these were built between 1950 and 1994. The vast majority built since 1950 are reinforced-concrete (RC) and steel bridges, both of which can undergo significant deterioration due to chloride-induced corrosion. During the period 1992-1999, between 15% and 20% of all bridges in the US were listed as "structurally deficient," that is, they can no longer sustain the loads for which they were designed[2]. As older bridges are replaced or rehabilitated, there is a trend of decreasing number and percentage of structurally deficient bridges while, over the same period, the number of bridges in the inventory rose by about 13,000. The 1998 bridge inventory data are presented in more detail in Table 1[3]. Of the three predominant materials of construction, the highest percentage of structurally deficient bridges were steel, followed by conventional RC and prestressed concrete.

Table 1. Structurally deficient bridges in 1998 based on material of construction.

	CONVENTIONAL RC	PRESTRESSED CONCRETE	STEEL	OTHER	TOTAL
Bridges in Inventory	235,151	107,666	200,202	40,395	583,414
Structurally Deficient	21,164	3,230	54,054	14,671	93,119
% Deficient	9	3	27	36	16

The cost to replace aging bridges increased by 12% from 1995 to 1999. In addition, there has been a significant increase in the required maintenance. Many prestressed concrete bridges will require maintenance in the next 10 to 30 years. Significant maintenance, repair, rehabilitation, and replacement activities for the nation's highway bridge infrastructure are foreseen over the next few decades before current construction practices reverse the trend.

A recent Federal Highway Administration (FHWA) report by Koch et al. estimated the annual direct cost of corrosion to the entire U.S. economy to be $276 billion[4]. The annual direct cost of corrosion for the bridge infrastructure was $8.3 billion[4]. The total estimate cost to replace structurally deficient bridges was $29.3 billion, annualized over a 10 year period to be $3.8 billion. The estimated annual direct life-cycle corrosion costs for non-deficient bridges, including construction, maintenance, patching, rehabilitation, cathodic protection, and cost of capital, are: (1) bridge decks – $1.1 to $2.9 billion; (2) substructure and superstructure (minus decks) -- $1.1 to $2.9 billion; (3) steel bridge maintenance painting – $0.5 billion. For "average" bridges using somewhat less than best maintenance practices this yields an estimated annual direct life-cycle cost of $4.5 billion. Estimated annual indirect costs to the user due to traffic delays and lost productivity are more than 10 times the $8.3 billion direct cost of corrosion.

Existing RC Bridges in Severe Environment: Problems develop in RC bridges when salt diffuses into the concrete, raising the salt concentration at the reinforcing bar-concrete interface above a threshold level for corrosion initiation, about 0.74 kg Cl/m^3 for black iron bar[5]. The passive film normally present on the reinforcing bar breaks down above this concentration, reducing the pH and initiating corrosion. The iron oxide reaction products formed by corrosion are substantially higher in volume than the iron consumed by corrosion, leading to tensile forces that crack the concrete, causing delamination of the cover concrete, and structural deterioration of the bridge. Cathodic protection (CP) is one of the most effective means for controlling corrosion damage in RC bridges. Oregon uses

conductive coating anodes on the concrete in CP systems to prevent further corrosion damage of coastal RC bridges. Total installed conductive coating anode area in Oregon is 81,000 m^2. Most of this area uses thermal-sprayed (TS) zinc anodes. Other anodes used are TS titanium, TS Al-Zn-In, zinc(Zn)-hydrogel, and solvent-based acrylic carbon paint. Effective current distribution to the reinforcing bar is achieved in complex structures while preserving the bridge external appearance. Acidification of the anode-concrete interface may reduce the anode bond strength to the concrete. In Oregon, TS zinc anodes have been used for 10 years and are expected to have a 25-year service life base on bond strength, while the carbon paint anode has served effectively for over 15 years.

New RC Bridges in Severe Environments:

Epoxy-coated reinforcing bar – Fusion-bonded epoxy-coated rebar (ECR) has been used in approximately 20,000 RC bridge decks and 100,000 total structures in the US. Superior performance is achieved in bridge decks when both mats are ECR compared to decks using only a top ECR mat. The use of an adequate, good quality, concrete cover; finishing and curing of the concrete; and the proper manufacturing and handling of ECR complement the use of ECR in providing effective corrosion protection for concrete bridge decks. AASHTO and ASTM specifications continue to evolve to improve the performance of ECR in RC bridges. Compared to black steel, the cost premium in new construction using ECR in both mats of bridge decks is about 1%.

Stainless steel reinforcing bar – Austenitic and duplex stainless steels have been shown in Oregon to provide an acceptable combination of corrosion resistance, yield strength, availability, and cost for reinforcing bar in new coastal bridge construction. Stainless steel has been specified for use in corrosion critical areas, such as decks, beams and prestressed girders. Black iron bar may be used in compressive members and is required to be electrically isolated from the stainless steel bar. The chloride corrosion threshold for Type 316 stainless steel (about 18 kg Cl/m^3[5]) is above the highest concentrations measured in Oregon coastal RC bridges in service for up to 70 years. As a result, use of stainless steel reinforcing bar is expected to yield bridge service lives exceeding 120 years with low maintenance requirements. In three new coastal bridge projects costing $21 million total, stainless steel bar added a premium of only 10 % to total project costs, compared to black iron bar.

Concrete – Oregon specifies the use of microsilica concrete in new coastal bridge construction, with a maximum microsilica component of 4 %. Typical concrete cover depths are 50 mm over all reinforcement including shear stirrups, with 76 mm specified for particularly harsh environments.

Steel Bridge Coatings Systems for Severe Environments: Paints are the most widely used material for protecting steel structures from corrosion damage. They create a barrier between the steel and corrodants that can last without maintenance in mild environments up to 20 years, and substantially shorter times in severely corrosive environments. Metalizing with zinc, aluminum, and their alloys produces a long-lasting protective coating that is a barrier to corrodants and also provides a degree of galvanic protection in areas of coatings damage and wear. Metallized coatings may be used as the bare sprayed metal, or as the sprayed metal plus sealer, or as the sprayed metal and sealer plus a paint topcoat. The relatively thick bare metal coating has the longest life-to-first-maintenance. Sealing the coating with no subsequent maintenance of the sealer yields the longest coating service life, the lowest life-cycle cost, and the most economical coating system. Topcoating is used in special circumstances for aesthetic purposes, particularly in public structures such as bridges. The high spray and deposit rates, and portability of today's equipment make metalizing competitive with painting on a first cost basis.

References

[1] H.O. Bonstedt, "A Marketing Approach to Bridge Longevity," Concrete International, Oct. 1998, pp. 65-68.
[2] The Status of the Nation's Highway Bridges: Highway Bridge Replacement and Rehabilitation Program (HBRRP) and National Bridge Inventory, FHWA, Thirteenth Report to the United States Congress, May 1997.
[3] "Rebuilding Our Bridges – Why and How," ASTM Standardization News, pp. 24 – 27, July 1994.
[4] G.H. Koch et al., *Corrosion Costs and Preventive Strategies in the United States*, Report No. FHWA-RD-01-156, Federal Highway Administration, USDOT, Washington D.C., March 2002.
[5] McDonald DB, Pfeifer DW, Sherman MR. *Corrosion Evaluation of Epoxy-Coated, Metallic-Clad and Solid Metallic Reinforcing Bars in Concrete*, Report No. FHWA-RD-98-153, Federal Highway Administration, USDOT, Washington DC, December 1998.

Resource-Efficient Weathering Steels for Uncoated Structures in Coastal Atmosphere

Toshiaki Kodama and Toshiyasu Nishimura
Corrosion Resistant Materials Research Group, NIMS, Japan

1. Introduction

Low-alloy weathering steels resistant to SOx pollution show poor performance in environments where airborne salinity is high. Recent researches on weathering steels have been focused on the rusting mechanism in the presence of chloride and development of new steels that are resistant in marine/coastal environments[1]. The paper focuses on 1) thermochemical aspect of rusting in chloride environments, 2) crystal structure of iron rust in a high salinity condition, 3) electrochemical reaction of rust and its catalytic properties in chloride media, 4) proposal of resource-efficient weathering steels.

2. Rust Formation on Steel in Chloride Media by Laboratory Cyclic Test

Figure 1 shows electrochemical polarization curves for rusted carbon steels after wet-and-dry cyclic test. Potentiostatic polarization curves were obtained in a 0.5% NaCl solution under both aerated and unaerated conditions. Cathodic current increases remarkably with an increase in number of wet/dry cycles[2]. The increase is attributed to the electrochemical reduction of rust rather than dissolved oxygen reduction or hydrogen evolution because of the reasons as follows: 1) Cathodic current increases with an increase in cycle number, or the amount of rust on metal: 2) Cathodic current starts to flow at potentials much nobler than that of hydrogen evolution. Also it should be noted that such an increase in cathodic current occurs only for rust formed in chloride media and only for rusts in contact with steel. Isolated rust shows no such effect on the cathodic reduction. The phenomena suggest that rust formed in chloride media shows specific reactivity in its reduction process, which in turn accelerates anodic reaction of substrate metal.

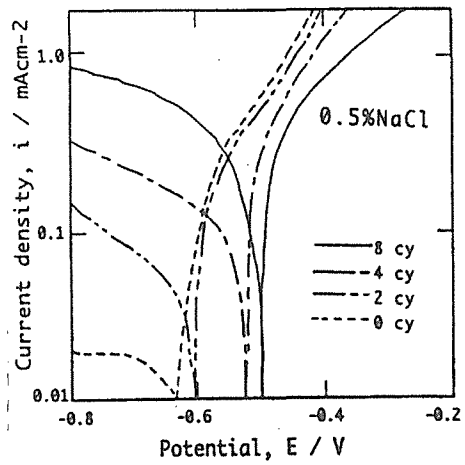

Fig 1. Polarization curves of rusted carbon steels processed by dry/wet method as a parameter of the number of cycles. Cathodic current markedly increases with increasing number of cycles.

Using a new technique named *in-situ* XRD structural change of rust was determined on actually corroding surface of steel in a cycle of wet-and-dry process. The formation of β-FeOOH (akaganeite) and Green rust I (GRI, mixed ferric and ferrous product) is evident in chloride containing atmosphere. The readiness to redox reaction of the metastable products is the principal mechanism of corrosion acceleration by chloride.

3. Effect of Alloying Element

A steel bearing 0.8 mass % Al showed smaller mass loss in wet/dry cycle test than that of carbon steel. The ratio of corrosion loss of carbon steel to 0.8 % Al steel increased with time and it reaches 75 % after 20 cycles. Polarization curves for a carbon steel and 0.8% Al-steel are shown Fig.2. Both samples had been treated 8 cycles in wet/dry corrosion cycle

test before polarization measurements.

EPMA cross sectional analyses showed the enrichment of Al in the inner layer of rust of Al bearing steel, where by transmission electron diffraction the formation of a spinel, suggesting $FeAl_2O_4$ is evident similarly to the case of the Ni-bearing steel [3,4].

Aluminum addition was effective in suppressing cathodic reaction but was not in anodic branch. The XRD analysis proved that β-FeOOH is less abundant in the rust of the Al-bearing steel. Since β-FeOOH is most readily reduced to Fe(II)-state in wet season its suppression is beneficial in decreasing cathodic current. In dry process $FeAl_2O_4$ inhibits the reoxidation to Fe(II)-state in dry process.

Such elements as Mo, W and P are most likely to be incorporated into the rust layer in the form of oxy-anions. These anions are effective in corrosion inhibition either by modification of ion selectivity or by the action of anodic inhibitor. Figure 3 shows the corrosion loss of new low-alloy weathering steels as a function of exposure time in subtropical coastal atmosphere with reference to those of carbon steel (SM) and conventional weathering steels (SMA). In place of Ni such elements as Al, Si and W are found to be the promising alloying additives for the creation of resource efficient weathering steels.

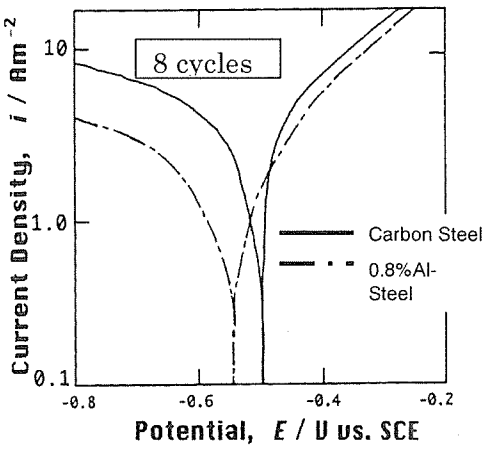

Fig. 2 Polarization curves for an Al-bearing steel obtained after the treatment of 8 cycles of wet/dry corrosion test.

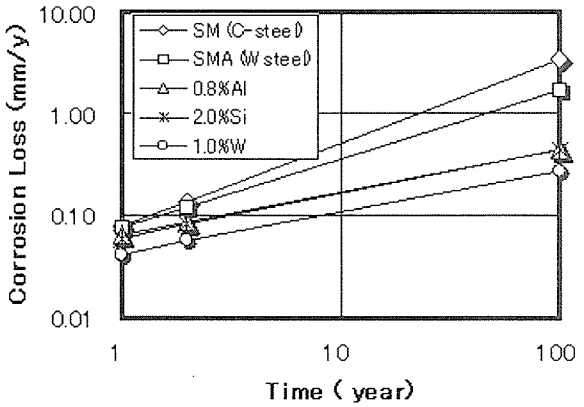

Fig3. Corrosion loss–time relations of new low-alloy weathering steels in comparison with conventional carbon steel(SM) and weathering steel(SMA)

4. Summary

It has been shown that the alloying elements in steel is incorporated into rust either forming double oxide like spinel, substituting Fe ion of FeOOH or Fe_3O_4 or forming iron salt in the form of oxy-anions. In the paper detailed mechanism of the incorporation alloying elements have been investigated and was interpreted by means of thermodynamics, which is expected to contribute much for the designing new low-alloy weathering steels.

References

1) T.Kodama and T.Nishimura: 12th Asian Pacific Corrosion Control Conf. Oct. (2001), Seoul; Proc vol. 2,1358
2) T. Nishimura. K. Kurosawa and T. Kodama: 196th Meeting of the Electrochem. Soc. (1999) paper-458.
3) T. Nishimura, H. Katayama, K. Noda and T. Kodama: Corros. Sci. 42 (2000) 1611
4) T.Nishimura, A.Tahara and T.Kodama: Materials Trans. 42(2001)478 Al

Trend in Low VOC, Environment-Friendly Organic Coatings for Infrastructures

H.Tanabe
Fundamental Research Department
Dai Nippon Toryo Co.Ltd.

1. Introduction

Environmental problems have been increasing through the world and the paint industry and paint application fields have been required to solve the environmental issues by collaboration. Japan Paint Manufacturing Association (JPMA) organized the study group on "Paint industry and global environment" in 1991 for considering how best to approach.

From the aspect of environmental problems in the coating industry, the total process of paint production from the design and manufacturing to the distribution, application and wastes disposal of paints has strong link with environmental protection.

The usage of solvent-reduced type paint has been increasing since 1960's due to the reason of photochemical smog pollution caused by some kinds of volatile organic solvents.

A number of countermeasures against environmental problems has been taken by the Japanese paint industry. : organic tin compound can not be used any more, for example.

However the paint industry still have a lot of environmental items to overcome today such as reducing the emission of organic solvents and reduction of heavy metal ingredient, as well as approaches to save energy together with the treatment and recycling of waste.

2. Trends of regulation

VOC is defined as an organic compound having boiling point between 50℃ and 240℃ to 260℃ according to WHO.

It seems that three regions of USA, Europe and Japan have their own approaches to VOC.

According to EPA(Environmental Protection Agency of USA), VOC is defined as any organic compound that participates in atmospheric photochemical reactions except those designated by EPA as having negligible photochemical reactivity. In Japan, JPMA described the definition of VOC for paint field. It is organic solvent that is emitted in the air with vapor pressure more than 0.01kPa (293.15K) or is volatile under the specific condition when in use, among class 1 designated chemical substances used generally for paint production and described in PRTR regulation. PRTR regulation (Pollutant Release Transfer Register) was established in 1999. Substances which were emitted more than specified amount for one year since January of 2001 are to be reported in June of 2002.

Furthermore, an individual (proper) approach is found in Japan. The study group for the problems of sick house (indoor pollution) organized in Ministry of Environment presented index figures of indoor concentration for 13 substances as of January, 2002. In case of formaldehyde which seemed to be most influent6ial, the figure is 100 μ g/m^3 . The

figure has been used by many organizations as an index.

3. Trend on VOC reduction and technology

VOC is mainly solvent in paint. According to a report,[2)] the production amount of paints was 2.2 million tons in 1990 in Japan and the amount of solvent used was about 0.95 million tons including solvent recovered.

The amount of solvent used by fields application, buildings, cars, electrical appliance, metal product and car repair was compared and put in order.

The highest ratio of solvent to paint was car repair, the new car, electrical appliance and metal production in order.

Solvent reduction ratio was calculated estimating from Scenario 1 and Scenario 2.

Scenario 1 is the case that applies technology for reduction without excess cost.

Scenario 2 is the case that applies high or future technology for reduction without cost consideration.

Total reduction rate were estimated 25% in case of Scenario 1 and 50 % , Scenario 2.

There are three technical approaches for reducing VOC.

(1) High solid paint (low VOC)
(2) Woter born paint(low VOC)
(3) No solvent paint(VOC free)

Improvement of application efficiency in coating process leads the reduction of VOC.

4. Conclusion

Nowadays environmental protection is indispensable issue, especially for the chemical industry. Because of this, it is very important for paint producers and applicators to reduce VOC. So the paint industry should make a best effort to do it.

References

(1) Report on the present and the future state of VOC in the Japanese paint industry JPMA, (1993)
(2) The annual investigation of actual situation on paint manufactures in Japan JPMA (1998)
(3) Council Directive 1999/13/Ec, OJC,29.3.(1999)

Nano-Structure of Protective Rust Layer on Weathering Steel Exposed in Nation-Wide Environments in Japan

M. Yamashita, H. Konishi*, J. Mizuki* and H. Uchida

Graduate School of Engineering, Himeji Institute of Technology, Hyogo 671-2201, Japan

* Synchrotron Radiation Research Center, Kansai Research Establishment, Japan Atomic Energy Research Institute, Hyogo 679-5143, Japan

1. Introduction

It is well known that the so-called "protective" rust layer formed on weathering steel has strong protective ability for atmospheric corrosion of the steel. The study of rust layers formed on steels and their control has been the principal theme in the field of atmospheric corrosion, since the rust layers have certain beneficial effects on the prevention of degradation of the steels. In the present research, we examine the nano-structure of the protective rust layer on weathering steel exposed for 17y in nation-wide environments in Japan by using X-ray diffraction (XRD) and X-ray absorption fine structure (XAFS) analysis techniques and Mössbauer spectroscopy.

2. Experimental procedure

Rust layers examined were formed on weathering steel (0.61Cr-0.36Cu-0.22Ni-0.008P) exposed horizontally to atmosphere underneath the girders of 5 bridges for 17 years in the main island of Japan. Rust samples were removed from the skyward surface by a razor until the steel surface appeared, and then ground into powder. The powdered samples were characterized by means of XRD, XAFS and Mössbauer spectroscopies. In order to quantify the rust constituents comprising goethite, γ-FeOOH, β-FeOOH, Fe_3O_4 and the X-ray amorphous substances, ZnO powder was employed as an internal standard for XRD and relative recoilless fraction of each oxide was considered for Mössbauer spectroscopy. XAFS spectra of the rust sample were taken around the Fe K-edge and Cr K-edge X-ray energies at Photon Factory synchrotron radiation facility.

3. Results and discussion

XRD spectra of the rust samples indicated that the X-ray detectable rust constituents were goethite, β-FeOOH and small amount of γ-FeOOH and Fe_3O_4. Total amount of γ-FeOOH and Fe_3O_4 was less than a few percent. After the quantitative determination, it was shown that the rust layers contained a large amount of the X-ray amorphous substance. The fit of the hyperfine parameters [1] of iron oxides and oxyhydroxides to the Mössbauer spectra of the rust samples revealed the mass fraction of each oxyhydroxide.

Figure 1 shows the mass fractions of ultrafine Cr-goethite which corresponds to the X-ray amorphous substance with the crystal size less than 15nm, Cr-goethite and β-FeOOH in the rust layer as a function of the salt content in atmosphere. In the range of low salt content, the rust layers were composed mainly of ultrafine Cr-goethite. Mass fractions both of ultrafine Cr-goethite and Cr-goethite showed their maximum at 0.04mdd, but it decreased and β-FeOOH increased in the higher salt content. The protective rust layer, comprising the X-ray amorphous substance and/or the goethite type phase, is believed to possess the structure of α-(Fe_{1-x},Cr_x)OOH, Cr-goethite [2]. Thus, maximum amount of Cr-goethites at 0.04mdd implies high protective performance of the rust layer.

It was demonstrated that the increase in Cr concentration in the Cr-goethite results in dense aggregation of small crystals, that provides high protective ability of the protective

rust layer for atmospheric corrosives, and provides cation selectivity[3], that impedes the penetration of aggressive corrosive anions such as Cl^- and SO_4^{2-}. It is necessary to elucidate the nano-structure, and thus the atomic arrangement, of the Cr-goethite because the protective performance is controlled by the structure of the Cr-goethite. Especially, Cr site in goethite structure is very important to discuss the role of Cr on the protective performance of Cr-goethite. The structural unit of goethite crystal is an $FeO_3(OH)_3$ octahedron where each Fe^{3+} is surrounded by three O^{2-} and three OH^-. The network of the octahedra gives the goethite structure. Double chains of the octahedra formed by edge-sharing run parallel to the [001] direction. These chains are linked to adjacent double chains by corner-sharing, which leads to the orthorhombic symmetry. Therefore, the goethite structure consists of double chains of octahedra alternating with double chains of vacant sites [4]. By considering a spatial site in the network of octahedra, the possible sites for Cr^{3+} in the goethite structure are considered to be two; one is the substitutable Fe^{3+} site and the other is in the double chains of vacant sites.

Figure 2 shows the Fourier transform, i.e., radial structure function (RSF), of the Cr K-edge extended x-ray absorption fine structure (EXAFS) spectrum of the rust layer formed under salt content of 0.041mdd, and those of the Fe and Cr K-edge EXAFS spectra of the artificial 3mass%Cr-goethite. The Fourier transform is not phase-corrected. It is said that Cr^{3+} is coordinated with O^{2-}. In addition, it should be noted that less correlation was obtained above 0.20 nm in RSF around Cr^{3+}, compared with RSF around Fe^{3+} in the artificial Cr-goethite. The nearest neighbour Fe-Fe distance appears as the double peak in RSF around Fe^{3+} in the artificial Cr-goethite. Then, if Cr^{3+} substitutes for the Fe^{3+} lattice site in the goethite structure, clear strong peaks due to the nearest neighbour Fe^{3+} or Cr^{3+} should be observed above 0.20 nm in RSF around Cr^{3+}. Therefore, the experimental results suggest that Cr^{3+} can be located in the double chains of vacant sites in the Cr-goethite in the rust layer. Thus we can say that Cr^{3+} in Cr-goethite in the rust layer can be positioned in the double chains of vacant sites with coordinating O^{2-}. This Cr^{3+} site can explain dense aggregation of small crystals and cation selectivity of Cr-goethite.

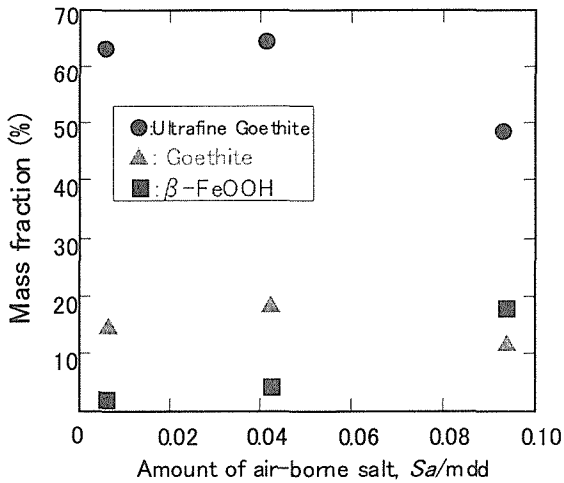

Fig.1 Mass fractions of ultrafine goethite (<15nm), goethite (>15nm) and β-FeOOH onthe skyward surface of weathering steel exposed holizontally as a function of amount of air-borne salt

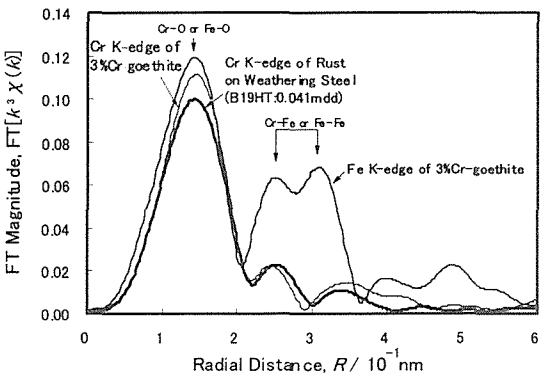

Fig.2 Fourier transform of the EXAFS spectrum, i.e., radial structure function, of the rust layer of the weathering steel at Cr K-edge and those of the artificial 3mass%Cr-goethite at Fe and Cr K-edges measured by using PF synchrotron radiation X-rays.

Public Works Research Institute, Japan Association of Steel Bridge Construction and The Japan Iron and Steel Federation are acknowledged for supplying precious samples.

References

[1] Yamashita, M., Misawa, T., Townsend, H.E. and Cook, D.C., J. Japan Inst. Metals, 64 (2000), No.1, pp. 77-78.

[2] Yamashita, M., Miyuki, H., Matsuda, Y., Nagano, H. and Misawa, T., Corros. Sci., 36 (1994), No.2, pp. 283-299.

[3] Yamashita, M., Miyuki, H., Nagano, H. and Misawa, T., Proc. 13th International Corrosion Congress, Melbourne, (1996), pp.258-264.

[4] Cornell, R.M. and Schwertmann, U., *The Iron Oxides*, VCH, Weinheim, (1996).

Characterization of Nanostructure of Rusts Formed on Weathering Steel

M.Kimura[1*], T.Suzuki[1], Y.Ikematsu[1], G.Shigesato[1], S.Suzuki[1,3] and H.Kihira[2]
[1]Adv. Tech. Res. Labs., [2]Steel Res. Labs., Nippon Steel Corporation, Japan
[3](Present)Inst. of Multidisciplinary Res. for Adv. Mater., Tohoku Univ., Japan
*kimura@re.nsc.co.jp

1. Introduction

Improvement of the corrosion resistance of steel without coating is very important from the viewpoint of life-cycle assessments of materials. A protective rust layer is known to form on the surface of steel by adding small amounts of chromium and copper are added [1]. This steel is called weathering steel and can be used as structural materials without coating. The rusts formed on weathering steel is composed of very fine grains which is believed to attribute to high corrosion resistance compared to conventional mild steel. However, the mechanism of formation of fine grains has not been fully understood mainly because of experimental difficulties to obtain the structure information of the rusts.

The rust mainly consists of iron oxyhydroxide; the structure of crystalline α-FeOOH is shown in Fig.1. The structure is composed of FeO_6 octahedrons, and they are connected by sharing of "edge" and/or "corner". The arrangements of FeO_6 in rusts are largely effected by corrosion conditions, and nano-scale information on the structure is essential to understand the mechanism of rust formation. In this work, x-ray absorption fine structure (XAFS) analysis and transmission electron microscopy (TEM) were used for characterizing the atomic structure and microstructure of rusts formed on weathering steel. A new concept of "$Fe(O,OH)_6$ network structure" in rusts is presented, which is the key to understand the mechanism of rust-formation with high corrosion resistance .

2. Experimental

A weathering steel (WS) and an Fe-5 mass % Cr alloy (CR) were exposed to various corrosion conditions. Rusts formed on the surface of specimens were analyzed by XAFS, which can determine the radial distribution function (RDF) of neighboring atoms around a specific kind of atom. RDF around iron and chromium were measured to make clear the arrangement of FeO_6 octahedrons and the effects of chromium as one of the additional elements. XAFS measurements were carried out for colloidal rusts in water as well as dried rusts to understand the formation mechanism. XAFS measurements were performed at beam lines BL-12C [2] at the Photon Factory, KEK, Tsukuba, Japan.

The microstructure of rusts was observed by field-emission transmission electron microscopy (TEM) for samples sliced using focused Ga ion beams. Electron energy loss spectroscopy was also measured to obtain the local structure.

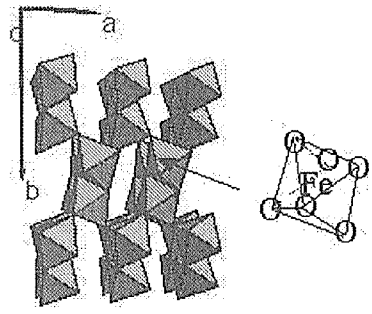

Fig.1 Atomic structure of crystalline α-FeOOH

3. Results & Discussion

TEM observation has shown that an inner layer in the rust is composed of very small crystallites (5-25nm) which can mainly be assigned to that of α-FeOOH. Much clearer enrichment of chromium was observed in finer grains than in larger grains. It is expected that fine grain size affects the crystal structure of the rust and that the chromium is deeply related to it.

Then the structure was analyzed by XAFS measurement, which is powerful for nano-crystal or amorphous specimens. Figure 2 shows RDF obtained by Fourier

transformation of Fe and Cr K-edges XAFS spectra: rusts formed on the specimen CR dipped in sea water for 2 weeks (CR2W) and exposed to air indoors for 15 years (CR15Y). XAFS spectra were measured rusts in water for CR2W(WET) and in air for the others. By comparing RDF's of the rusts with the crystalline α-FeOOH (STD-α), it is shown the first peaks located at about 0.15 nm in the RDF's are attributed to the first nearest neighbor (1st NN) correlation of Fe-O. The peaks at about 0.27 and 0.32 nm in RDF's correspond to the second (2nd NN) and the third nearest neighbors (3rd NN) correlation of Fe-Fe and Fe-O, respectively. The fact that the 1st NN peaks in the RDF's of all rust sample are as high as that of crystalline α-FeOOH(STD-α) indicates the formation of octahedron $Fe(O,OH)_6$ units at the very early stage of corrosion. In the process of corrosion, the $Fe(O,OH)_6$ units developed and forms "$Fe(O,OH)_6$ network structure" as shown by the peaks of 2nd NN and the 3rd NN. However, their heights are weaker than those in α-FeOOH, suggesting that the periodic arrangement of $Fe(O,OH)_6$ units in the network is distorted and/or disordered (Fig.3).

RDF around Cr for CR2W(WET) shows the effects of chromium addition. Chromium also forms $Cr(O,OH)_6$ octahedrons, as shown by the clear peak observed in the 1st NN peak of the RDF. However, the atomic distance observed in the 2nd NN peak corresponding to Cr-Fe correlation, about 0.23 nm, is smaller than the value observed in peaks of Fe-Fe correlation in the RDF's of α-FeOOH and the actual rust, about 0.27 nm. These results indicate that the $Cr(O,OH)_6$ units cause the large distortion or disorder in the "$Fe(O,OH)_6$ network structure" .

Further consideration on the formation mechanism is presented in the terms of kinetics of electro-chemical reaction based on the experimental results

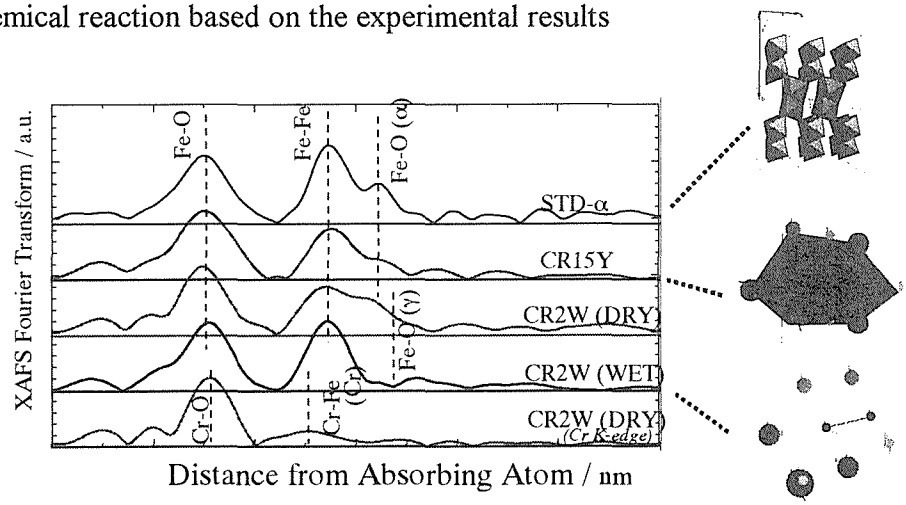

Fig. 2 RDF around Fe and Cr of rusts formed on the specimen and a crystalline α-FeOOH.

4. Conclusion

It has been shown that the difference of "$Fe(O,OH)_6$ network structure" is the key for the formation of rusts with high corrosion resistance. The chromium addition caused the deformation of the network structure, resulting in fine grains.

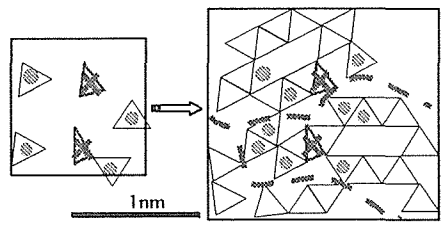

Fig.3 Schematic diagram of development of "$Fe(O,OH)_6$ network structure".

References

[1] C. B. Larabee and S. K. Coburn, Int. Congress on Metallic Corrosion, London, U.K., 1962, pp.276.
[2] M. Nomura, J. Synchrotron Rad. 5(1998), pp.851.
[3] M. Kimura et al, J. Japan Inst.Metals 66(No.3)(2002) (in print).

Computer Aided Corrosion Prediction for Durability Design of Weathering Steel Structures

Hiroshi KIHIRA
Nippon Steel Corporation, Steel Research Laboratories, Japan

1. Introduction

Weathering steel is applicable to minimum maintenance structures based not on the *Antei-Sabi Concept*, but on the *Durable State Concept* [1,3,6]. Computational software for corrosion prediction of weathering steels in variety of environmental conditions was developed using the latter concept. As a demonstration, corrosion loss of 3Ni weathering steel is projected for 100 years to assess a probability to achieve *durable state*.

2. Durable state concept for weathering steel bridges with semi-eternal service life

In Japan, conventional JIS-SMA type of weathering steel is applicable to the environment in which less than 0.3mm corrosion loss per side is expected for 50 years of exposure duration [2]. Such environment corresponds to the value of air-born salt deposition rate less than 0.05 mg-NaCl/dm^2/day (mdd). It is important to recognize that fifty years does not mean a bridge life, 0.3 mm of corrosion loss does not define the criteria of structural stability. Japanese authoritative guidelines for steel bridge design revised just recently, clearly states that degradation of bridge members to occur in prolonged period of time must be taken into account at the design stage to realize long term structural durability. In fact, this is one of the largest changes in paradigm of steel bridge technologies in Japan, since no clear explanation about corrosion of steel members was stated in the previous guidelines. It was most likely that essential message within "the *Durable State Concept* [1]" proposed by Rust Chemistry Committee in Japan Society of Corrosion Engineers was accepted. The indefinite word, "*Antei-Sabi* (magic rust to let corrosion rate be zero)," no more exists in the revised authoritative bridge design guide lines, while unpainted weathering steel is recognized to be applicable because of its slow corrosion rate. Durable state is defined as a condition in which corrosion rate of weathering steel is slow enough not to form anomalous rust[1,3]. As far as weathering steel is used in the environments in which corrosion loss is to be less than 0.5mm per side for 100 years of exposure, the durable state is to be established. It is also assessed that this level of penetration is too minute to affect stability of steel structures [3], so that semi-eternal service life may even be possible.

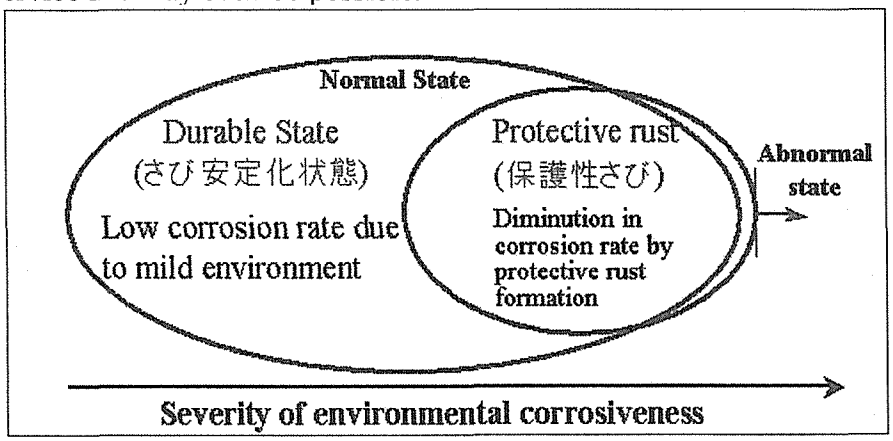

Fig.1 Schematic representation of the Durable State Concept.

3. Computational corrosion prediction to assure durability of weathering steels.

In order to achieve durable state, conventional (JIS-SMA) weathering steel is applicable

in the environmental condition where salt deposition rate is less than 0.05 mdd [2]. However, recently commercialized 3Ni weathering steel [4] may be applicable to much severer environments. Also, surface treatment to reduce corrosion rate [5] may be helpful to enhance durability of weathering steel bridges as assessed elsewhere [6]. It is general [1,2,6] that penetration curve of weathering steel can be expressed by the Eq.(1),

$$Y = AX^B \qquad (1)$$

where X is time in year, Y: penetration (mm), A: the first year corrosion loss (mm), and B: index of corrosion rate diminution. Since A and B values have not been obtainable directly from environmental data so far, mathematical schemes taking in to account chemical kinetics to estimate these parameters were established [3,4], and a computational software was developed. As a demonstration of the developed software, corrosion simulations at Tokyo-Bay Coast conditions (average ambient temperature = 15.4℃ and average relative humidity =69% to obtain time of wetness by Kucera *et.al.*'s method [7], TOW=3008.7h; average wind velocity, W = 4.3m/s; NaCl deposition rate, C = 0.4 mdd; sulfur oxides deposition rate, S = 0.14 mdd) are carried out as in Fig.2. From these results, it can be said that 3Ni weathering steel is 99% likely to achieve *durable state* even in such a severe corrosive atmosphere, where conventional JIS-SMA weathering exhibits 0% possibility. Generally to say, corrosion of weathering steel is affected not only by NaCl deposition rate, but also by various factors as shown in Eq.(2) [3]. Thus, penetration curves may alter depending upon atmospheric corrosiveness index, Z, at construction site.

$$Z = 1\times10^6 \cdot TOW \cdot \exp(-0.1\cdot W)\cdot\frac{C+0.05\cdot S}{1+10\cdot C\cdot S}\cdot\exp\left(\frac{-50(\mathrm{kJ/mol})}{R\cdot T}\right) \qquad (2)$$

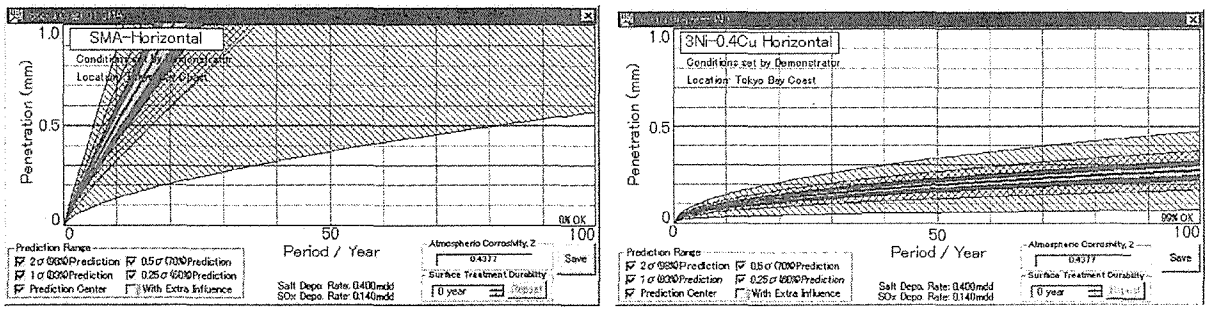

Fig.2 Corrosion prediction at Tokyo-Bay Coast model where NaCl:0.4mdd, SO_x:0.14mdd.

References

[1] T. Ohtsuka, T. Misawa, *Proc. 132nd Symposium of Corrosion Science and Engineering*, "SABI [Rust] Chemistry on the Phase-III toward Realizing Minimum Maintenance Bridge Conception," Japan Society for Corrosion Engineers, (2001.June 25) [Japanese]

[2] Public Work Research Institute - Ministry of Construction, The Kozai Club (Iron and Steel Mill Products Association), and Japan Association of Steel Bridge Construction: *Report on Application of Weathering Steel to Highway Bridges (XX)*, (1992.3) [Japanese].

[3] H. Kihira: Hand out material at meeting of Creative Project at Tokyo Institute of Technology, Dept. Civil Engineering (2002.3.27). [Japanese]

[4] H. Kihira, A.Usami, K.Tanabe, M.Ito, G.Shigesato, Y.Tomita, T.Kusunoki, T.Tsuzuki, S.Ito, T.Murata, *Electrochemical Society Proceedings* Vol.99-26, p127, (1999); H.Kihira, S.Ito, S.Mizoguchi, T.Murata, A.Usami, K.Tanabe: *Zairyo-to-Kankyo*, **49**(1), 30-40, (2000).

[5] Y. Ito, S. Yamaguchi, K. Masuda, C. Kato: *Zairyo-to-Kankyo'98*, B-113, p63 (1998) [Japanese].

[6] H.Kihira: 17th U.S.-Japan Bridge Engineering Workshop p7-35, Tsukuba, Japan, Public Works Research Institute (Nov.12-14, 2001).

[7] V.Kucera, J.Tidblad, A.A.Mikhailov: ISO/TC156/WG4-N314 Annex A, 1999-03-30.

New Weathering Steels of Extremely-Low Carbon Bainitic Type with Excellent Weldability

K.Shiotani, K.Nishimura, T.Hoshino, and K.Amano
Technical Research Laboratories, Kawasaki Steel Corporation, Japan

1. Introduction

A weathering steel(JIS G 3114) gradually forms a dense protective rust layer on the surface through a long time exposure in an atmosphere and corrosion rate is reduced to an extremely low level. However, in coastal regions where airborne salinity content is high, conventional weathering steel sometimes does not develop a sufficient protective rust layer, and the corrosion rate is not suppressed. On the other hand, thicker and higher strength weathering steels are recently needed. Strengthening of steel by means of increasing C and alloy element contents leads to low weldability. Therefore, investigation to relax the restrictions imposed on the use of conventional weathering steel due to limitations in its weldability and resistance to chlorides must be conducted. This has induced the development of the new weathering steels for rural and coastal uses. These newly-developed steels are introduced in this paper.

2. Improvement of Weldability and Resistance to Chlorides

2.1 Weldabilty

In order to improve the weldability, the new technology of extremely-low carbon bainitic steel[1] was applied. Figure 1 shows the results of maximum hardness tests under the arc-strike welding condition for new 570MPa grade weathering steels along with those for the conventional Q-T steel. The maximum Vickers hardness values of the new weathering steels were approximately 270 points. These values are significantly lower than 350 points, which is generally accepted as the upper limit of HAZ hardness for preventing weld crackings. Those results demonstrate their superior resistance to weld hardening. Furthermore, the HAZ toughness was evaluated by heat cycle tests with a peak temperature of 1400℃. The new weathering steels showed very high Charpy energy values that exceed the minimum requirement of 47 J at estimated weld heat inputs range up to 20 kJ/mm, indicating that the high heat input welding up to 20kJ/mm can be used.

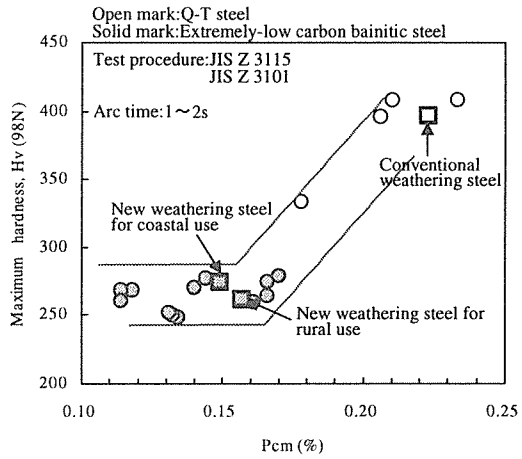

Fig.1 Effect of Pcm on maximum hardness for 570MPa grade steels in arc strike welding

2.2 Resistance to Chlorides

Elements such as Ni, Cu, Cr, Mo, and P have been considered to be effective for improving the resistance to chlorides. The steel samples were then subjected to seawater spray tests to evaluate the effects of these elements on the corrosion rate of steel. The addition of nickel was found to be the most effective for minimizing the corrosion rate. Figure 2 shows the relationship between the duration of the seawater spray tests and corrosion loss for conventional weathering steel and extremely-low carbon bainitic steels with varied Ni contents. The corrosion loss diminished with increasing Ni content. With a Ni content of 2.5 mass%, the corrosion loss was approximately 15% of that of the conventional weathering steel after two years of testing. The corrosion rate also became sufficiently low, indicating that the rust was trans-

formed into a stable state. Thus, the addition of at least 2.5 mass% Ni was found to be effective for improving the resistance to chlorides.

The new weathering steel of extremely-low carbon bainitic type for coastal use containing 2.7mass%Ni (0.02C-2.7Ni steel) was subjected to exposure tests in Okinawa where airborne salinity was 0.8mdd, for one year. The analyzed rust layer[2] formed on the surface of the 0.02C-2.7Ni steel was a dense one, which mainly consisted of amorphous rust and had a characteristic feature of uniform Ni distribution. The amount of chlorine existing at the rust-metal interface was very small. Furthermore, the pH values of the rust layer near the metal substrate were investigated for the 0.02C-2.7Ni and conventional steels exposed for 2 years at the place where is a distance of 2m from the coastal line. The pH value of the 0.02C-2.7Ni steel was higher than that of the conventional one. The high pH for the 0.02C-2.7Ni steel is due to the small content of chlorine. Above analyzed results suggest that the superior corrosion resistance under high airborne chloride conditions is caused by the dense and the low anion selective rust layer with Ni[3], which prevents chlorine from penetrating to the surface of the metal substrate(Figure 3).

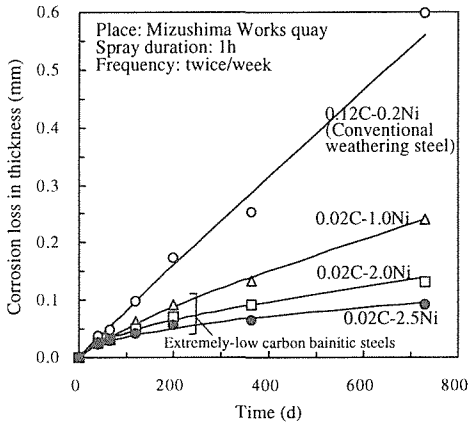

Fig.2 Corrosion loss in thickness vs. time curves for extremely- low carbon bainitic steels as a function of Ni content and the conventional weathering steel, based on seawater spray tests

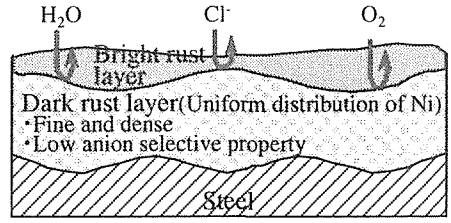

Fig.3 Mechanism of corrosion prevention of new weathering steel for coastal use.

3.Chemical Compositions and Mechanical Properties

Based on the above-described findings, two types of weathering steel were developed: one for a rural use and the other for a coastal use. Table 1 lists chemical compositions of the newly-developed steels. The steel for rural use contains Ni,Cu, and Cr as alloying elements to increase the weathering resistance and meets the reqirement of the chemical composition specified by JIS G 3114. The steel for coastal use contains 2.7mass%Ni to improve the resistance to chlorides. The steel for rural use satisfies the tensile and toughness requirements of the 570MPa grade, also the steels for coastal use satisfy the requirements for 400MPa, 490MPa and 570MPa grades, all in the as-rolled condition.

Table 1 Chemical compositions of new weathering steels

(mass%)

Steel	Grade	C	Si	Mn	P	S	Cu	Ni	Cr	Ceq	Pcm
Rural use steel	570MPa	0.02	0.32	1.37	0.011	0.004	0.49	0.24	0.51	0.37	0.16
Coastal use steel	400MPa	0.02	0.29	0.30	0.011	0.002	0.42	2.75	0.02	0.15	0.11
	490MPa	0.02	0.30	1.02	0.009	0.003	0.38	2.67	0.02	0.27	0.15
	570MPa	0.02	0.29	0.99	0.011	0.003	0.37	2.70	0.02	0.27	0.15

Ceq = C+Mn/6+Si/24+Ni/40+Cr/5+Mo/4+V/14
Pcm = C+Si/30+Mn/20+Cu/20+Ni/60+Cr/20+Mo/15+V/10+5B

4.Conclusion

This development made it possible to produce the steel plates that have superior rural and coastal weathering resistance along with excellent weldability. These products are expected to provide an important contribution to the reduction of construction and maintenance costs of bridges and other steel structures.

References

[1]M.Okatsu, T.Hayashi, and K.Amano:Kawasaki Steel Giho, **30**(1998)3,131 [2]K.Shiotani, F.Kawabata, and K.Amano:Kawasaki Steel Giho, **33**(2001)2,97 [3] K.Noda, T.Nishimura, H.Masuda, and T.Kodama:Pro. 47th Jpn. Conf. Materials and Environment, (2000), 25

Analysis and Clarification of Chemical State for Alloying Element in Iron Rust

T. Nishimura and T. Kodama
Corrosion Resistant Material Research Group, NIMS, Japan

1. Introduction

In Japan, there are many infrastructure facilities in coastal areas, thus it is necessary to use high corrosion resistant steels in saline environment. In addition, weathering steels that minimize the maintenance cost have been attracting attention. Thus in order to establish the guiding index of weathering steels for coastal areas, we investigated the chemical state of alloying elements in the iron rust using binary potential - pH diagrams and physical analysis.

2. experimental procedure

The corrosion test consisted of 1) wetting sample surfaces with 0.4 L/m^2 of a 0.5 mass% NaCl solution, and 2) drying the specimen in a chamber maintained at 25℃, 60% RH for 12 hours.

The sample material was low alloy steel which contain 1.0mass%Ni, 0.8masss%Al, and 1.0mass%W, respectively, in carbon steel. After corrosion test the rust formed on the steels was analyzed by XPS, TEM and EPMA.

3. Results and discussion

A binary-phase potential (E) -pH diagram has been investigated to evaluate the chemical stability of various kinds of complex iron rust (Fe-X) finding a corrosion-resistance principle of low alloy steel. It was found that there are the following types of corrosion-resisting elements in the rust (1) iron substitution type (Ni), (2) oxide formation type (Al), and (3) oxygen-acid salt type (WO_4). The iron substitution type and the oxide formation type elements make complex spinel oxides (Fe_2NiO_4 and $FeAl_2O_4$) with iron in neutral environment in E-pH diagrams as shown in Fig.1 and Fig.2. In actual rust of Ni-bearing steel after the corrosion test, Ni was found as bivalent state from XPS and was included in spinel structure (Fe_3O_4 type) from TEM observation [1]. This fact agrees with the formation of Fe_2NiO_4 in E-pH diagram. As for the Al-bearing steel, Al was found in the inner part of the rust from EPMA and was included in spinel structure from TEM observation [2]. This fact also agrees with the formation of $FeAl_2O_4$ in E-pH diagram. In the corrosion tests, Ni or Al-bearing steel showed higher corrosion resistance than carbon steel. Thus it is possible to obtain high corrosion resistance by the creation of complex spinel such as Fe_2NiO_4 and $FeAl_2O_4$ in an inner layer.

On the other hand it was found that the oxygen-acid salt type element (WO_4) was not absorbed into the iron rust. $FeWO_4$ is formed between the upper rust (FeOOH) and the base metal (Fe) as shown in E-pH diagram (Fig.3). As in general $FeWO_4$ is the insoluble salt, it is thought to act as an anodic inhibitor against the corrosion. In actual rust of W-bearing steel after the corrosion test, W was found as WO_4 state from XPS and it was excluded from the iron rust and concentrated into the defects of the rust [3]. This fact agrees with the formation of $FeWO_4$ in E-pH diagram. Moreover in the corrosion test, the addition of a small quantity of W gives higher corrosion resistance than carbon steel, which is though to because WO_4 acts only the defect of the rust just like as PO_4.

4. Conclusion

Spinel structure element ($FeAl_2O_4$, Fe_2NiO_4) and oxygen-acid salt element (WO_4) in E-pH diagrams showed high corrosion resistance in actual saline environment (Fig.4).

5. References

[1] T.Nishimura, H.Katayama, K.Noda and T.Kodama, Corrosion Sci., 42(2000), p1611-1621.
[2] T.Nishimura, K.Noda and T.Kodama, Materials Trans., 42(2001), No.3, p478-483.
[3] T.Nishimura, K.Noda and T.Kodama, Corrosion, 57(2001), No.9, p753-758.

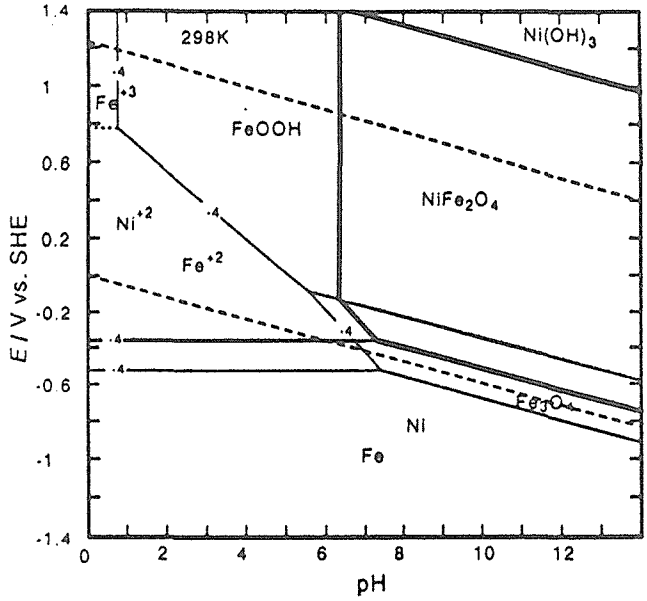

Fig.1 Fe-Ni potential-pH diagram.

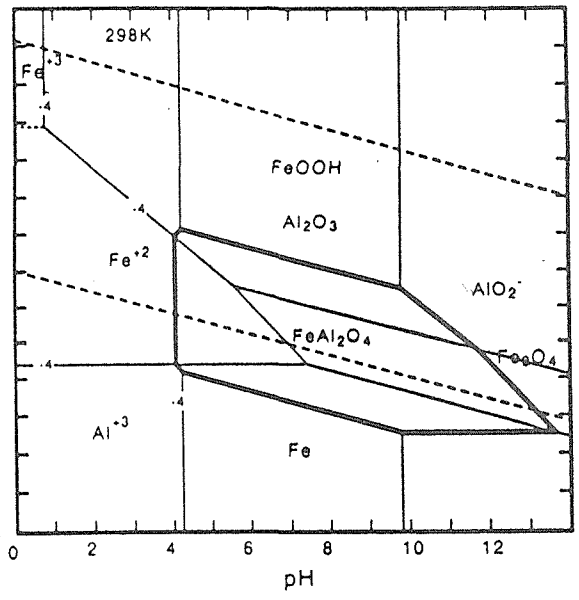

Fig.2 Fe-Al potential-pH diagram.

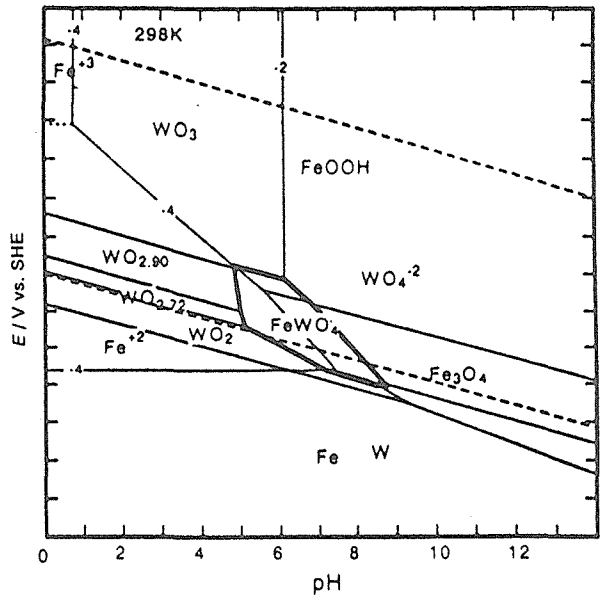

Fig.3 F-W potential-pH diagram.

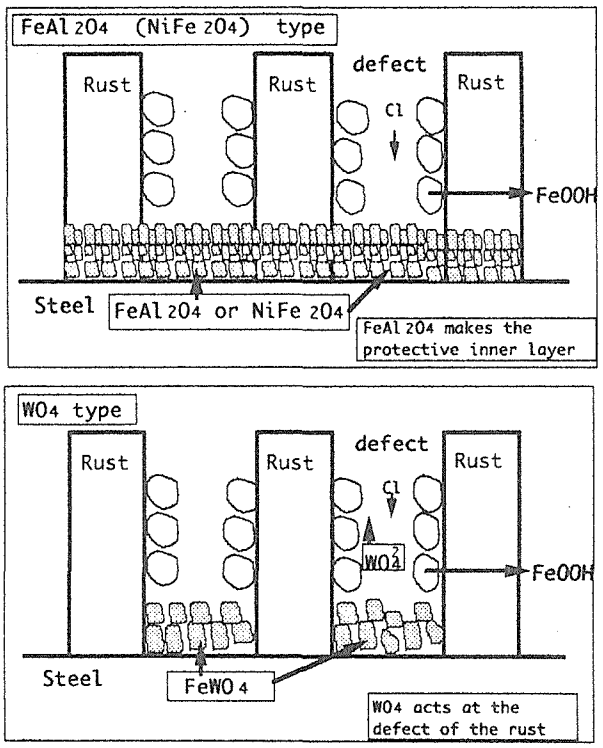

Fig.4 Schematic diagrams of the Protective rust layers.

Evaluation of Corrosion Environments of Structural Parts of Weathering Steel Bridges by Monitoring with Corrosion Sensors

M. Takemura, H. Kajiyama, S. Fujita

Materials & Processing Research Center, NKK Corporation, Japan

1. Introduction

Weathering steels, on which protective rust layers form in long term exposure to the atmosphere, can be used for steel structures such as bridges without coating to reduce the maintenance cost. However, the protectiveness of the rust layers of conventional weathering steels such as JIS SMA are not effective enough in environments with large amount of airborne salt and/or high humidity. Furthermore, the behavior of deposition of airborne salt and the change of humidity depend on the structural parts. In this study, the corrosion environment of each structural part of an experimental weathering steel bridge exposed at coastal area was evaluated by monitoring with ACM (Atmospheric Corrosion Monitor) sensors [1], [2], [3].

2. Experimental Procedure

An experimental bridge, shown in Fig.1, whose size is 15 mW X 4 mL X 3 mH is located at Tsu, Mie Pref. Its plate girders are made of JIS SMA (0.35%Cu-0.5%Cr) and 1.5%Ni-0.3%Mo steel, developed for air borne salt rich areas by NKK Corporation [1]. ACM (Atmospheric Corrosion Monitor) Sensors were attached to the structural parts as shown in Fig.2, and the corrosion environments were monitored for 1 year. Specimens of JIS SMA were also attached next to the sensors to compare the ACM sensor output and their thickness loss. The composition of the rust layer formed on each structural part is also analyzed with X-ray diffraction.

3. Results and Discussion

The output of the ACM sensors characterized the corrosion environments of each structural part as shown in Fig. 3. The output was largest in the upper faces of lower flanges and smallest in the inner and the upper parts of webs, which would be associated with the deposition and accumulation of airborne salt. Fig. 4 shows that the output of the ACM sensors was strongly associated with the thickness loss of specimens of JIS SMA. It is suggested that the thickness loss of structural part of uncoated weathering steel is estimated from the sensor output. The composition of the rust layer is also discussed in the presentation.

4. Summary

In order to evaluate the corrosion environments of each structural part of weathering steel bridges quantitatively, the monitoring method with ACM sensors was examined. In monitoring corrosion environments around the experimental weathering steel bridge, the output of the ACM sensors characterized the corrosion environment of each structural part and was strongly associated with the thickness loss of JIS SMA. It is suggested that the thickness loss of structural part of uncoated weathering steel is estimated from the sensor output.

References

[1] T. Takaku, Y. Mihara, S. Fujita, K. Matsui, M. Kato, M. Honda, NKK Technical Report, 165(1999), pp.17-21.

[2] T. Motoda, Y. Suzuki, T. Shinohara, Y. Kojima, S. Tsujikawa, W. Oshikawa, M. Itokawa, T. Fukushima, and S. Izumo, Zairyo-to-kankyo (Corro. Eng.), 43(1994), No.10, pp.550-556.

[3] I. Kage, S. Fujita, Proceedings of GALVATECH '98(1998), pp.394-398.

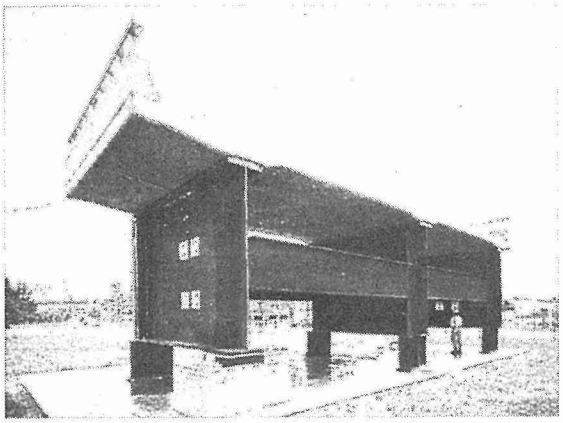

Fig.1 Experimental bridge.

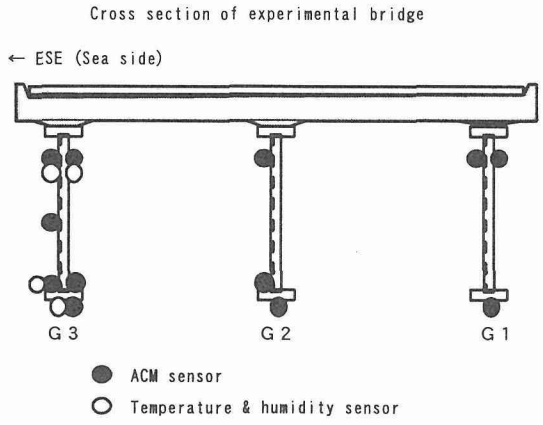

Fig.2 Positions of sensors.

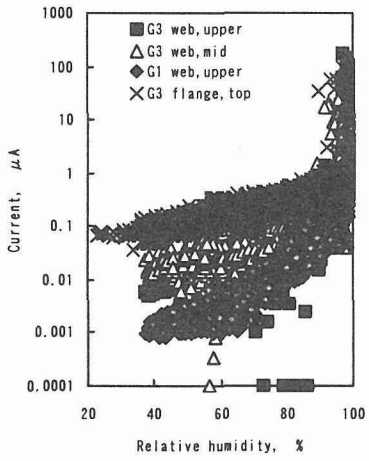

(a) Outer parts

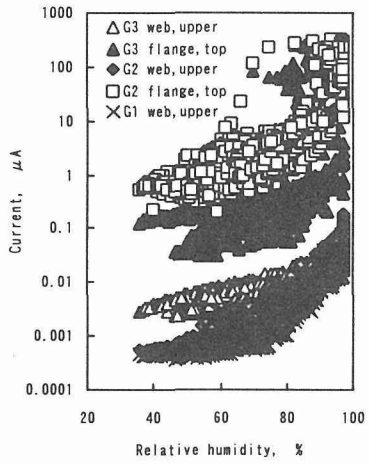

(b) Inner parts

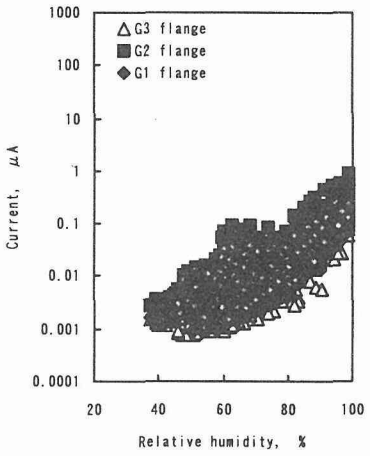

(c) Lower faces of lower flanges

Fig.3 Relationship between ACM sensor output and relative humidity (July, 1998).

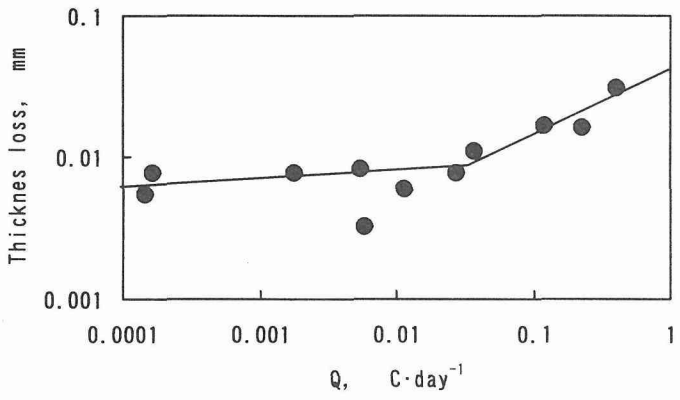

Fig.4 Relationship between thickness loss of JIS SMA and average current of ACM sensor.

MICROSTRUCTURE CHARACTERISTICS AND CORROSION BEHAVIOUR OF HVOF SPRAYED METALLIC COATINGS

AJ Sturgeon & RE Dolby
TWI Ltd, Granta Park, Abington, Cambridge, UK

1. Introduction

The use of HVOF sprayed coatings of corrosion resistant alloys to protect an underlying steel substrate has received much attention in recent years [1,2,3]. This is in part due to the very low levels of porosity that can be achieved with the HVOF process. Such coatings are considered for applications where a barrier layer is needed to protect against corrosion in seawater or corrosive solutions, such as mineral or organic acids. However, even with the attainment of low porosity (less than 2 vol.%) microstructures, HVOF sprayed coatings do not appear to offer the same level of corrosion resistance as corresponding bulk materials. The aim of the work reported here was to determine the level of corrosion performance that can be expected from 300μm thick coatings of 316L stainless steel and 625 nickel alloy deposited on a low carbon steel substrate using the JP5000 HVOF spraying process.

2. Experimental

Electrochemical test techniques are used to provide a quicker and more qualitative tool for evaluating the corrosion behaviour of bulk alloy materials in aqueous environments. More recently, such techniques have also been applied to thermal sprayed metallic coatings to provide an accelerated test method to rank their resistance to corrosion. The electrochemical corrosion test comprised of cyclic anodic polarisation in artificial seawater solution (3.5% NaCl) purged with nitrogen, with a pH of 8.2 and at a temperature of 25°C.

3. Results and Discussion

Typical cross sections of the stainless steel coatings are shown Figure 1. These figures illustrate the lamella nature of the coating microstructures, with the deformed powder particles and inter-particle boundaries clearly visible. The figures also reveal that oxide and porosity is located at the inter-particle boundaries. Similar microstructures were observed for the nickel alloy coating.

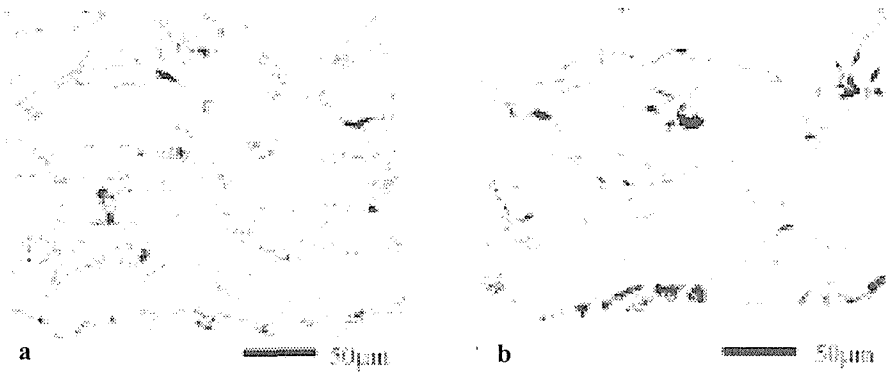

Figure 1. Cross sections of stainless steel coatings prepared with 14-45μm powder (a) and 25-53μm powder (b).

The stainless steel and nickel alloy coatings prepared with the smaller size powders contain higher amounts of oxide at the inter-particle boundaries. Measured porosity and oxide levels for the coatings are given Table 1.

Table 1. Porosity and oxide levels

Coating	Particle size	Porosity	Oxide
	μm	Volume % (±0.5)	Weight % (±0.2)
316L Stainless steel	15-45	0.9	2.9
	25-53	1.5	0.8
625 Nickel alloy	16-44	2.2	3.3
	25-53	2.5	0.7

The corrosion test results indicate that a HVOF sprayed coating of 625 nickel alloy can provide significantly better corrosion resistance, and consequently give better protection to a carbon steel substrate, than a similar high quality coating of stainless steel. This work also indicates that for the nickel alloy, a smaller size powder gives a coating with noticeably better corrosion resistance. This improvement in corrosion performance is achieved despite a much higher oxide content in the deposited coating. Measured values of porosity are similar for the nickel alloy coatings prepared with the smaller and larger powder sizes. It appears that a smaller sized powder is able to produce a coating microstructure more resistant to localised corrosion attack, possible due to differences in the type of porosity in the coatings or in the nature of the inter-particle boundaries. These results also show that the corrosion resistance of the nickel alloy coating does not match that of the same alloy in its bulk form. The nickel alloy coating gives a much higher corrosion current than bulk 625 nickel alloy, and has values slightly higher than those measured for bulk 316L stainless steel (below its pitting potential). A steel substrate coated with HVOF sprayed nickel alloy can offer corrosion resistance similar to bulk stainless steel, but not that of bulk nickel alloy.

4. Summary and Conclusions

- HVOF sprayed coatings of nickel alloy provided significantly better resistance to corrosion in a seawater environment than HVOF sprayed coatings of stainless steel.
- For the nickel alloy coating deposited using the JP5000 HVOF system, a smaller powder size range of 15-45μm gave a coating with better resistance to corrosion than a coating prepared using a larger powder size, despite the coating having a higher oxide content.
- A steel substrate coated with HVOF sprayed nickel alloy may have the ability to offer corrosion resistance (in a seawater environment) similar to bulk stainless steel, but not that of the nickel alloy in bulk form.

References

[1] S. Kuroda et al: Microstructure and corrosion resistance of HVOF sprayed 316L stainless steel and Ni base alloy coatings, Thermal Spray - Surface Engineering via Applied Research, Ed. CC Berndt, Pub. ASM International, (2000)

[2] C. M. Eminoglu et al: Potentiodynamic corrosion testing of HVOF sprayed stainless steel alloy, Tagungsband Conference Proceedings, Ed. E. Lugscheider, P.A. Kammer, Pub. DVS, Germany (1999)

[3] A. J. Sturgeon and D. Buxton: The electrochemical behaviour of HVOF sprayed coatings, Thermal Spray - Surface Engineering via Applied Research, Ed. CC Berndt, Pub. ASM International, (2000)

Fabrication of TiO_2 coating photocatalyst onto infrastructure surface

M. Fukumoto, Y. G. Jung and T. Suzuki
Department of Production Systems Engineering,
Toyohashi University of Technology, Japan

1. Introduction

Titanium dioxide has become of a major interest lately as a functional material for NOx elimination in the environment, when the material is irradiated to ultraviolet rays [1, 2]. As it is actually difficult to find an additional space for installing TiO_2 material at the polluted area typically in large cities, fabrication of the coatings directly onto the infrastructure surface existed in those areas seems to be the most realizable way. Therefore, the necessary conditions for such kind of coating formation process are high performance, environmentally high resistance, high adhesive strength to the substrate and so on.

In this study, the NOx elimination photocatalyst coating was tried to be fabricated by the thermal spray process, and feasibility of the photocatalyst coatings by the thermal spraying was examined. The effect of adsorbents addition to TiO_2 and NO_X elimination property was mainly investigated.

2. Experimental

Powder material used is a commercially available anatase phase TiO_2 because the photocatalytic performance is superior in anatase phase to other phases. However, flowability of the powder is fairly low because of its extremely small diameter. An agglomeration treatment for the powder with PVA binder was performed by the spray drying method. The agglomerated powder has a globular shape, and a mean diameter distribution of 10-30μm. Commercially available plate tile with 45mm x 45mm x 7mm size was used as a substrate material.

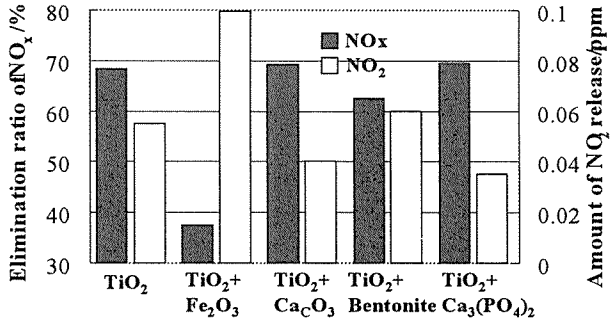

Fig. 1 Comparison of NOx elimination and NO release property in mixed powders.

The adsorbents used are $Ca_3(PO_4)_2$, Fe_2O_3, $CaCO_3$ and Bentonite. These adsorbents were added to TiO_2 powder as a NO_2 adsorption material in this research. The adsorbent added agglomerated powders showed a globular shape similar to that of the TiO_2 powder. High Velocity Oxy-Fuel (HVOF) device was used for the thermal spraying.

3. Results and Discussion

NOx elimination and NO release property of each agglomerated powders are shown in **Fig. 1**. In the figure, it was recognized that TiO_2+ $CaCO_3$ and TiO_2 + $Ca_3(PO_4)_2$ showed excellent property in the NOx elimination. However, the generation of NO_2 was less in the TiO_2+ $CaCO_3$ powder compared to that of the TiO_2+ $Ca_3(PO_4)_2$. The effect of mixing ratio of $Ca_3(PO_4)_2$ to TiO_2 was investigated for the TiO_2+ $Ca_3(PO_4)_2$ mixed powders. In **Fig. 2**, it is recognized that the amount of NO_2 release is fairly restricted in each mixed powder compare to the original powder. The difference among these mixed powders, however, was not admitted within the experimental conditions used. The cross section microstructures of the coating made from these mixed powders were shown in **Fig. 3**. Calculated anatase remaining ratio and anatase contents were shown simultaneously in the figure. In the figure, fairly high anatase remaining ratio and anatase content in each coating was admitted. This

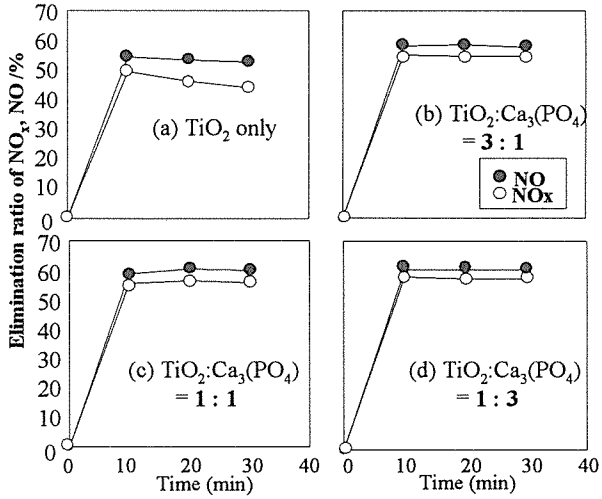

Fig. 2 Time dependence of elimination ratio of NOx and NO.

indicates that the powder was not affected so much by the heating of the flame. NOx elimination properties of the coatings made from mixed powder are shown in **Fig. 4**. NOx elmination property decreased with increase of $Ca_3(PO_4)_2$ addition while the amount of NO_2 release increased. This tendency seems to relate to the decreasing of the specific surface area of TiO_2 powder. This was clarified by the XRD analysis. The decrease in TiO_2 peak strength was admitted with the increase of $Ca_3(PO_4)_2$ addition. In other words, the increase of TiO_2 ratio in the coating can bring about the higher NOx elimination property.

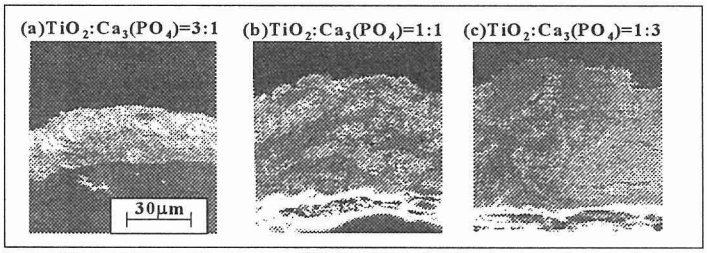

Volume ratio of TiO_2 : $Ca_3(PO_4)_2$	(a) 3 : 1	(b) 1 : 1	(c) 1 : 3
Anatase remaining ratio	0.708	0.789	0.69
Anatase content (%)	65.7	74.7	64.1

Fig. 3 SEM image, anatase remaining ratio and anatase content for each HVOF sprayed coating.

The effect of Ni addition was examined for a further improvement of the photocatalytic property in TiO_2 + $Ca_3(PO_4)_2$ system. The mixture ratio of each material was varied in some extent and the results of NOx elimination and NO release properties are shown in **Fig. 5**. It is recognized in the figure that the NOx elimination property strongly depends on the mixture ratio. At this moment, excellent property of the powder was given in the mixing ratio of 4: 4: 2. It is suggested that a further improvement of the photocatalytic property may be established by optimizing the mixing ratio of the adsorbents.

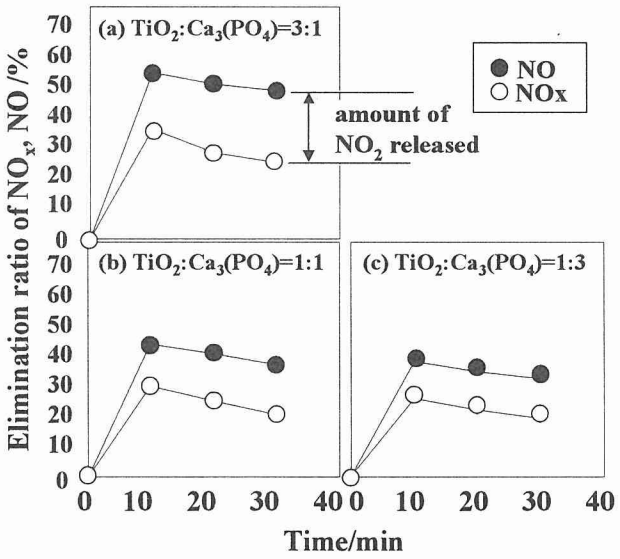

Fig. 4 Time dependence of elimination ratio of NOx and NO.

4. Conclusions

1) Both $CaCO_3$ and $Ca_3(PO_4)_2$ were recognized to be effective as an adsorbent for the improvement of NOx elimination and NO release property of the TiO_2 coating.

2) Considerably higher anatase remaining ratio, and anatase content were admitted in the HVOF coating. This indicates that the powder was not affected so much by the heating of the flame. Increase of TiO_2 ratio in the coating can bring about the higher NOx elimination property.

3) It was suggested that a further improvement of the photocatalytic property may be established by optimizing the mixing ratio of the adsorbents.

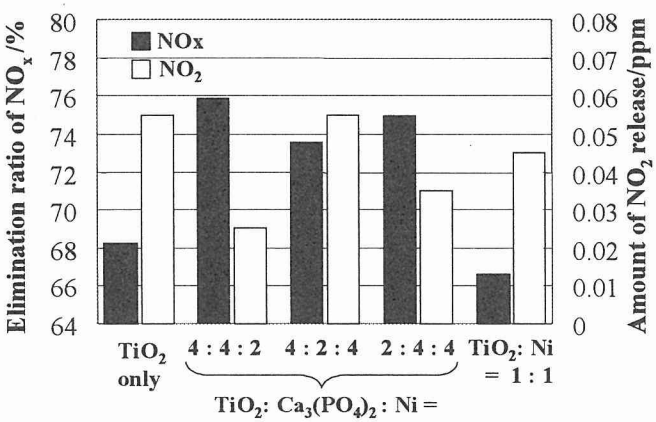

Fig. 5 Comparison of NOx elimination and NO release property in mixed powders.

References

[1] R. I. Bickley, T. G. Carreno, J. S. Lees, L. Palmisano and R. J. Dtilley, Journal of Solid State Chemistry, **92**(1991), pp.178-190.

[2] I. Sopyan, S. Murasawa, K. Hashimoto and A. Fujishima, Chemical Letter, (1994), pp.723.

Development of Dense Corrosion Resistant Coatings By an Improved HVOF Spraying Process

S. Kuroda, T. Fukushima, J. Kawakita
Joining and Interface Research Group, NIMS, Japan

1. Introduction

High Velocity Oxy-Fuel (HVOF) spray is a relatively new thermal spray technique, which propels powder material by a supersonic flame jet to velocity over 500 m/s. HVOF sprayed coatings are generally dense with less oxidation of feedstock materials as compared to coatings formed by other atmospheric thermal spray processes. Hence, their use in industry has been increasing in the fields of wear and corrosion resistant coatings.

Porosity in sprayed alloy coatings is critical if the coating is used as a corrosion barrier in the as-sprayed condition. Oxidation is also important since it tends to degrade the coatings' performances as corrosion barrier or TBC bond coat. One of the ultimate goals of thermal spray technology is therefore to form a dense (zero porosity) and clean coating (low oxidation). In order to achieve such a goal, we have developed an inert-gas shroud and succeeded in fabricating coatings with essentially zero porosity and minimum oxidation [1].

2. Experimental procedures

A high-pressure HVOF spray gun (JP5000, TAFA, US) was used to spray 316L stainless steel powder onto SS400 (JIS) mild steel substrates. The chemical composition and size of these powder and substrate are listed in **Table 1** and the spraying conditions are given in **Table 2**.

Table 1. Chemical composition of the spray powder and the substrate. (mass%)

SUS316L (TAFA1236F), Powder size:25-53μm
Fe bal, Cr 16.8, Ni 10.8, Mo 2.05, N 0.131, O 0.026
Low carbon steel (SS400), Plate: 50x100x5mm
Fe bal, C 0.11, Si 0.22, Mn 0.5, P 0.017, S 0.016

Table 2. List of spray conditions including the gas shroud attachment.

	Ox (STD)	Neb	Re
Fuel flow rate (l/min)	0.33	0.41	0.44
Oxygen flow rate (l/min)	860	670	600
Combustion pressure (MPa)	0.65	0.59	0.57
Barrel length (cm)	10, 20		
Spray distance (mm)	80		
Torch traverse velocity (m/s)	0.7		
Powder feed rate (g/min)	60		
N_2-1 flow rate (l/min)	1500, 2500		
N_2-2 flow rate (l/min)	450		

A schematic illustration of HVOF spraying with a gas shroud is shown in **Fig.1.** A mixture of fuel (kerosene) and oxygen is ignited in the combustion chamber and the resultant high-temperature gas flows through the converging-diverging nozzle and the barrel. The gas shroud attachment is used to inject an inert gas at the exit of the barrel in order to control oxidation of sprayed particles during flight. It consists of a double-walled metal tube, which is water-cooled and possesses two inlet ports to introduce nitrogen gas. One port (N_2 gas 1) is located at the entrance of the shroud and the other port (N_2 gas 2) is located at the exit of the shroud. The flying velocity of HVOF sprayed particles was measured by an in-flight particles diagnostic instrument (DPV2000, TECNAR, Canada) and the molten fraction of sprayed particles was measured by he gel-capture method developed in the laboratory [2]. Pore size distribution within the deposits was measured by a mercury intrusion (Autopore II 9220, Micromeritics, USA) and the oxygen content was determined by the inert-gas fusion method.

3. Results

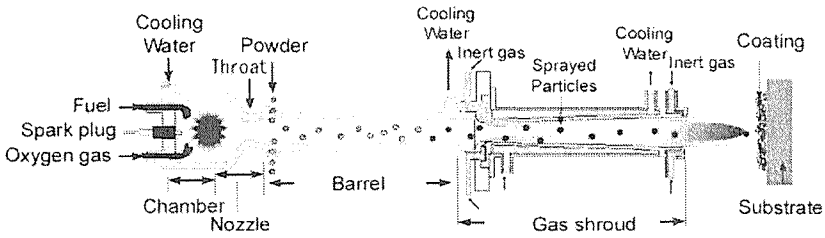

Fig.1. Schematic of HVOF spraying with a gas shroud.

Fig.2 shows the correlation between the average velocity of sprayed particles measured at the substrate position and the total porosity within the sprayed coatings. By extending the barrel length from 100 to 200 mm, the velocity increased by approximately 100 m/s and further increase by about 30 m/s was achieved by the gas shroud. The general trend evident in the figure is that the coating porosity decreased with the particles' velocity and zero porosity was achieved by the combination of the 200mm barrel with the gas shroud at velocities over 750 m/s.

Fig.3 shows the total porosity and oxygen content within the coatings obtained under various spraying conditions. With the 100mm barrel, attachment of gas shroud was effective for reducing the oxygen content especially with the fuel rich fuel, however, porosity increased due to the cooling of particles. With the 200 mm barrel, even though the coating oxidation tends to be high without gas shroud, attaching the gas shroud successfully achieved zero porosity with minimum oxidation.

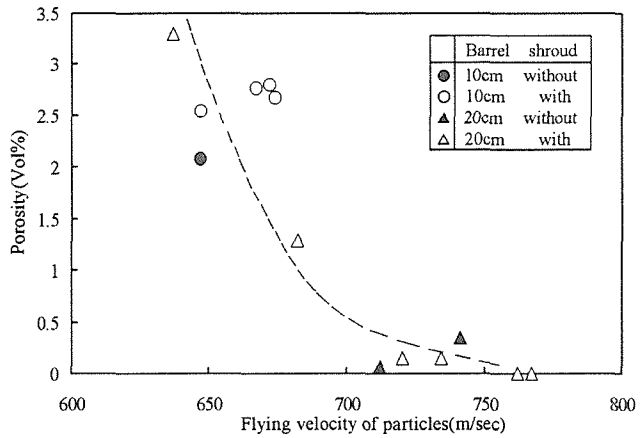

Fig.2. Correlation between the total porosity of HVOF sprayed 316L stainless steel coatings and the average velocity of sprayed particles.

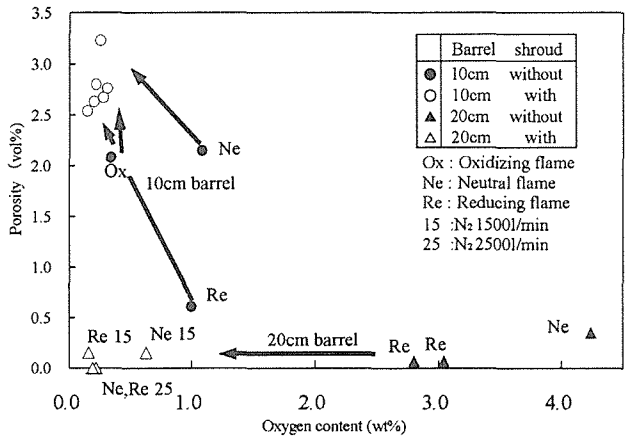

Fig.3. Summary of nitrogen gas shrouding in terms of total porosity and oxygen content.

These results indicate that the temperature of sprayed particles should be close to the melting point of the powder material to ensure sufficient deformation at the impact. Molten fraction of particles, however, did not show clear correlation with the porosity.

4. Conclusions

By attaching a gas shroud to a commercially available HVOF gun, dense coatings of 316L stainless steel with oxidation below 0.2 wt% was obtained. Application of this technique to other alloys such as Hastelloy and evaluation of corrosion resistance of these coatings both by electrochemical methods and marine field tests are now in progress [3, 4].

5. References

[1] T. Fukushima, H. Yamada, J. Kawakita, S. Kuroda, Proc. ITSC 2002, March 2002, Essen, pp.912-917.

[2] Yamada, H., S. Kuroda, T. Fukushima, H. Yumoto, Proc. ITSC 2001, May 2001, Singapore, pp.797-804.

[3] J. Kawakita, T. Kodama, S. Kuroda, Proc. ITSC 2002, March 2002, Essen, pp.681-685.

[4] S. Kuroda, T. Fukushima, J. Kawakita, T. Kodama, Proc. ITSC 2002, March 2002, Essen, pp.819-824.

Electrochemical Evaluation and Field Exposure Tests of HVOF Sprayed Alloy Coatings for Marine Environments

J. Kawakita, T. Fukushima, S. Kuroda, and T. Kodama
Corrosion Resist Materials Group, NIMS, Japan

1. Introduction

The aim of our group in the present research project (STX-21) is to achieve coating of the corrosion resistant material by improvement of the thermal spray technique. The application of this coating is supposed to be on-site repair of the titanium-clad steel and to be protection of the weld in a splash zone and a tidal zone of the marine structure. High Velocity Oxy Fuel (HVOF) spraying was adopted due to its potential of making a dense and less-oxidized coating. The coating materials are a nickel-base alloy, HastelloyC, and SUS316L stainless steel, which are known for their high corrosion resistance. In this paper, the laboratory electrochemical evaluation of these coatings and their field exposure tests were presented.

2. Experimental

The HVOF sprayed coating was prepared onto a mild steel, SS400, by an apparatus JP-5000 and feedstock powders of HastelloyC and SUS316L, manufactured by TAFA Co. Recently, the attachment for this machine was devised and installed, which had the shroud mechanism by an inert gas of N_2. The thickness of the coating was 400 μm. The chemical composition of the coating and its open porosity were determined by the chemical analysis and the mercury intrusion porosimetry, respectively. In the laboratory test, the corrosion resistance was evaluated by the AC impedance and the electrochemical polarization measurements. The surface area of the sprayed specimen was 2 cm^2 in circle and the test solution was artificial seawater at 300K. In the field exposure test, a sprayed panel in size of A4 was used. Such panels were fixed at the appropriate position in the splash, tidal and submerged zones. This test started in November 2000.

3. Results and discussion

Fig. 1 shows the typical result of the laboratory immersion test. The polarization resistance is closely related to the corrosion rate. Accordingly, the higher polarization resistance of the specimen corresponds to its higher corrosion resistance. As this SUS316L coating had 1.6 vol% of porosity, a drop in resistance at the initial stage during immersion indicated the initiation and the propagation of corrosion of the substrate, caused by penetrating the solution through connecting pores. The standard HastelloyC coating keeps the almost constant resistance, resulted from its smaller porosity below 0.1 vol%. The gas shroud brought about 0 vol% of porosity, i.e. under limit of detection. Furthermore, the on-shroud HastelloyC coating decreased in oxide content down to 0.21wt%, compared to 0.62wt% for the standard one. This fact was considered to advance the corrosion resistance of the on-shroud HastelloyC coating.

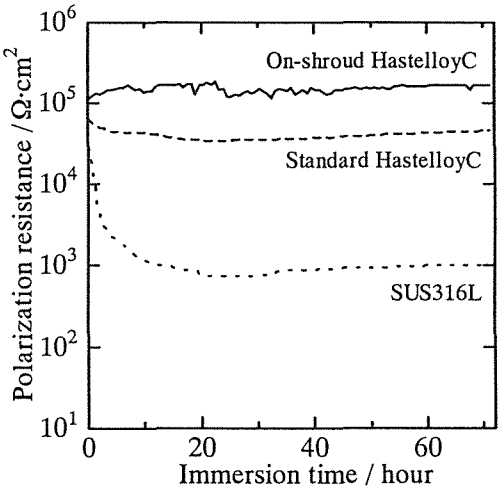

Fig. 1 Variation in polarization resistance of HVOF sprayed coatings with immersion time in aerated artificial seawater at 300K.

The fluctuation in resistance of the on-shroud coating, however, suggested the occurrence of localized corrosion. This type of corrosion was confirmed also on its polarization curve, as

shown in Fig. 2. The position of other two curves and their shape indicated mainly the poor corrosion resistance of the coatings except the on-shroud coating. The photographs of the specimens after immersion test are presented in Fig. 3. The SUS316L coating had many reddish-brown corrosion products on its surface, indicating the corrosion of the substrate (Fig.3a). As expected from this result, its field exposure test for three months brought about the bad consequence and the whole surface of the SUS316L sprayed panel was covered with the rust (Fig. 4a). In the field exposure test, the corrosion damage of the sprayed panel depended on the time for contacting the coating with seawater. Although the standard HastelloyC coating had a significantly small black spot was observed in the laboratory immersion test, large rusts appeared localizedly on its surface in the field test (Fig. 3b and Fig. 4b). This result indicated clearly the risk of corrosion caused by the existence of a penetrating pore in the long run. In fact, our subsequent study revealed the standard HastelloyC coating had the through-pore even with 400 μm in thickness. The on-shroud HastelloyC coating had some black spots on its surface after the laboratory immersion test (Fig. 3c), suggesting the occurrence of pitting corrosion on the coating. According to our detection method of through-pore, this coating had no through-pore. In addition, the good performance was demonstrated in the field exposure test (Fig. 4c). Therefore, the pitting corrosion in the on-shroud coating did not affect the substrate.

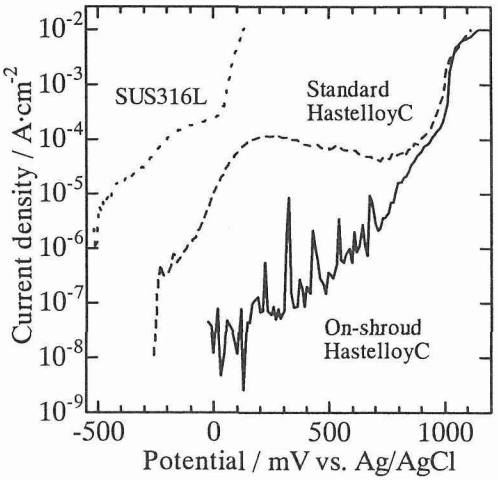

Fig. 2 Polarization curve of HVOF sprayed coatings in de-aerated artificial seawater at 300K.

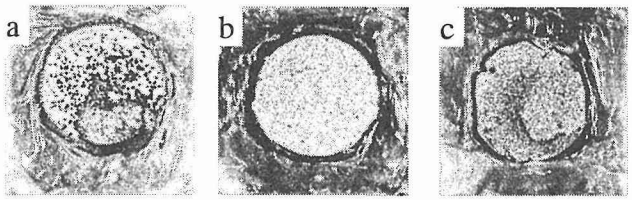

Fig. 3 Photographs of HVOF sprayed coatings immersed in aerated artificial seawater at 300K for 3 days, (a: SUS316L, b: standard HastelloyC and c: on-shroud HastelloyC).

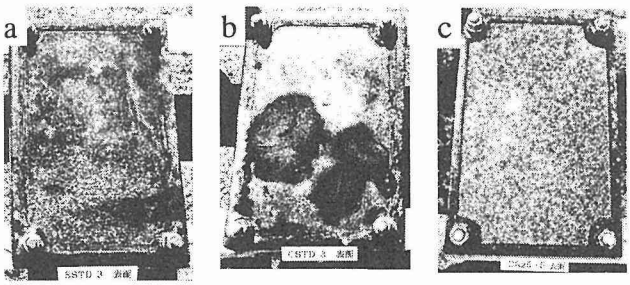

Fig. 4 Photographs of HVOF sprayed coatings exposed in submerged zone of actual sea for 3 months, (a: SUS316L, b: standard HastelloyC and c: on-shroud HastelloyC).

4. Conclusions

The electrochemical evaluation discriminated the corrosion resistance of the HVOF sprayed alloy coatings and showed the effect of the substrate on the corrosion resistance. The field exposure test revealed that the penetrating porosity was a primary determining factor of the corrosion rate for the HVOF sprayed alloy coating.

Resistance of Thermal Sprayed Coatings of Zn, Al and Zn-Al Alloy against Atmospheric Corrosion

Tsuguo Suzuki[1], Hironobu Nuriya[2], Kazuo Ishikawa[3] and Yoshiharu Kitamura[4]

[1]Suzuki Consultant Office, 2-14-13 Kanagaya, Asahi-ku, Yokohama 241-0812, Japan
[2]College of Industrial Technology, Nihon University, 1-2-1 Izumi-cho, Narashino 275-0006, Japan
[3]Tokyo Metallikon Co. Ltd, 2-18-13 Keihinjima, Ohta-ku, Tokyo 143-0003, Japan
[4]Kitamura Technical Consultant Office, 972 Yamanouchi, Kamakura 247-0062, Japan

1. Introduction

Atmospheric corrosion behavior of thermal sprayed coatings of Zn, Al and Zn-Al alloy, and various kinds of painting on them were evaluated through the long term weathering test for over 22years at Tokyo and Sapporo. Outline of the results was reported already elsewhere[1]. In this paper, the mechanism of the corrosion protection and the characterization of the sprayed films without painting are discussed based on the results of the electrochemical and surface analytical investigations for both the as-sprayed and the exposed specimens.

2. Experimental

Coatings of specimen were prepared by flame spraying with wires of Zn, Zn-15Al, and Al, 3.2mm in diameter, on a blasted carbon steel substrate, 100×50×3mm.. In the electrochemical polarization measurements, the detached film after spraying on a bright steel, solid wire before spraying, and the carbon steel were also tested to clarify the protection mechanism.

The exposure tests were conducted at Tokyo and Sapporo for 22years. The test panels were faced to due south, at a horizontal angle of 35 degrees.

Polarization characteristics were measured in a solution of aerated 0.1MNa_2SO_4, 30℃. Potentiodynamic anodic polarization was started with a sweep rate of 20mV/min, after reaching a steady state potential in a prescribed condition within the electrolytic cell.

SEM image and EPMA elemental mapping were observed to clarify the distribution of Zn and/or Al as the metallic components and S and Cl as the environmental pollution components in the sprayed films before and after the long-term exposure test.

3. Results and discussion

SEM images and EPMA elemental mappings on the cross section of the films for the as-sprayed Zn, Zn-15Al alloy and Al show that a layered fine structure is observed on the sprayed Zn film, which contains much amount of oxygen, but little defects, and that the film of the sprayed Zn-Al alloy has a random layer structure, which contains many defects and voids. On the other hand, the sprayed Al has a little oxygen comparing to Zn, and contains several defects in the dense and indistinct layered structure.

Anodic polarization curves of the as-sprayed specimen, the detached film, and the solid wire for Zn, Zn-15Al alloy and Al showed those as follows; (1)In the anodic polarization behavior of Zn and Zn-15Al, there is no difference between the as-sprayed specimen and the solid wire. This indicates that the chemical factors such as oxidation in the spraying process, and the physical factors such as surface roughness, defects or voids, have little effect on the anodic dissolution process of the sprayed films of Zn and Zn-15Al alloy. Furthermore, the same behavior between the sprayed specimen and the detached film proves no effect of the substrate steel on the anodic process of the sprayed system. The fact suggests that the galvanic

action between the sprayed metals and the steel substrate is negligible small, and that the protection by the spraying is based on the barrier films rather than the sacrificial anode. (2)The sprayed Al showed a less noble corrosion potential than that of the solid wire, but the same passive behavior in the anodic polarization. No galvanic action between the sprayed Al and the steel substrate was also recognized in the same manner as the Zn and Zn-Al alloy. From the results, the protection by the sprayed Al is also due not to the sacrificial anode but to the barrier film.

No rusting was found apparently on 3 types of the sprayed specimens exposed for 22years at Tokyo and Sapporo, proving the enough duration of the protection through the period. The results of the SEM observation and the EPMA elemental mapping for the component elements and the environmental pollution elements after the long-term exposure showed the facts as follows; (1) In case of the sprayed Zn film, the corrosion products containing the pollution components of S and Cl was formed on just the outermost layer of the sprayed surface, and not penetrated inside the film. As described later, the stable outer layer should decrease the surface activity of the sprayed film and the anodic dissolution. (2)In the film of the sprayed Zn-15Al alloy, the pollution components were recognized to penetrate down to the substrate, and to detach the inter-spraying layers. The protection ability of the film was estimated at its final stage to the limit of the resistance. (3)The sprayed Al film was also deteriorated to expand the defects filled with the corrosion products. The protection of the film was also estimated at the limit of the use.

Anodic polarization curves of the exposed specimen at Tokyo and Sapporo, comparing with the as-sprayed specimen show the results as follows; (1)The anodic dissolution current for Zn decreased 1～2 orders of multitude by the long-term exposure, suggesting an effect of the corrosion inhibition by the outer surface layer consisting of the corrosion products. The degree of the inhibition was larger at Tokyo than at Sapporo. (2)On the other hand, the corrosion potential of Al shifted to a more noble potential than that of the carbon steel, so as to diminish the sacrificial ability for the cathodic protection. The passive behavior still remained in the anodic polarization. The facts suggest the protection of Al for the steel substrate be derived from the coating as a barrier film. An increased passive current in the exposed specimen comparing with that of the as-sprayed specimen substantiates the deterioration of the sprayed Al film mentioned above.

4. Conclusions

(1)Corrosion prevention by the thermal sprayed Zn, Zn-Al alloy and Al coatings was due to a barrier effect rather than an effect of the electrochemical cathodic protection.

(2)All of three kinds of the coatings showed a sufficient protection against the atmospheric corrosion for over 22years.

(3) A thin protective layer containing the corrosion products formed on the outermost layer of the sprayed Zn decreased the surface activity and the anodic dissolution. The pollution components of S and Cl were not found to penetrate inside the film.

(4) The sprayed Zn-15Al alloy showed a similar polarization characteristic to the sprayed Zn, but the pollution components were found to penetrate down to the substrate, and to detach the inter-spraying layers. The protection ability was at its final stage to the limit of the resistance.

(5)Passive behavior of the sprayed Al continued still for 22years, but the film deteriorated to expand the defects filled with the corrosion products. The protection of the film was also at the limit of the use.

(6) Corrosivity of the atmosphere caused by S and Cl was larger at Sapporo than at Tokyo. The influence of the airborne salinity and the air pollution substances is more severe at the coast of Japan Sea rather than the coast of Pacific Ocean.

References

[1] Y. Kitamura, H. Nuriya, M. Seki, K. Ishikawa and S. Yoshida, *Proceedings of the 30th Scientific Lectures Meeting, College of Industrial Technology, Nihon University,* 1997, p.25.

Deposition of component controlled steel coatings by atmospheric thermal plasma spray using shroud equipped thermal spray gun.

○T. Yamazaki, Y. Ando, S. Tobe
Ashikaga Institute of Technology, Japan

1. Introduction

As environments where materials are used become severe, thermal spray coatings come to be demanded high corrosion resistance properties and high wear resistance properties. Therefore, recently, the reactive thermal spray technique comes to be regarded as an important process and many studies on reactive thermal spray techniques come to be carried out. However, most of reactive thermal spray processes are conducted under low pressure environments or inert gas environments because these processes should be done in precisely controlled atmosphere. Therefore, there are some problems such as limitation of the size of the specimen due to the size of the vacuum chamber, long operation time due to evacuation time or time for substitution between ambient gas and inert gas, high initial cost and maintenance cost of the vacuum chamber and so on.

In this study, in order to develop an easy reactive thermal spray process without using vacuum chamber, fabrication of oxygen and nitrogen free steel coating by atmospheric thermal plasma spray using shroud equipped thermal spray gun and fabrication of nitrided steel coatings by introducing nitrogen were carried out. As spray powder and thermal spray gun, commercial sus316 powder and Praxair SG100 were used, respectively.

2. Experimental equipments

In this study, Plasma dyne company production 3600 automatic production style thermal plasma spray equipment was used as thermal plasma spray equipment. The substrate was blasted after degrease washing by acetone. In order to confirm the ambient air barrier effects of shroud, the shroud was attached at the top of the plasma gun which could prevent the contact between plasma and the atmosphere (Fig.1). Thermal spray was carried out with changing spray distance from 60mm to 120 mm to investigate the influence of the spraying distance upon the components of the thermal spray coatings. After thermal spraying, structure analysis of the specimen surface by X-ray diffraction (CuK α , 40kV, 100mA) was carried out.

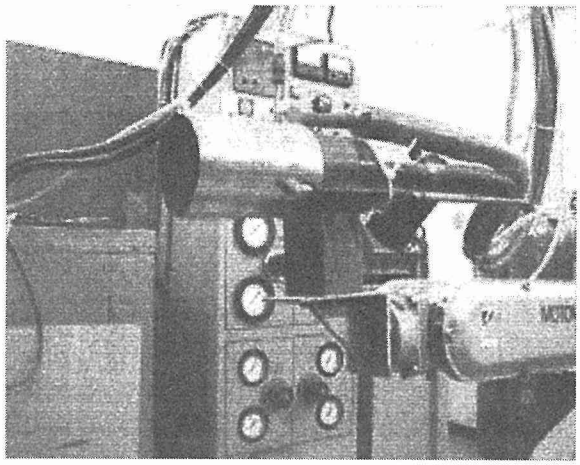

Fig.1 Photograph of the thermal spraying apparatus and shroud.

3. Experimental condition

Thermal spray gun was PLASMA DYNE SG100. Thermal Spraying was conducted in open air. Plasma discharge power was 30[V], 700[A]. Ar was used as working gas, and working gas flow rate was indicated as 50 [PSI] in the outlet pressure of the working gas supplying system. Thermal spray material was Fe powder whose grain size was between 10 μ m to 45 μ m. The powder feed rate was 1.00rpm in powder feeding disk's rotating speed. The substrate was 60

×25×2mm^t SS400 plate.
The shroud was made of SUS304 stainless steel cylindrical pipe. As X-ray diffraction measurement equipment, RINT2000 was used.

4. Results and discussion

Figures2 and 3 show XRD patterns of Fe coatings deposited by thermal plasma spraying using Ar gas on the condition of 80mm in spraying distance in the case of conventional thermal spray gun use and shroud equipped thermal spray gun use, respectively. Some iron oxide peaks were observed in the XRD pattern of the sample in the case of conventional thermal spray gun use and it was confirmed that oxidation of iron powders due to the ambient air occurred even on the condition that inert Ar was used as working gas. On the other hand, as far as XRD patterns were investigated, any iron oxide peaks couldn't be observed in the XRD pattern of the sample in the case of shroud equipped thermal spray gun use. Even on the conditions of the other spraying distances, almost the same phenomena could be confirmed. From these results, it was confirmed that oxidation of iron powders during operation could be protected dramatically by using shroud equipped thermal spray gun.

5. Conclusion

In order to develop an easy reactive thermal spray process without using vacuum chamber, deposition of steel coatings by atmospheric thermal plasma spray using shroud equipped thermal spray gun were carried out. Consequently, oxygen and nitrogen in the thermal spray coatings could be diminished by using the shroud, besides, iron nitride was confirmed in the coatings on the conditions that nitrogen was introduced into the shroud. From these results, this technique was found to have a high potential for reactive thermal spray process conducted in open air.

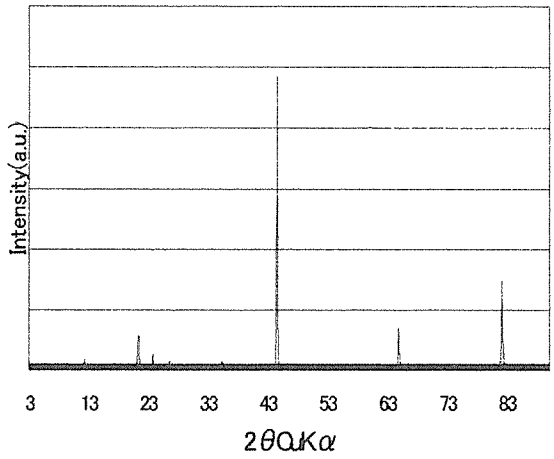

Fig.2 XRD pattern of Fe coating deposited by thermal plasma spraying using Ar gas on the condition of 80mm in spraying distance.

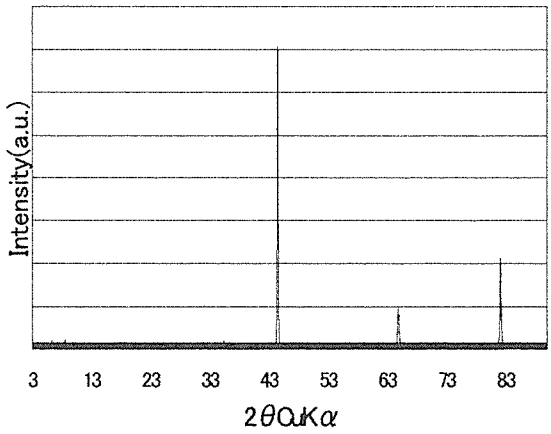

Fig.3 XRD patterns of Fe coatings deposited by thermal plasma spraying using Ar gas on the condition of 80mm in spraying distance in the case of shroud use.

Improvement of wear resistance of steels by nitriding using supersonic expanding nitrogen plasma jets

Y. Ando, T. Saito, S. Tobe, H. Tahara* and T. Yoshikawa*
Ashikaga Institute of Technology, Japan
*Osaka University, Japan

1. Introduction

Plasma jets have been successfully used as heat sources of thermal plasma spraying process. However, since the plasma jets is accelerated to supersonic under a low pressure environment, the plasma jets can be used low temperature plasmas with high chemical reactivity due to supersonic adiabatic expansion and frozen flow. From this viewpoint, nitriding of titanium plate using supersonic expanding nitrogen plasma jets under a low pressure environment used to be carried out in our previous study. As a result, it was proved that the plasma jets had enough reactivity to form a hard and thick titanium nitride layer on the surface of a titanium plate by only a few minutes plasma jets irradiation at 30Pa chamber pressure. In this study in order to develop a practical low temperature and high rate nitriding process, nitriding of nitriding steel, carbon steel and stainless steel using this process were carried out and wear resistance of these nitrided samples were investigated.

2. Experimental

Experimental apparatus for the surface nitriding consists of vacuum chamber, plasma torch, gas supply system, power supply system and vacuum pump shown as Fig. 1. Sample holder was placed in the vacuum chamber and plasma torch has the optimally designed supersonic expansion nozzle for use at 30 Pa chamber pressure. Three samples were horisontally set on the sample holder and the sample of the left side was placed as the axial center of the plasma jet irradiates this sample (This sample will be indicated as "center" in the following sentences). As working gas, nitrogen and hydrogen were in this study. The discharge power was 7.5 kW (50 V, 150 A), and the mass flow ratio of hydrogen/ nitrogen was 1/3 (3.2 SLM/ 9.6 SLM). The nitriding time was 5 min. Irradiating distance was varied from 180mm to 600 mm. Nitriding temperatures during operation were measured by pyrometer fixed outside of the vacuum chamber. The surface structures of nitrided samples are investigated by means of X-ray diffraction (CuKα, 40 kV, 30 mA). The surface hardness of the nitrided sample was measured by Vickers hardness testing. Wear testing was conducted by so-called Block on Disk method. Figure 2 shows schematic diagram of one of the apparatuses for wear testing.

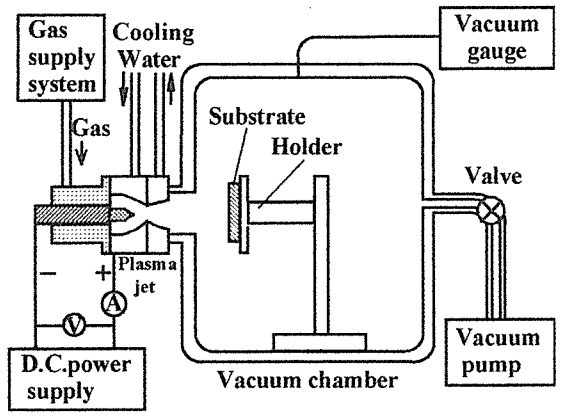

Fig.1 Schematic diagram of the apparatus for surface nitriding

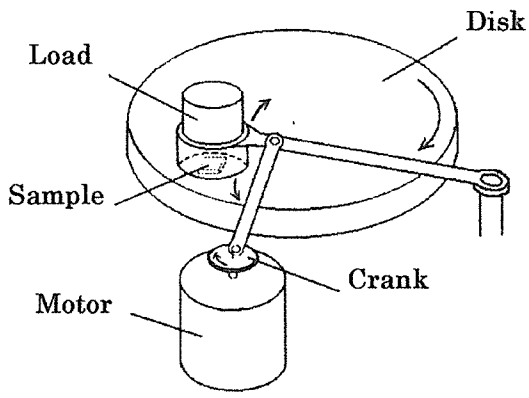

Fig.2 Schematic diagram of the wear testing apparatus.

Samples are φ25 mm x 3 mm^t coin shaped SACM645, S45C, SKD61 and SUS304. The surfaces of these samples were polished by #1000 emery paper before operation.

3. Results

Figure3 shows radial profiles of surface hardness of the nitrided samples on the condition of 180mm in irradiating distance. In any cases, surface hardening was occurred by only 5 minutes nitriding. Especially, Surface hardness became over Hv800 and over 20 μ m thick hard layer was formed on the surface of the substrate in the case of SACM645 and SUS304. Besides, even on the condition of 600mm in irradiating distance, surface hardening occurred in the case of SACM645 and SUS304. As for cross sections of the nitrided samples, as shown in Fig.4 which shows the cross section of the SACM645 sample nitrided on the condition of 180mm in irradiating distance, thick nitrided layer whose thickness was almost the same as that of the hard layer could be observed. Fig. 5 shows wear testing results in the case of SACM645 on the condition that #2000 sand paper was used as contact material. Although the total wear mass loss of the non-nitrided sample and nitrided sample at 15000 m wear distamce were of mass 10.2 mg, the mass loss of the nitrided sample by hydrogen/ nitrogen plasma jets was of mass 2.3 mg.

4. Conclusion

In order to develop a practical low temperature and high rate nitriding process, nitriding of nitriding steels were carried out. Consequently, surface hardening was obviously promoted on the condition that hydrogen/ nitrogen mixture gas were used as working gas in the cases of all substrates. Especially, hard layers with over 1000Hv in hardness were formed without any surface damages on the surfaces of the samples by only 5 minutes operation in the cases of nitriding steel and stainless steel. Besides, according to the results of wear testing, wear resistance properties of them were dramatically improved.

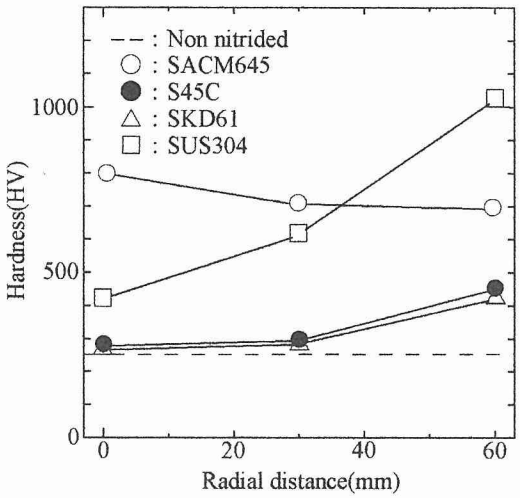

Fig.3 Radial profiles of surface hardness of the nitrided samples.

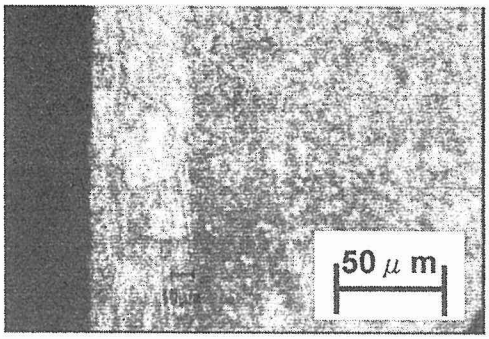

Fig.4 Optical micrograph of the Cross section of the nitrided SACM645 sample.

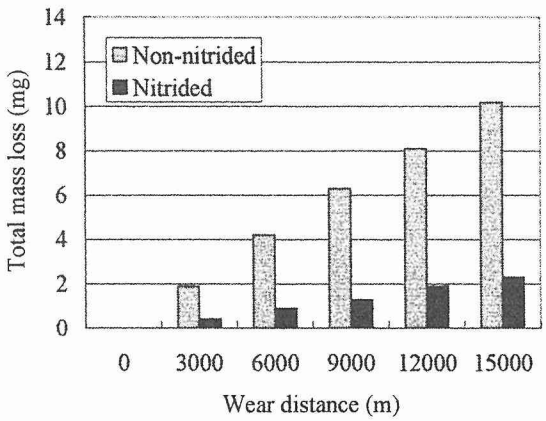

Fig.5 Wear testing results of the non-nitrided sample and the nitrided sample in the case of SACM645 using #2000 sand paper as contact material.

Atmospheric Corrosion Database of Low Alloy Steels in NIMS

Akira TAHARA, Hideki KATAYAMA and Toshiaki KODAMA

National Institutes for Materials Science, JAPAN

1. INTRODUCTION

Corrosion resistance is not an intrinsic property of materials, but is their interactive value with the environments. Since corrosion is a type of materials degradation following chemical reaction with the environments, corrosion data (such as the metal loss) were the very complex function with multiple variables (materials and environmental factors, such as temperature, chemical species and mechanical stresses etc.). The complexity of corrosion data makes it difficult to construct the corrosion database, especially in designing the data structures. Although a great effort has been devoted to the construction of corrosion database by many institutions, there exist a very few of systems open to the public[1)-4)].

With the progress of the study on the development of new structural materials resistant to of marine and coastal environments (a STX-21 project) at NIMS, the construction of corrosion database is deemed essential for a new material-designing particularly in the field of low-alloy weathering steels. The present paper reviews several topics on the above database system.

2. NECESSARY ELEMENTS FOR CORROSION DATABASE

Fig. 1 shows our image of the NIMS corrosion database systems. The necessary elements for this database will be two parts. First element is the user-interface, or functions. Second element is the contents of the database. Needless to say, most important part is the enhancement of the contents. However, some useful and beneficial functions are also occupied on an important part of the database system for many users. The most important one will be the efficient search engine or the thesaurus.

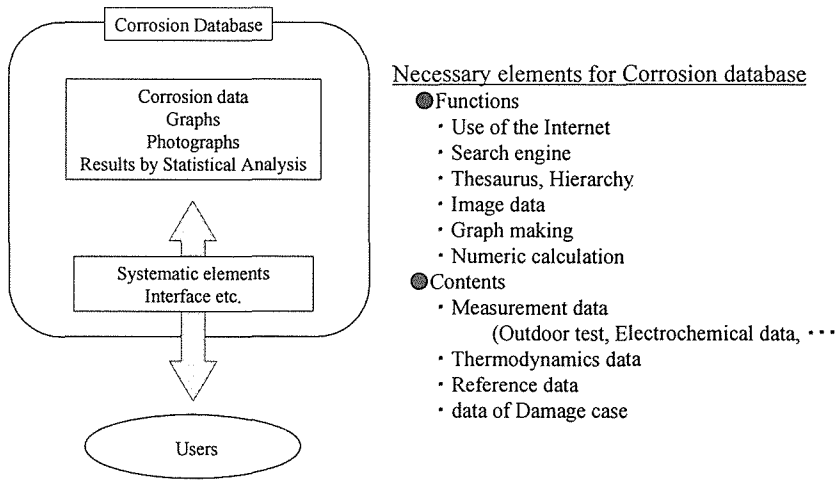

Fig.1 Image of corrosion database.

3. CONSTRUCTION OF THE NIMS CORROSION DATABASE

Fig.2 depicts a framework of the NIMS corrosion database system. This system is constructed of two server systems, "database server" and "network server" system. For the software of each server system, "Oracle workgroup server" and "application server" are used. Oracle workgroup server is a database server system, and our main database is constructed on this software. Oracle application server, a network server system, is controlled the communications on the network systems for users. Communications between each server applications are executed by SQL/Net system. In this database, the kinds of data are the character, numeric, graph and photograph data. The character and numeric data are stored on the database server system. The graph and photograph data are stored as a JPEG -type file in the database server, and the file names are used as an index of each data in this system.

When clients are going to access to the NIMS corrosion database, they connect to the workgroup server by a web browser on the internet system at first. They need to receive the attestation of "login"

for the database system. After this process, the gate of this system is opened to them.

NIMS corrosion database system actually consists of two query systems for the atmospheric corrosion tests data and chemical potential diagrams data. Fig.3 shows the flowchart of these query systems. The first one is the query system for the results of atmospheric corrosion tests executed by NIMS. The NIMS atmospheric corrosion tests have been executed for some low alloy steels at three exposure sites (Tsukuba, Choshi, and Miyakojima Island) in Japan. On the query system of the atmospheric corrosion DB, numeric data and photograph data can be searched. The numeric data is composed of metal losses of specimens and environmental factors of exposure sites, such as temperatures, relative humidity, deposition rates of sea salt etc. After searching the numeric data, clients are able to make some graphs by selecting each term of the x- and y-axes from the searching results on the network. As the graph making tool, the plug-in (ChartFX) of Internet Explorer is used. Therefore, there is a limitation that only users of "Internet explorer" can use this function.

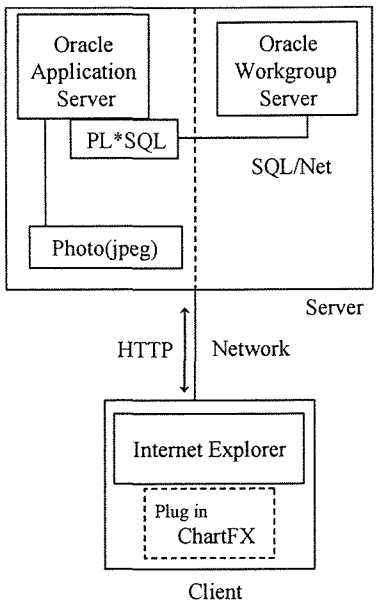

Fig.2 System of "NIMS Corrosion Database".

The second is the query system for the chemical potential diagrams data. The contents of this system are mainly about 40 kinds of the potential-pH diagrams for metal - H_2O systems. Clients can search some diagrams by elements and temperatures. These diagrams have been constructed numerically by using thermo-chemical data and saved as a GIF formatted file. Each chemical reaction data has been linked to the corresponding diagram data.

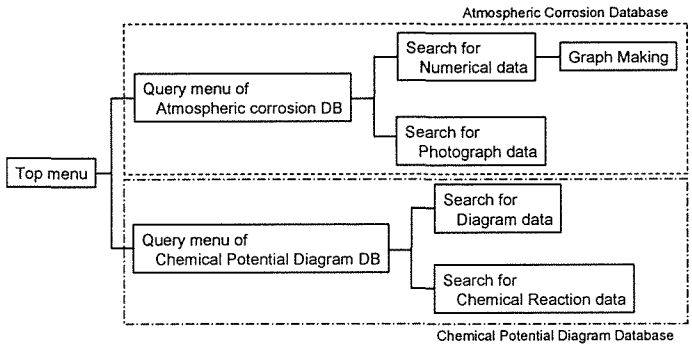

Fig.3 Flowchart of query system of NIMS corrosion

Fig.4 shows the example of the graph making after searching the atmospheric corrosion data. After making a graph, clients are able to change the conditions of graph axes and other formats of a graph.

This system is operating for the limited clients experimentally and will operate to the public soon.

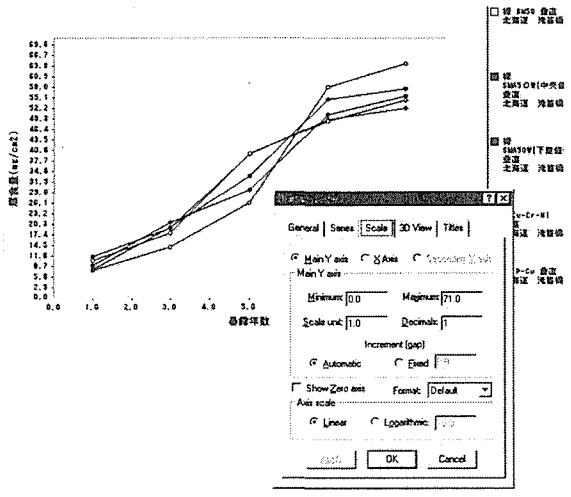

Fig.4 Example of the graph making.

References

1) E.D.During : "Corrosion Atlas, Third Edition", Elsevier(1997)

2) D.L.Gramer : "Corrosion Data Survey-Metals Section, Sixth Edition", NACE(1985)

3) http://www.nace.org/

4) http://www.cp.umist.ac.uk/

High Nitrogen Austenitic Steels: The New Corrosion Resistant Materials

Markus O. Speidel

Institute of Metallurgy
Swiss Federal Institute of Technology, ETH
CH 8092 Zurich, Switzerland

Type 304 and 316 are the most widely used austenitic stainless steels. These steels have been invented about ninety years ago, and their "stainlessness" is based on the beneficial role of chromium and molybdenum in forming and repairing a protective oxide layer. In order to achieve the face centered cubic crystal lattice with its favorable toughness, about ten percent nickel are added. Naturally, many alloy development efforts have carried the chromium and molybdenum contents higher in order to achieve even better resistance to corrosion, but this has also necessitated higher nickel contents, thus increasing significantly the cost of the more corrosion resistant steels.

The development of high nitrogen austenitic stainless steels can reverse this trend. Nitrogen is used to replace nickel, at least partially, and thus, the alloy cost has the potential to come down significally. The major benefit of nitrogen, however, is its beneficial influence on corrosion, particularly localized corrosion such as

- pitting corrosion
- crevice corrosion
- stress corrosion cracking

These forms of corrosion are reviewed systematically, and quantitative correlations are given which relate the corrosion resistance of the alloys in a particular environment to the alloy

composition. It is shown that both, pitting corrosion resistance and crevice corrosion resistance of a very large number of austenitic stainless steels can be correlated quantitatively with the alloy composition equivalent MARC (measure of alloying for resistance to corrosion) where

$$MARC = Cr + 3.3\ Mo + 20\ C + 20\ N - 0.5\ Mn - 0.25\ Ni$$

and the element symbol stands for the alloy content of that element in weight-percent.
The present paper demonstrates how this correlation has been used to create some of the most corrosion resistant austenitic stainless steels in existence.

Stress corrosion cracking in chloride containing solutions has been a problem even since steels type 304 and 316 have been used on a large scale. The new, nitrogen rich austenitic stainless steels, together with their adjustments in basic composition resist stress corrosion cracking, even in their high-strength and cold worked condition in concentrated NaCl solutions up to at least 105°C, where 304 and 316 and some of the duplex stainless steels fail readily by transgranular stress corrosion cracking.
This resistance to stress corrosion cracking is, however extended to high temperature water or nuclear reactor coolant at 288 to 350 °C only, if the basic composition contains high concentrations of nickel.
This development might thus become the future austenitic stainless steel in nuclear boiling water reactors (BWR), performing free of stress corrosion cracking.

Creation of High Nitrogen-bearing Stainless Steel and Its Mechanical Properties

Y, Katada, S. Sagara, Y. Kobayashi and T. Kodama
Corrosion Resistant Materials Research Group, NIMS, Japan

1. Introduction

The objective of this research is to develop a resource-saving type austenitic stainless steel with highly corrosion-resistant properties in seawater. Two key technologies were adopted to put forward the research. One is highly nitrogen-addition, and the other cleanliness of the material. In order to attain the both key technologies simultaneously, a pressurized electro-slag re-melting (P-ESR) furnace was newly developed in NRIM for the first time in Japan. Highly nitrogen-bearing stainless steel with more than 1mass% N was successfully created by P-ESR without addition of manganese, which showed excellent crevice corrosion resistant properties in artificial seawater [1][2]. In the present study mechanical properties of HNS such as tensile strength, proof stress, charpy impact energy were investigated.

2. Experimental procedure

The major specifications of the P-ESR developed in NIMS were as follows: maximum weight of ingot: 20kg in Fe-base; maximum pressure of nitrogen gas: 5MPa. Melting tests by the P-ESR were conducted under the conditions of 0.5～4 MPa in nitrogen gas pressure, 2000～3000A in AC current and 0.5～0.6kg/min in melting rate. FeCrN powder was used as the nitrogen source, which was packed in stainless steel pipes, sintered, and then spot-welded on the surface of the electrode. Flux used in the tests was a mixture of CaF_2 and CaO, all of which were added into the crucible before the melting test.

3. Results and Discussions

3.1 Melting Tests by P-ESR

Table 1 shows examples of melting test results by P-ESR. From these results it is obvious that the nitrogen contents of each heat is almost the same level as that of designed N level. As for the deoxidation by Ca-addition the oxygen content of each heat was decreased down to the level of 20-30 ppm. It was also found that the content of impurities such as P and S were decreased due to the purification effect by Ca -addition compared to those of primary electrodes. It was also empirically confirmed that the relation between nitrogen content and pressure could be predicted by using Sievert's law even at high N content.

Table 1 Examples of chemical compositions of HNS by P-ESR

Ch.No.	Materials	Position	C	Si	Mn	P	S	Ni	Cr	Mo	Ca	N	O
1	0%Ni18%Cr2%Mo1%N	Top	-	0.13	0.11	0.007	-	0.06	18.06	2.07	0.0006	1.01	0.0025
		Mid.	0.026	0.12	0.10	0.008	<0.0001	0.06	18.20	2.08	0.0006	1.04	0.0029
		Bot.	-	0.11	0.11	0.008	-	0.06	18.43	2.08	0.0004	1.08	0.0024
2	4%Ni23%Cr0%Mo0.8%N	Top	-	0.14	0.07	0.006	-	4.19	23.06	<0.01	0.0006	0.80	0.0029
		Mid.	0.024	0.13	0.08	0.006	<0.0001	4.16	22.96	<0.01	0.0006	0.81	0.0029
		Bot.	-	0.12	0.08	0.006	-	4.15	23.14	<0.01	0.0004	0.84	0.0030
3	4%Ni23%Cr2%Mo1%N	Top	-	0.15	0.09	0.007	-	4.2	22.99	2.03	0.0006	1.00	0.0029
		Mid.	0.026	0.14	0.08	0.007	<0.0001	4.22	22.92	2.05	0.0006	1.03	0.0030
		Bot.	-	0.13	0.08	0.007	-	4.20	23.23	2.04	0.0006	1.06	0.0032
4	4%Ni23%Cr2%Mo1%N	Top	-	0.15	0.09	0.007	-	4.15	23.13	2.03	0.0012	1.01	0.0025
		Mid.	0.027	0.17	0.08	0.007	<0.0001	4.17	22.98	2.06	0.0012	1.02	0.0022
		Bot.	-	0.17	0.07	0.007	-	4.16	23.18	2.05	0.0007	1.09	0.0024
5	SUS304L+0.8%N	Top	-	0.34	1.45	0.028	-	8.04	23.42	0.12	0.0008	0.86	0.0029
		Mid.	0.038	0.34	1.45	0.028	0.002	8.08	23.63	0.12	0.0008	0.87	0.0028
		Bot.	-	0.33	1.51	0.029	-	8.05	23.87	0.13	0.0006	0.89	0.0033

3.2 Mechanical properties of HNS

Figure 1 indicates the temperature dependences on tensile stress and proof stress of 23%Cr-4%Ni-1%N. Heat treatment of the material was solution treatment of 1473K for 30min followed by water quench. Solid and dashed lines indicate the relevant data of Type 316 stainless steels for reference. It was found from this figure that HNS showed good mechanical properties in the wide range of temperature from 77K to 773K. Fig.2 shows temperature profile on elongation (EL) and the reduction of area (RA) of HNS as well as the reference data of Type316. It was also found that EL and RA of HNS were almost the same level as those of Type316.

3.3 Charpy impact test

Charpy impact test of No.4 in Table 1 was carried out. Fig.3 indicated the Charpy impact test data in terms of Charpy impact energy and the area fraction of ductile fracture. Reference data of Type 304 from a literature was also indicated.

It was found from Fig.3 that striking transient temperature of about 223K was observed, while Type 304 showed no striking transient temperature. It was also found that there was a good relation between Charpy impact energy and lateral expansion of HNS

4. Conclusions

1. By using a P-ESR method, high nitrogen-bearing austenitic statinless steel with more than 1mass% of nitrogen content was successfully fabricated without the addition of manganese.
2. Good mechanical properties of HNS in terms of tensile strength and proof stress were confirmed in the wide range of temperature.
3. After Charpy impact tests of HNS, striking transient temperature of about 223K was observed. The upper shelf energy was about 360 J/cm^2.

References

[1] Y. Katada et al., Proc. of THERMEC '2000 (2001), B1-7.

[2] Sagara, M. et al., Proc. of the 20th Meeting of The Electrochemical Society, The 52ndMeeting of the International Society of Electrochemistry, USA (2001).

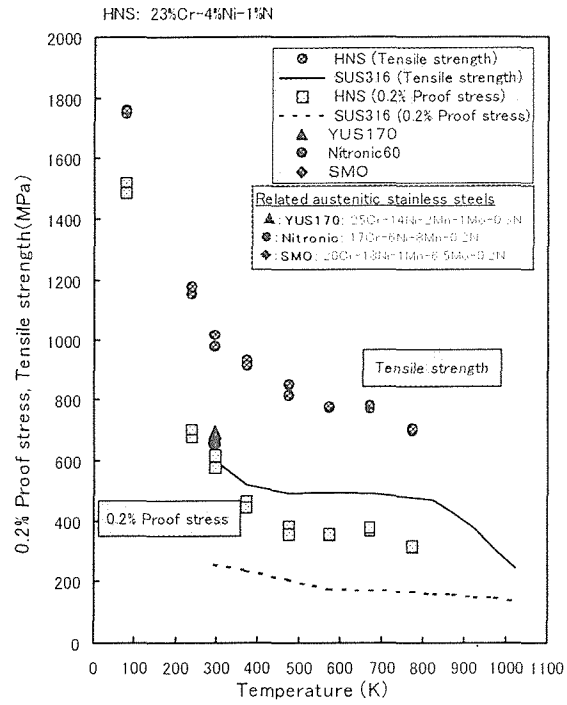

Fig. 1 Temperature dependence on tensile strength and proof stress of HNS

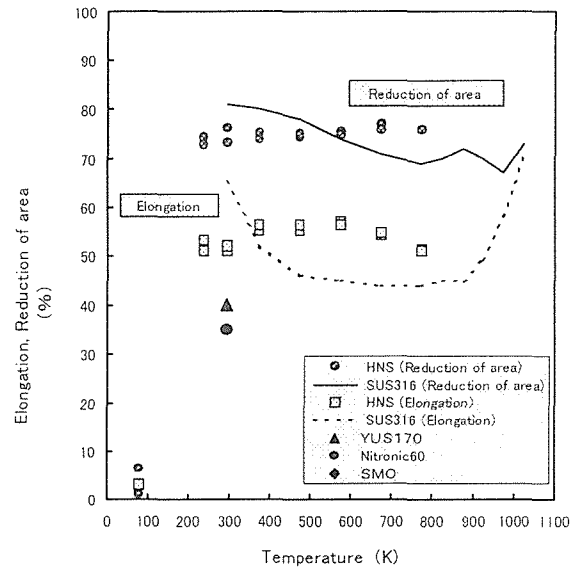

Fig.2 Temperature dependence on reduction of area and elongation.

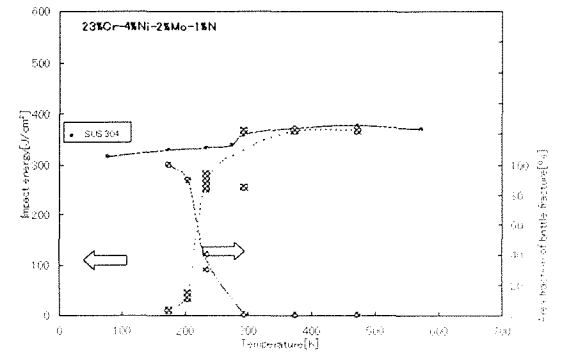

Fig.3 Impact energy of HNS

Study on the Weldability of High Nitrogen Stainless Steels

M. Ogawa, K. Hiraoka, Y. Katada, M. Sagara, and S. Tsukamoto
Joining and Interface Research Group, NIMS, Japan

1. Introduction

High nitrogen-bearing stainless steels (HNS) containing about 1mass% nitrogen without addition of Mn showed superior localized corrosion resistance and mechanical properties [1]. The weldability of the HNS is an important issue to be solved from the viewpoint of engineering sense. Because of nitrogen supersaturation at a molten state under the atmospheric pressure or at a solid state below the solvent temperature range, blowhole formation and nitride precipitation are intrinsic problems in the welding process. In this report, the effect of suppression of the blowhole inclusions and the localized corrosion properties of the weld metal using high Cr-Mo steel welding consumables were discussed as well as the chromium nitride precipitation behavior at heat affected zone (HAZ).

2. Experimental procedure

23Cr-4Ni-2Mo-1N,23Cr-4Ni-2Mo-0.8N and 27Cr-3Ni-1N steels were used as base metals. All steels were melted by pressurized electro-slag remelting method. High Cr containing steels were used as welding consumables in order to increase the nitrogen solubility at molten state. Welding of HNS was performed by gas tungsten arc (GTA), CO_2 laser and plasma arc welding under the condition of one-side one-pass butt welding. The localized corrosion resistance of the weld metals or welded joints was examined by the measurement of critical pitting corrosion temperature in 6% $FeCl_3$ solution.

3. Results and discussion

3.1 Suppression of blowhole inclusions in the weld metal

When HNS were welded without welding consumables, the weld metal included many blowholes. On the contrary, when HNS were welded using high Cr containing steel as welding consumable and the dilution rate was held at a low value, no blowholes were observed. To control the nitrogen content in the molten metal smaller than its nitrogen solubility was effective to suppress the generation of blowhole [2].

3.2 Localized corrosion resistance of the weld metal

The critical pitting corrosion temperature (CPT) of the weld metals dropped compared with those of base metals because of the micro segregation of alloy elements. FA solidification mode was most suitable to minimize the CPT drop after comparison with other solidification modes [2]. But as shown in Fig.1, the zone where the base metal melted and solidified to be mixed incompletely with the welding consumable certainly existed near the fusion line. Pitting often occurs at this zone. In this zone, weld metal was solidified as A mode despite that the weld metal composition was designed to solidify as FA mode. Therefore the minimum pitting corrosion resistance equivalent (PRE) value in this zone became smaller than that in ordinary weld metal. The composition of the welding consumables should be designed accounting this minimum PRE value.

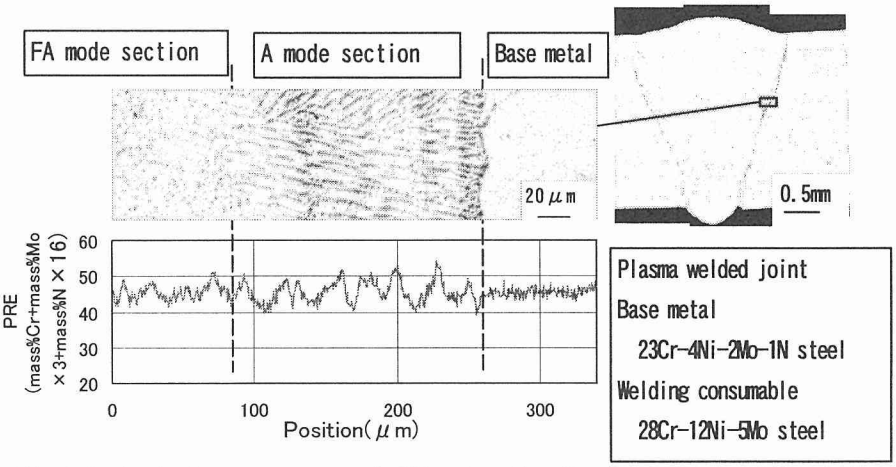

Fig. 1 Optical microstructure and PRE value distribution near the fusion line

3.3 Chromium nitride precipitation behavior at HAZ

At the grain boundary in the HAZ, Cr_2N precipitates were observed and resulted in the degradation of localized corrosion resistance. Fig 2 shows the time-temperature-precipitation curves of a few HNS. In the case of 23Cr-4Ni-2Mo-1N steel, aging at the temperature range from 1173 to 1373K for 2 seconds caused CPT drop compared with that of the base metal [3]. The aging time that caused CPT drop could be slightly delayed to as long as 4 seconds by the reduction of N content from 1N to 0.8N. In the case of 27Cr-3Ni-1N steel, the aging time that caused CPT drop was also slightly delayed due to the expansion of the temperature range where austenitic single phase was stable by higher Cr and Mo free composition.

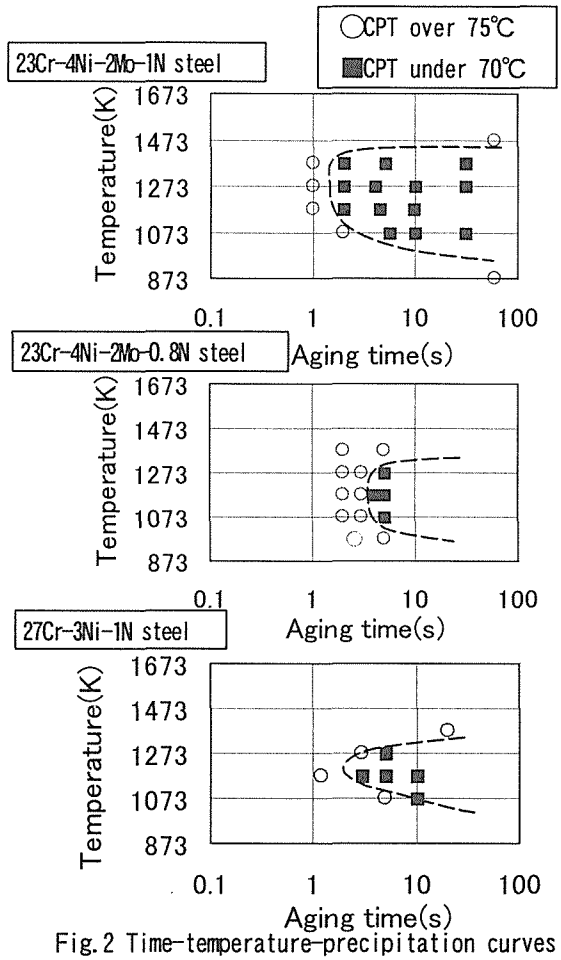

Fig. 2 Time-temperature-precipitation curves

3.4 Pitting corrosion resistance of welded joints

CPT of HNS welded joints are shown in Fig.3. Horizontal axis shows the holding time over 1073K at HAZ. All specimens shown in this figure were pitted at HAZ. Only the laser welded joint and the plasma welded joint under the smallest heat input condition exhibited 348K CPT. In the case of the larger heat input plasma welded joints and the GTAW joint, serious decrease of CPT was observed. To use the 23Cr-4Ni-2Mo-0.8N steel as base metal gave just a little relief of the CPT decrease compared with the 23Cr-4Ni-2Mo-1N steel.

4. Conclusion

Weldability of HNS containing about 1mass% nitrogen was investigated. Obtained results were summarized as follows.

(1)Blowhole inclusion was suppressed by using high Cr containing welding consumables.

(2)The weld metal in the incompletely mixed zone solidified as A mode and minimum PRE value in this zone decreased compared with that in ordinary weld metal which solidified as FA mode.

(3)Cr_2N precipitated at HAZ by short time aging. Precipitation could be slightly delayed by adjusting the base metal composition.

(4)The small heat input welded joints by laser and plasma welding showed 348K CPT.

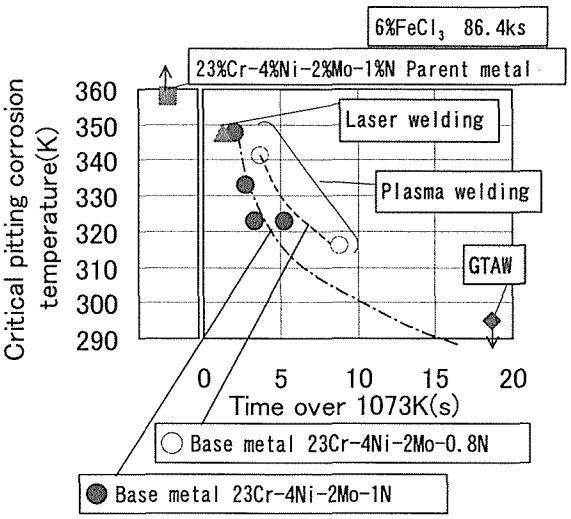

Fig. 3 CPT of welded joints

References

[1] Katada Y.., Sagara M., Ogawa M., Baba H., and Kodama T., Proc.4th Workshop on the Development of High Performance Structural Steels for 21st Century, pp.333-336.

[2] Ogawa M., Hiraoka K., Katada Y., Sagara M.., Siga C., Quar. J. Japan Welding Soc.,20-1(2002),pp.96-105.

[3] Ogawa M., Hiraoka K., Katada Y., SagaraM.., Tsukamoto S., Siga C., Quar. J. Japan Welding Soc.,20-1(2002),pp.106-113.

Mechanical Properties of Weld Metal For High Nitrogen Stainless Steel

Osamu Kamiya*, Yasushi Kikuchi**, Zhan W. Chen***
* Faculty of Engineering and Resource Science, Akita University
**Joining and Welding Research institute, Osaka University
***Faculty of Science and Engineering, Auckland University of Technology

1. Introduction

The high nitrogen stainless steel (HNS) are high strength and high toughness at low temperature and good corrosion resistance. However, the properties introduced by nitrogen additions could be affected by welding [1,2]. We investigated the relationships between microstructure and fracture toughness of the welds were then studied. Furthermore, the effect of post weld heat treatment was examined to improve the low temperature fracture toughness.

2. Experimental procedure

The gas metal arc (GMA) welding was performed inside the chamber with 1.8m^3 volume capacity for the high pressure up to 6.1 MPa. The arc length was approximately 7mm, the current was 260A and the moving speeds of test plate were 3.3mm/s.

The materials used are shown in Table 1. Nitrogen contents in weld metals were determined by using O-N gas analyzer. Charpy impact test with half-size were performed at low temperature from 290K to 77K. The PWHT heat treatment temperature range is from 773K to 1573K.

Table 1 Chemical compositions of materials used.
(Mass %)

Material			C	Si	Mn
Base metal 316L			0.018	0.70	1.22
Filler wire Y316L			0.019	0.39	1.75
High Nitrogen steel			0.020	0.15	6.00
Ni	Cr	Mo	N	O	Fe
12.08	17.38	2.03	0.0230	0.0035	Bal.
11.20	19.98	2.34	0.0169	0.0020	Bal.
10.00	23.00	2.00	0.480	-	Bal.

3. Results and discussion

Welding in high nitrogen pressure Figure 1 shows the nitrogen content (N) in the first pass weld- metal as a function of the nitrogen pressure during welding. The values of N increase with the increase in the pressure, reaching 0.65% at 6.1Mpa. Figure 2 show the pores present in the HNS welds made at atmospheric pressure of Argon. A number of fine pores can be observed near to the fusion boundary of partial melting zone.

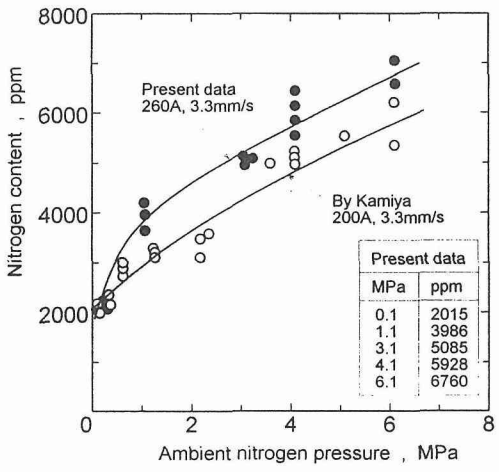

Fig. 1 Effect of the ambient nitrogen pressure on the nitrogen content of welded metal.

Mechanical Properties Results of the Charpy impact tests are shown in Fig.3 for the as-weld. The impact value increases with the increase in nitrogen content up to 0.4%. Slightly above this value, there is a

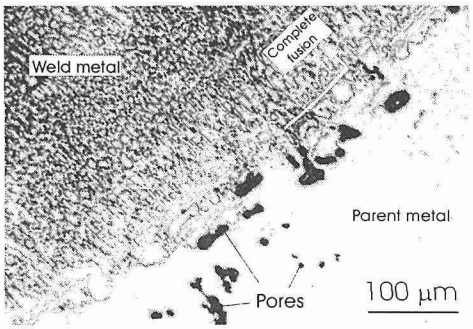

Fig. 2 Micrographs of the weld metal in 0.1Mpa gas shield. (N=0.78% in Parent metal)

brittle transition where impact energy decreases sharply with the further in nitrogen content. Figure 4 surmised the effect of heat-treatment on impact energy values. Comparing with the phase diagram of Fig. 5, the formation and solution of the brittle Cr_2N phase corresponds to the impact toughness. For N content lower than 0.5% in 20Cr-12Ni steel, the toughness could be improved by heat treatment at temperatures higher than approximately 1500 K. This is because Cr_2N were dissolved in the γ-phase solid solution. However, for N content higher than 0.5%, toughness could not be improved by any heat treatment, despite the fact that Cr_2N was dissolved. This behavior could be related to the formation of solidification micro-cracks.

Effect of Mn Addition Extensive metallographic examination has revealed that Mn addition has prevented the formation of solidification micro-cracks and an example is illustrated in Fig. 6. It is likely that the impact energy is very sensitive to these micro-cracks in Mn-free welds when testing at low temperatures. In the case of Mn addition, the solidification front was a complex and had resulted in a lower density of the weak and brittle inclusions along the grain boundaries.

5. Conclusions

Toughness increases with nitrogen content when N<0.4%. When N>0.5%, Cr_2N formed in grain boundaries resulting in brittle fracture. Heat treatment over 1400K increased the fracture toughness of the weld metal. The fracture toughens is constant low at N content higher than 0.5% because of the micro hot cracking. Mn addition in weld metal prevented the formation of micro-cracks and increased the fracture toughness.

References

[1] O. Kamiya and Y. Kikuchi, Materials Science Forum Vols. 318-320, Trans Tech Publications, Switzerland, 1999, 609-614.

[2]T. Ogawa and T. Koseki. Welding Journal, 67(1988) 8s-17s.

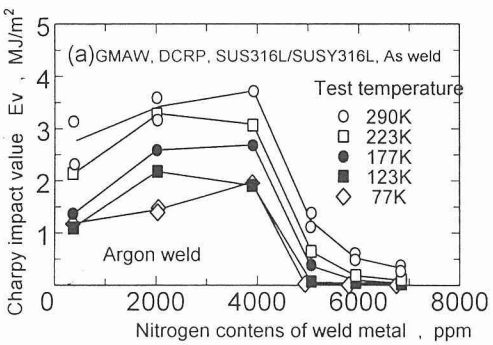

Fig. 3 Influence of nitrogen content and heat treatment on Charpy impact values.

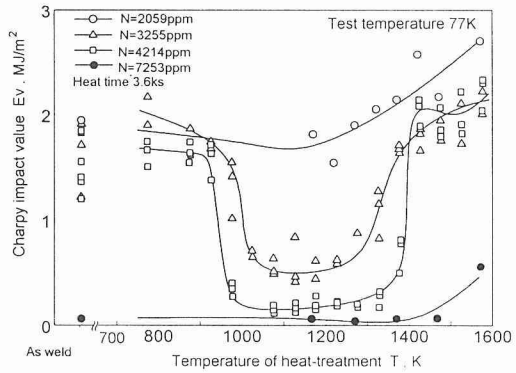

Fig. 4 Effects of heat treatment temperatures on Charpy impact values.

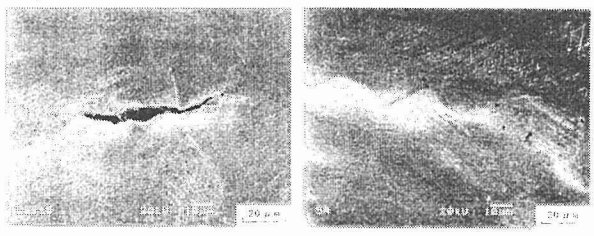

Fig. 6 SEM micrographs of high nitrogen weld (N>0.5%), (a) Micro cracks were observed in the grain boundary (b)Mn addition prevented the cracking.

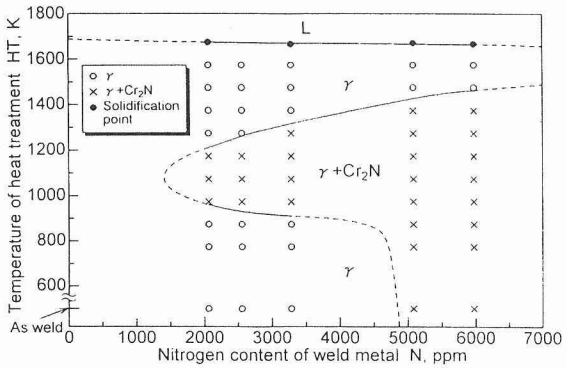

Fig. 5 Sectional phase diagram of Fe-18Cr-12Ni-N.

Localized Corrosion Behavior of High Nitrogen-bearing Austenitic Stainless Steels in Seawater Environment

M. Sagara, Y. Katada and T. Kodama
Corrosion Resistant Materials Research Group, NIMS, Japan

1. Introduction

In seawater environment, localized corrosion of stainless steels become a problem. It is well known that alloying chromium, molybdenum or nitrogen are effective in order to improve pitting and crevice corrosion resistance of stainless steel. As resource saving type stainless steel with excellent localized corrosion resistance, ultra-high nitrogen-bearing stainless steels of about 1 mass% with high purity were obtained by pressurized electroslag remelting (P-ESR) method. In this study, crevice corrosion behavior of high nitrogen-bearing stainless steels up to 1.1 mass % were investigated in artificial seawater.

2. Experimental procedure

23%Cr-4%Ni-0/2%Mo-0.7/1.1%N stainless steels were used as test specimen. Specimens were highly purified with ultra-high nitrogen of about 1 mass% obtained by P-ESR system. In this system, ingots were produced by remelting the premelt-electrode under high pressure with nitrogen gas. To obtain test specimen, ingots were cut, forged, and hot rolled, followed by solution heat treatment. It was confirmed that all materials used in tests had an austenite single-phase microstructure.

Crevice corrosion resistance of stainless steels was evaluated by means of electrochemical corrosion test using multiple crevice specimens. The test solution was artificial seawater. After scanning potential by 1mV/min from the corrosion potential to a fixed potential(E_{set}), then the specimen was held at the potential during for 48 hours. The fixed potential was raised up by every 25mV. Crevice corrosion potential (CCP) is defined as the noblest potential at which crevice corrosion does not occur through the test. Generation of the crevice corrosion is confirmed not only by visual observation after the tests but also the current response under the test. Surface analysis was conducted by X-ray photoelectron spectroscopy (XPS) using monochromatic-AlK_α X-rays (hν=1486.6eV) over an area of about 200mmϕ.

3. Results and discussion

Crevice corrosion resistance of nitrogen-bearing stainless steels was evaluated by electrochemical crevice corrosion tests. Fig.1 shows an example of scanning potential and current response during crevice corrosion test of 23%Cr-4%Ni-0%Mo-1%N steel at 35℃ (E_{set}:+550mV vs.SCE). Current observed during potential scanning was the passive current. After potential was set to constant potential (E_{set}), passive current tended to decrease gradually. The increase of current after 30h indicates the generation of crevice corrosion. After the test, crevice corrosion was visibly reconfirmed for the specimens, which showed this kind of current profile. It should be noted from Fig.1 that continuous current observation might be effective for the monitoring the generation of crevice corrosion.

Figure 2 shows a relationship between CCP and nitrogen contents in artificial seawater. It was seen that there was a positive correlation between nitrogen contents and CCP. Crevice corrosion of steels attached arrows were not recognized in any potential below 0.9V vs.SCE. It was also found that ultra high nitrogen stainless steels containing molybdenum have superior crevice corrosion resistance.

Surface of high nitrogen stainless steel was analyzed by using XPS. Take-off angle was changed to determine the depth profile. After polarization at passive potential region (+300mV vs.SCE), alloying nitrogen or nitride peak of N1s spectra appeared at higher take off angle measurement. So, it was found that nitrogen concentrated at inner layer such as the interface between passive film and bulk metal. The enriched nitrogen at the interface may be possible to improve crevice corrosion resistance.

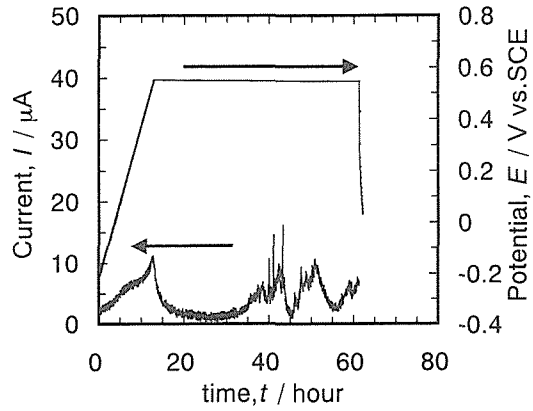

Fig.1 Scanning potential and current response during crevice corrosion test of 23%Cr-4%Ni-0%Mo-1%N steel in artificial seawater at 35℃.

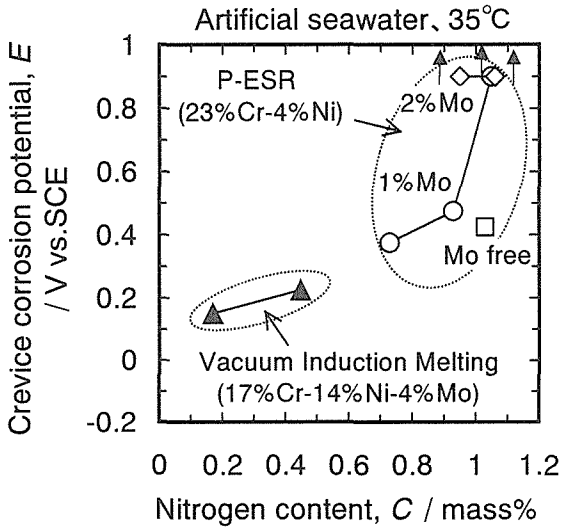

Fig.2 Relationship between crevice corrosion potential and nitrogen content in artificial seawater (35℃)

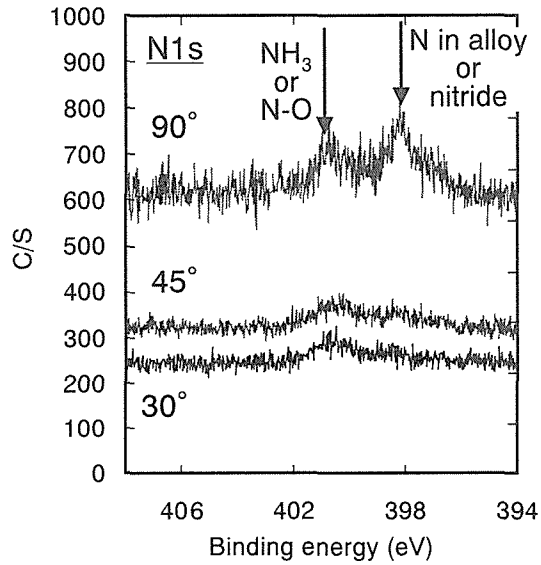

Fig.3 ESCA spectra (N1S) recorded after polarization of 23%Cr-4%Ni-0%Mo-1%N at +300mV vs.SCE in artificial seawater for 2h. The take off angle was changed.

4. Conclusion

(1) By the electrochemical evaluation in artificial seawater, high nitrogen-bearing austenitic stainless steels created by P-ESR have good crevice corrosion resistance.

(2) At the passive state of high nitrogen stainless steels, it is indicated that nitrogen tends to concentrate at inner layer of the surface.

Influence of Alloying Elements on Pitting Corrosion Resistance of High Nitrogen-Bearing Cr-Mn Steels

M. Fujisawa, Y. Katada, and T. Kodama
Corrosion Resistant Material Research Group, NIMS, Japan

1. Introduction

Utilizing the high nitrogen solubility in austenitic phase, nitrogen can be introduced into the surface of steels by a diffusion process called ''nitrogen absorption in solid state[1]'' or ''solution nitriding[2]''. In this process, solute nitrogen content is subjected to the nitrogen gas pressure and heating temperature. This process will be effective for improving localized corrosion resistance of stainless steels in chloride-containing environment. In this study, high nitrogen-bearing Fe-Cr martensitic steel and Fe-Cr-Mn austenitic steel were produced by this process, and the pitting corrosion resistance was investigated. The combined effect of Cr and N on the corrosion resistance was also discussed.

2. Experimental Procedure

Chemical compositions of specimens are shown in Table 1. These steels were hot-rolled and cold-rolled to 1.4mm thickness. As the nitrogen absorption treatment, these sheets were heated at 1423-1473K for 24-48h in N_2 gas of 0.015-0.1MPa followed by water-quenched. Microstructure of the specimens ware analyzed by X-ray diffraction analysis and optical microscopic observation. Pitting potential measurement were carried out in 3.5mass%NaCl solution de-aerated by argon gas at 303K and the compositions of the passive film were analyzed by Auger electron spectroscopy (AES).

Table1. Chemical compositions of specimens before nitrogen absorption treatment in mass%.

	C	Si	Mn	P	S	Cr	N
Mn free	0.015	0.41	0.29	0.030	0.005	9.98	0.0100
	0.010	0.41	0.31	0.032	0.006	12.90	0.0092
	0.010	0.29	0.31	0.029	0.004	14.90	0.0105
	0.010	0.29	0.22	0.027	0.004	18.11	0.0120
15Mn	0.017	0.27	14.9	0.030	0.008	11.84	0.0100
	0.012	0.26	15.3	0.027	0.005	15.10	0.0063
	0.012	0.27	15.2	0.028	0.005	18.11	0.0086

3. Results and Discussion

3.1 The amount of nitrogen and the phase after nitrogen absorption treatment

Fig.1 shows the saturated nitrogen contents of steels heated at 1473K in 0.1MPa N_2 gas atmosphere. Dashed lines indicate the calculated solubility at 1873K. The solubility of nitrogen at solid state is higher than that in liquid state. The nitrogen contents of martensitic steels and austenitic steels were 0.2-0.6mass% and 0.5-1.0mass%, respectively.

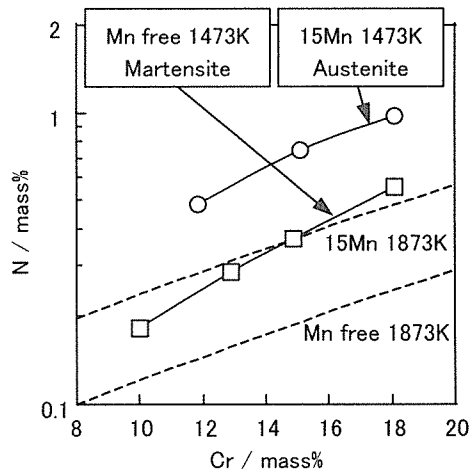

Fig.1 Equilibrium solute N content of Fe-Cr-N and Fe-Cr-Mn-N steels in 0.1MPaN_2 gas atmosphere.

3.2 Pitting potential measurement

Fig.2 shows the effect of nitrogen absorption treatment on pitting potential of the steels in 3.5mass%NaCl at 303K. It was found that nitrogen absorption treatment in solid state was very effective for improving the resistance to pitting corrosion. The effect of the treatment is

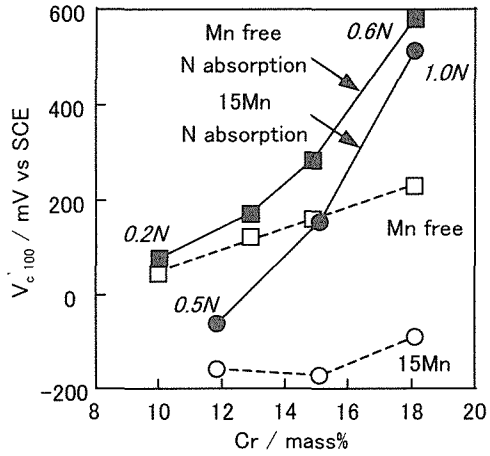

Fig.2 Effect of nitrogen absorption treatment on pitting potential ($V_{c'100}$) of Fe-Cr-Mn steels in 3.5mass%NaCl at 303K. [The condition of nitrogen absorption treatment: 1473K,0.1MPaN_2]

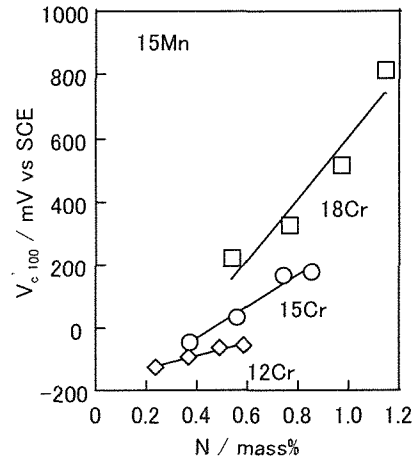

Fig. 3 Effect of N and Cr content on pitting potential ($V_{c'100}$) of Fe-Cr-15Mn-N austenitic steels in 3.5mass%NaCl at 303K.

remarkable in high Cr-containing steel which absorbs much nitrogen.

Fig.3 shows the effect of Cr and N content on pitting potential of Fe-Cr-15Mn-N austenitic steels in 3.5mass%NaCl at 303K. Irrespective of Cr content in steels, the pitting potential rises with the increase in N content. However, it was noticed that pitting potential of those steels with higher Cr content indicates stronger effect of N.

Fig.4 shows the AES depth profile of passive film formed on Fe-18Cr-15Mn-1N austenitic steel in 3.5mass% NaCl at 303K. Judging from the oxygen content in the passive film, N may be enriched in the interface of metal and passive film. The enhanced corrosion resistance of high nitrogen-bearing Fe-Cr-Mn steel may be attributed to the enrichment of N.

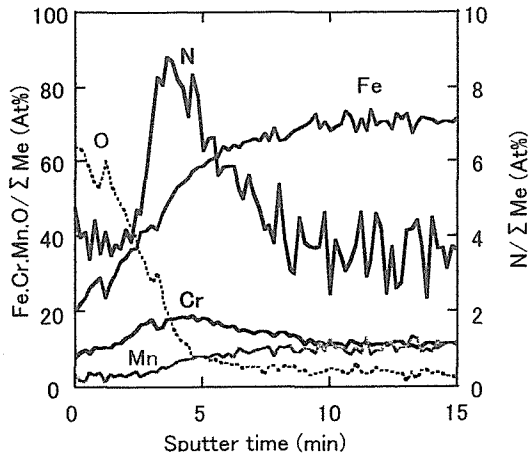

Fig. 4 AES depth profile of passive film formed on Fe-18Cr-15Mn-1N austenitic steel in 3.5mass%NaCl at 303K.

4. Conclusions

High nitrogen-bearing Fe-Cr martensitic steel and Fe-Cr-Mn austenitic steel were produced by the nitrogen absorption treatment in solid state, and the effect of Cr and N on the pitting corrosion resistance was investigated.

(1) The nitrogen absorption treatment in solid state is effective for improving pitting corrosion resistance.

(2) The effect of nitrogen addition on pitting corrosion resistance is remarkable in high Cr-containing steel.

References

[1] Nakamura.N and Takaki.S, ISIJ International, 36(1996), pp.922-926.

[2] Berns.H and Siebert.S, ISIJ International, 36(1996), pp.927-931.

Effect of grain refinement on strength and corrosion resistance of AISI 304 stainless steels

A. Di Schino*, I. Salvatori** and J.M. Kenny*

*Materials Engineering Center, University of Perugia, Italy.
**Centro Sviluppo Materiali, Italy.

Although there have been many studies on fine grained ferritic steels, only few works are on grain refinement of austenitic stainless steels and, in particular, on the influence of the grain size on the corrosion resistance of this class of materials. The grain size of ferritic steels can be refined by thermo-mechanical processes including phase transformation, but in austenitic stainless steels, due to the absence of a phase transformation at working temperatures, the grain diameter is usually controlled by recrystallization after cold working [1] or imposing (uniaxial or multiaxial) very severe deformations in order to start dynamic recrystallization [2].

The only way to have a phase transformation is to create martensite during cold rolling.

In particular, ultrafine grained AISI 304 stainless steel of 0.8 μm average grain size was obtained by applying martensitic transformation (i.e. rolling at subzero temperatures) and annealing at low temperatures in order to get austenitic reversion [3]. In this paper, the effect of grain size on the tensile properties and on the corrosion resistance of an AISI 304 stainless steel is reported.

Fig.1 shows the dependency of the yield stress (R_{p02}) and tensile strength (R_m) on grain size: it is clear that both R_{p02} and R_m linearly increase with increasing $d^{-1/2}$. The same trend is shown in Fig.2, where hardness versus grain size is reported. It means that, in the AISI 304 stainless steel, Hall-Petch relationship holds at least down to 0.8 μm of grain size.

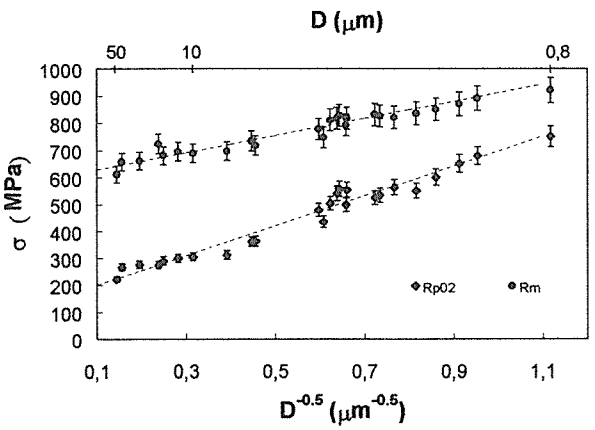

Fig.1 Tensile properties versus grain size for AISI 304 .

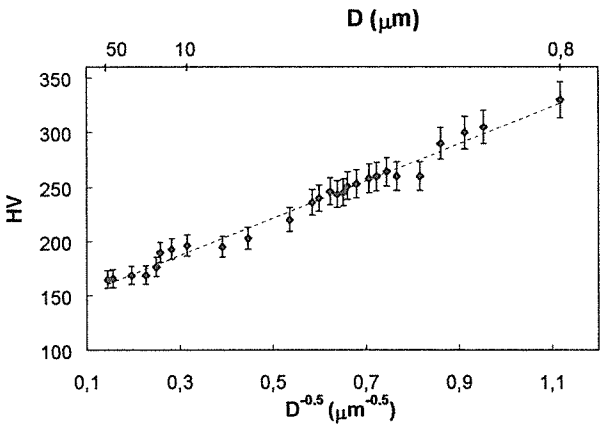

Fig.2 Hardness versus grain size for AISI 304.

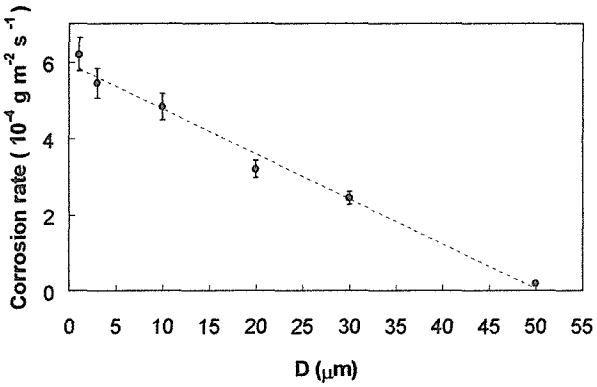

Fig.3 Relation between the general corrosion rate in boiling 5% H_2SO_4 solution and the average grain size.

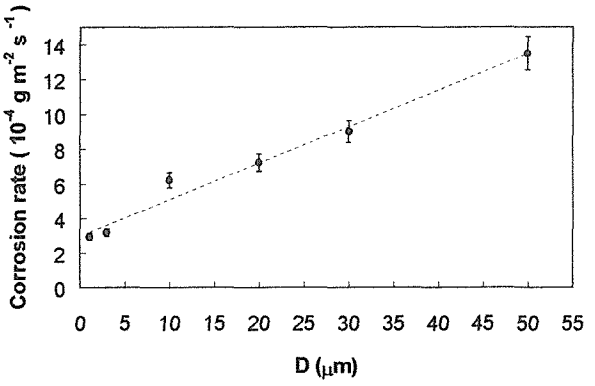

Fig.4 Relation between the intergranular corrosion rate in boiling Streicher solution and the average grain size.

Preliminary tests in order to ascertain the general corrosion rate of AISI 304 stainless steel were carried out in 5% H_2SO_4 boiling solution for 36 ks for samples having different grain sizes, ranging from 0.8 to 50 μm. The corrosion rate of AISI 304 increases with decreasing grain size (Fig. 3). These results can be interpreted in terms of defects concentrated in grain boundaries; increasing the grain boundary surface area by grain refinement seems to cause passive film destabilization, and thus ultrafine-grained steels show a reduction of the general corrosion resistance.

The intergranular corrosion rate of AISI 304 stainless steel was measured in H_2SO_4-$FeSO_4$ (Streicher solution) for 36 ks, and the results are shown in Fig.4. The corrosion rate decreases with decreasing grain size. As intergranular corrosion is caused by the precipitation of carbides at grain boundaries, the corrosion rate is affected by the volume fraction of carbides per unit grain boundary area. As grain boundary per unit volume increases with decreasing grain size, the degree of Cr depletion, caused by carbide precipitation, will decrease for a given C content. Hence, grain boundaries are less sensitised in fine grained materials.

The pitting corrosion tendency of AISI 304 steel was evaluated in 10% $FeCl_3$-$6H_2O$ solution at room temperature for 36 ks. In this case, grain refinement leads to an improved pitting corrosion resistance. The pitting of coarse grains initiates at few sites, with large and deep individual pits. In contrast, the pitting of ultrafine grained steel initiates at several sites, but with smaller individual pits, which results in a lower corrosion rate. This can be quantitatively explained by a decreasing anodic current density; in fact, the increase of pitting corrosion sites in the ultrafine grained steel leads to a decrease of cathodic area and the consequent decrease of anodic current density.

From these preliminary results the ultrafine grained AISI 304 stainless steel exhibits a higher resistance to local corrosion susceptibility.

References

[1]Reed-Hill, R.E.,"Physical metallurgy principles" PWS Publishing Company (1994).

[2]Kiyoshige, K. and Pyusuke,S., *J. Japan Institute of Metals*, **44** (1980) 1037.

[3]Di Schino, A., Kenny, J.M., Salvatori, I. and Barteri, M, in *Proc. of the 4th International Conference on Stainless Steel*, Paris, in press.

Strengthening of a structural high nitrogen austenitic stainless steel by grain refinement

I. Salvatori*, A. Di Schino** and J.M. Kenny**

*Centro Sviluppo Materiali, Italy.
**Materials Engineering Center, University of Perugia, Italy.

Austenitic stainless steels have been indispensable for the progress of technology during the last 80 years. Due to the cost of nickel and to the prospected possibility of allergic reactions caused by this element, more and more laboratories and industries are trying to develop a new class of austenitic stainless steels with a low content of nickel [1]. In order to maintain the austenitic microstructure, nickel reduction is balanced by nitrogen addition. Nitrogen addition to austenitic stainless steels is also very effective for improving yield strength and corrosion resistance [2]. In order to further increase the strength, it is possible to combine the effect of nitrogen addition and grain refining.
Due to the absence of phase transformation at usual working temperatures, a way to promote grain refining can be a martensitic transformation rolling at subzero temperature and then annealing to get austenite reversion. In another paper [3] we examined the effect of subzero rolling on grain refinement on AISI 304 stainless steel.
The purpose of this study is to examine the relationship between microstructure and mechanical properties of a high nitrogen austenitic stainless steel with ultrafine grained structure obtained by means of cold rolling and subsequent annealing. The chemical composition of the steel is shown in Table.1.

Table.1 Chemical composition of the high nitrogen steel (mass %)

Cr	Ni	Mn	Cu	Si	Mo	N	P	S	C
18.5	1.07	11.4	1.07	0.12	0.08	0.37	0.022	0.003	0.037

Samples taken from an industrial hot rolled strip were rolled at about T=-100°C and then annealed using a laboratory furnace to get austenite reversion. The effects of annealing temperature on grain size is shown in Fig.1 for T=900°C and T=1100°C. Results show that for T=1100°C grain boundary diffusion is activated with a consequent grain growth, while for T=900°C the average grain size (2.5μm) is almost constant in time.
The effect of grain size on tensile properties is shown in Fig.2, also similar measurements on a standard AISI 304 stainless steel are shown. The positive effect of nitrogen addition in increasing steel strength for a given grain size are outlined; furthermore, grain size effect in strengthening is observed for both steels.
In particular, the Hall-Petch dependency for the yield strength (R_{p02}) is found to be valid for the examined grain size ranges of both the high nitrogen steel [50-2.5 μm] and the AISI 304 stainless steel [50-0.8 μm] [3]. In Fig.3 hardness versus the square root of grain size is reported for both the high nitrogen and the AISI 304 stainless steel. Fig.4 shows that the ductility of the high nitrogen steel is slightly lower than that of the AISI 304 stainless steel. Total elongation it is reduced by decreasing grain size in both steels.

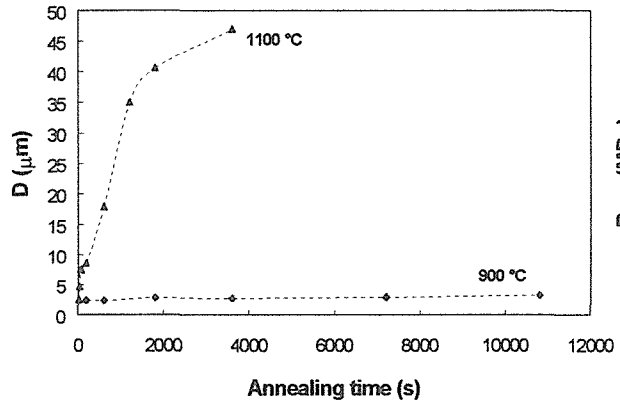

Fig.1 Time-temperature effect on the recrystallization of high nitrogen steel.

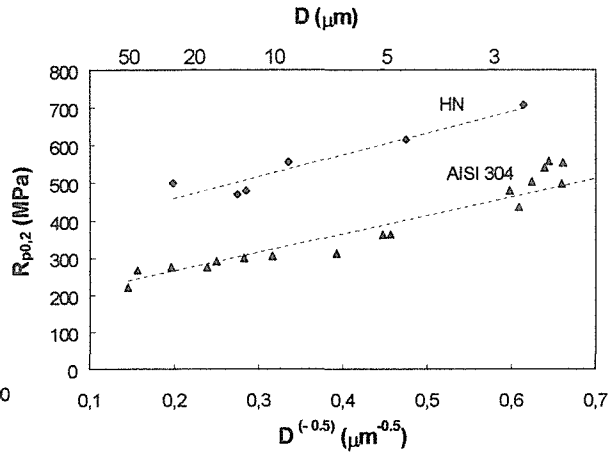

Fig.2 Grain refinement effect on the yield strength of high nitrogen steel in comparison to the AISI 304 stainless steels.

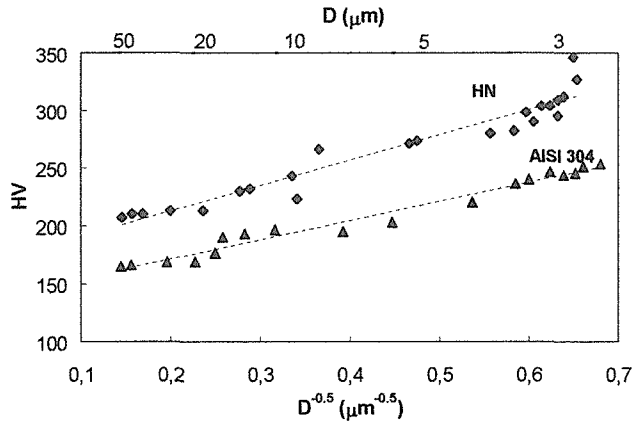

Fig.3 Grain refinement effect on the hardness of high nitrogen steel in comparison to the AISI 304 stainless steel.

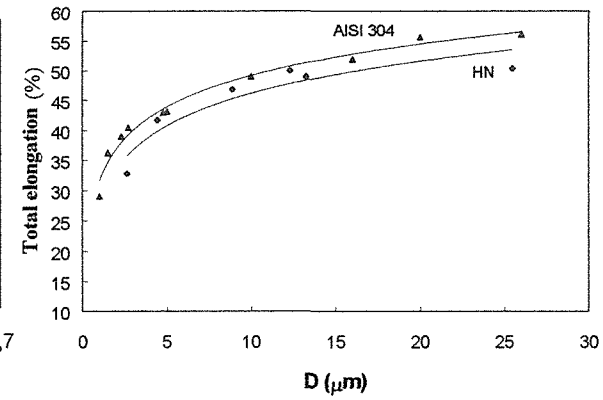

Fig.4 Grain refinement effect on the ductility of high nitrogen steel in comparison to the AISI 304 stainless steel.

In conclusion, the refinement of grain size in a high nitrogen austenitic stainless steel down to 2.5 μm can be achieved. Furthermore, in this material the Hall-Petch relationship is found to hold for the examined grain size range. A strong strengthening (200 MPa) was noted when grain size was reduced from 50 to 2.5 μm.

References

[1]Speidel, M., in *Proceedings of the 5th International Conference on High Nitrogen Steels*, Stockolm, July 1998, 241.

[2]Di Schino, A., Kenny, J.M., Mecozzi, M.G. and Barteri, M., *Journal of Materials Science*, **35**, 4803, 2000.

[3]Di Schino, A., Salvatori, I. and Kenny, J.M., in *Proc. of the 1st International Conference on Advanced Structural Steels*, Tsukuba, in press.

Effect of Nitrogen Alloying on the Pitting of Stainless Steel

H. Yashiro, D. Hirayasu and N. Kumagai
Faculty of Engineering, Iwate University, Japan

1. Introduction

It has been noticed that alloyed nitrogen improves corrosion property of stainless steels. Several possibilities have been pointed out regarding the role of alloyed nitrogen in localized corrosion [1,2]. Nitrogen shifted pitting potential to nobler direction but the extent varied depending on the condition such as temperature and concentration of chloride ion [3]. The present paper studied the effect of temperature and concentration of chloride on the pitting behavior of type 310 stainless steel to clarify the feature of pitting resistance of nitrogen alloyed stainless steels.

2. Experimental

Three kinds of type 310 based stainless steels were prepared containing 0.023 (310), 0.149 (310N(1)) and 0.325 (310N(2)) mass % of nitrogen, respectively. Pitting potentials (E'_{pit}) were determined as a function of temperature and concentration of chloride ion through measurements of anodic polarization curves at 1 mV s^{-1} in aerated NaCl solutions. Potentials were measured using an internal Ag/AgCl/KCl(2 mol dm^{-3}) reference electrode and expressed as measured.

3. Results and discussion

Effect of temperature Fig. 1 shows E'_{pit} for three steels in 3 mol dm^{-3} NaCl solution as a function of temperature. E'_{pit} for 310 steel showed a gradual shift to less noble direction with increase of temperature, while E'_{pit} for 310N(1) steel exhibited a sharp fall at 323 K. 310N(2) steel was most resistant to pitting at every temperature but the differences in E'_{pit} among three steels were less pronounced at 353 K, where E'_{pit} lied below 400 mV for all steels. The feature is quite similar to the case of nitrate addition to a solution for nitrogen-free steel[4].

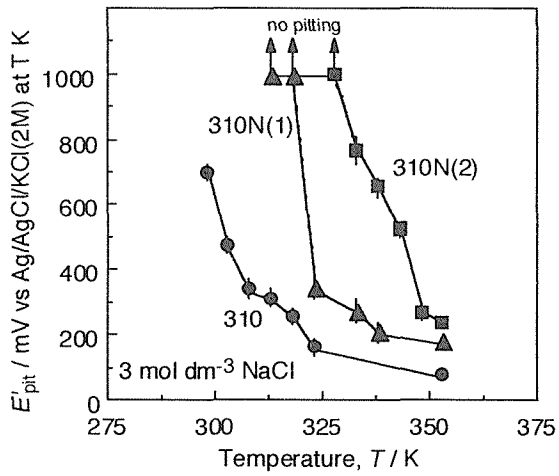

Fig. 1 Effect of tempearture on E'_{pit} in 3 mol dm^{-3} NaCl solution

Effect of concentration of NaCl Fig. 2 shows the relationship between E'_{pit} and concentration of NaCl at 323 and 353 K, respectively. At 323 K, 310 steel followed a usual relation between E'_{pit} and concentration of chloride ion: $E'_{pit} = a - b\log C_{NaCl}$ with a= 260 (mV) and b=200(mV/decade). E'_{pit} for 310N(1) steel did not follow the relation but showed a sharp fall

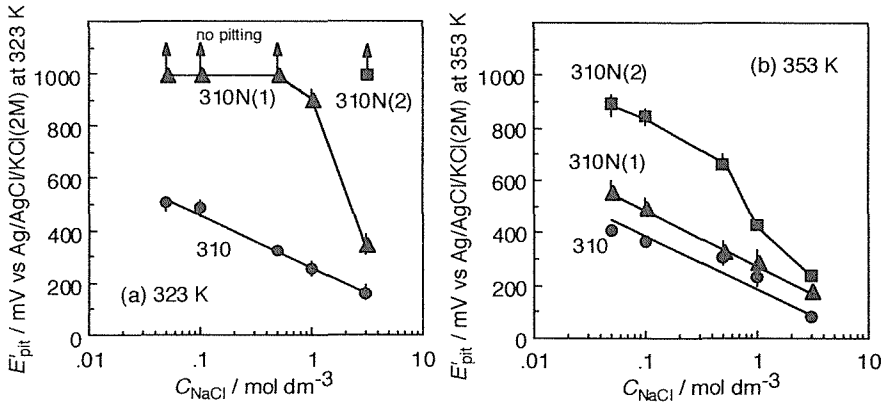

Fig. 2 Effect of concentration of NaCl on E'_{pit} at 323 K(a) and 353 K (b).

at 3 mol dm^{-3}. The feature is similar to Fig. 1. At 353 K, on the other hand, E'_{pit} for 310N(1) steel, as well as for 310 steel, showed a usual relationship with $\log C_{NaCl}$. The values of a and b at 353 K were: a= 200 and b=180 for 310 steel and a= 290 and b=210 for 310N(1) steel. The relation did not stand for 310N(2) steel even at 353 K. It seems that the linear relation between E'_{pit} and $\log C_{NaCl}$ stands when solution temperature exceeds critical values for each steels, while E'_{pit} shows a jump at lower temperatures when C_{NaCl} is not too high.

Effect of combination of temperature and concentration of NaCl Fig. 3 summarizes E'_{pit} as a function of temperature and concentration of NaCl for three steels. Iso-pitting potential lines were drawn every 100 mV. It is clearly seen that nitrogen alloying widens no pitting area. But the shapes of iso-pitting potential lines for these steels seem unusual. Iso-pitting potential lines usually lean toward high concentration or high temperature, because E'_{pit} becomes less noble with them. These steels have critical temperature, around which E'_{pit} is very sensitive to temperature but not to concentration of NaCl. The values of critical temperature are ca. 313 K for 310 steel and ca. 333 K for 310N(1) steel. E'_{pit} strongly scattered at 333K for 310N(1) steel below 3 mol dm^{-3}. The critical value for 310N(2) steel is not clear from Fig. 3 but seems to be around 363K. The critical temperature depended on the content of nitrogen: the higher the content, the higher the critical temperature. Thus, alloyed nitrogen offers remarkable pitting resistance under the conditions: temperature being below the critical value and combination of temperature and chloride concentration being mild enough for E'_{pit} to lie above 400 mV.

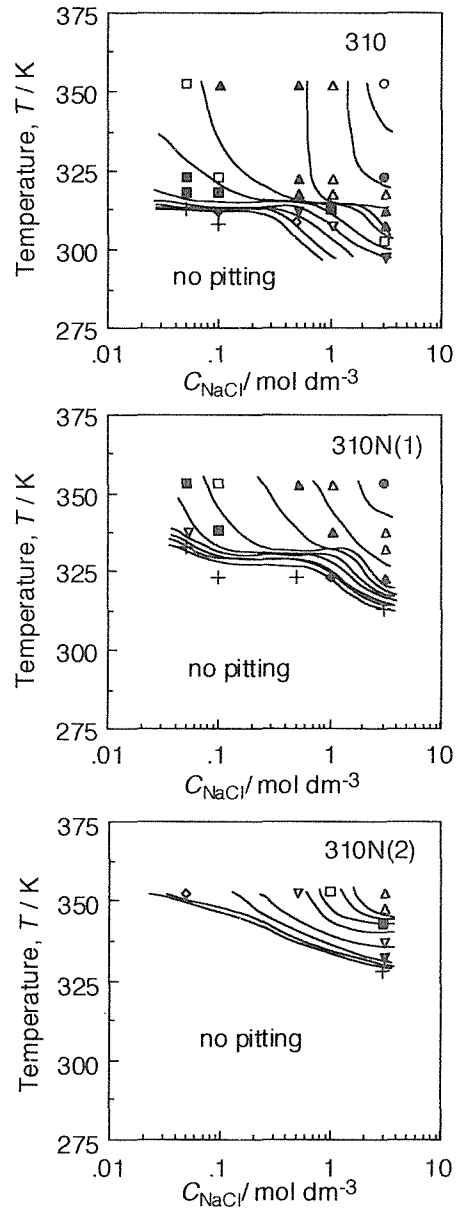

Fig. 3 E'_{pit} as a function of C_{NaCl} and temperature. E'_{pit}: 0-100 mV(○) , 101-200(●), 201-300(△), 301-400(▲), 401-500(□), 501-600(■), 601-700(▽), 701-800(▼), 801-900(◇), 901-1000(◆), >1000(no pitting) (+)

4. Conclusion

Nitrogen alloying to type 310 stainless steel enlarged the immune area against pitting in terms of temperature and concentration of chloride ion. The steels had a critical temperature above which E'_{pit} had a usual linear relation with $\log C_{NaCl}$ while E'_{pit} jumped below it except when concentration of chloride ion was so high that E'_{pit} lay below 400 mV.

References

[1] K. Osozawa, Zairyo-to-Kankyo (Corros. Eng.), 47(1998), No.9, pp.561-569.
[2] R. F. A. Jargelius-Pettersson, Corros. Sci., 41(1999), pp1639-1664.
[3] H. Yashiro, D. Takahashi, N. Kumagai, K. Mabuchi, Zairyo-to-Kankyo (Corros. Eng.), 47(1998), No.9, pp.591-598.
[4] H. Yashiro, A. Oyama, K. Tanno, Corrosion, 53(1997), No.4, pp.290-297.

Passive Film Modification toward Preventing Stress Corrosion Cracking of Stainless Steel

Takumi Haruna, Takeharu Nakamura*, and Toshio Shibata**
Department of Materials Science and Processing, Osaka University, JAPAN
*Present: Murata Manufacturing Co. Ltd.
**Present: Fukui University of Technology

1. Introduction

Stress corrosion cracking (SCC) of stainless steels has still been experienced in a variety of environments and applications. Various countermeasures such as alloying, stress free/relief design, fabrication and environmental control have been applied to avoid the SCC failure of this material. Surface modification is also considered to be one of the methods preventing the SCC[1]. It was reported that the improvement in pitting resistance of Type 304 stainless steel was successfully accomplished by the passive film modification which was achieved by the electrochemical activation and passivation treatment at a specified potential[2]. Therefore, we have applied this passive film modification technique to preventing SCC of Type 304 stainless steel in concentrated chloride solution containing small amount of thiosulfate.

2. Experimental

Type 304 stainless steel (C:0.66, Si:0.58, Mn:0.82, P:0.029, S:0.002, Ni:8.75, Cr:18.29, Mo:0.14, Cu:0.14 in mass% and Fe:bal.) sheet was machined into tensile specimens with gage section of $20mm^{L}x4mm^{W}x2mm^{t}$. The specimens were annealed at 1323 K for 600 s followed by water-quenched, and polished mechanically to #6/0. The specimen was then activated at a constant potential of 0.27 $V_{Ag/AgCl}$ for 600 s in 0.5 kmol m^{-3} H_2SO_4 at 343 K. This potential corresponds to the active peak potential in the polarization curve of this system. After the process, the specimen was passivated at various potentials for 1.8 ks in the same acidic solution. Consequently, the specimen was rinsed with distilled water, dried, and transferred to the SCC test cell.

SCC behavior of the passivated specimen was examined by the slow strain rate testing (SSRT) method. Initial strain rate was 8.3×10^{-6} s^{-1}. This SSRT apparatus have the CCD camera system for dynamically observing the initiation and propagation of multiple cracks[3]. The solution for the SCC test was 20 mass% NaCl solution containing 10^{-2} kmol m^{-3} $Na_2S_2O_3$ at pH 4 which was adjusted by HCl[4]. The test temperatures were 333 and 373 K. The SCC test was carried out under air open and natural corrosion conditions. The following potential was expressed referring to an Ag/AgCl electrode.

3. Results and Discussion

Figure 1 shows the effects of passivation potential on strain at the maximum stress obtained from the SSRT method. At both temperature of 333 and 373 K, the passivation treatment at a potential of 0.55 V induced the maximum in the strain, namely the SCC was effectively suppressed as the specimen was passivated at the potential around 0.5 V.

From the dynamic observation of multiple cracks, it was confirmed that each crack was initiated from each pit, and the crack length increased almost linearly with the testing time. As a crack initiation factor, the strain at initiation of the main crack which resulted in the fracture of the material in the SCC test was dependent on the passivation potential, and the

strain exhibited a maximum peak around 0.5 V. Moreover, total number of cracks observed on the gage section of the specimen minimized at the same passivation potential. It means that the initiation of pits and cracks is successfully retarded in the use of the specimen passivated around the potential.

Crack propagation rate was calculated from change in length of each crack observed with the CCD camera system with time. The crack propagation rate was almost constant value of 6 x 10^{-8} m s^{-1}, independent of the passivation potential. This fact indicates that modification of passive film, even which retards crack initiation process, does not affect suppressing the crack propagation process.

Changes in thickness and atomic ratio of Cr^{3+} to (Cr^{3+}+Fe^{2+}+Fe^{3+}) of oxide layer for the modified passive film determined by XPS with passivation potential were examined. The passivation process made the composition of the oxide layer more chromium-rich than activation process only. Furthermore, the maximum chromium content and thickness was found from the oxide layer at the passivation potential of 0.55 V. Shibata et al. investigated improving effect of pitting resistance for Type 304 stainless steel passivated by HNO_3, and revealed that the high pitting resistance is resulted from both the enrichment of chromium and thickening of the oxide layer of the passive film[5,6]. The mechanism for suppressing the initiation of SCC is considered to be same as that for the improving pitting resistance. It is very surprised that the similar passivation treatment to 304 stainless steel provides the suppressing effect of initiation of pitting and cracking, although dynamic strain is applied to the specimen and the modified passive film might be continuously ruptured.

4. Conclusions

(1) Several passivation potentials were applied to Type 304 stainless steel activated at 0.27 V in sulfuric acid solution at 343 K in order to modify its passive film. The specimen passivated around 0.5 V showed quite low SCC susceptibility in 20 mass% NaCl solution containing 10^{-2} kmol m^{-3} $Na_2S_2O_3$.
(2) The passivation treatment effectively suppressed the initiation of pitting and cracking.
(3) The treatment did not influence the crack propagation process.
(4) The suppressing effect of SCC initiation is resulted from thickening and enrichment of chromium in the oxide layer of the passive film.

Acknowledgements

I thank Dr. Fujimoto, Osaka University for his XPS analysis and discussion on the passive film.

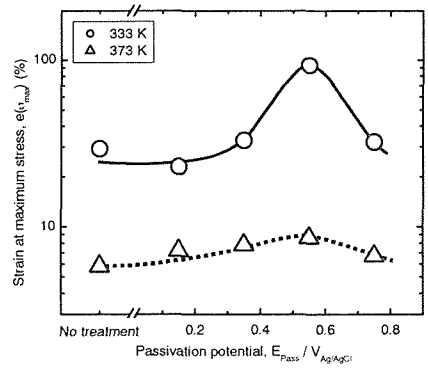

Fig.1 Effect of passivation potential on strain at maximum stress for Type304 stainless steel in 20 mass% NaCl solution containing 10^{-2} kmol m^{-3} $Na_2S_2O_3$.

References

[1] T. Fukuda and M. Akashi: Proc. Stainless Steel '91, ISIJ, (1991) p.168.
[2] T. Shibata and H. Tonbe: J. Metal Finishing Soc. Japan, 39 (1988) 824.
[3] T. Shibata and T. Haruna: Corros. Eng., 41 (1992) 809.
[4] T. Shibata, T. Haruna, S. Fujimoto and S. Nakane: Tetsu-to-Hagane, 77 (1991) 1511.
[5] T. Shibata, O. Yamazaki and S. Fujimoto: Corros. Eng., 48 (1999) 44.
[6] T. Shibata, O. Yamazaki and S. Fujimoto: Corros. Eng., 48 (1999) 155.

Corrosion Resistance of Stainless Steels in Comparison with the Properties of Artificial Passivity

K.Sugimoto
Department of Metallurgy, Graduate School of Engineering,
Tohoku University, Japan

1. Introduction

The chemical composition of passive films on stainless steels has been studied extensively to determine why the steels have good corrosion resistance. The high corrosion resistance of steels may be associated with the enrichment of passive films. To better understand the protective nature of passive films, however, we must elucidate the quantitative relationship between the dissolution rate and the composition of the films. For this purpose, a simulation experiment using thin composite oxide films with known composition, which are artificially formed to simulate the properties of real passive films, so-called artificial passivation films[1], seems effective. This is because the dissolution rates such oxide films on an insoluble substrate can be determined even in aggressive media where the dissolution rates of real passive films are ambiguous due to the active dissolution of steel matrix through defects in the films.

2. Formation of artificial passivation film

CVD and PVD techniques are available for synthesizing thin oxide films on foreign substrate. Fe_2O_3-Cr_2O_3, NiO-Cr_2O_3 and Fe_2O_3-Cr_2O_3-NiO films were formed by metalorganic chemical vapor deposition (MOCVD)[1] and Fe_2O_3-Cr_2O_3-MoO_2 films were prepared by ion-beam sputter deposition (IBSD)[2].

3. Comparison of corrosion natures between real and artificial passivation films

This time, the potentiostatic dissolution behavior of Fe_2O_3-Cr_2O_3 artificial passivation films, which were formed by IBSD, has been examined in 1M HCl. The dissolution rate of the films as a function of potential was measured by *in-situ* ellipsometry. The dissolution rate of the films as a function of potential obtained (Fig. 1) was compared with the dissolution rate of Fe-Cr alloys as a function of potential obtained in the same solution (Fig. 2). The films show the reductive dissolution (Region I) and the transpassive dissolution (Region III), but no pitting dissolution (Region II) (Fig. 1). It was found that pitting dissolution of the alloys occurs in the reductive dissolution range of the films (Region I) in which the Fe_2O_3 component of the films suffers from cathodic

reduction (Fig. 2). When the Cr content of the passive films on Fe-Cr alloys exceeds the critical value at which the Fe_2O_3-Cr_2O_3 artificial passivation film attains no reductive dissolution, no pitting occurs on the Fe-Cr alloys. The critical value of the cationic mass fraction of Cr, X_{Cr}, was ca. 0.6 and the X_{Cr} value of the passive films formed on the Fe-30Cr alloy in 1M HCl was estimated to be X_{Cr} = ca. 0.6. In the potential range between the reductive dissolution and the transpassive dissolution of the Fe_2O_3-Cr_2O_3 artificial passivation films (Region II), the Fe-Cr alloys become immune against pitting.

4. Conclusion

It can be concluded that the attainment of X_{Cr} = ca. 0.6 of passive film is very important for the attainment of immunity against the passive film breakdown in 1M HCl. If there is a locally Cr-depleted part, of which Cr content is less than X_{Cr} = 0.6, in the passive film with the X_{Cr} value higher than 0.6, the part suffers from the reductive dissolution and then pitting occurs by the anodic dissolution of matrix alloy at the part.

References

[1]Sugimoto, K, Seto, M, Tanaka, S. and Hara, N, J. Electrochem. Soc.,140(1993), No.6, pp.1586-1592.

[2]Son, M, Akao, N, Hara, N. and Sugimoto, K, J. Electrochem. Soc.,148(2001), No.1, pp.B43 –B50.

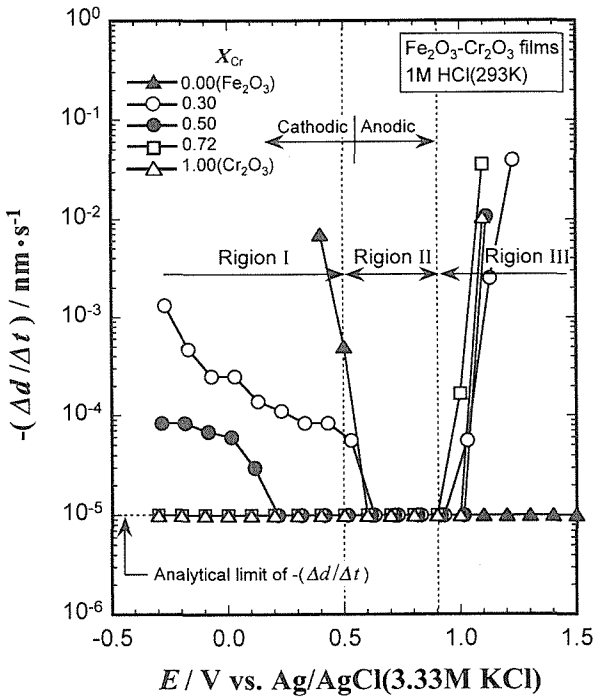

Fig. 1 Thinning rate of film thickness as a function of potential for Fe_2O_3-Cr_2O_3 films.

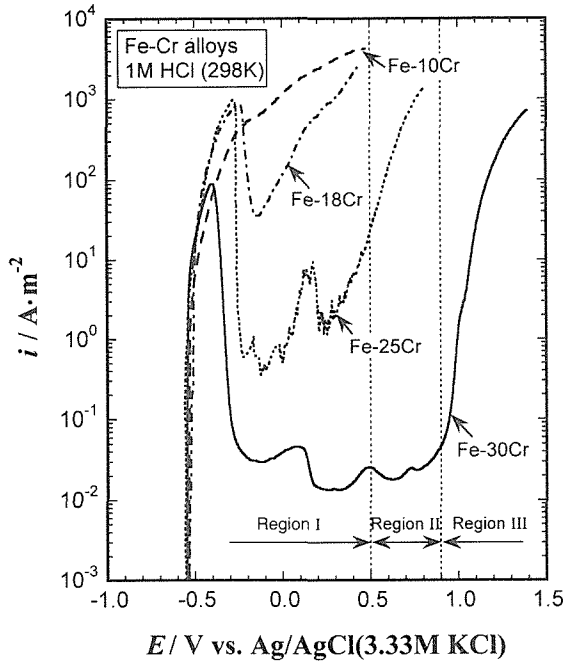

Fig. 2 Anodic polarization curves for Fe-Cr alloys in 1M HCl at 298K.

Synergistic effect of impurities on the transpassive corrosion of high-purity Fe-18Cr-14Ni alloys

M. Mayuzumi, J. Ohta, K. Kako, and E. Kawakami
Surface Science Department, CRIEPI, Japan

1. Introduction

Transpassive corrosion is a phenomena observed in stainless steels(SS) exposed to high temperature, concentrated nitric acid(HNO_3) solutions with and without highly oxidizing ions and manifest itself as a general corrosion with intergranular corrosion, even though the SS is in solution annealed condition. It is an important degradation mechanism of stainless steels for use in a nuclear fuel reprocessing plant[1] and has been studied extensively from various metallurgical aspects. The previous studies suggest that the intergranular corrosion should be caused by the segregation of impurities to grain boundaries and the resultant formation of active sites.

In our previous study[2], we have reported the corrosion behavior of high-purity(HP) Fe-18%Cr-Ni alloys with total impurities of 0.01% produced by a cold crucible method in a high vacuum chamber. The high-purity alloys showed almost no intergranular corrosion in 13 kmol/m^3 HNO_3 with and without Ce^{4+} ions. Thus, it was concluded that the alloy of 99.99% purity is good enough for a base material to examine the effect of impurity or alloying elements on the transpassive intergranular corrosion of SS

The purpose of this study is to clarify the combined effect of minor impurities(C, P and S) with Si and Mn on the transpassive intergranular corrosion of HP Fe-18%Cr-14%Ni alloys in concentrated, boiling HNO_3.

2. Experimental

2.1.Specimen

HP Fe-18%Cr-14%Ni(hereafter HP18Cr-14Ni) alloys with controlled levels of Si, Mn, C, P, and S were produced by a cold crucible method from high-purity materials as ingots of 8kg. Table 1 shows the chemical composition of the produced alloys. The alloys containing all of C, P and S were prepared as three different specimens (CPS-1 through CPS-3) to check the reproducibility of the corrosion data for the nominal impurity contents. The impurity levels were less than 0.01% excluding the target impurity elements.

Specimens of 25 mm long, 8 mm wide and 3 mm thick were cut from plates of the alloys after cold rolling of 60% to 70%. After machining, the specimens were solution annealed at temperature of 1373 K for 3.6 ks in vacuum of 10^{-4} Pa. In addition, an aging treatment of 973 K for 3.6 ks also was applied to half of the specimens. All specimens were polished with #600 emery papers after the heat treatment.

2.2.Corrosion Test

Corrosion tests were performed in boiling 13 kmol/m^3 HNO_3 solutions. Three specimens from the same material were corroded at the same time in a glass flask containing the boiling test solutions. After a pre-determined immersion time of 180 ks or 360 ks, the specimens were removed from the flask, ultrasonically cleaned for 3.6 ks to 7.2 ks, and then weighed to calculate the weight loss. This procedure was repeated periodically until termination of the immersion test. The test solution was replaced after each measurement. At the end of the test, in addition to the weight measurement, intergranular corrosion depth(ICD) also was measured on two out of three specimens after cross-sectioning along the rolling direction.

Surface observation by scanning electron microscopy (SEM) was done on the specimens at each measurement during the test to determine the corrosion morphology.

3. Results and discussion

HP18Cr-14Ni-1Mn-0.5Si alloy was selected as the base material to examine the effect of the other minor impurities, since the alloy showed minimum corrosion rates regardless of the heat treatment condition and no intergranular corrosion in solution annealed condition.

Solution annealed(SA) HP18Cr-14Ni-1Mn-0.5Si, SA HP18Cr-14Ni-1Mn-0.5Si-C, SA HP18Cr-14Ni-1Mn-0.5Si-S and SA HP18Cr-14Ni-1Mn-CPS alloys did not show any intergranular corrosion after the corrosion test. However, SA HP18Cr-14Ni-1Mn-0.5Si-P and SA HP18Cr-14Ni-1Mn-0.5Si-CPS alloys showed intergranular corrosion. This result suggests that intergranular corrosion was induced by a synergistic effect of Si and P, since each of 0.5%Si or 100 ppm P addition did not cause intergranular corrosion in SA HP18Cr-14Ni alloys.

The corrosion rates of various impurity doped alloys were almost the same regardless of single addition of C, P or S, or the simultaneous addition of the three impurities, and were 50% to 70% of a commercial Type 304L. The ICD of, for example, SA HP18Cr-14Ni-1Mn-0.5Si-CPS alloys distributed less than 15 μm in contrast to 10 μm to 35 μm for the commercial Type 304L. The resultant average ICD was <7 μm for the alloys, almost one third of the Type 304L having an average ICD of 19 μm. Thus SA HP18Cr-14Ni-1Mn-0.5Si alloys exhibit a superior corrosion resistance by reducing each minor impurity level to 100 ppm.

4. Conclusion

A synergistic effect of Si and P was suggested to induce intergranular corrosion in SA HP18Cr-14Ni alloys. In spite of the synergistic effect, SA HP18Cr-14Ni-1Mn-0.5Si alloys containing C, P, and S at 100 ppm level each showed a higher corrosion resistance than a commercial Type 304L SS in 13 kmol/m^3 HNO_3.

Table 1 Chemical composition of specimen

Specimen	Additive content (%)					Impurity content (ppm)		
	Fe	Cr	Ni	Si	Mn	C	P	S
HP18Cr-14Ni	Bal.	18.50	13.50	0.0006	0.0002	4	2	4
HP18Cr-14Ni-1Mn-0.5Si	Bal.	18.82	13.57	0.46	0.91	8	NA*	4
HP18Cr-14Ni-1Mn-0.5Si-C-1**	Bal.	19.03	13.85	0.41	0.90	103	NA	4
HP18Cr-14Ni-1Mn-0.5Si-C-2**						78		
HP18Cr-14Ni-1Mn-0.5Si-P	Bal.	18.29	13.73	0.48	0.97	8	107	5
HP18Cr-14Ni-1Mn-0.5Si-S-1	Bal.	18.17	13.93	0.49	0.97	8	NA	103
HP18Cr-14Ni-1Mn-0.5Si-S-2								76
HP18Cr-14Ni-1Mn-0.5Si-CPS-1	Bal.	19.10	13.90	0.44	0.97	92	147	136
HP18Cr-14Ni-1Mn-0.5Si-CPS-2						74		90
HP18Cr-14Ni-1Mn-0.5Si-CPS-3	Bal.	19.42	13.46	0.39	0.80	99	110	125
HP18Cr-14Ni-1Mn-CPS	Bal.	18.44	14.20	NA	1.01	89	124	108

Remarks: * Not analyzed; **: upper part(No.1) and lower part(No.2) from a same ingot;
CPS: containing 0.01%C, 0.01%P and 0.01%S, nominally.

<Reference>

[1] "Special Issue for Reprocessing", PNC Technical Review 55 (Tokyo, Japan: Power Reactor and Nuclear Fuel development Corp.,1985).

[2] M.Mayuzumi, J.Ohta, K.Kako, Corrosion, 56(2000), No.1, pp.70-79.

Characterization of Stainless Iron Metal Plates Under Compression

(A. Fayza and A. Zghal)
Laboratory of Mechanics, Structures and of Technological Development,
LMSTD – ESSTT Tunis

1. Introduction

Among the most serious problems in the resistance of a stainless iron material, stand the phenomenon of instability. Indeed, failings of the stainless iron material owed to the phenomenon of instability are very numerous and their incomparable properties make that boards in stainless iron material occupy a good part of the structure of a plane. Remain to specify that thin panels with stainless iron material can be exposed to problems of instability, especially if the choice of the structure is not optimized appropriately. In panels with stainless iron material can appear, more or less seriously, all depends on the nature of the path of loading, of the amplitude of the working loads and of the geometrical configuration of the structure (dimensions and form).

.Several attempts were carried out thereafter of which most recent is due to K.K Shukla, Y. Nath. [1]. In their analysis, they were based on the resolution of the equilibrium equations by an approximation of with the help of the polynomials of Chebychev, but in their analysis the plastic buckling problem was not evoked in this study. By an oteher way, the effects of boundary conditions was in fact, well developed by Mojtaba Azhari, Sina Hoshdar and Mark Andrew Bradford [2], they have argument bubble functions to the ordinary finite stripe method (FSM), in order to calculate the elastic local buckling of rectangular plates, with various boundary and loading conditions. In their experimental study, recently, Kevin D. Murphy and David Ferreira [3] have also present a buckling analysis of rectangular clamped plates based on energy consideration. Using Von Karman plate's theory, in order to determine the critical load of bifurcation for thermal buckling analysis but, with consideration of a linear material behavior.

The evaluation of the plastic buckling behavior of elastic-plastic structures has been addressed both analytically and numerically. Although providing a valuable insight into the plastic buckling phenomenon, these contributions did not lead to an accurate evaluation of the maximum load (attained at a finite deflection), even for simple problems.

In this survey, initially, we have described briefly the field and the objective of this study, and we have given a formulation of the instability problem as well as the bases of resolution.
The formulation of the elastoplastic buckling theory of structures, was described, using the Hill [4] assumption of a three dimensional solid structure. In the last part we have treated experimental investigations and the various applications carried out with the stainless iron metal plates, under compressive buckling loads. Aspect ratio, boundary conditions, materials properties and constitutive laws in plastic buckling have been well analyzed.

The plates were all of 16 inches long and varied in width from 2 to 16 inches by step of 2 inches, and in thickness from 0.0196 at 0.118 inch by step of approximately 0.0196 inch. Loads were applied by an appropriate testing-machine, which allow the variation of boundary conditions. Load was applied until the plate failed to take any more load.

2. Formulation

It is noticed that as a consequence of a model of 1^{st} order implies that the plane deformations linearly vary in the thickness of the plate. By neglecting the transverse shearing strains (Assumption of Love-Kirchhoff), we obtain two additional relations.

Thus, the formulation of the problem doesn't use more than three independent variables: u, v and w. Since we deal with thin sections of which the ratio h/b < 1/20, we can admit in what follows these assumptions. We consider a plane stress state and we neglect the influence of transverse shearing. The plates considered are agreed with Kirchooff hypothesis. For the homogenous plates and from the theory of elasticity the stress-strain relation is a new relation, called buckling equation, between the efforts of membrane and the lateral distortion makes it possible to determine the initial configuration of the plate when it buckle.

One notices, in the application on plastic buckling for example, that certain elements have a little influence on the critical load, as the boundary conditions. In the formulation of the problem, a considerable profit is noted on the size of the problem, and thus on the speed of calculations.

3. Conclusion

Experimental and theoretical analysis detailed in this work, assure that:
Short plate in stainless iron metal, (with low aspect ratio r < 1) allow compensating significant compressive loads, before buckling. We could shown the limits of proportionality of the respective ratios a/b and b/h for which will occur a buckling in the plastic field, while giving an estimate of the critical load with our analytical approach for two types of phenomenological behavioral laws, (J2F) law and (J2D) law.
Sight the intrinsic properties of the stainless iron metal, we notice that for plates having the same geometry (a, b, and h) we can increase their buckling strength to uni-axial or biaxial compression, by adopting particular supports on the unloaded edges, (in the case of uni-axial compression), or by adopting adequate factor λ/h, (in the case of biaxial loading), with λ is the proportionality factor of load and h, being the thickness of the plate.
With through the relations between these parameters, we can optimize the geometry of a stainless iron metal panel subjected to the elastoplastic compressive buckling, while adopting a compromise between the geometrical factors and those of load.
Finally in this theoretical and experimental analysis, we explored the performances offered by the intrinsic mechanical properties of the stainless iron metal according to instability by elastoplastic buckling. What was used as a data base for a better optimization in the future by implementing other factors of great importance, in the optimization phase of these structures, as well as metallurgical factors, such as, orientation and size of the grains metal in the matrix of stainless iron metal and the rate of work hardening according to the thickness.
Thus, we can choose new generation of stainless iron metal intended especially to support particular loadings of buckling while preserving characters of resistances and sedentary, offered by these.

References:

[1] K.K Shukla, Y. Nath: analytical solution for buckling and post-buckling of laminated plates. International Journal of non-linear Mechanics 2001.N° ◦36, pp.1097-1108.
[2] Mojtaba Azhari], Sina Hoshdar and Mark Andrew Bradford: International journal for numerical method in engineering 2000. N° 48, pp. 583-593.
[3] Kevin D. Murphy and David Ferreira: international Journal of Solids and structures 2001. N° 38, pp. 3979-3994.
[4] R. Hill, a general theory of uniqueness and stability of elastic-plastic solids. J. Mech, Phys. Solids 1958. N° 6 pp. 236-249

A New Surface Treatment by Pulsed Plasma Nitriding for Chromium Plated Austenitic Stainless Steel

P.Kuppusami, A.Dasgupta and V.S. Raghunathan
Materials Characterisation Group
Indira Gandhi Centre for Atomic Research
Kalpakkam-603 102, INDIA

1. Introduction

Plasma nitriding has become a powerful technique over other methods owing to several advantages[1]. This technique allows low substrate temperature treatment; it produces less warping and distortion and offers increased wear, corrosion and fatigue resistance. Recently plasma nitriding of chromium plated type 316 stainless steels has gained importance as it offers properties superior to nitrided type 316 stainless steel [2]. Chromium nitride has been recently found applications in forging, drawing etc owing to their abrasive resistance. This coating is also an alternative to the use of stellite alloys for hardfacing in fast reactors because of enhanced resistance against galling of contacting surfaces, fretting and corrosion. In this paper, the pulsed plasma nitriding behaviour of chromium plated type 316 stainless steel is investigated. We have used pulsed DC source to nitride the samples as it offers a very fine dosing of input plasma energy into the work load, good temperature uniformity on the work piece with different geometries and homogeneous treatment even into small holes and slots. The paper also presents case depth, hardness and the activation energy for the diffusion of nitrogen in the nitrided chromium plated coatings on type 316 stainless steel.

2. Experimental

Type 316 Stainless steel samples of dimensions 100mm x 60mm x 10mm were chromium plated at M/s Plate Metals Pvt Ltd., Chennai-600041. The coupons were given heat treatment at about 510 K for 3h to avoid hydrogen embrittlement problem. The coating had a hardness of 900HV at a load of 100g prior to nitriding. Prior to plasma nitriding, sputter cleaning was conducted in an argon atmosphere at a pressure of about 0.7 kPa by biasing the samples negatively (500V pulsed DC) at a temperature of 523 K for 2 hrs. To study the nitriding behaviour of the chromium plated stainless steel samples, the parameters such as nitrogen to hydrogen ratio, nitriding temperature and time were varied. The flow rates of nitrogen and hydrogen were monitored using mass flow controllers and the temperature was controlled by varying the duty cycle and hence the ion current at constant voltage. An auxiliary heater was used to increase the sample temperature to the desired set values. X-ray diffraction(XRD), scanning electron microscopy and microhardness tester were used to characterize the nitrided samples.

3. Results and Discussion

The plasma nitriding of the samples were carried out for various durations in the temperature range 833-1273K. XRD analysis of the samples indicated the presence of Cr_2N phase in the Cr matrix at low substrate temperatures. The intensity of the Cr_2N diffraction lines was found to increase with increase in the nitriding temperature. The hardness-depth profiles showed a uniform decrease in hardness as a function of depth for the samples nitrided at 923 K, 45 h, while the profiles have a sharp variation at the interface for the samples nitrided at 1173 K, 3h.

The observed case depths, hardness and diffusion co-efficient of nitrogen in chromium are shown in table 1. It is noticed from the table that when the nitriding temperatures are less than 973 K, the case depths were very small and the hardness obtained were less than 990 HV and at temperatures more that 1073 K, there was a considerable increase in case depth and hardness exceeding 1400HV.

Table 1: Experimental Conditions Used for Plasma Nitriding of Cr plated Type 316 Stainless Steel Samples

Temperature (K)	Time (h)	Case Depth (μm)	Vickers Hardness (HV)	Diffusion Co-efficient(m^2/s)
833	20	5	550	$1.25x10^{-16}$
973	3	6	850	$3.33x10^{-15}$
1073	3	15	1400	$20.83x10^{-15}$
1173	3	25	1650	$57.87x10^{-15}$
1273	3	40	1850	$148.15x10^{-15}$

Based on the time of nitriding (t) and case depth (X), the diffusion co-efficients of nitrogen (D) were calculated from the relation $X^2 \approx 2\sqrt{Dt}$. These values are shown in table1. The activation energy for nitrogen diffusion in chromium determined from lnD versus 1/ T plot was found to be about 131.4 kJ/mole. Previously, we have reported [3] the activation energy of 69.4 kJ/mole for diffusion of nitrogen in the nitrided layer of type 316 austenitic stainless steel. It is interesting to note that the activation energy for nitrogen diffusion in chromium plated stainless steel is significantly higher than that of austenitic stainless steel. This causes a significant reduction in the nitrided layer formation in the Cr plated stainless steel at low nitriding temperatures. It is further suggested that the rate of diffusion has been restricted due to the formation of hard impervious Cr_2N phase at the surface of the Cr plating.

4. Conclusions

The process conditions for plasma nitriding of Cr-plated stainless steel were investigated as a function of nitriding temperature and time. The results indicated a very small nitrided layer thickness at temperature less than 973K and it is found to be significant at temperatures more than 1073K. The formation of hard Cr_2N phase was found to restrict the diffusion rates of nitrogen in Cr- plated austenitic stainless steel.

References

[1] Jones, C.K. Martin, S,W. Sturges, D.J. and Hudis, M, Heat Treatment'73, Metals Society, London(1973), pp.71-73.

[2] Menthe, E. and Rie, K.T, Surface and Coatings Technology 112(1999), pp.1217-1220.

[3] Kuppusami, P. Terrance, A.L.E. Sundararaman, D. and Raghunathan, V. S, Surface Engineering (1993), pp. 142-147.

Surface Analysis of Corrosion

Hugh S. Isaacs

Materials Science Division
Brookhaven National Laboratory
Upton, NY 11973, USA

In situ techniques for the study of corrosion have many advantages. The major advantage is a direct correlation when a controllable variable is changed such the potential or addition of an inhibitor. There are various techniques available. Many are electrochemical, such as polarization resistance or impedance measurements. Others may employ scanning of the surface. These again may be electrochemically related such as current density mapping with a reference probe or a vibrating electrode, surface impedance mapping, potential mapping using a Kelvin probe technique or the more recent atomic force microscope and scanning tunneling microscope that that can give down to a atomic scale morphology of the surface. However, many corrosion problems require a relatively large dimensional scale of the order of centimeters or larger.

One approach for analysis of these larger areas is visual observation of the surfaces. This may be done by direct observation of the corrosion taking place or with the use of indicators to intensify changes in the electrolyte. Indeed, metallography and photography has been used extensively. With the development of modern video techniques other visual approaches have become easier to apply. From a study of video methods it was found that changes are difficult for the human eye to monitor, but if the visual changes are speeded up then the changes become obvious. Examples of these applications will be presented and discussed.

The use of indicators to identify corrosion was developed in the 1920's by Evans to monitor the corrosion of iron. Gels with indicators have also found use. The additions of a broad range pH indicator to solutions, used in corrosion experiments, emphasize the changes in the pH around the anode and cathode and can be used to located and monitor where these process are taking place. The low pH is a result of a hydrolysis reaction of dissolved metal ions

$$M^{n+} + m\,H_2O = M(OH)_m^{(n-m)+} + m\,H^+$$

The stability constants for this reaction are important in determining the pH. Thus a much lower pH is seen for stainless steel because of the higher stability constant of $Cr(OH)^{2+}$ than that of iron $Fe(OH)^+$ $Zn(0H)^+$ is the least stable of these cations and the location of the anodic site is thus more difficult to monitor. The high pH at the cathode results from the reduction of dissolved oxygen by the reaction

$$O_2 + 2\,H_2O + 4\,e^- = 4OH^-$$

The amount of convection that takes place in aqueous solutions has been seen to be surprisingly high. These convection currents can, however, be an important factor as to how or if, corrosion takes place. As will be shown, convection may inhibit or alter the progress of corrosion. This occurs even when only thin layers of about 2mm of solution are used. The use of viscous solutions, for example by the use of sucrose, helps to reduce the convection, but convection can

still interfere with the location of anodic and cathodic sites. Gels overcome this difficulty. It should be emphasized that the use of these different types of electrolytes may interfere with the experiment. This has been found when dilute electrolytes have been used e.g. the wide range indicator was found to inhibit the corrosion of iron when added to mMolar solutions of chloride or sulfate. In experiments with higher salt concentrations, little interference has been found.

A series of experiments will be presented to emphasize the use of accelerated video experiments in the analysis and understnding of pitting and crevice corrosion of iron and stainless steels. The experiments on iron have shown that the early stages of the formation of crevices behave in an unexpected manner because of the sensitivity of iron to pH changes. It was found that corrosion initiates preferentially at corners and not within crevices because of pH changes within the crevice increase rather than decrease as is generally expected. The development of corrosion at corners was found to be highly dependent on convection. Spreading of crevice corrosion was prevented or repressed when natural convection currents were high enough to prevent migration of a low pH solution from corroding regions.

The effect of concentrated solutions build-up on subsequent corrosion of stainless steels has been studied using video techniques. With stainless steels a corrosion behavior similar to that of iron has been observed when test solutions become very aggressive. The spread of active areas of corrosion within crevices has been studied. From the growth behavior of the active area it was concluded that processes was dependent on a critical concentration of dissolved dissolution products that leads to undermining or breakdown of the passive film.

Novel Methods of Detecting Non-Homogeneity in Surface Films

M. Seo and K. Fushimi
Graduate School of Engineering, Hokkaido University, Japan

1. Introduction

Some fluctuations in environmental factors such as solution pH, electrolyte concentration, and electric field as well as material factors provide non-homogeneity in surface films formed on the substrate materials. Several methods, e.g., scanning electrochemical microscopy (SECM), micro-ellipsometry, micro-Raman spectroscopy and micro-droplet method, have been developed for detecting non-homogeneity in surface films. These methods have not a high resolution in atomic or molecular level such as scanning tunnel microscopy or atomic force microscopy but are powerful for detecting non-homogeneity in a mezzo-scopic level which is important for better understanding of pitting corrosion.
In this paper, the principle of SECM which is capable of detecting the lateral distribution of electrochemical reactivity on surface films is described and the results obtained by application of SECM to aqueous corrosion systems are introduced and discussed.

2. SECM

In SECM, a micro-disk electrode is employed as a probe for detecting the lateral distribution of electrochemical reactivity on surface films. The SECM probe is scanned above the specimen surface to image the surface electrochemical reaction as shown in Fig. 1. The details of the principle and theory were reported by Bard et al. [1-5].

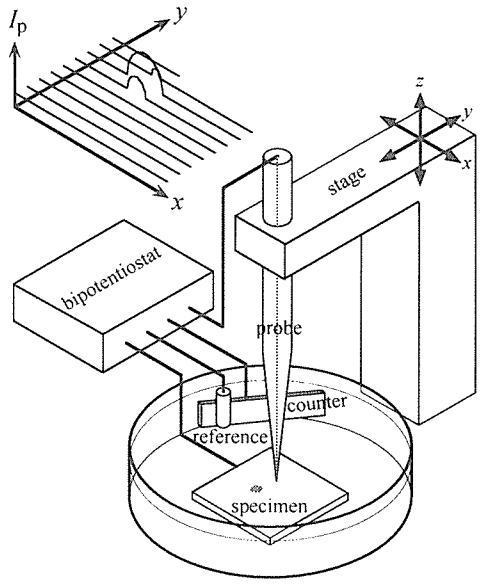

Fig. 1 Schematic diagram of SECM apparatus.

3. Non-homogeneity of passive film formed on a polycrystalline iron electrode

Pitting corrosion starts when passive film is locally broken down and the repair is not sufficient. For better understanding of pitting corrosion, it is important to investigate non-homogeneity of passive film since the local breakdown would initiate preferentially at the thinnest or the most defective part of the passive film. Fushimi et al. have applied SECM to investigate non-homogeneity of passive film formed on a polycrystalline iron electrode [6,7]. The redox current of $Fe(CN)_6^{3-/4-}$ flowed through the SECM probe electrode depended on the distance between the probe and iron electrodes and the thickness of passive film. The probe current image obtained by scanning probe electrode with a constant distance gave the thickness distribution of passive film on a polycrystalline iron electrode. It was found that the thicker film was covered on the grain oriented to {100} as compared with other grains oriented to {110} and {111}.

4. Liquid-phase ion gun to induce local breakdown of passive film on iron

SECM can be employed not only for imaging the lateral distribution of surface electrochemical reactivity but also for inducing a certain surface electrochemical reaction locally. It is well known that the local breakdown of passive film on iron is induced in

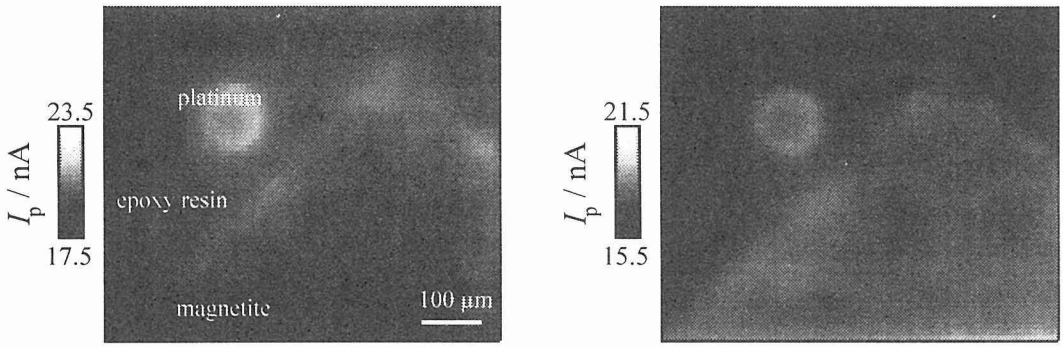

Fig. 2 Feedback mode SECM images of magnetite and platinum electrodes measured in pH 8.4, 0.03 M $K_4Fe(CN)_6$ solution without (left) and after (right) cathodic polarization of magnetite electrode at 1 μA cm^{-2} for 20 min in pH 3.3 Na_2SO_4 solution. The magnetite and platinum electrodes were embedded in epoxy resin. Scanning platinum probe electrode with a diameter of 10 μm was polarized at 1.2 V (SHE) for the SECM imaging.

solutions containing chloride ions. When a silver microelectrode covered with silver chloride was used as a probe electrode and polarized cathodically, chloride ions can be generated locally, i.e., operated as an ion gun. Chloride ions generated from the ion gun are localized above the passive film on iron to induce local breakdown of the film [8]. The induction period for the local breakdown showed the dependence on film thickness and aging time [9]. The mechanism of local breakdown leading to pit growth will be discussed in detail.

5. In-situ electrochemical monitoring and sensing

The SECM probe electrode is also effective for detecting reaction products from specimen surface in solutions. Ferrous and ferric ions could be detected during anodic polarization of iron electrode [10]. It was found that the active dissolution rate depends on the substrate grain orientation. Furthermore, SECM was applied to analyze the galvanic corrosion when magnetite was in contact with carbon steel [11]. Hydrogen evolved from magnetite could be detected during cathodic polarization of magnetite electrode. The current efficiency of 50% for hydrogen evolution on magnetite electrode was estimated from comparison with the hydrogen evolution on platinum electrode. It was found that cathodic polarization of magnetite electrode also leads to change in oxidation state of iron to metallic. This alteration increased the surface conductivity of magnetite as shown in Fig. 2.

References

[1] R.C. Engstrom, M. Weber, D.J. Wunder, R. Burgess and S. Winquist, *Anal. Chem.*, **58**, 844 (1986).
[2] A.J. Bard, F.-R.F. Fan, J. Kwak and O. Lev, *Anal. Chem.*, **61**, 132 (1989).
[3] A.J. Bard, F.-R.F. Fan, D.T. Pierce, P.R. Unwin, D.O. Wipf and F. Zhou, *Science*, **254**, 68 (1991).
[4] A.J. Bard, F.-R.F. Fan and M.V. Mirkin, in "*Electroanalytical Chemistry*", Vol. 18, A.J. Bard, Editor, p. 243, Marcel Dekker, New York (1994).
[5] A.J. Bard and M.V. Mirkin, "*Scanning Electrochemical Microscopy*", Marcel Dekker, New York (2001).
[6] K. Fushimi and M. Seo, *Zairyo-to-Kankyo*, **46**, 797 (1997).
[7] K. Fushimi, K. Azumi and M. Seo, *ISIJ Int.*, **39**, 346 (1999).
[8] K. Fushimi, K. Azumi and M. Seo, *J. Electrochem. Soc.*, **147**, 552 (2000).
[9] K. Fushimi and M. Seo, *J. Electrochem. Soc.*, **148**, B450 (2001).
[10] K. Fushimi and M. Seo, *Electrochim. Acta*, **47**, 121 (2001).
[11] K. Fushimi, T. Yamamuro and M. Seo, *Corros. Sci.*, **44**, 611 (2002).

In-situ, Nanoscopic Measurements of Atmospheric Corrosion of Steels

H. Masuda
Corrosion Resistant Material Research Group, NIMS, Japan

1. Introduction

One of the biggest problems when we use stainless steels near seashore environments is the visible rust formation by sea salt particles. It is commonly said that critical amount of attached sea salt particles exists for the visible rust formation [1]. To study the mechanism of visible rust formation, $MgCl_2$ droplets with different concentrations were attached on the stainless steel and the rust formation was studied by using a super Kelvin force microscope (SKFM) which we have developed recently [2], a color laser microscope and EDX image mapping.

2. Experimental procedure

In SKFM, the scanning device for X-Y direction is used an accurate X-Y stage. The maximum scanning area is limited to 1 X 1 cm. The minimum step of the X-Y stage is 0.1 μm. The tip used for SKFM measurement was the conductive gold-coated Si tip with the resonant frequency of around 25 kHz. The SKFM image was taken every 1 hour or 2 hours with data points of 256 x 256. The test specimens used were SUS304 and SUS430 stainless steel and were dry-polished up to 0.3 μm roughness. Droplets of 0.025 - 1 % $MgCl_2$ with diameter of 0.3 - 0.8 mm were attached on the specimen, then they were kept under the constant temperature (297 K) and the relative humidity range of 40 to 60 %. Beside SKFM observation, EDX analysis and the color laser microscope observation were also done.

3. Result and Discussion

Figure 1 show the SKFM image of SUS304 stainless steel with attaching 0.025 % $MgCl_2$. The equivalent salinity is estimated 0.3 mg/dm^2. The potential of the part where the droplet of $MgCl_2$ was attached was about 120 mV more negative than that of dry-polished part on the average and the potential of the part where the corrosion proceeds was about 120mV more negative than that of the part where the droplet of $MgCl_2$ was attached. However, after 13 hours corrosion stopped and the potential of the part where the corrosion proceeded before had become about 100mV more positive than that of the part where the droplet of $MgCl_2$ was attached and the potential of the part where the droplet of $MgCl_2$ was attached was about 80 mV more negative than that of dry-polished part on the average (Fig. 1(b)). The corrosion initiated other part after 20 hours (Fig. 1(c)). Thus corrosion proceeds with repeating initiation and extinction of pitting type of corrosion. The corrosion product of 20 μm diameter or less was observed several parts 108 hours after the start of the test by an optical microscope, but no corrosion (rust) was observed by the visual observation.

Fig. 2 show the SKFM image of SUS304 stainless steel with attaching 0.1 % $MgCl_2$. The equivalent salinity is estimated 1.0 mg/dm^2. The potential of the part where the droplet of $MgCl_2$ was attached was about 20 mV more negative than that of dry-polished part on the average at the beginning (Fig. 2(a)). The potential of the part where the droplet of $MgCl_2$ was attached, however, became more negative with time. The potential difference between the part where the droplet of $MgCl_2$ was attached and the dry-polished part became 0.9V at maximum 14 hours after the droplets had been attached (Fig. 2(b)). The macro anode and cathode site were detected at corroding part. The increase of the height of corrosion product indicates the progress of corrosion. The optical microscope observation shows that liquid of brown color existed at the corroding part. EDX analysis showed the enrichment of chloride ion and the lack of magnesium ion near corroding part. Since oxide was partly observed at corroding part, the corrosion product was composed with the mixture of rust and liquid of metal chloride. MnS inclusion was detected inside the droplet, but was not detected at corroding part.

Shinohara reported very interesting results about the relation between the visible rust

formation and the equivalent salinity. That is, the critical equivalent salinity exists for the growth of rust up to the visual size. The critical equivalent salinity is reported about 0.4 mg/dm^2 for SUS304 stainless steel. Our experimental result shows that no visible rust was found when equivalent salinity is low and that visible rust was found when the equivalent salinity is above 0.4 mg/dm^2. When $MgCl_2$ liquid layer is thin, oxygen can be supplied to the specimen surface from the air because the diffusion layer in the liquid is thin. While when the liquid layer is thick, oxygen can not be supplied to the specimen surface from the air. This may be the reason that no rust was formed at corroding part and that the tarnished area is produced by the oxidation of Fe^{2+} ion diffused from the corroding part when the liquid layer was thick.

4. Conclusion

In-situ observation of corrosion initiated from a small droplet of $MgCl_2$ solution was done under low relative humidity condition by Super Kelvin force microscope (SKFM. The results show that the corrosion morphology can be divided into 2 types. 1. Corrosion progressed inside of specimen with corrosion product when the liquid layer of $MgCl_2$ was thin. 2. Corrosion progressed inside of specimen without corrosion product when the liquid layer of $MgCl_2$ was thick.

References

[1] S. Motoda, T. Shinohara, Y. Suzuki and S. Tsujikawa, Zairyo-to-Kankyo, 50, 162 (2001)
[2] H. Masuda, Corrosion, 57, 99 (2001)

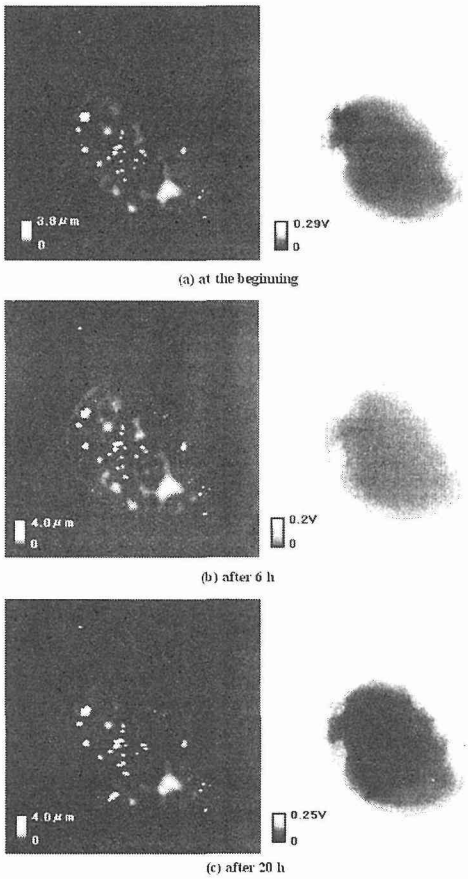

Fig.1 SKFM images of SUS304 stainless steel with attaching 0.025% $MgCl_2$.

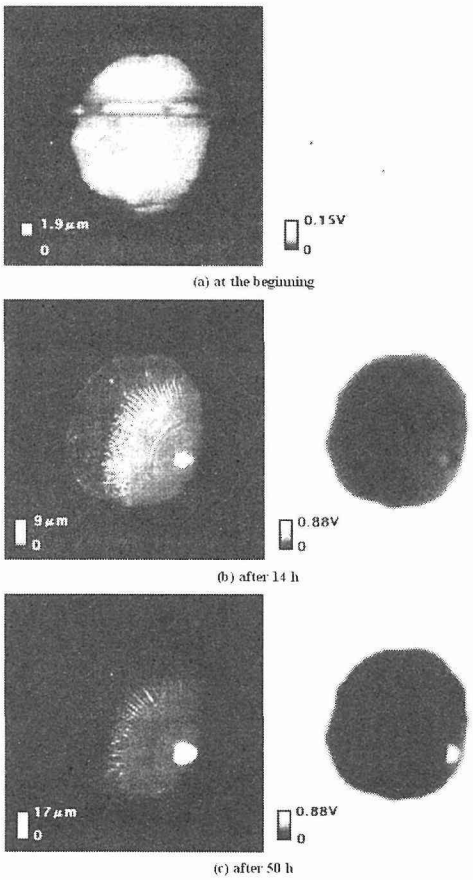

Fig.2 SKFM images of SUS304 stainless steel with attaching 0.1% $MgCl_2$.

New experimental approach to estimate the local anodic currents from the corresponding potential transients measured under open-circuit conditions

H. Inoue, Y. Tanaka, and Y. Maeda

College of Engineering, Osaka Prefecture University, Japan

1. Introduction

A prepitting event, the nucleation and the repassivation of a metastable pit, is considered to resulting in a potential transient. In the oxidizing environments, the transient has a waveform that rapidly drops to the less noble potential and then slowly recovers: the RD-type transient. This type of transient is commonly regarded as being brought by a change in the local anodic current during the prepitting event; however, the quantitative relation between them is still controversial [1,2]. To tackle this subject, we developed an experimental technique to estimate the form of the local anodic current in an open-circuit condition from the corresponding potential transient measured in the same condition [3]. We call this technique the Reverse Potential Setting (RPS) method. Inoue and others had applied the RPS method to the analysis of the potential transients of the Type-304 stainless steel in a chloride solution, and shown the electrons produced by the local anodic dissolution were solely used for the discharge of the interface capacity of the specimen, not for the electrochemical cathodic reaction on that [3].
In this study, the potential transients of pure-iron in a chloride solution were analyzed by using the RPS method.

2. Reverse Potential Setting (RPS) method

In this method, as shown in Fig.1, the potential transients measured in an open-circuit condition were reversely set to the specimen under the same condition through a potentiostat. In the solutions of the higher conductivity, the electrolysis currents produced by this potential setting were regarded as the equivalent to the local anodic currents that had brought the potential transients in the open-circuit condition.

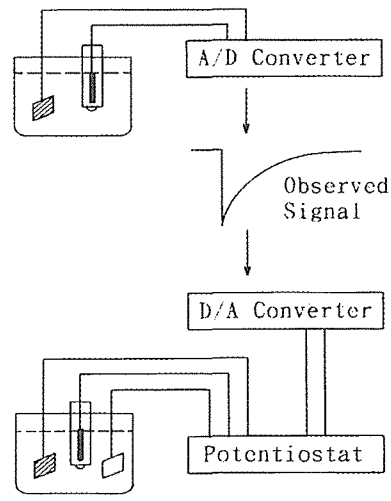

Fig.1 Conceptual illustration of the RPS method

3. Experimental procedure

Pure-iron (>99.99%) was used for the material of the specimen. It was finished with aluminum powders, and then ultrasonically cleaned in acetone. The surface of it was covered with a sealant leaving the 25mm^2 of the exposure area. A 0.2M NaCl solution including 200ppm $NaNO_2$ was employed for the test solution. Open-circuit potential of the specimen was measured every 0.5s with an Ag/AgCl reference electrode and a digital-voltmeter, at the ambient temperature. The reproduced potential data at 10ms interval through a D/A converter with a 25μV resolution were used for the reverse potential setting. The potential data at 10ms intervals were determined by linear interpolation of the data measured 0.5s intervals. The potential transient reproduced like this was set to the specimen through a

digital potentiostat; the electrode potential and the electrolysis current output were registered simultaneously at 0.5s interval using multi-channel A/D converter with 12-bit resolution.

4. Results and discussions

Three typical results obtained by the RPS method are shown in Fig.2- (A), (B), and (C). The fine lines in the upper part of each figure show the form of the potential transients used for the setting, and the bold lines in the figures display the changing rate ($\Delta E/\Delta t$) of them. The lines in the lower part are changes in the electrolysis currents, which are considered equivalent to the local anodic currents in the open-circuit condition. The chain lines on the middle of the figures indicate the time that the $\Delta E/\Delta t$ reached to zero.

In these figures, the currents reach the peaks when the $\Delta E/\Delta t$ reached to the maximum rates. This suggests that the electrons produced by a local anodic dissolution were consumed by the discharge of the interface capacity of the specimen (non-faradic reaction). However, even in the potential recovering stage; after the period divided by the chain lines, the positive currents are still existing in a certain period, and the intensity of the currents at the time when the potentials reach the E_{min}s are increased with the amplitude of the transients (E_0-E_{min}.) This means that the electrons produced by the anodic dissolution were also consumed by the electrochemical cathodic reactions (faradic reaction).

From these results, in the case of pure-iron in the chloride solution, it was considered that the counter-reaction of the local anodic dissolution was brought by both the non-faradic and the faradic reaction, though in the case of stainless steel, the former reaction had solely dominated it.

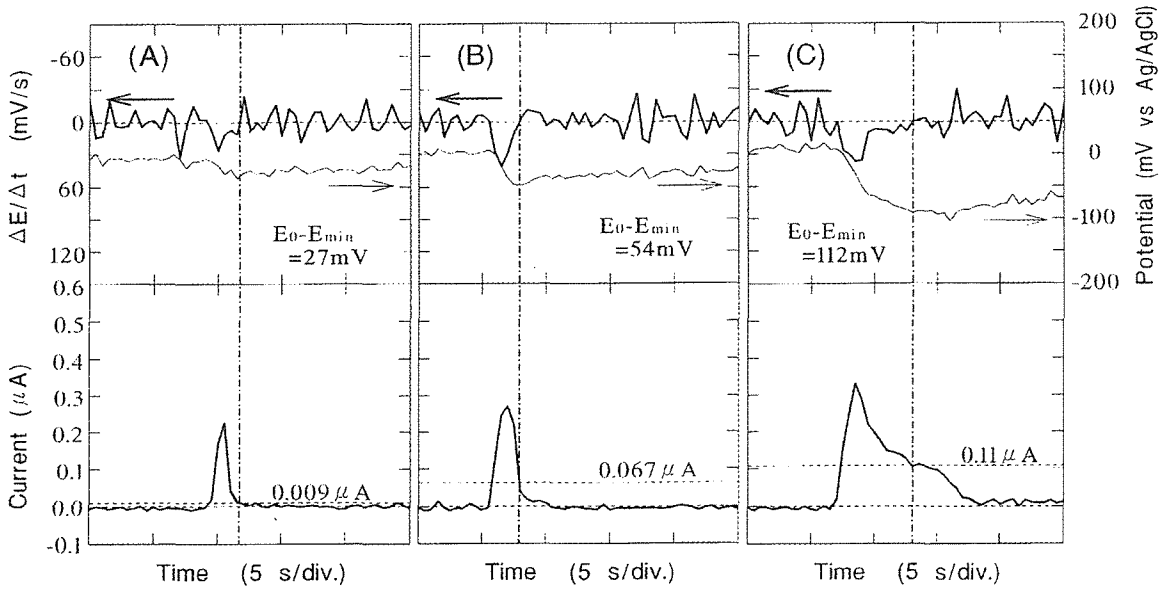

Fig.2 Typical results obtained by the analysis using the RPS method

5. Reference

[1] Hashimoto, M., Miyajima, S., and Murata, T., A stochastic analysis of potential fluctuations during passive film breakdown and repair of iron. Corros. Sci. 33 (1992), No.6, pp.885-904.

[2] Isaacs, H.S., Comments on the paper [1]. Corros. Sci. 34 (1993), No.3, pp.525-528.

[3] Inoue, H., Yamakawa, K., Kikuchi, T., and Yoneda, Y., The estimation local anodic current by reverse application of corrosion potential fluctuations. Corros. Eng. 45(2002), pp.25-32.

In situ observation of pitting of stainless steel by SR-XAFS

M. Kimura[1*], M. Kaneko[2] and T.Suzuki[1]
[1]Adv. Tech. Res. Labs., [2]Steel Res. Labs., Nippon Steel Corporation, Japan
*kimura@re.nsc.co.jp

1. Introduction

In environments containing appreciable concentrations of Cl^- or Br^-, in which stainless steels remain essentially passive, they tend to corrode at specific areas and to form deep pits. This is called pitting and is a form of localized corrosive attack that produces pits. It is very important to observe the state and concentration of metal and chloride ions under various conditions (pH, potential, temperature,...etc.) in an aqueous environment to understand pitting behavior of stainless steel. X-ray absorption and fluorescence techniques have been applied to *in situ* chemistry studies of localized corrosion. However, because of experimental difficulties, there have been few reports on direct observation of structures of ions inside pits.

In this study, we have tried to develop an *in situ* observation technique by XAFS (X-ray Absorption Fine Structures) measurements conducted on a special electrochemical cell to elucidate pitting: measure a change of concentration and coordination states of dissolved metal ions and aggressive anions near the solution/steel interface.

2. Experimental

In situ observation techniques using XAFS have been newly developed [1]. Figure 1 shows schematic diagram of the electrochemical cell for in situ XAFS measurements. A 10mm width x 30mm length x 0.1mm thickness sheet of Fe-18%Cr-12%Ni-2%Mo alloy sandwiched by Kapton films with epoxy glue was attached plastic reservoir above contained 1M LiBr solution. A potential of the steel was controlled by a potentiostat at 0.8V v.s Ag/AgCl reference electrode to corrode entire cross-section of the sample uniformly. After dissolving a few mm depths, XAFS measurements were carried out. All XAFS spectra were measured by transmission geometry shown in Fig.1. Beam size was 0.1mm height x 10mm width. The electrochemical cell attached with a stage moving X-Y-Z direction by a stepping motor was moved along Z direction to carry out XAFS measurement from dissolving interface to the bulk solution. XAFS measurements were also carried out for LiBr, LiCl solutions, and solutions and powders of chromium chlorides, bromides, oxides, hydroxides as references. XAFS measurements were performed at beam lines BL-12C [2] at the Photon Factory, KEK, Tsukuba, Japan.

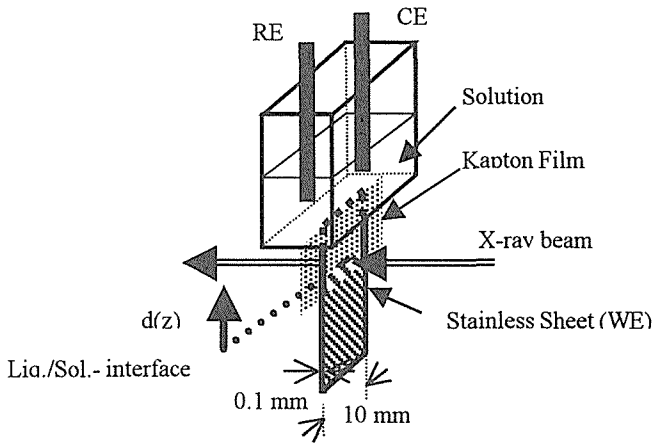

Fig.1 Schematic illustration of electro-chemical cell for *in situ* XAFS measurements.

3. Results & Discussion

Ion concentrations in the pit were investigated by *in situ* measurements of absorption at the edges. Fig.2 shows concentration of ions depends on the distance *d(z)* for chromium and bromide ions inside the artificial crevice. It is seen that the concentrations of Cr and Br are linearly dependent on the distance *d(z)*, suggesting the dissolution rate can be determined by diffusion of ions. Bromide ions shows higher concentration than expected based on the linear dependence (Fig.2), which may be caused by of lower diffusion coefficient[3].

Figure 3 shows the Fourier transforms of Cr- and Br-edge spectra of *in situ* measurements. Cr-edge spectra for all *d(z)* show peaks almost all at the same position around 0.20 nm, and the coordination number is about 5-6. The distance is located between the Cr-Br distance of $CrBr_3$ and the Cr-O distance of $Cr(OH)_3$. In contrast with this, Br-edge spectra differ as *d(z)* differs; the peak shifts toward a larger one as the distance *d(z)* increases. This shift may result from the change in coordination of Br. The curve fitting of the spectrum at *d(z)*=0.20mm showed a result for the model where Br is coordinated by Cr and O better than that where Br is coordinated simply by O. But the curve fitting for *d(z)*=3.50mm showed that Br is coordinated simply by O.

These results suggest that the Cr^{3+} ion is coordinated by OH and H_2O in the pit and that some of the ligands are exchanged by Br^- especially near the interface, which are clearly seen by Br-edge spectra. These facts indicate the formation of $CrBr_3$ salt near the interface and that hydro-bromo complex might be formed near the interface leading to lower pH than that calculated by simple hydrolysis reaction of metal salts.

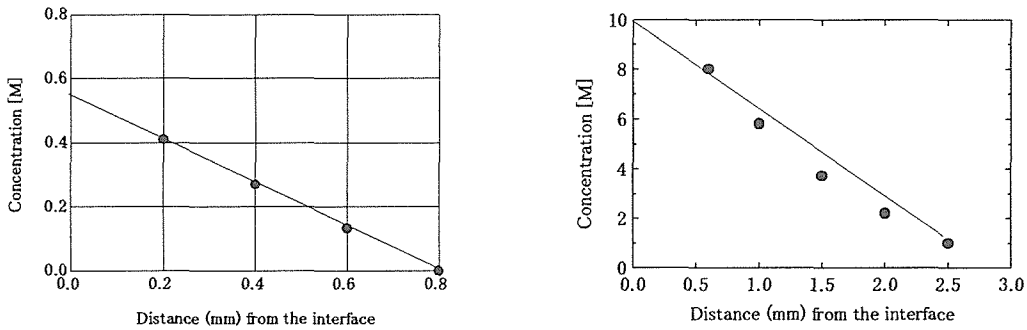

Fig.2 Chromium (left) and bromide ion concentration inside the artificial crevice.

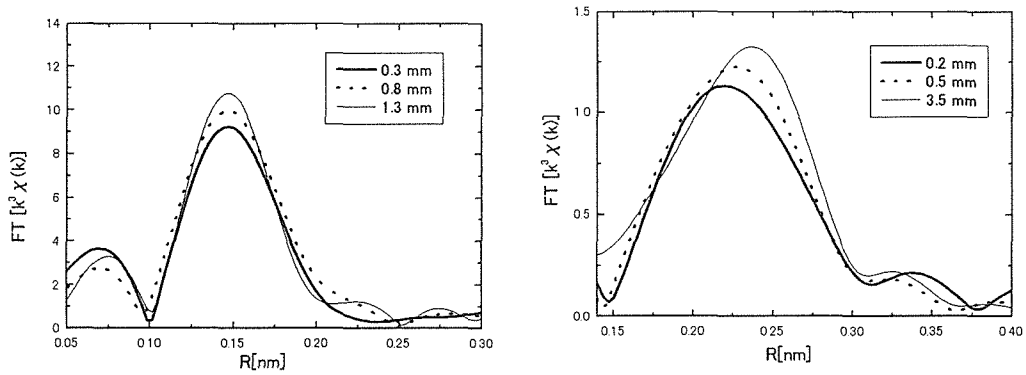

Fig.3 Fourier transforms of Cr-(left) and Br-edge spectra of *in situ* measurements.

4. Conclusion

A novel technique in corrosion science has been developed, and successfully shown that the concentration gradient and the change in the structure of ions inside a pit are a function of the distance from the interface. Linear dependence of concentration was observed. Coordination state of bromide ion at the interface was different from that of bulk solution, which might correlate with formation of hydro-bromo-complex at the interface.

References

[1] M. Kimura, M. Kaneko and T. Suzuki, J. Synchrotron Rad.,8(2001), pp.487.

[2] M. Nomura and A. Koyama, in *X-ray Absorption Fine Structure*, edited by S. S. Hasnain (Ellis Horwood, London, 1991), pp. 667.

[3] H. S. Isaacs et al., J. Electrochem. Soc., 142(1995)., pp.1111-1118.

Raman Spectroscopy for Corrosion Products Formed on Zinc and Zinc Coated Steels in Humid Air with NaCl Particles

Toshiaki Ohtsuka and Masaru Matsuda
Graduate School of Engineering, Hokkaido University, Sapporo, Japan

1. Introduction

Zinc-coated steel has widely been used as the high corrosion-resistive materials for car and construction. In these applications, the atmospheric corrosion is of considerable importance. The corrosion products produced in atmospheric environment were investigated by various ex-situ or in-situ methods. The products were identified to ZnO, $Zn(OH)_2$, $[Zn(OH)_2]_4Zn(Cl)_2$ (zinc hydroxy chloride or simonkollite), and $[Zn(OH)_2]_3[Zn(CO_3)]_2$ (hydrozincide), and the composition of the products greatly depends on the environmental condition.

In order to survey the corrosion process and mechanism of zinc, the in-situ techniques are desirable for the measurement of the corrosion products. In-situ infra-red reflection absorption spectroscopy (IRRAS) was applied for the measurements of corrosion products of zinc with NaCl precipitate in humid atmosphere containing CO_2. [1.2] Raman spectroscopy is also available for the in-situ measurement. Raman spectra of the corrosion products on zinc in aqueous and atmospheric environments have been reported by various authors. [3-6]. In this paper transient of the corrosion products is examined by in-situ Raman spectroscopy during the atmospheric corrosion of zinc with NaCl precipitate. It has been found that humidity largely influences the corrosion products.

2. Experimental

The optical corrosion cell was made of cylindrical glass, in which laser light of 514.5 nm wavelength from Ar ion laser at about 100 mW was incident to zinc plate and Raman scattering light from surface of the zinc plate was collected in the direction normal to the incident light. Artificial air (79 % 0_2 and 21 % N_2) containing a given water vapor was introduced into the cell. To control the relative humidity (RH), the air was passed before the cell inlet through pure water in a glass vessel that was controlled at a constant temperature below the room temperature of 25°C. The Raman spectra of the corroding zinc plate were periodically taken during 3 d or the longer exposure.

Before the corrosion experiment, NaCl particles were precipitated by dropping 10 μl of 3 wt% NaCl aqueous solution on zinc plates with rectangular form of 1x 2x 0.1 cm and drying in a vacuum desiccator. After drying, the NaCl particles precipitated at a density of about 0.4 $\mu g/cm^{-2}$.

3. Results

Before introducing the humid air, weak Raman spectrum of $Zn(OH)_2$ was observed on the zinc plate. Corrosion of zinc with NaCl precipitate proceeds after the introduction of humid air. When RH in the air introduced was less than 80 %, only Raman peaks corresponding to ZnO were observed, their intensities increasing with exposure time.

When RH in the air was higher than 80 %, the spectra completely changed. The initial spectra of the products were identified to aqueous $ZnCl_2$. The peak intensities of the initial $ZnCl_2$ layer depended on the RH value, increasing with increase of RH. The other spectra grew at the latter stage of the corrosion, corresponding to those of simonkollite ($[Zn(OH)_2]_4Zn(Cl)_2$). The exposure period time up to appearance of simonkollite was dependent on the RH value. With the higher RH, the time to the appearance became shorter.

4. Discussion

The corrosion products greatly depend on the environmental condition. The zinc plate with NaCl precipitate is corroded with formation of ZnO at the RH lower than 80 %. The corrosion of the zinc takes place at the RH higher than 80 % with different products. The initial water layer formed on zinc dissolves NaCl precipitate and corrodes zinc with electrochemically coupled reactions of $Zn \rightarrow Zn^{2+} + 2e$ (anode) and $O_2 + H_2O + 4e \rightarrow 4OH^-$ (cathode). The proceeding corrosion thus changes the water layer from NaCl solution to $ZnCl_2$ solution containing NaOH. As the concentration of $ZnCl_2$ increases according to the electrochemical reactions of zinc corrosion, simonkollite begins to precipitate from the concentrated $ZnCl_2$ solution by the following reaction.

$$4Zn^{2+}\ 4OH^- + ZnCl_2(aq) \rightarrow [Zn(OH)_2]_4Zn(Cl)_2$$

Reference

1. D. Persson, S. Axelsen, F. Zou. And D. Thierry, Electrochem. and Solid-State Letters, 4(2), B7 (2001)
2. F. Zhu, X. Zhang, D. Persson, and D. Thierry, Electrochem. and Solid-State Letters, 4(5), B19 (2001)
3. J. Kasperrek and M. Lenglet, La Revue de Metallurgie-CIT/ Science et Genie des Meteriaux, 1997, 713 (1997)
4. A. H.-Le Goff, S. Joiret, B. Saidani, and R. Wiart, J. Electroanal. Chem., 263, 127 (1989)
5. M. Keddam, A, H,-Le Goff, H. Takenouti, D. Thierry and M. C. Arevalo, Corros. Sci., 33, 1243 (1992)
6. M. C. Bernard, A. H.-Le Goff, and N. Phillips, J Electrochem. Soc., 142, 2162 (1995): 142, 2175 (1995).

Effect of water film thickness on atmospheric corrosion rate of carbon steel

Hideki Katayama, Kazuhiko Noda, Toshiaki Kodama and Masahiro Yamamoto*
National Institute for Materials Science (NIMS)
1-2-1 Sengen, Tsukuba-shi, Ibaraki 305-0047, JAPAN
* Nippon Steel Corporation (NSC)
20-1 Shintomi, Futtsu-shi, Chiba 293-8511, JAPAN

1. Introduction

In order to clarify the mechanism of an atmospheric corrosion that is greatly influenced by various environmental factors, it is necessary to examine the relationship between environmental factors and corrosion behavior. We developed the concentric-ring type corrosion sensor to analyze the atmospheric corrosion process of carbon steels. In this study, the corrosion sensors with an artificial seawater droplet were exposed to outdoor environment for a month. From the monitoring data of the corrosion rate and the environmental factors, the relationship between the corrosion rate of carbon steel and the environmental factors was investigated in detail.

2. Experimental

The concentric-ring type corrosion sensor (hereafter, corrosion sensor), which consists of ring and rod electrodes of SS400 steel, was used as the monitoring sensor of an atmospheric corrosion rate. The scheme is shown in Fig.1. The gap between two electrodes was determined at 100μm.

The exposure test was carried out for a month at Tsukuba located 50km northeast of Tokyo. After the corrosion sensors were installed outdoors as shown in Fig.2, the diluted artificial seawater 1600μl was dropped on it. The seawater levels were adjusted to 10, 1.0, 0.1 and 0.01mg/cm^2 NaCl conversion. The corrosion sensors were placed under the shielded condition with a concrete roof to prevent the washing of the sea salt deposition on steel surface by rainfall. The impedances at 10kHz (Z_{10kHz}) and 10mHz (Z_{10mHz}) were continuously measured using the corrosion monitor (Riken Denshi CT-5) with a multiplexer controlled by a computer. The bias ac potential between two electrodes is 10mV.

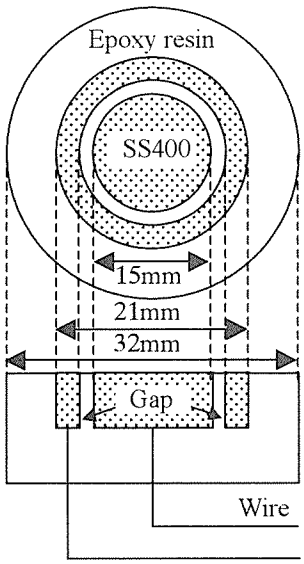

Fig.1 Scheme of concentric-ring type corrosion sensor.

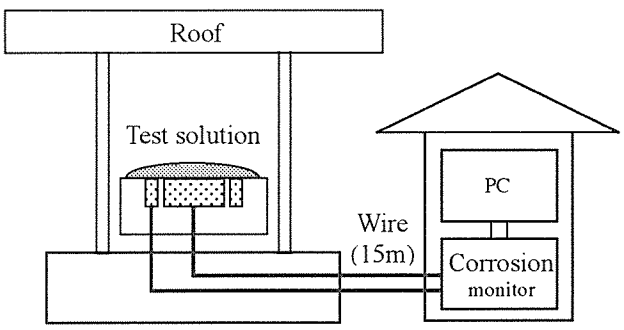

Fig.2 Schematic diagram of the outdoor monitoring system.

3. Results and discussion

The impedance characteristics for the corrosion reaction of a metal can be generally represented by the typical equivalent circuit of the interface between electrode and solution. Therefore, Z_{10kHz} and Z_{10mHz} in this study correspond to the solution resistance (R_s) and the sum of the solution resistance and the polarization resistance ($R_s + R_p$), respectively.

Figure 3 shows the change in the $1/R_p$ of the corrosion sensor with various amount of the sea salt deposition. It is known that the $1/R_p$ is proportional to the corrosion rate. The fluctuation of the corrosion rate corresponds to one-day cycle of the corrosion rate, indicating that the repetition of the corrosion rate occurs in actual environment. The corrosion sensor with the 10mg/cm^2 sea salt deposition gave relatively constant values for a month. The $1/R_p$ of the corrosion sensor with the 1.0mg/cm^2 showed higher fluctuation, and its value was often larger than that with the 10mg/cm^2. The average corrosion rate of the corrosion sensor with the 0.1mg/cm^2 was small, and its fluctuation was not large.

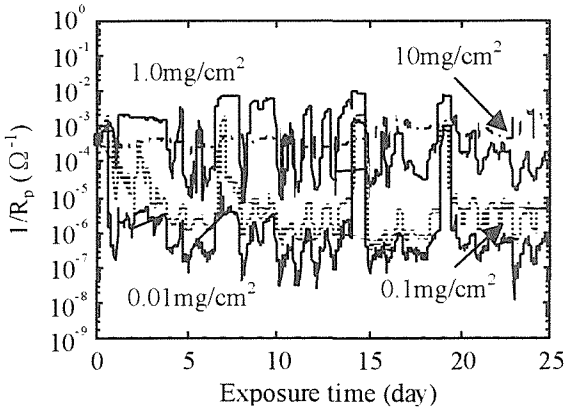

Fig.3 Change in 1/Rp of corrosion sensor with sea salt deposition for a month in outdoor environment.

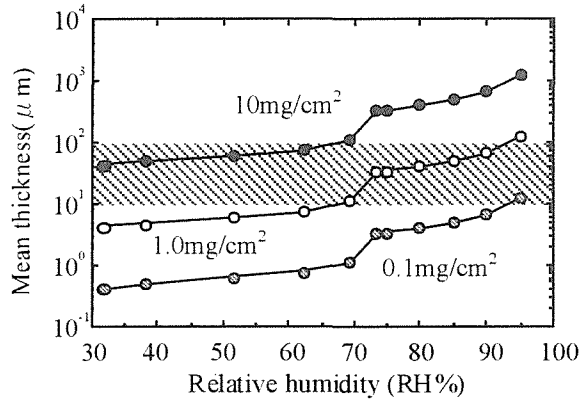

Fig.4 Relationship between the relative humidity and the mean thickness of liquid phase formed by the water absorption of the deposited sea salt.

On the effect of an airborne sea salt on the corrosion rate of carbon steels, the corrosion loss generally increases with increasing the amount of the airborne sea salt. As shown in Fig.3, the results for the corrosion sensors with the sea salt deposition of less than 1.0mg/cm^2 is identical with the fact mentioned above. In the case of the 10mg/cm^2 and the 1.0mg/cm^2 corrosion sensor, however, the result does not always agree with the fact. In order to investigate the reverse phenomena of their corrosion rates, the surfaces of their corrosion sensors were observed during the exposure test. In the daytime, the surface of the 10mg/cm^2 corrosion sensor had not dried yet, while the 1.0mg/cm^2 corrosion sensor had dried. As the result of the visual observation, the thicker water film was formed on the 10mg/cm^2 corrosion sensor than the 1.0mg/cm^2 corrosion sensor. Thus, it is concluded that the corrosion rate under relatively thin water film shows the high value. Furthermore, the mass of the absorbed water at various relative humidity was calculated thermodynamically. The result is shown in Fig.4, where the ordinate represents the average thickness of water film. In comparison of the monitoring data in Fig.3 and the environmental data, the reverse of the corrosion rate occurred at above 70%RH. Therefore, the corrosion rate of carbon steel showed a maximum in the hatched region in Fig.4, i.e., at the average water film thickness of several tens to about a hundred μm.

References

[1] A. Nishikata, S. Kumagai and T. Tsuru, Zairyo-to-Kankyo, 43(1994), No.2, pp.82-88.

Electrochemical Corrosion Measurements using Scanning Focused Light Beam

S. Fujimoto, T. Haruna and T. Shibata*

Department of Materials Science and Processing,
Graduate School of Engineering, Osaka University,
2-1 Yamada-oka Suita, Osaka 565-0871, Japan
*Fukui University of Technology
6-1 Gakuen 3-Chome, Fukui City, Fukui 910-8050, Japan

Although electrochemical measurements can analyse corrosion behaviour quantitatively and theoretically, most of them provide only uniform information. However, serious corrosion damages usually appear as localised attack. Therefore, techniques to analyse local electrochemical process have been required for corrosion study. Various type of scanning micro probe techniques have been developed in order to investigate electrochemical behaviour, such as, scanning vibrating electrode, scanning micro impedance probe, scanning micro reference electrode, etc.[1]. Scanning vibrating electrode technique (SVET) and scanning micro reference electrode provide distribution of corrosion site[2]. The lateral resolution of such technique depends not only on the size of the probe but also on dispersion of ionic current in the electrolyte. Therefore, the resolution is limited by diffusion of ionic species. Some authors had developed the electrochemical microprobe system with the focused laser irradiation, which has advantage to be focused in to less than 1 μ m in diameter. The scanning light can contribute to activate electron from valence band to conduction band to generate photo current, and also to enhance electro-chemical reaction by local heating. In this presentation we review our studies on scanning electrochemical microscopy using focused laser irradiation as *in situ* corrosion measurement techniques.

In the first, the thermally activated scanning laser enhanced electrochemical microscopy is presented[3,4]. The focused light beam (*ca.* 10 μm in dia.) generated by Ar ion laser was irradiated and scanned on specimen immersed in aqueous solution and polarised at a constant potential. The thermally accelerated current due to light irradiation was measured and displayed as 3-D map. An example of change in current due to difference of alloy composition is demonstrated in Fig.1. The laser spot was scanned across the diffusion joined boundary of Fe-8Cr and Fe-18Cr alloy, which were kept at various applied potentials in 0.5 kmol m^{-3} H_2SO_4 solution. As shown in this figure, the larger enhanced current was observed for the lower Cr content area in he active potentials, *i.e.*, -390 and –200 $mV_{Ag/AgCl}$, whereas the higher Cr content area exhibited the larger enhanced current at transpassive potential of 1600 $mV_{Ag/AgCl}$. At the passive potential of 250 $mV_{Ag/AgCl}$, however, a slight

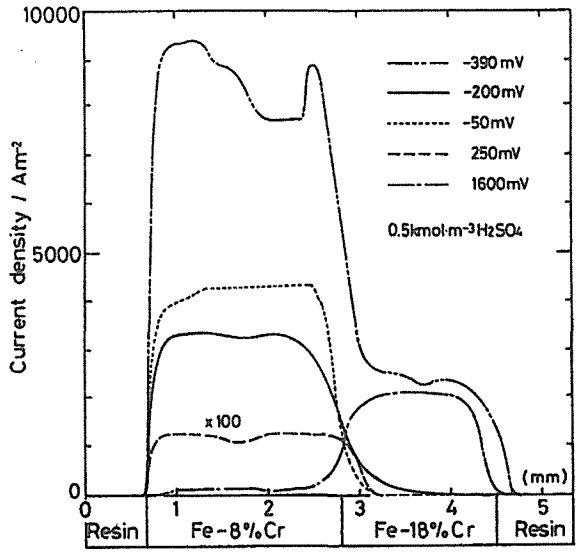

Fig.1 Line profiles for the photo-thermal enhanced current imaging across the boundary between Fe-8Cr and Fe-18Cr alloys.

enhanced current is observed for Fe-Cr and not any for the Fe-18Cr. It is concluded that the light enhanced current is roughly proportional with the factor of several tens to the current without light irradiation which is measured by polarization. Therefore, a difference in the Cr content in the alloy could be displayed across grain boundary or different phases. The scanning laser electrochemical microscopy image was obtained for a duplex stainless steel. The larger enhanced current was observed for ferritic phase. Therefore, the microscopic image showing difference of each grain were successfully displayed as a 3-d enhanced current mapping.

The focused ultra-violet light beam was also applied to display the localized distribution of photo-electrochemical response of passive film. A He-Cr laser beam was focused and scanned over Fe-Cr alloys which was polarized at passive potential. The photo current due to electron transition was detected using lock in amplifier. The steady state photo current for various Cr content Fe-Cr were similar, but the larger photo current was observed as transient peak soon after exposure of *uv* light. Therefore, the current amplitude generated by modulation of laser could be evaluated using lock-in-technique. The change in the photo current across the grain boundary of sensitised Type304 stainless steel is shown in Fig.2. In this figure two peaks of photo current across the sensitised grain boundaries are clearly displayed. With this technique, the position at which the Cr content is locally reduced was displayed. The pitting corrosion was generated the same position which was also confirmed using optical microscopy.

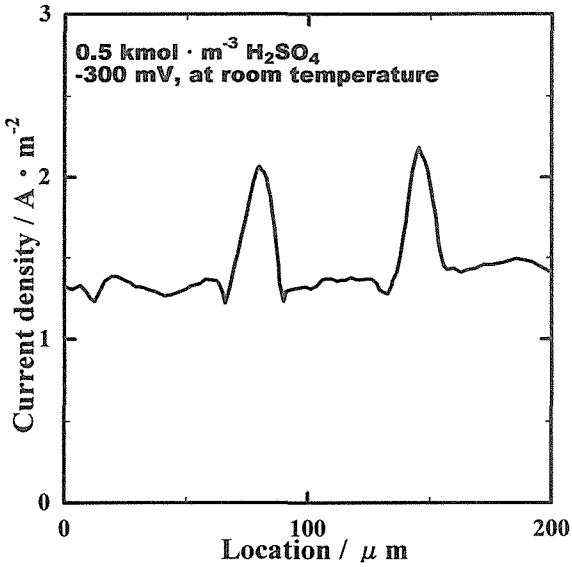

Fig.2 Line profiles for the focused uv light generated photo current imaging across the grain boundary of sensitised Type304 stainless steel.

The Ar ion laser beam was also applied for detection of hydrogen permeation in steel. Lateral distribution of accelerated cathodic current, which coincides with the evolution of hydrogen which was introduced on the other side of the specimen, was measured for high strength steel.

In this presentation, the advantage and applicability of the scanning focused light beam microscopy technique is discussed comparing with other scanning micro-electrode methods.

References

[1] H. S. Issacs and B. Vyas, "Electrochemical Corrosion Testing", ASTM STP 727, p.3 (1981).

[2] S. Fujimoto, T. Shibata and Y. Tanaka, Proceedings of 11th International Corrosion Congress, Florence April 1990. Vol.5, p.511-518.

[3] 2. S. Fujimoto, T. Shibata and T. Shono, Proceedings of International Conference on Water Chemistry in Nuclear Power Plants, Fukui, April, 1991. p.783-787.

[4] S. Fujimoto, T. Shibata and T. Shono, Corrosion Science, 32 [5/6], (1991), 669-672.

Surface potential and pH distribution in initial rusting process of low alloy steels

K. Noda, M. Yamamoto*, H. Masuda and T. Kodama
Materials Engineering Lab.,
National Institute for Materials Science (NIMS), JAPAN
*Steel Research Lab.,
Nippon Steel Corporation (NSC), JAPAN

1. Introduction

In atmospheric corrosion study of iron and steels, it is difficult to evaluate the corrosion behavior, because the conventional electrochemical method can not be applied to the study. Recently, as the observation of the atmospheric corrosion surface, a few new techniques have been applied in order to understand the behavior. The surface potential and the surface pH are also the essential factor which controls corrosion behavior as an environmental parameter, so some researcher has tried to measure the potential distribution [1-4] and the pH distribution. In this report, the rusting process of the artificial sea salt adherence iron and low alloy steel (Fe-Cr, Fe-Ni steel) was observed, and the potential distribution on the surface rusting was examined to investigate the Cr and Ni additive effect on the atmospheric corrosion in the seashore environment. The pH gradation on the surface under the atmosphere corrosion process of the low alloy sheets was determined by using the scanning chemical microscope (SCHEM), and the effect of additive element on localized function was evaluated by this result.

2. Experimental

The pure iron and low alloy steels (Fe-3mass%Cr, Fe-3mass%Ni steel) were used as the test samples. A droplet of the artificial seawater and $MgCl_2$ solution which is the component of the sea water was attached on the sample. After that, the sample was held in the room-temperature and the rust growth process was observed and the surface potential was measured by AFM/KFM system.

The low alloy steels (Fe-3mass%Cr, Fe-3mass%Ni steel) were also used as the test sample to investigate the localized pH under atmospheric corrosion environment. Corrosion cycle test was also done in order to investigate the corrosion morphology on the low alloy steels. After the tests, the rust layer was removed from the surface, the observation of the surface roughness was occur. In pH measurement, 0.1M KCl was added in the agar as an electrolyte, and the process of the corrosion by chloride ion and the moisture in this agar was chased as a surface pH distribution. The pH measuring area was 15 mm x 15 mm on the samples and in every 30 minutes. The surface pH distribution was measured by scanning chemical microscopy (SCHEM) shown in Fig.1.

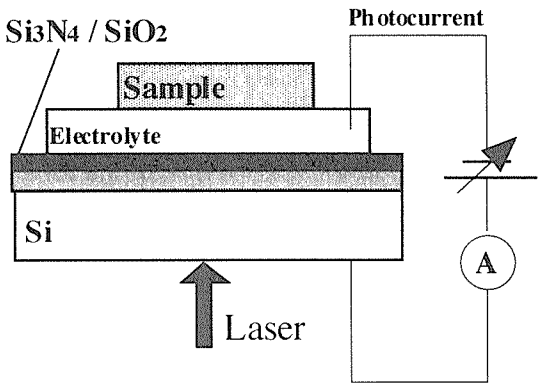

Fig.1 Schematic diagram of SCHEM for pH distribution measurement.

3. Results and discussion

At relative humidity (RH) of 40%, growth rate of rusting on iron greatly increased in comparison with the case of RH of 30% under $MgCl_2$ condition. At lower RH value magnesium chloride crystal was observed by AFM in the saline particle, while only liquid droplet was detected on iron surface placed at RH40%. At 40%RH, the growth of the rust formed in the filiform shape was observed in the droplet circumference part [5]. The relative humidity was made 40%RH after dropping the artificial sea water, and then the profile on the surface and potential distribution was measured by AFM. At the part of the less noble potential site, the filiform shaped rust grew along with the time process in this place. Therefore, it was shown that potential became less noble at the part of rusting, and the place where the dissolution reaction of the iron produced could be limited for the growth part of the rust. If the part of less noble potential can be found, prediction can be done the growth point of the rust, and the growth direction of rusting.

Figure 2 shows the pH distribution of the corroded surface on the low alloy steels after 30 min and 1 hour. The pH distribution on the Fe-Ni low alloy steel was spread for the homogeneity in all the area after 1 hour. In the case of Fe-Cr low alloy steel, after 1 hour the localized pH distribution was appeared. As the surface pH profile became heterogeneous, the corrosion on the Fe-Cr alloys under the atmospheric corrosion environment progresses for the heterogeneity. Therefore, the corrosion was caused by the pH localization with the dissolution of alloy elements. When the anodic dissolution of Cr was carried out, it is easy to decline pH and severe condition was achieved at the local site. And then the steel contained Cr was produced localized corrosion.

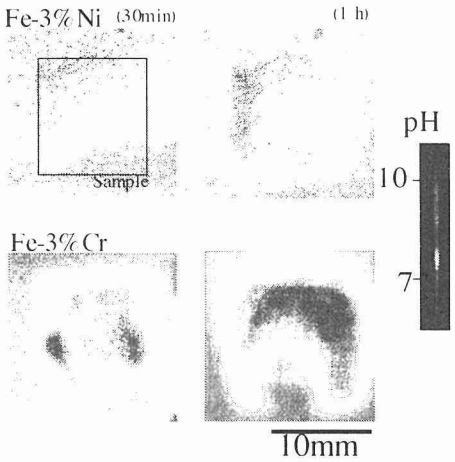

Fig.2 The pH distribution of the low alloy steel (Fe-3mass%Ni, Fe-3mass%Cr) at 30min and 1h during corrosion test.

4. Conclusions

1) The rust grew up around the droplet circumference department, and the corrosion morphology was a micro filiform in initial rusting process of steels under sea shore environment.

2) The rust growth was facilitated rapidly above 40% relative humidity under the artificial sea water and the $MgCl_2$ droplet adherence conditions. It was attributed in the $MgCl_2$ solution environment of the high concentration.

3) The small addition of Cr and Ni as the contained amount of alloy element was effective on decreasing of the corrosion rate in atmospheric corrosion environment. It could be found out by using SCHEM that the corrosion behavior on the Fe-Cr alloy was localized corrosion behavior.

References

[1] M.Stratmann, *Corros.Sci.*,**27** (1987) 896
[2] K.Noda, M.Itou, A.Nishikata and T.Tsuru, *Zairyo to Kankyo*, **47** (1998) 396
[3] A.Tahara and T.Kodama, *Zairyo to Kankyo*, **47** (1998) 391
[4] M.Yamashita, T.Doi and H.Nagano, *Zairyo to Kankyo*, **47** (1998) 384
[5] K.Noda, H.Masuda and T.Kodama, *Proc. 14th Int. Corros. Cong. 1999*, (1999)

The Effect of Surface Fixed Charge on Corrosion

M. Masuda, H. Sakamoto, K. Harada & Y. Hayashi
Dep. of Mat. Sci. & Eng., Fac. of Eng., Kyushu Univ., JAPAN

1. INTRODUCTION

The stainless steels are used in various environments because of their passivation films of the high corrosion resistance. The various artificial coatings have been examined to improve the corrosion resistance under more severe environment. However, it was pointed out that there were inevitable defects in these coating films. Especially penetrated pinhole defect became to a starting point of pitting corrosion and caused the deterioration of coated material quality. We investigated the multi-layered coating films to decrease the coating defects and found out that a proper layer order increased corrosion resistance. This effect was explained with a surface fixed charge of coating films. In this paper, we report new measurement method of surface fixed charge using with electrochemical atomic force microscope.

2. EXPERIMENTAL

The oxide films were prepared on stainless steel with the RF sputtering apparatus (ULVAC Co., BC2227). We also prepared multi-layered oxide films to evaluate the layer effect on the corrosion behavior. The film preparation condition is shown in Table 1. X ray photoelectron spectroscopy (XPS) and X ray diffraction (XRD) were used for analyzing the oxide film structure. The defect area of oxide films was evaluated with the critical passivation current of anodic polarized steel in 0.5M-H_2SO_4+0.05M-KSCN aqueous solution. The inductively coupled plasma spectrometry (ICP) analyzed the dissolved ions into the test solution from the oxide film coated steels. The anodic polarization measurements were carried out to examine the influence of the layer order of oxide films on the corrosion behavior. We made new measurement method for surface fixed charge of oxide film using the Electrochemical Atomic Force Microscope (EAFM) (SII Co., SPI3800). The scanning tip of the EAFM (SII Co., SI-AF01-A) was coated with the same oxide film of specimen, and the atomic force was measured as a function of the distance between the tip and the specimen. The tip and specimen of same oxide film have same polarity of surface fixed charge in the test solution. The EAFM measurement detects the combination of atomic force and Coulomb force. Only Coulomb force is affected by solution pH, so we can easily distinguish the Coulomb force and the atomic force. As measuring the Coulomb force in the test solutions of various pHs, minimum Coulomb force shows pH for point of zero charge (pH_{pzc}).

Table 1 *Oxide Films Preparation*

Substrates	SUS304, SUS410
Targets	Al_2O_3, SiO_2, Ta_2O_5, TiO_2, ZrO_2
Formation Condition	Gas Pressure Ar 5.3Pa, RF Power 40 kW/m^2, Substrate Temperature 573 K, Film Thickness 1 μm

3. RESULTS AND DISCUSSION

The XPS analysis showed that the chemical composition of oxide films were good agreement with the stoichiometric structure. The XRD analysis indicated that most of the oxide films were amorphous or fine crystals. The ICP analysis of the corrosion test solution showed that only substrate steel was dissolved in the solution and did not detect any element of oxide film in the corrosive solution. The oxide film of lower pH_{pzc} decreases the passivation current density and shows high corrosion resistance. This phenomenon is explained as the effect of surface fixed charge caused by the difference between oxide pH_{pzc} and solution pH. The oxide film of

lower pH_{pzc} than the test solution pH gets negative surface charge and the oxide film of higher pH_{pzc} gets positive value. The ion migration through the oxide film is affected by the surface fixed charge of oxide film. The lower pH_{pzc} oxide film layered over the higher pH_{pzc} oxide has a larger corrosion resistance than the reversely layered oxide films. And the corrosion resistance increases with the increase of the difference between two oxide layer pH_{pzc}. This phenomenon was also confirmed in pitting corrosion properties of oxide-coated steels. The pitting corrosion is generated by the anion condensation, and the ion migration and the condensation are affected by the surface fixed charge of oxide film. Such effect of pH_{pzc} was also found in the incubation time of pitting corrosion. The incubation time of the steel with the top layer of lower pH_{pzc} oxide was longer than that of the steel with the top layer of higher pH_{pzc} oxide.

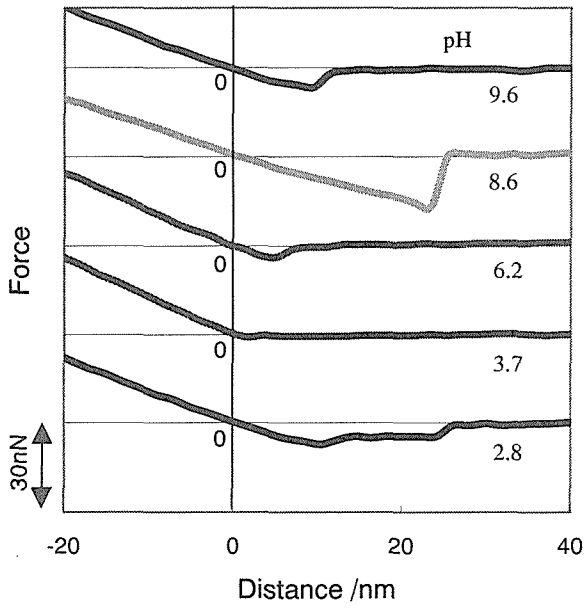

Figure 1 *Relationship between Force & Distance of EAFM.*

The relation between force and distance of the EAFM tip to the specimen in various pH solutions are shown in Figure 1. After contacting with specimen, the tip was moved until detached. The force between tip and specimen changes to attractive from repulsive with the increase of the distance, and jumps to almost 0 when the tip is detached absolutely. This adhesive force between tip and specimen changes largely by solution pH as shown in Figure 1. The adhesive force consists of the atomic force and Coulomb force. Because the atomic force is not affected by solution pH, the cause of the change of these force-distance curves is Coulomb force. This Coulomb force is repulsive because the tip and specimen with the same oxide coating have the same polarity of the electric charge. With the increase of the surface charge, the repulsive force increases and the tip is easily detached from the specimen. As the result, the maximum adhesive force shows the surface fixed charge becomes zero in a certain solution pH. So, we can get pH_{pzc} value of oxide film with the force-distance curves in various pH solutions.

4. CONCLUSIONS

We evaluated the corrosion resistance of the stainless steel covered with the oxide films by the RF sputtering method. The passive current density decreased with the decrease of the pH_{pzc} of oxide film, and the corrosion resistance was improved. In the case of double-layered oxide films of different pH_{pzc}, the steel of the top layer of lower pHpzc oxide had the lower passive current density and had the high corrosion resistance. The steel of the top layer of lower pH_{pzc} oxide had the excellent pitting corrosion resistance. These phenomenon could be explained by the effect of the difference of surface fixed charge. We proposed the new method using EAFM to measure surface fixed charge of oxide films and decided pH_{pzc} value of them.

Relationship between Localized Corrosion of Stainless Steel in Seawater and Activity of Marine Microorganisms Adhering to Surfaces

N. Washizu
Corrosion Resist Materials Group, NIMS, Japan

1. Introduction

It has been known that the open circuit potentials (OCP) for stainless steels exposed to natural seawater are ennobled and that the ennoblement can cause the localized corrosion on the surfaces of stainless steels. OCP for stainless steels exposed to synthetic seawater are not shifted as noble as OCP in natural seawater. Therefore, it is regarded that marine microorganisms would make such differences in OCP, which have the influence on occurrence of localized corrosion. The aim of this paper is a clear explanation of the mechanism acting on the ennoblement of OCP for stainless steels. For this purpose, the effect of hydrogen peroxide produced by marine microorganisms on OCP was examined.

2. Experimental procedures

Type 316 L stainless steel coupons were exposed to natural seawater for a month at various seasons. After the exposures, the specimens covered with native biofilms were used for some laboratory experiments. The concentration of hydrogen peroxide in native biofilms formed on the specimens was gauged with analytical test strips and OCP for the specimens were also measured.

Catalase and Peroxidase are typical enzymes, which resolve hydrogen peroxide into other chemical species. To disintegrate hydrogen peroxide in native biofilms on the specimens, one of these enzymes was dosed to the water, to which the specimens were exposed. Then the water temperature was varied from 23℃ to 33℃(suitable for action of the enzymes). The concentration of hydrogen peroxide and OCP were measured at each temperature.

3. Results and discussion

Fig. 1 shows the concentration of hydrogen peroxide in the native biofilms and OCP for the specimens exposed to natural seawater in summer, autumn, and winter. At a summer season (August) the concentration of hydrogen peroxide was higher than 10ppm and OCP were nobler than 0.6V vs. SHE. On the other hand, the hydrogen peroxide concentration was lower than 1ppm and OCP were less noble than 0.3V vs. SHE at a winter season (January). This result can reveal that marine microorganisms in the biofilms produced more hydrogen peroxide in the summer than in the winter, and that the higher concentration of hydrogen peroxide in the summer made OCP nobler than in the winter.

The values of hydrogen peroxide concentrations in the native biofilms on the specimens, which had been exposed to natural seawater at a summer season, are given in Table 1. At each temperature (23℃ and 33℃), the hydrogen peroxide was detected and its concentration was ranging from 10 to 30ppm in the native biofilms on the surfaces of the specimen exposed to the water including no enzyme. In the case of enzyme-dosed water, hydrogen peroxide was not detected at the elevated temperature (33℃). This result reveals that hydrogen peroxide in the biofilms was disintegrated and that there was almost no hydrogen peroxide in the biofilms covering the specimens exposed to the water with Catalase or Peroxidase at 33℃. With the water temperature dropping to 23℃, the hydrogen peroxide in the biofilms was concentrated again and its concentration rose to be values equal to the concentration without the enzyme.

Fig. 2 shows OCP for the specimens exposed to the water with and without Catalase. Before elevation of water temperature (23℃), OCP for the specimens covered with native biofilms reached approximately 0.6V vs. SHE both with and without Catalase. At the elevated water temperature (33℃), OCP for the specimen with the native biofilms in the Catalase-

dosed water fell to values equal to OCP for specimen without biofilms (0.2V vs. SHE), while OCP for the specimen with the biofilms in non-Catalase water remained nobler than 0.5V vs. SHE. This difference of 0.3V in OCP indicates the action of hydrogen peroxide in native biofilms. At 33℃, hydrogen peroxide was disintegrated with Catalase and there was almost no hydrogen peroxide in the biofilms as Table 1 shows. Table 1 also indicates that there was hydrogen peroxide in the biofilms with no enzyme. Hydrogen peroxide in the biofilms is, therefore, supposed to ennoble OCP from 0.2V vs. SHE to values higher than 0.5V vs. SHE. OCP were ennobled again according to the drop in water temperature.

Fig. 3 shows the variation of OCP for the specimens exposed to the water with Peroxidase, which is another enzyme to disintegrate hydrogen peroxide. OCP behaved in the same way as the experiment with Catalase. This result makes it more convincing that the ennoblement of OCP is caused by hydrogen peroxide in native biofilms.

4. Conclusions

Marine microorganisms in native biofilms produce hydrogen peroxide. Microorganisms are more active and produce more hydrogen peroxide in summer than in winter. A major cause of the ennoblement of OCP for type 316L in natural seawater is hydrogen peroxide in native biofilms.

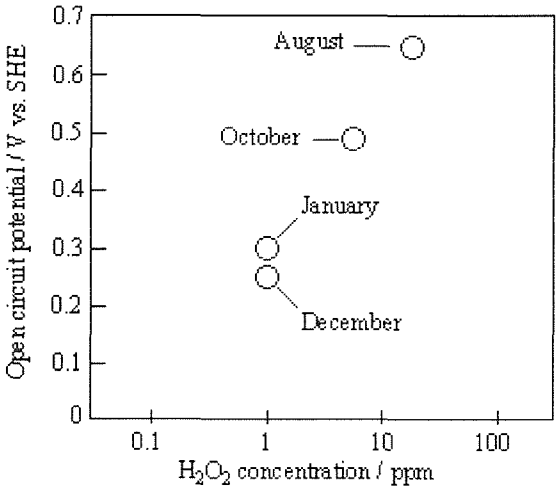

Fig. 1 Variation in concentration of hydrogen peroxide and open circuit potential for type 316L.

Table 1 Concentration of H_2O_2 in biofilms.

Temp.	Enzyme	$[H_2O_2]$
23℃	No enzyme	10 - 30 ppm
	Catalase	10 - 30 ppm
	Peroxidase	10 - 30 ppm
33℃	No enzyme	10 - 30ppm
	Catalase	< 1 ppm
	Peroxidase	< 1 ppm
23℃	No enzyme	10 - 30 ppm
	Catalase	10 - 30 ppm
	Peroxidase	10 - 30 ppm

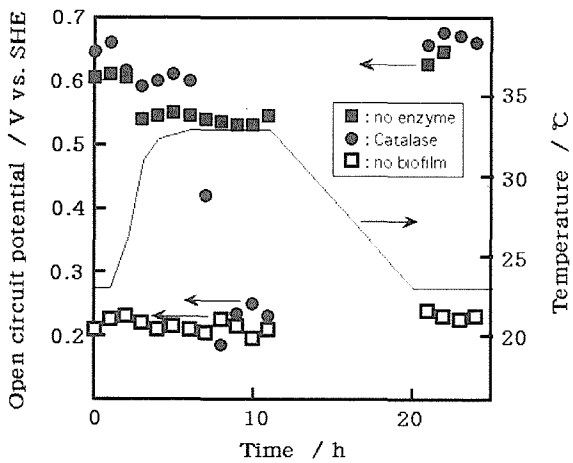

Fig. 2 Effect of varied temperature and Catalase on open circuit potential for type316L.

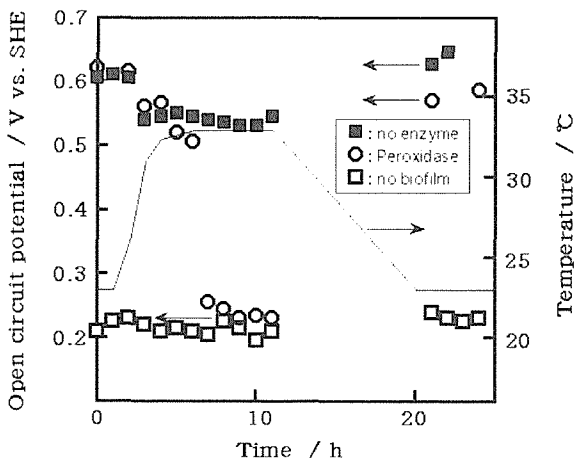

Fig. 3 Effect of varied temperature and Peroxidase on open circuit potential for type316L.

Author Index

Author Index


NIMS